INAUGURAL-DISSERTATION
zur
Erlangung der Doktorwürde
der
Naturwissenschaftlich-Mathematischen Gesamtfakultät
der
Ruprecht-Karls-Universität
Heidelberg

vorgelegt von
Dipl.-Ing. Pau Montes
aus València (Spanien)

Tag der mündlichen Prüfung: 06.12.2006

Dynamic Cone-beam Reconstruction for Perfusion Computed Tomography

Gutachter:

Prof. Dr. Dr. h.c. mult. Willi Jäger
Prof. Dr. Dr. h.c. Hans Georg Bock

KURZFASSUNG

Perfusions-CT (Computertomographie) ist ein dynamisches Bildgebungsverfahren für die Bestimmung der Durchblutung von Gewebe. Das begrentzte Sichtfeld jetziger CT-Detektoren beschränkt die Anwendung auf Perfusionsstudien kleiner Volumen. Die Einführung von Oberflächendetektoren in CT wird es künftig ermöglichen, Perfusionsstudien ganzer Organe durchzuführen, was die klinische Relevanz der Perfusions-CT steigern wird. Andererseits, wird dies die Patientenbelastung sowie auch die Ansprüche an die Rekonstruktionshardware (aufgrund der großen generierten Datenmenge) erhöhen. Diese Dissertation befasst sich mit dynamischen Rekonstruktionsalgorithmen für Scanner mit Oberflächendetektoren im Rahmen der Perfusions-CT. Ihr Schwerpunkt liegt in der Entwicklung von Verfahren, die effizient bezüglich der Patientendosis und des Rechenaufwands sind.

Der erste Teil der Arbeit ist der dynamischen Rekonstruktion von Objekten mit zeitabhängigem Dämpfungskoeffizienten gewidmet. Als Ergebnis einer theoretischen Analyse stellt man fest, dass die Rekonstruktion aus Projektionen eines begrenzten Winkelintervals über mehrere Rotationen als nicht-ideale Abtastung mit einem regulären Abtastmuster interpretiert werden kann. Die dynamische Rekonstruktion erfolgt dann durch die Schätzung eines kontinuierlichen Signals aus den Abtastwerten mit einem effizienten Interpolationsverfahren. Es wird ein Zeitinterpolationsansatz vorgeschlagen, der auf polynomialer Splineinterpolation beruht. Dieser Ansatz erhöht die Zeitauflösung für eine gegebene Abtastrate und ermöglicht dadurch den Einsatz von Scannern mit niedrigen Rotationsgeschwindigkeiten für dynamische Bildgebung. Unter der Annahme, dass die maximale Frequenz des dynamischen Prozesses bekannt ist, kann man die Abtastrate gemäß dieser Frequenz anpassen, um nur die notwendigen Daten für die Schätzung des kontinuierlichen Signals aufzunehmen. Dies führt zu einer Reduktion der aufgenommenen Daten und daher des Rechenaufwands der Rekonstruktion.

Im Zeitinterpolationsansatz wird Rauschen nicht berücksichtigt. Der Rauschpegel in CT ist umgekehrt proportional zur angewandten Röntgendosis. Gemäß der o.g. Abtastungsinterpretation kann man Rauschen reduzieren, indem die Bandbreite des geschätzten Signals auf die Bandbreite des schnellsten Perfusionssignals im zu rekonstruierenden Volumen begrenzt wird. Dies wird als optimal-SNR Schätzung bezeichnet. Eine optimal-SNR Rekonstruktion kann unabhängig von der Anzahl der durchgeführten Scans vollbracht werden, solange die Abtastbedingung erfüllt wird. Auf diesem Prinzip aufbauend wird der Zeitinterpolationsansatz zu einem Zeitglättungssansatz mit polynomialen Splines erweitert. Dieser Ansatz ermöglicht es, die Bandbreite der rekonstruierten Sequenz anzupassen, so dass eine optimal-SNR Rekonstruktion für die angewandte Dosis erzielt wird. Im Vergleich zum Standard-Rekonstruktionsverfahren kann dies zweifach genutzt werden. Entweder reduziert man die Dosis, während die Bildqualität erhalten bleibt, oder man verbessert die Bildqualität bei Anwendung der gleichen Dosis.

Die Ergebnisse dieser Arbeit stellen den ersten Schritt in Richtung auf die Benutzung von C-bogen Systemen in Perfusionsbildgebung dar.

ABSTRACT

Perfusion CT (Computed Tomography) is a dynamic imaging technique whose aim is to assess the blood supply to tissue. The limited field of view of current CT detectors restricts its use to perfusion studies of a small volume. The introduction of large area detectors in CT, however, will allow perfusion studies of entire organs, increasing the clinical relevance of perfusion CT. On the other hand, this will also increase patient exposure and requirements for the reconstruction hardware as a consequence of the huge amount of acquired data. This thesis deals with dynamic reconstruction algorithms for scanners with large area detectors within the framework of perfusion CT. Its main focus lies on the development of methods efficient in terms of both the X-ray exposure and the computational cost.

The first part of the thesis is devoted to the problem of dynamic reconstruction of objects with time dependent attenuation. Theoretical analysis reveals that the reconstruction from projections in a limited angular interval over several rotations can be interpreted as a non-ideal sampling on a regular grid. Dynamic reconstruction can then be performed by estimating a continuous signal from the samples using an efficient interpolation scheme. A temporal interpolation approach based on polynomial spline interpolation is proposed. This approach increases the temporal resolution for a given sampling rate and thus enables the use of slow rotating scanners for dynamic imaging purposes. Assuming that the maximum frequency of the dynamic process is known, the sampling rate can be adapted according to this frequency in order to acquire only the necessary data to estimate the continuous signal accurately. This leads to a reduction of the acquired data and therefore of the computational complexity.

The temporal interpolation approach does not consider noise. The noise level in the images is inversely proportional to the applied dose. According to the sampling interpretation, noise can be reduced by limiting the bandwidth of the estimated continuous signal to the bandwidth of the fastest perfusion signal in the volume of interest. This is denoted as optimal-SNR estimation. Optimal-SNR reconstruction can be carried out independently of the number of scans performed during acquisition as long as the sampling condition is fulfilled. Based on this principle, the temporal interpolation is extended to a temporal smoothing approach with polynomial splines. This approach allows adapting the temporal bandwidth of the reconstructed sequence, yielding an optimal SNR reconstruction for a given total applied dose. This can be used either to reduce dose while preserving image quality as in standard reconstruction, or alternatively to increase image quality while using the same dose as in the standard procedure.

Finally, the results obtained in this thesis represent the first step towards the use of C-arm systems for perfusion imaging purposes.

ACKNOWLEDGEMENTS

First and foremost, I wish to express my special thanks to my supervisor Prof. Willi Jäger for giving me an opportunity under difficult circumstances, providing a fruitful research environment and for letting me follow ”my way”.

This research project has been financially supported by Siemens AG, Medical Solutions and partially by the International Graduate School IGK710, ”Complex Processes: Modeling, Simulation and Optimization”. Their contribution is gratefully acknowledged.

I am deeply indebted to Dr. Günter Lauritsch at Siemens AG, Medical Solutions for his support and guide during the whole project as well as for taking his time to discuss constructively every aspect of the work.

Additionally, I would like to thank:

My colleagues of the Applied Analysis and Visualization and Numerical Geometry Groups for the open and friendly working environment. Particularly Dr. Susanne Krömker for always having an open door for any imaginable question, Dr. Franziska Matthäus for her patient listening and valuable feedback, and Dr. Thomas Lorenz, Eberhard Michel and Igor Doktorski for their effort and infinite patience in trying to explain maths to an engineer.

The personnel at the IWR who have been source of stimulating discussion and constructive solution finding. Particularly, my second advisor Prof. Georg Bock and Dr. Moritz Diehl for accounting for a different scientific point of view and Prof. Fred Hamprecht for providing original suggestions and for his time.

Prof. Sabine Heiland and Dr. Peter Schramm from the department of Neuroradiology of the University of Heidelberg for introducing me to the clinical side of medical imaging.

The personnel at the departments of Angiography, Fluoroscopic and Radiographic systems and Computed Tomography at Siemens AG, Medical Solutions for giving me the opportunity of presenting the intermediary results of this thesis at their respective seminars and for their valuable feedback. Particularly Ernst Klotz and Dr. Annabella Rauscher for the fruitful discussions.

Researchers at external departments or institutions who gave me the opportunity to discuss my results with them: Dr. Christian Lantuejoul, Prof. Michael Unser, Prof. Wolfgang Kuchinsky, Prof. Marc Kachelrieß and Prof. Willi Kalender.

My proofreaders: Prof. Sabine Heiland, Dr. Franziska Matthäus, Dr. Susanne Krömker, Dr. Guillermo Ayala, Dr. Ralf Schulz, Dr. Günter Lauritsch, and specially Dr. Richard Webb for his priceless language style advice and Dr. Thomas Walter for taking his time when he had none.

Gabriela Schocke for providing a drop of humour to sweeten every bitter coffee during my stay at the IWR.

Silvia Harmsen for providing an excellent atmosphere in the office, solving any Latex problem even before I had it and providing stroopkoeken on a regular basis.

Dr. Guillermo Ayala and my father for their patient listening and their online statistics support.

My mother who supported me in her most difficult circumstances and believed in me until the last moment of her life.

Finally, my sincere thanks go to Mareike for her support and understanding, her capacity to make difficult situations bearable just with a smile, and many other things I cannot find words for.

To Mareike

To my parents

CONTENTS

LIST OF FIGURES

LIST OF TABLES

CHAPTER 1.

INTRODUCTION

1.1. MOTIVATION. A CONTRIBUTION TO PERFUSION CT IMAGING

Perfusion CT is a dynamic imaging technique based on Computed Tomography whose aim is to assess the blood supply to tissue. In perfusion CT a series of CT scans is performed after the injection of a contrast agent. The reconstructed sequence of images contains information about the temporal evolution of the concentration of contrast agent. This information is used to compute image maps of functional parameters that describe the state of the blood supply. This technique has already found its way into clinical routine. Together with perfusion MRI (Magnetic Resonance Imaging), they represent the primary imaging techniques for patients with symptoms of stroke [Wiesmann et al., 2004]. Perfusion CT enables diagnosis in the majority of the cases and presents a series of advantages compared to perfusion MRI; these include higher availability of CT scanners, shorter protocol times and lower cost. On the other hand, perfusion MRI allows more reliable diagnosis of some pathologies. However, the diagnostic capabilities of perfusion CT are not yet fully exploited as indicate the results of several clinical studies in the last years, e.g. [Wintermark et al., 2002] and [Schramm et al., 2004]. One of the main limitations of perfusion CT is that it produces functional maps of only a limited number of slices, i.e. only a small volume. The advent of large area detectors will enable perfusion CT studies of a volumetric region of interest which will lead to an increase in the clinical relevance of this method.

The high number of scans together with the dynamic nature of the process of contrast agent flow cause a series of limitations in perfusion CT. Some of these aspects will gain in importance with the introduction of large area detectors. One of the most constraining aspects is the exposure of the patient to X-ray radiation. X-rays are ionising radiation so that the dose applied should be kept as low as possible. Unfortunately, the noise level in CT images is inversely proportional to the dose applied. In perfusion CT, the amount of dose is due to not only one but several CT scans. For this reason, the dose in each of them has to be kept low and therefore images are very noisy. This strongly constrains the computation of functional parameters. Another limiting issue is the huge amount of data obtained during the scans. These data must be processed fast by the reconstruction algorithm to a sequence of images. This sequence is the input for the software package that computes the functional parameters. With large area detectors, the amount of input data increases dramatically and becomes a very restrictive aspect for the reconstruction algorithm. On the algorithmic side, a point to consider is the time dependence of the attenuation coefficient. Standard CT reconstruction algorithms are usually based on the assumption that the object does not change during the scan time. After an injection of contrast agent, however, the attenuation value of blood is time dependent. For this reason, only CT imaging devices with high rotational speeds can be used for perfusion imaging purposes. Finally, due to the long acquisition times of typically 40 s, the patient might move on the patient bed. This is a major problem since without

correction, the acquired dataset becomes useless and the patient is exposed to ionising radiation in vain.

This thesis deals with dynamic reconstruction algorithms for perfusion CT. Its main focus is on the development of reconstruction algorithms for large area detectors which are efficient in terms of both X-ray exposure and computational cost.

1.2. Description of the Contents

The first part of this thesis is composed of two review chapters which provide the fundamentals for the work developed. Chapter 2 is devoted to the description of the biomedical context. It describes the function of microcirculation and shows how it can be assessed using dynamic CT. It finishes with a discussion about the limitations of this procedure. The following chapter describes the principles of Computed Tomography from the physical principles of X-ray generation to 3D reconstruction from cone-beam projections. It is designed as a reference for the CT concepts used in the following chapters.

Chapters 4 to 6 contain the original contribution of this thesis. In chapter 4, we concentrate on the problems caused by the dependence of the attenuation coefficient on time. We first propose a model for the temporal evolution of the concentration of contrast agent which will be used throughout the thesis. Subsequently, we provide a theoretical analysis of reconstruction from projections of an object with time dependent attenuation. Following, we use the obtained theoretical results to propose a temporal interpolation approach for dynamic reconstruction which efficiently exploits the acquired data. This approach can be used either to attain a high temporal resolution or to reduce the necessary input data and thus the computational complexity of the reconstruction. We finalise this chapter by presenting numerical simulations both to verify the theoretical analysis and to assess the performance of the presented approach.

In chapter 5 we address the problem of dynamic reconstruction in the presence of noise. We first introduce a model for the temporal behaviour of noise in dynamic CT. Based on this model we propose a method to obtain an optimal noise level in the reconstructed sequence for a given applied total dose. These results are used to extend the temporal interpolation to a temporal smoothing approach. This new method enables dynamic reconstruction with an optimal signal to noise ratio for a given total dose even with slow rotating systems.

The used software tools are described in chapter 6. The central part of this chapter is concerned with the description of the *CT Project* library, a C++ library for dynamic reconstruction from cone-beam projections developed during this thesis. All static and dynamic reconstruction algorithms appearing in the text are implemented in this library. This library implements all the static and dynamic reconstruction algorithms that appear in the text.

In chapter 7 we provide a general conclusion about the results obtained in this thesis and some proposals for further research.

Finally, a series of appendices completes the text. Appendix A contains a list of abbreviations and a explanation of the notational conventions. The fundamentals of signal processing used in chapters 4 and 5 are presented in appendix B. Appendix C gives a description of the phantoms used in the numerical simulations. The last appendix, provides an analysis of the computational complexity for the proposed algorithms.

The main original contributions of this thesis are:

- A theoretical analysis of the effect of rebinning and FDK-like reconstruction with projections from a time dependent object (sections 4.3.3 to 4.3.5).
- The TIA-TFDK and TIA-CFDK algorithms for dynamic reconstruction from cone-beam projections (section 4.4.3).
- An analysis of the temporal behaviour of noise in dynamic CT (section 5.2).
- The TSA-TFDK and TSA-CFDK algorithms for dynamic reconstruction with optimal SNR from noisy cone-beam projections (section 5.3.2).

CHAPTER 2.

FUNCTIONAL IMAGING WITH CT

This chapter provides a description of the biomedical context of this thesis. First, perfusion CT is introduced in the context of functional imaging as a technique that allows to assess the state of the microcirculation of a tissue. After a short introduction in the physiology of circulation, the concept of perfusion is discussed and its relevance to assess the state of a tissue is stressed. A method is presented to compute perfusion and other functional parameters from the temporal evolution of the concentration of a tracer in blood. We describe the clinical procedure followed to obtain a sequence of CT images containing the temporal evolution of the concentration of a tracer (perfusion CT protocol). Finally, we discuss the limitations of this technique.

2.1. INTRODUCTION. MEDICAL IMAGING TECHNIQUES

Medical imaging was born with the discovery of X-rays by Röntgen in 1895. For the first time it was possible to examine the interior of the body with non-invasive techniques. X-ray projection imaging became immediately an essential tool for medical diagnostics where they are still widely used. An X-ray beam with constant intensity experiments a different attenuation depending on the tissue it goes through, the detected intensity provides then information about morphology. Despite their relevance in diagnostics, their limitation was early identified. The attenuation effects of the traversed tissues are superposed, so that only the tissues which cause a very high attenuation are represented well in the image. This drawback could be first overcome with the introduction of Computed Tomography in the early seventies. The presentation of the first Computed Tomography scanner by Hounsfield in 1972 and the publication of his work one year later [Hounsfield, 1973] marked the beginning of a new era in the field of medical imaging. This technique allowed to obtain images of a transversal section of the body with non-invasive methods. The introduction of spiral CT at the late 80s extended the use of computed tomography to fast volumetric imaging [Kalender, 2000].

In the middle 80s an alternative imaging modality was introduced in the medical field: Magnetic Resonance Imaging (MRI). Contrary to CT, MRI does not use X-rays but a strong magnetic field and radio wave pulses in the MHz frequency range. By exciting certain molecules (typically water) of a tissue in a constant magnetic field by radio wave pulses of a certain frequency, these molecules emit themselves radio waves which are appropriately detected. The measured signals are used to compute an image.

Both imaging techniques provide detailed information about morphology and have been widely used since their introduction for the identification of pathologies based on changes of the morphology. The X-ray attenuation coefficient depends mainly on the density of the tissue. For this reason, CT images provide detailed information about tissues with high physical density as bone and

calcifications. On the other hand, since the excited molecules are usually water, MRI provides a higher sensitivity to differentiate soft tissue. The clinical application areas of both methods overlap in many cases.

This short introduction to morphological imaging in medical applications cannot be closed without mentioning ultrasound imaging. While CT and MRI use electromagnetic radiation in different frequency ranges for imaging purposes, ultrasound imaging uses pressure waves. In ultrasound imaging, the different reflexion properties of tissues are exploited to generate slice or 3D images. Among all imaging techniques, ultrasound is the less invasive and is therefore widely used for fetal imaging and also in pediatric radiology. It exhibits, however, a very poor spatial resolution compared to other techniques as CT or MRI.

2.1.1. Functional Imaging

An alternative to morphology imaging, nuclear medicine, appeared at the end of the 60s with a different aim: visualising function. The principle of nuclear medicine consists in injecting an organ specific radiopharmaceutic contrast agent to the patient and measuring the decay quanta emitted from the body. From these measurements an image is reconstructed which gives information about organ activity. The result is the visualisation of a biochemical process. Two methods are differentiated depending on the radionuclides used. In Single Photon Emission Computed Tomography (SPECT) the radionuclides decay emitting gamma quanta. In Positron Emission Tomography (PET) they decay emitting positrons [Oppelt, 2005]. The measured activity is associated with a position in space but no information about morphology is delivered. For this reason these methods are often superimposed to morphological information from CT or MRI data.

During the last two decades the field of functional imaging has stopped being exclusive to nuclear medicine. The introduction of functional MRI (fMRI) and the whole variety of techniques of molecular imaging have made functional imaging an active area of research which has led to numerous new applications. Several imaging modalities that were initially used for the visualisation of morphology have found their way into this growing field. These have the advantage to provide both functional and morphological information in a unique procedure but, on the other hand, they only cover a small range of applications. Within this context, techniques both with CT and MRI have been developed to assess the state of microcirculation; these techniques are commonly known as perfusion CT and perfusion MRI. The methods developed in this thesis are situated within the context of perfusion CT.

2.2. Overview of Circulation and Microcirculation

In this section the physiological concepts used throughout this thesis are presented. If not otherwise indicated, the information was extracted from [Schmidt et al., 2000, Guyton and Hall, 1996].

The main purpose of the circulation is the delivery of nutrients to the tissues and the removal of cellular excreta. The transport of nutrients is performed by blood that circulates in the vascular system. This system consists of vessels of different types; these are classified in arteries, arterioles, capillaries, venules and veins (see figure 2.1). The function of arteries is to transport blood under high pressure to tissues. They end in arterioles which are the last small branches of the arterial

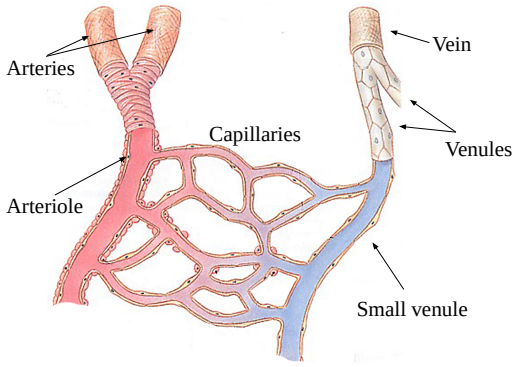

Figure 2.1. Types of vessels in the vascular system and a capillary network. Image from [Parker, 2006].

system. Blood flows further to the capillaries where the exchange of nutrients and other substances with cells takes place. Finally, the outflow is collected by venules which converge to veins.

Blood circulates through the vascular system in a continuous cycle. A scheme of this cycle is shown in figure 2.2. Oxygenated blood leaves the lungs and flows towards the right side of the heart through the pulmonary vein. From there it is pumped into the aorta and distributed through the arteries towards all tissues of the body. After it transits the capillaries, blood is collected by veins and flows finally through the venae cavae to the left side of the heart from where it is pumped towards the lungs. There it is oxygenated and starts its cycle again.

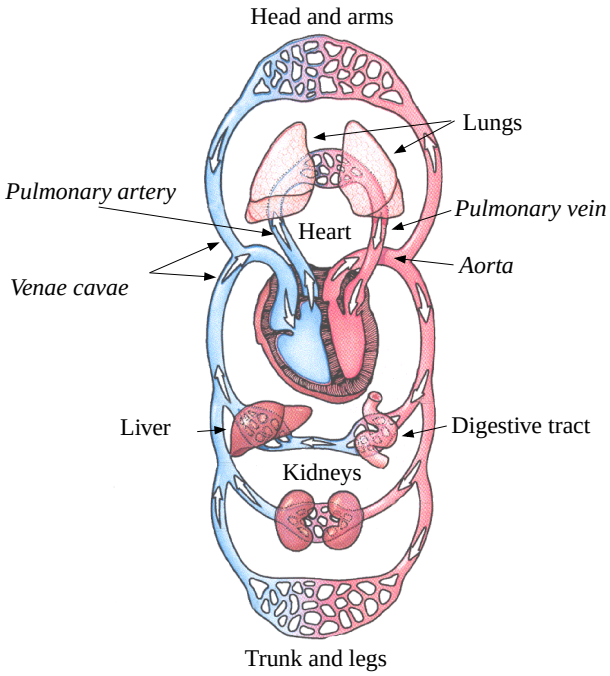

Figure 2.2. Scheme of the blood cycle. Image from [Teachnet, 2006].

Vessel type	Cross sectional area	Velocity
Aorta	2.5 cm^2	33 cm/s
Arterioles	40 cm^2	2.06 cm/s
Capillaries	2500 cm^2	0.03 cm/s
Venules	250 cm^2	3.3 cm/s
Venae cavae	8 cm^2	10.3 cm/s

Table 2.1. Approximate total cross sections of vessels of each type and average velocity of blood.

Due to the different elasticity of vessels and the continuous adaption of vessels to tissue needs, blood flow in vessels is a very complex process. There are though some general facts that can be outlined. The different types of vessels have different typical cross-sectional areas. If we put all vessels of the same type together we get a total cross-sectional area for each type of vessel which is given in table 2.1. The same volume of blood that leaves the vessels of one type, i.e. arteries, in a given time interval, flows into vessels of the next type, i.e. arterioles. The volume of blood per unity of time equals the velocity of blood times the cross-sectional area. Since the total cross-sectional areas are different for each vessel type, it follows that the velocity of blood in each vessel type is inversely proportional to the corresponding total cross-sectional area. Typical values are given in table 2.1.

Another important aspect is that blood flows, in general, parallel to the axis of the vessel, i.e. blood is a laminar fluid. There are some situations where blood flow becomes turbulent, e.g. when blood is pumped by the heart into the aorta or arteria pulmonalis or in partially blocked vessels (stenosis). This disturbances are, however, very localised both in space and in time.

2.2.1. Microcirculation in Tissue

The concept of microcirculation applies to the fragment of the circulatory path from the arterioles to the venules (see figure 2.1). Here, the most important function of the circulation occurs: the delivery of nutrients to the tissues and the removal of cellular excreta.

The human body is composed of tissues, i.e. substances made up of cells that perform a similar function. The space between cells in tissue is called interstitium and the fluid in these spaces interstitial fluid. The capillary networks through the tissues are sufficiently dense for every cell to be ”close” to a capillary. This ensures that every cell can receive nutrients carried by blood and deliver residual substances to it. This exchange process is principally carried out by diffusion through the thin capillary walls. Tissue supply needs are not constant; the vascular system provides mechanisms to adapt the blood flow in the capillary network to its needs by dilation and contraction of blood vessels. We will use hereafter the term *tissue* to denote the cells and the capillary network that supplies them.

The walls of the capillaries are composed of an unicellular layer of endothelial cells surrounded by a membrane. These cells are connected to each other in such a way that an intercellular cleft between cells is left. The exchange takes place both through the cell walls and through the cellular clefts. Big molecules are transfered through the latter. The intercellular space between cells differ in some organs to meet their special needs. In particular in the brain, the junctions between cells are tight so that only very small molecules pass into the brain tissue. This is known as the blood-

brain barrier. In the liver, the clefts are wide open and therefore big molecules can freely diffuse to the extravascular space (interstitium).

The fundamental physiological parameter that describes the process of blood supply to a tissue is perfusion. It describes the nutritive blood supply to an element of tissue. Quantitatively, in the context of perfusion imaging, it is defined as the millilitres of arterial blood delivered per minute per millilitre of tissue [Edelman et al., 1996]; hence, it has units of rate (min^{-1}). Another important parameter is blood volume which represents the fraction of tissue volume occupied by blood. Tissue function is critically dependent on blood supply. Hence, perfusion levels provide valuable information about the state of a tissue. However, their combination with blood volume measurements extends dramatically the diagnostic possibilities [Miles and Griffiths, 2003]. A reduction in perfusion leads to a compensatory dilatation of blood vessels. Continuated low perfusion levels though lead to irreversible tissue damage (infarct). Infarction is associated with loss of the autorregulatory dilatation of vessels. Therefore reduced perfusion with increased blood volume indicates a reversible damage, whereas a matched reduction in perfusion and blood volume suggests infarction.

2.3. Measurement of Perfusion with CT

In this section, methods to derive perfusion measurements from CT data are presented, technical details about CT will be given in chapter 3.

Computed Tomography (CT) produces slice images representing the spatial distribution of an X-ray attenuation coefficient. By injecting certain chemical substances intravascularly, the X-ray absorption of blood can be increased, enhancing thus its contrast in the image. As a consequence, these substances receive the name of contrast agents. Contrast agents exist for any medical imaging modality. In the case of CT, these agents are iodine-containing organic compound solutions which are transported by blood [Miles et al., 1997].

The methods used to perform perfusion measurements with CT are based on tracking the concentration of a tracer transported by blood. A very attractive property of CT is that the grey value in the images, i.e. the X-ray attenuation coefficient, is proportional to the concentration of contrast agent [Miles et al., 1997]. This suggests to use a contrast agent as tracer and, after the injection, obtain a series of CT images of a given region and subtract from every image the background, i.e. a CT image of the region obtained without contrast agent. In the sequence obtained, the evolution of the signal intensity of a pixel in the CT image over time is proportional to the temporal evolution of the concentration of contrast agent. The total amount of contrast agent that flows through a vessel is denoted as bolus. For this reason, this method is also known as bolus tracking.

2.3.1. From Tracer Concentration to Functional Parameters

A wide variety of approaches have been proposed to compute blood supply related functional maps from the temporal evolution of a tracer transported by blood [Miles and Griffiths, 2003]. The aim of this section is to illustrate the kind of information that these models need as input in order to provide quality requirements for the sequences of CT images. Since these requirements are similar for all approaches, this section is restricted to a compartmental analysis-based approach for cerebral perfusion: the slope method. This is the method implemented in the *Perfusion CT*

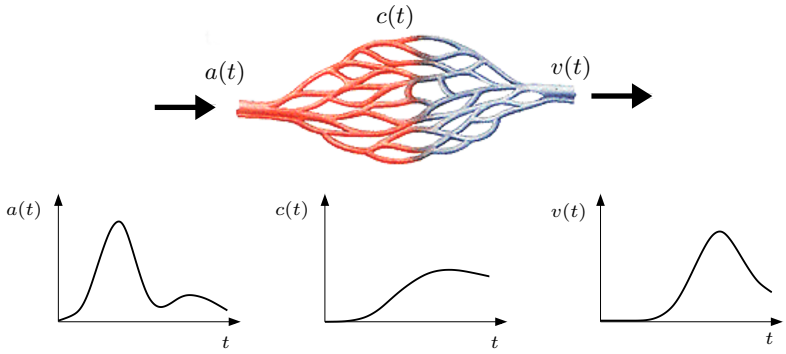

Figure 2.3. One compartment model. $a(t)$ denotes the concentration of contrast agent in the input artery at time t, $c(t)$ in tissue and $v(t)$ in the output vein. Image from [Farabee, 2006].

software (Siemens AG, Medical Solutions, Forchheim, Germany) which is used in chapter 5. The presentation follows [Klotz and König, 1999].

The main aspect to be considered before deriving a model is whether contrast agent remains within the vessels or it can diffuse to the interstitial fluid. In the case of the brain, molecules of contrast agent are large in the sense described in section 2.2.1 and cannot pass through the blood-brain barrier; hence, they remain intravascular if the blood-brain barrier is not disrupted.

In a compartmental analysis approach, the regions where the tracer distributes are divided in compartments. Typically a one compartment model is used if the agent remains intravascular and a two compartment model is used if it diffuses into the interstitium. One compartment is in any case the intravascular space in the tissue. In the two compartment model the second compartment is the interstitium. Compartmental analysis is based on three main assumptions ([Zierler, 1965] and [Miles et al., 1997]):

- The tracer does not affect blood flow.
- The tissue is homogeneous, i.e. it contains no concentration gradients.
- Tracer and blood mix instantaneously after inflow.

We describe here the so-called slope method which is based on a one compartment model. This method is used for cerebral perfusion CT and assumes that the tracer remains intravascular.

Figure 2.3 shows a scheme of the one compartment model. It is composed of an input artery, the tissue supplied by this artery and finally the output vein. From the quantitative definition of perfusion given in section 2.2.1 perfusion can be computed as a flow per unit volume

$$f = \frac{F}{V}. \tag{2.1}$$

Blood flow might change during the time the study is performed, but the quantity measured is an average [Shephard et al., 1983]. Hence, f and F are quantities averaged in a time interval $[0, t_s]$. Applying conservation of mass

$$F \int_0^{t_s} a(t)dt - F \int_0^{t_s} v(t)dt = Vc(t_s). \tag{2.2}$$

This leads to the following formula to compute perfusion

$$f = \frac{F}{V} = \frac{c(t_s)}{\int_0^{t_s} a(t)dt - \int_0^{t_s} v(t)dt} \tag{2.3}$$

This formula is the starting point for a wide variety of methods to compute perfusion. In order to derive the slope method, the differential form of (2.3)

$$f = \frac{\frac{dc(t)}{dt}}{a(t) - v(t)} \tag{2.4}$$

is considered. Since this relationship holds for any time, it holds also for t_{ms}, the time of maximum slope for the tissue concentration curve

$$f = \frac{\frac{dc(t_{ms})}{dt}}{a(t_{ms}) - v(t_{ms})}. \tag{2.5}$$

The time at which contrast agent outflow through the output vein starts is denoted as t_{vout}. Assuming $t_{vout} > t_{ms}$, $v(t_{ms}) \approx 0$ (no venous wash-out), then

$$f = \frac{\frac{dc(t_{ms})}{dt}}{a(t_{ms})}. \tag{2.6}$$

Rearranging (2.6) and differentiating

$$\frac{d^2c(t)}{dt^2} = f\frac{da(t)}{dt} \quad \text{for} \quad t < t_{vout}. \tag{2.7}$$

The left part of (2.7) vanishes at the time the slope $c(t)$ is maximum, i.e. $t = t_{ms}$, therefore also does $da(t)/dt$. As a conclusion, $a(t)$ reaches its maximum at $t = t_{ms}$ and the maximum slope formula to compute perfusion can be computed as

$$f = \frac{\max\left\{\frac{dc(t)}{dt}\right\}}{\max\{a(t)\}}. \tag{2.8}$$

Many software packages provide the related parameter CBF (cerebral blood flow) which can be calculated as $CBF = fV$.

An expression for the computation of cerebral blood volume (CBV) can be derived in a similar way

$$CBV = \frac{\max\{c(t)\}}{\max\{v(t)\}}. \tag{2.9}$$

The temporal evolution of the concentration of contrast agent is the decisive quantity for the computation of functional parameters. Throughout this thesis we refer to this temporal evolution as the *dynamic process*. Since it is proportional to the attenuation value, we also refer to it as *time-attenuation curve* (TAC) or simply *perfusion signal*.

2.3.2. PERFUSION CT PROTOCOL

A perfusion CT protocol is the clinical procedure followed with each patient to obtain blood supply-related functional maps with CT. It consists of three steps:

1. Injection of contrast agent.
2. Acquisition/reconstruction: generation of a sequence CT images.
3. Computation of perfusion parameters.

Contrast agent is injected intravenously in the cubital vein. As shown in the previous section the maximum value of the concentration in an output vein is needed for the computation of CBV. If the curve extends over a too long period of time, it might happen that the maximum is not registered by the CT sequence. Moreover, it is easier to fulfil the no venous wash-out assumption if the bolus is short in time. For these reasons the contrast agent should be injected at a high injection rate (ml/s). On the other hand, too high injection rates might not be well tolerated by some patients. In practice, injection rates up to 20 ml/s are used [Klotz and König, 1999]. Another important factor is the quantity of contrast agent injected. A higher amount of contrast agent will increase the level of the time-attenuation curves and make them therefore easier to detect in the presence of noise. On the other hand, it will make the bolus expand over a longer period of time which, as described above, might cause problems as well. Furthermore, a high amount of X-ray contrast agent might have toxic side effects so that its quantity should be minimised. Typically, values around $40 - 50$ ml are used [Miles and Griffiths, 2003]. Following the blood cycle (figure 2.2), contrast agent passes through the left side of the heart, through the lungs and through the right side of the heart before it reaches the brain. The transit through the heart and lungs makes the bolus expand over a long period of time.

During the time contrast agent flows, a series of CT scans of a region of interest is performed. The main parameters for the acquisition and reconstruction of these images are the following:

- Total protocol time: T_{tot}.
- Time between image frames of the output sequence: T_{fr}.
- Rotation time of the X-ray tube: $T_{2\pi}$.
- X-ray tube voltage: V.
- X-ray tube current: I.
- Slice thickness: Δ.

The first three parameters are self-explanatory; the last three are CT specific parameters and will be discussed in chapter 3. There is no standard choice for these parameters. Since they are determinant for the calculation of the X-ray dose applied to the patient (see sections 3.1.4 and 5.1) we provide in table 2.2 the values used at the Department of Neuroradiology (University of Heidelberg Medical School); these values will be referred to as the standard perfusion CT protocol throughout the thesis.

The reconstructed sequence of images is used as input for the computation of functional parameters. As stated in the previous section, there is a wide variety of methods to calculate functional parameters from the temporal evolution of the concentration of a tracer. One of these methods, the so-called slope method, was described in the previous section.

Parameter	Value	Units
T_{tot}	40	s
T_{fr}	1	s
$T_{2\pi}$	0.5	s
V	120	kV
I	220	mA
Δ	10	mm

Table 2.2. Parameters for the reference perfusion CT protocol.

2.4. Discussion. Limitations of Perfusion CT

State-of-the-art Computed Tomography scanners use detectors which cover a very small volume so that the region of interest for perfusion studies is very limited. As a consequence of this, it may happen that crucial information for the diagnosis is left out of the visualised region. The actual trend in Computed Tomography is the development of large area detectors. With these detectors, perfusion studies of a much larger region of interest will be possible which will overcome the problem of the limited field of view.

There are, however, other constraining aspects which limit this procedure. These are mainly a consequence of the acquisition over a long period of time and of the dynamic nature of the process of contrast agent flow. The most important are the following:

Patient exposure/noise CT is an X-ray-based imaging modality. Since X-rays are ionising radiation, the X-ray dose applied should be kept as low as possible. Unfortunately the noise level in CT images is proportional to the dose applied. In perfusion CT, the amount of dose is due to not only to one CT scan but to several ones. For this reason, the dose in each of them has to be kept low and therefore images are very noisy. The measurement of the temporal evolution of the concentration of contrast agent in tissue becomes a challenging issue in the presence of high noise. With large area detectors the exposed region will become larger which will increase the constraining aspect of this dose/noise trade-off.

Measured data/reconstruction time The acquisition of data over several rotations generates a huge amount data. These data have to be processed fast by the reconstruction algorithm to generate a sequence of CT images which is the input for the software package that computes the functional parameters. The introduction of large area detectors will dramatically increase the amount of input data. As a result, the computational time of the reconstruction will become a very limiting issue.

Non-constant attenuation values Typically 1 image/s is reconstructed from the measured data during 40 s. The reconstruction algorithms used to compute the image frames are based on the hypothesis that the object of the scan does not change during the time the necessary data to reconstruct an image frame are acquired. However, contrast agent flow is a dynamic process so that the object does change. Hence, acquired data are inconsistent. This is a limiting aspect for scanners with a low rotational speed.

Motion and deformation Due to the long acquisition times of typically 40 s, the scanned region

of interest (ROI) might move or be deformed. Typical cases are deformation through patient breathing or movement of the patient on the patient bed.

CHAPTER 3.

COMPUTED TOMOGRAPHY

This chapter deals with both the physical and the mathematical principles of Computed Tomography. It introduces concepts that will be used throughout this thesis. CT is an X-ray-based imaging modality; images are computed from measurements of the attenuation of an X-ray beam going through the patient. The first part of the chapter is devoted to the physical principles of X-ray generation and detection as well as the interaction of X-ray radiation with matter. Within this context, the X-ray attenuation coefficient and the CT image as spatial distribution of the attenuation coefficient are introduced. The concept of patient exposure to ionising radiation (dose) and its interdependency with image quality is discussed. The second part of the chapter is concerned with mathematical methods to compute images from the measurements of the attenuation of the X-ray beam. The discussion is limited to the so-called analytical reconstruction methods and among them, to the filtered backprojection algorithm, which is the most widespread method in medical applications. The filtered backprojection algorithm is deduced from Radon's inversion formula for one dimensional projections in parallel and fan-beam geometry. Finally, the discussion is extended to 3D reconstruction algorithms from 2D projections.

3.1. PHYSICAL PRINCIPLES: X-RAY RADIATION

The presentation given in this section has the objective to provide the basic physical principles needed to understand CT concepts used throughout this thesis. Its content, if not otherwise indicated, was extracted from [Oppelt, 2005], [Dössel, 2000] and [Barret and Myers, 2004].

3.1.1. X-RAY GENERATION

X-ray radiation are electromagnetic waves of wavelength in the range from 0.006 to 1.25 nm. Their energy is in the range from 1 to 500 KeV. Figure 3.1 shows a scheme of a typical X-ray tube used for the generation of X-rays in medical applications. It is mainly characterised by the tube voltage U the tube current I and the anode material (typically molybdenum, tungsten or copper). Electrons leave the cathode due to thermo-electrical effects, are accelerated in vacuum by the electric field and acquire a kinetic energy $E_{kin} = eU$ (where $e = 1.6 \cdot 10^{-19}$ As). The accelerated electrons then penetrate the anode where they lose their energy. The loss of energy can be caused by three kinds of interaction. If a penetrating electron collides with a bound electron of the inner shell of an anode's atom with enough energy, the bound electron is knocked out of its shell. As a result, an electron from a higher energy level fills up the vacancy and X-ray quanta are emitted. The emitted energy corresponds to the energy difference between levels. E.g. if an electron from the K-shell is knocked out and an electron of the L-shell fills its vacancy, the emitted radiation

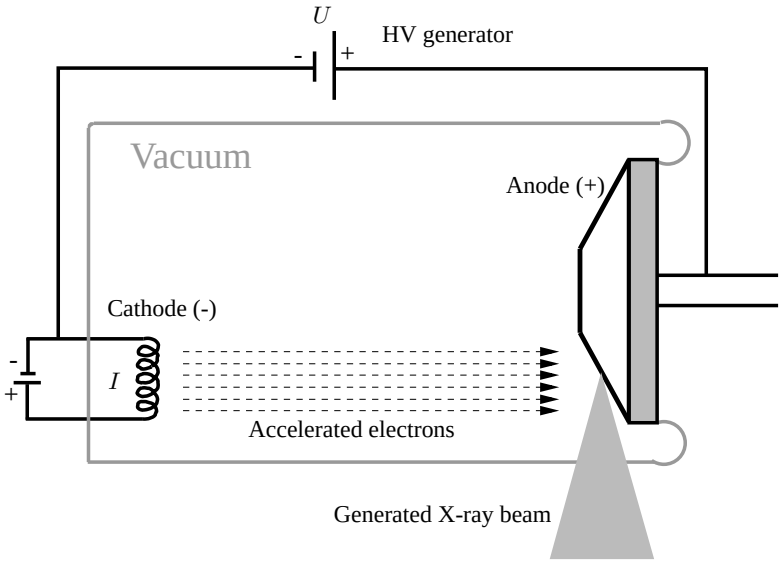

Figure 3.1. Scheme of an X-ray generator.

has the energy $\hbar\nu = E_K - E_L$. Hence, the produced spectrum is discrete. The energy level corresponding to each shell is characteristic to every material. The radiation caused by this kind of interaction is therefore denoted as *characteristic radiation*.

In the second type of interaction, the incident electron is decelerated by the electric field of the nuclei in the anode; this results in the emission of radiation. The braking process takes place in multiple stages at which radiation is emitted until all energy is lost. Hence, radiation of every possible energy below the maximum eU is generated, i.e. the spectrum of the emitted radiation is continuous. Radiation generated by this effect receives the name of *bremsstrahlung*. Figure 3.2 shows the bremsstrahlung and the characteristic K-radiation for a Tungsten anode and a tube voltage of $U = 150$ kV.

At this point it should be remarked that only a very small proportion of the incident electrons interact with the anode's structure in one of the two ways described above. Over 99% of the kinetic energy is lost in electron collisions and is converted to heat. This makes the cooling of the anode a crucial issue in the design of the X-ray tube. The X-ray energy emitted corresponds to less than 1% of the input electrical energy; this proportion is further reduced by the fact that only a small solid angle of the generated X-ray beam is used to generate an image.

The generated X-ray beam consists of X-ray quanta of different energies according to the spectrum of the target material and the tube voltage U. The number of quanta is a measure of energy therefore the number of quanta per unit time (flux) is a measure of power. Finally, an important magnitude for the rest of the chapter is the flux density, i.e. the energy per unit time and area. We denote the flux density by $\varrho(E)$ which indicates that it depends on the energy E. The total flux density, i.e. the flux density integrated over all energies, is denoted by ϱ_t. It depends on

$$\varrho_t \propto Z \cdot I \cdot U^n, \tag{3.1}$$

where Z is the atomic number of the target material and n depends on how the beam is filtered after leaving the X-ray source.

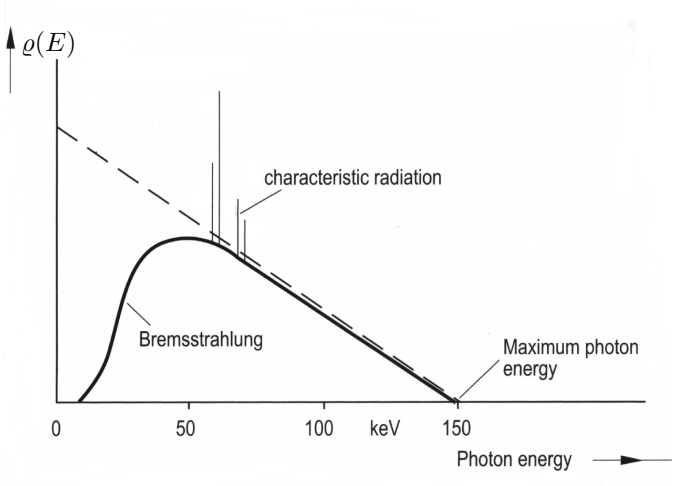

Figure 3.2. Bremsstrahlung and characteristic K-radiation for Tungsten in an X-ray tube operated at $U = 150$kV. From [Oppelt, 2005].

3.1.2. Interaction of X-ray with Matter

X-ray radiation suffers an attenuation when going through matter. This attenuation is due to the absorption of energy by the tissue and the deviation of the beam from its original straight trajectory (scattering). Both effects can be summarised in an attenuation coefficient μ. This attenuation coefficient represents the amount of attenuation per unit length due to a given material. Let us assume that quanta of a given energy E pass through an infinitesimal layer of thickness dl of a material. According to Beer's law, the proportion of interacting quanta (i.e. of lost quanta) $d\varrho/\varrho$ is

$$\frac{d\varrho}{\varrho(E)} = -\mu dl. \tag{3.2}$$

If the object the beam passes through is composed of different materials, the attenuation coefficient depends on the position in space $\mathbf{x} \in \mathbb{R}^3$, i.e. $\mu(\mathbf{x})$. The linear attenuation coefficient μ is the decisive magnitude in Computed Tomography since its spatial distribution forms the CT image. Its value depends on the density and atomic number of the material and on the energy of the incident quanta. Therefore, for a given energy E, only materials with a different density or atomic number can be differentiated in the CT image.

Assuming that the quanta follow a trajectory L after leaving the X-ray source, (3.2) can be integrated to compute the flux density after travelling along the path described by L

$$\varrho(E) = \varrho_0(E) e^{-\int_L \mu(\mathbf{x},E)dl} \tag{3.3}$$

where $\varrho_0(E)$ is the flux density for a given energy E in the X-ray beam leaving the tube. The total flux density, ϱ_t, is obtained by integrating over all energies

$$\varrho_t = \int_0^{eU} \varrho_0(E) e^{-\int_L \mu(\mathbf{x},E)dl} dE. \tag{3.4}$$

3.1.3. X-RAY DETECTION: QUANTUM NOISE

Modern CT detectors are based on solid state devices; a radiation sensitive solid state material converts the absorbed X-ray quanta into visible light. The light is then detected by a photodiode that converts it to an electrical signal. The electrical signal is then amplified and digitised. The produced signal is proportional to the number of incident quanta. There a two main sources of noise in this detection process. The first is due to the quantum nature of the incident X-ray radiation and is denoted as quantum noise. The second one is the electronic noise generated by the data acquisition system. We will limit the presentation in this section to the description of quantum noise. Throughout this thesis it is assumed that the detectors used are quantum limited, i.e. that only the quantum nature of radiation has a significant influence in image statistics.

As stated previously, the flux density at the detector in (3.4) is energy per unit time and area. Hence, in order to collect quanta to generate an output signal, a certain area is required. For this reason, the surface of the detector is composed of pixels of a certain area S. The amount of quanta, q, that reach a given pixel during a time interval of length T, can be calculated as

$$q = \int_T \int_S \varrho_t ds dt. \tag{3.5}$$

This value, fluctuates around an average value with a variance equal to the average number of quanta $\bar{q}$. The probability of counting m quanta when the average is $\bar{q}$ is given by the Poisson distribution

$$Pr(m) = \frac{\bar{q}^m}{m!} e^{-\bar{q}}. \tag{3.6}$$

Since the variance is equal to the mean, the signal to noise ratio (SNR) is

$$SNR = \frac{\bar{q}}{\sqrt{\bar{q}}} = \sqrt{\bar{q}}. \tag{3.7}$$

Hence, the effect of noise decreases with increasing number of incident quanta.

Expressions (3.5) and (3.7) show the interdependency of noise, pixel size and measuring time. According to (3.7), the number of photons should be as high as possible. In order to achieve this, (3.5) suggests three possible alternatives. The area of the pixels S can be increased, but this leads to a loss of spatial resolution (see section 3.2.4.1). Increasing the acquisition time T leads to a loss of temporal resolution. Finally, the density of incident quanta ϱ_t can be augmented by increasing the tube current (see section (3.1.1)); as we will see in the next section, both longer acquisition times and higher tube currents have the undesired effect of increasing patient exposure. The final parameter choice depends on each particular application.

As commented above, a way to increase the SNR is to increase the area of the pixels. In some applications, this is done by combining the measurements of several slices of the detector to a unique signal. The resulting measurements, however, correspond to a slice with a certain thickness, which implies a loss of spatial resolution in the axial direction. As a consequence, artifacts may appear in the reconstructed image. These are known as partial volume effects.

In section (3.1.1) we saw that the flux density is proportional to the tube current. Therefore, according to (3.5) and (3.7),

$$SNR \propto \sqrt{I \cdot T}. \tag{3.8}$$

3.1.4. PATIENT EXPOSURE: DOSE

The attenuation of the X-ray beam passing through matter has as a consequence the ionisation of single atoms and therefore the modification of their chemical properties. This might lead, depending on the amount of energy delivered by the beam, to irreparable damage in cells. As a consequence of this, cells are repaired or destroyed as a natural result of the healing process of the biological tissue. In less probable cases, cells might survive with modifications which might lead in short or long term to the development of cancer.

As stated above, the potential damage depends on the amount of energy deposited in the tissue. This leads to the definition of energy dose

$$D = \frac{\text{energy deposited in tissue}}{\text{mass of the tissue}}, \tag{3.9}$$

measured in Gray: Gy=J/kg. The measurement of dose according to (3.9) for the methods developed is out of the scope of this thesis. However, since dose is a crucial aspect in CT, we derive in the following a simple rule of thumb that will allow us in later chapters to discuss the efficiency of the developed methods in terms of dose in a simple way.

The energy deposited in the tissue is related to the energy emitted by the X-ray source. The energy delivered by the X-ray beam during a period of time of duration T is, according to (3.1)

$$\varrho_t T \propto I \cdot T \cdot Z \cdot U^n. \tag{3.10}$$

This expression cannot be directly interpreted as an estimate for dose. According to it, increasing the tube voltage would increase the dose, which is not true since radiation of lower energies is better absorbed than radiation of higher energies and therefore using low energy radiation increases the dose. Nevertheless, for a certain tube voltage U expression (3.10) shows that there is a linear relationship between the delivered energy and the product $I \cdot T$. This product, is usually denoted as the mAs product and is frequently used to estimate the dose. Note that this estimation does not correspond to the definition given in (3.9) since it does no consider the spectrum of the radiation and the mass of the tissue. It is, however, a practical magnitude in order to compare algorithms in terms of dose efficiency. For this reason, we will use hereafter the mAs product as an estimation for the dose applied

$$D \propto I \cdot T. \tag{3.11}$$

In clinical practice, this estimation must be handled with care. It only makes sense in order to compare examination protocols with the same CT scanner [Kalender, 2000].

Expressions (3.8) and (3.11) reveal a typical trade-off situation. While increasing the tube current by a factor of a has the positive effect of increasing the SNR by a factor of $\sqrt{a}$, it has at the same time the negative effect of increasing the dose by a factor of a. Note that we are talking here about noise in the measured data, the effect of noise in the image will be discussed in section 3.2.4.2.

3.2. 2D RECONSTRUCTION

While in classical radiographs the measured attenuation pattern constitutes the X-ray image, in Computed Tomography these measurements are the input data for a reconstruction algorithm that

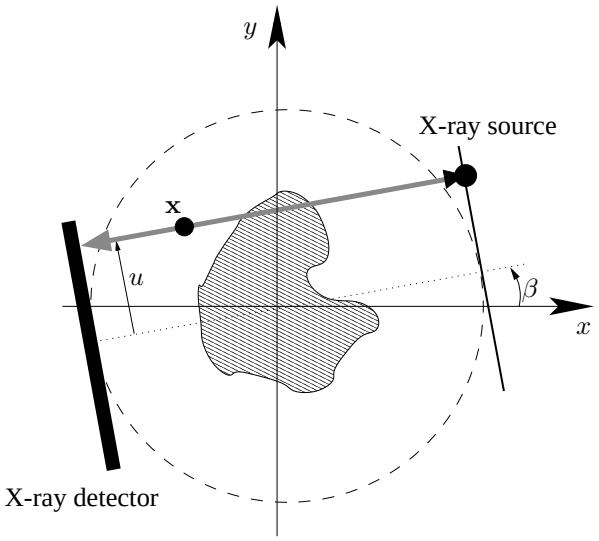

Figure 3.3. Scheme of a CT scanner of the first generation.

computes the CT image. The computation of the CT image from the acquired measurements is denoted as reconstruction algorithm.

In an article published in 1917 [Radon, 1917], J. H. Radon stated that a 2D function is, under certain conditions, uniquely determined by the values of integrals along all possible straight lines passing through it. We denote these values as Radon values. Keeping this in mind, consider a setting as the one described in figure 3.3. The source can be translated along a line parallel to the detector and both the detector and the source can be rotated synchronously around the origin of coordinates. A pencil beam is emitted from the source and is detected by a continuous detector. The beam is assumed to be monochromatic, i.e. all quanta have the same energy. Furthermore, the detector is assumed to have an infinitely short temporal response. Under these conditions the detector will measure the flux density ϱ. This density is given by (3.3). By rotating the source-detector arrangement by an angle β and translating the source by u at each β position we obtain

$$\varrho(\beta, u) = \varrho_0 e^{-\int_{L(\beta,u)} \mu(\mathbf{x}) dl} \tag{3.12}$$

where the trajectories $L(\beta, u)$ are straight lines in all directions passing through the object. Dividing by ϱ_0 and taking the logarithm, we obtain the so-called *projections*

$$P_\beta(u) = -\ln\left(\frac{\varrho(\beta, u)}{\varrho_0}\right) = \int\limits_{L(\beta,u)} \mu(\mathbf{x}) dl. \tag{3.13}$$

Hence, projections are the values of the integrals of the attenuation coefficient along lines passing through the object. If $\beta \in [0, \pi]$, $u \in [-u_{max}, u_{max}]$ and $\mu(\mathbf{x}) = 0$ for $\|\mathbf{x}\| > u_{max}$, $P_\beta(u)$ represents the values of all line integrals passing through the object, i.e. all Radon values. Therefore, according to Radon's result, it is possible to determine $\mu(\mathbf{x})$ from such projections.

3.2.1. CT Reconstruction as an Inverse Problem

The reconstruction of $\mu(\mathbf{x})$ from the measured data $P_\beta(u)$ is a typical example of an inverse problem

$$\Xi\{\mu(\mathbf{x})\} = P_\beta(u) \quad \rightarrow \quad \mu(\mathbf{x})? \tag{3.14}$$

The function Ξ, defined by (3.13), is applied to $\mu(\mathbf{x})$ and it produces the measured data $P_\beta(u)$; from these measurements we want to recover $\mu(\mathbf{x})$. There are many different approaches to tackle (3.14), they are mainly divided in:

Analytical methods An analytical expression for the reconstruction is derived from properties of the Radon transform [Natterer, 1986]. This usually entails a series of physical assumptions (see section 3.2.4).

Iterative methods The problem is discretised and an approximate solution is computed by iterative methods. In the so-called Algebraic Reconstruction Technique (ART), expression (3.13) is discretised yielding a huge linear system of equations [Kak and Slaney, 1988]. Statistical reconstruction methods otherwise take into account the random nature of the measurements; they are based on the minimisation of the distance between the measured data and the estimations given by a statistical model [Natterer and Wübbeling, 2001].

Analytical methods have the advantage to be fast and deliver good quality results under standard scanning conditions. Iterative methods on the other hand are more robust against problems as missing projections, projection angles that are not regularly distributed on $[0, \pi]$ or non-standard acquisition geometries. Furthermore, iterative methods are more flexible from the modelling point of view, i.e. they can be modified to include physical effects which are neglected to obtain (3.13). All this is, however, at the cost of computational complexity. For this reason, the most widespread CT reconstruction method for medical applications is nowadays an analytical method: the filtered backprojection [Natterer and Wübbeling, 2001]. In other medical imaging modalities as PET or SPECT though the effect of noise is much more constraining. Here statistical reconstruction methods are widely applied [Fessler, 2000].

3.2.2. CT Images

In section 3.1.2 we introduced the concept of CT image as the spatial distribution of the attenuation coefficient $\mu(\mathbf{x})$. We also saw in the same section that this quantity depends on the energy of the incident quanta. Hence, for different values of the voltage in the X-ray tube, we will obtain different values in the image. In order to have a reference value, CT images are displayed as so-called CT values [Kalender, 2000]. These, are computed as

$$\text{CT value} = 1000 \times \frac{\mu - \mu_{\text{water}}}{\mu_{\text{water}}} \tag{3.15}$$

and are measured in HU or Hounsfield Units. Hence, the attenuation of water is always 0 HU by definition. Since the attenuation value of air is $\mu_{\text{air}} \approx 0$ cm^{-1} independently of the energy, its value in the CT image will be ≈ -1000 HU. Therefore, the CT values of water and air serve as a reference in any CT image.

CT images have typically a pixel depth of 12 bits and the CT value range goes from -1024 HU to 3071 HU. The human visual system cannot discern more than (typically) 80 grey levels. For

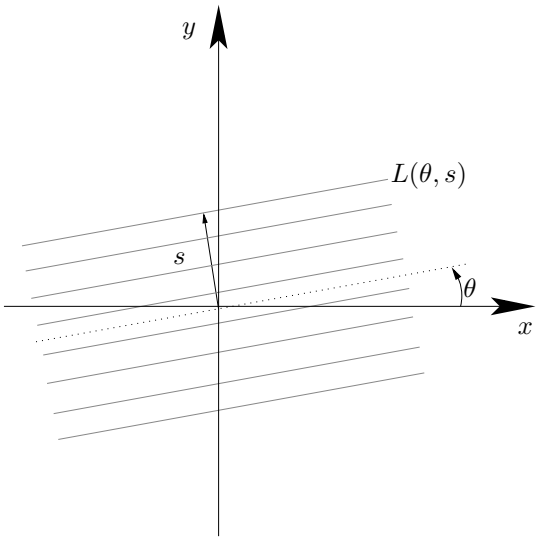

Figure 3.4. Radon transform parameters.

this reason, for the visualisation of CT images, the complete grey scale is assigned to an interval of interest or *window* [Kalender, 2000]. The values under the lowest window value are displayed as black, whereas the values over the highest window value are displayed as white. As an example, in order to visualise bone, a window of $[-250, 2250]$ HU can be used, whereas for the differentiation of soft tissue in the brain typically values around $[20, 80]$ HU are used. A very wide window is appropriate for the visualisation of tissues with great differences in their attenuation values. A narrow window allows the differentiation of small attenuation differences. With a narrow window also artifacts and noise become more patent. In this thesis, the window is given in form of a grey value interval: $[V_{min}, V_{max}]$ HU.

3.2.3. Radon Transform

The 2D Radon transform maps a function on $\mathbb{R}^2$ into the set of integrals along lines of $\mathbb{R}^2$ [Natterer, 1986]. For $f \in \mathscr{S}(\mathbb{R}^2)$ (see appendix B), the Radon transform is defined as

$$R(\theta, s) = \int\limits_{L(\theta,s)} f(\mathbf{x})dl = \int\limits_{-\infty}^{+\infty}\int\limits_{-\infty}^{+\infty} f(x, y)\delta(-x\sin(\theta) + y\cos(\theta) - s)dxdy, \tag{3.16}$$

with $\theta \in [0, 2\pi]$ and $s \in]-\infty, +\infty[$. Figure (3.4) illustrates the meaning of the parameters θ and s; s is the signed distance ($\theta = 0$, $s = y$) from the origin to each line, whereas θ is the angle of the line passing through the origin with the x-axis. If $f \in \mathscr{S}(\mathbb{R}^2)$ then, for a given θ, $R(\theta, s) \in \mathscr{S}(\mathbb{R})$. Under these conditions, f is uniquely determined by $R(\theta, s)$ and a formula for the inversion of the Radon transform can be given

$$f(\mathbf{x}) = \frac{1}{4\pi^2}\int\limits_{0}^{2\pi}\int\limits_{-\infty}^{+\infty} \frac{1}{-x\sin(\theta) + y\cos(\theta) - s}\frac{\partial R(\theta, s)}{\partial s}dsd\theta. \tag{3.17}$$

3.2.4. Analytical Methods: the Filtered Backprojection

If we compare (3.13) and (3.16), we conclude that the projections computed from the measured data correspond to the Radon transform, i.e.

$$P_\beta(u) = R(\beta, u). \tag{3.18}$$

However, it should be kept in mind that (3.13) is the result of several simplifications. The most important among them are ([Kalender, 2000] and [Hiriyannaiah, 1997]):

- Beer's law does not consider the possibility of the incident quanta being deviated from their trajectory (scattering).
- Quanta of lower energies are better absorbed than quanta of higher energies. Hence, while passing through the object the proportion of quanta of higher energies in the X-ray beam increases. This effect is known as *beam hardening*. This effect is not taken into account in (3.13).
- The X-ray beam has been assumed to be monochromatic.

These approximations have an impact on image quality in form of artifacts and loss of accuracy. The effects on the image might be, in some cases, alleviated by using correction algorithms but they cannot be eliminated; their importance depends on the application. In practice, these image artifacts rarely prevent from diagnosis in clinical routine [Kalender, 2000].

While the approximations listed above cause effects that cannot be easily modelled, there are other approximations that allow a theoretical analysis. We refer particularly to the random nature of the detection process (noise) and the finite number of detector elements and projection angles (sampling). The effect of these approximations is discussed in the next sections.

The filtered backprojection algorithm is the most widespread reconstruction algorithm for Computed Tomography in medical applications; it can be derived from Radon's inversion formula (3.17). According to figure (3.3), we can calculate the distance from the origin to the ray that passes through a certain point $\mathbf{x}$ as

$$u'(\mathbf{x}, \beta) = -x\sin(\beta) + y\cos(\beta). \tag{3.19}$$

Assuming that $P_\beta(u)$ are projections from a function $f \in \mathscr{S}(\mathbb{R}^2)$ we can rewrite (3.17) as

$$f(\mathbf{x}) = \frac{1}{4\pi^2}\int_0^{2\pi}\int_{-\infty}^{+\infty} \frac{\partial P_\beta(u)}{\partial u}\frac{1}{u'(\mathbf{x},\beta) - u}\,du\,d\beta. \tag{3.20}$$

The inner integral is the convolution of $\frac{1}{u}$ with $\frac{\partial P_\beta(u)}{\partial u}$ evaluated at $u'(\mathbf{x}, \beta)$. In Fourier domain the convolution is the product of the corresponding Fourier transforms (see appendix B)

$$\left(\frac{1}{\cdot} * \frac{\partial P_\beta(\cdot)}{\partial u}\right)(u'(\mathbf{x},\beta)) = \int_{-\infty}^{+\infty} (-i\pi\,\mathrm{sign}(\varsigma))(i2\pi\varsigma)\hat{P}_\beta(\varsigma)e^{i2\pi\varsigma u'(\mathbf{x},\beta)}d\varsigma, \tag{3.21}$$

where we used the following Fourier transform pairs

$$\begin{aligned} \tfrac{1}{u} &\overset{FT}{\longleftrightarrow} -i\pi\text{sign}(\varsigma) \\ \tfrac{\partial P_\beta(u)}{\partial u} &\overset{FT}{\longleftrightarrow} i2\pi\varsigma\hat{P}_\beta(\varsigma). \end{aligned} \tag{3.22}$$

Substituting (3.21) in (3.20) leads to

$$f(\mathbf{x}) = \frac{1}{2}\int_0^{2\pi}\int_{-\infty}^{+\infty} |\varsigma|\hat{P}_\beta(\varsigma)e^{i2\pi\varsigma u'(\mathbf{x},\beta)}d\varsigma d\beta. \tag{3.23}$$

Note that (3.23) only holds under the assumption that $f \in \mathscr{S}(\mathbb{R}^2)$. In practice, however, f must not be smooth; moreover, it may not even be continuous. Indeed, a more realistic assumption on f is that it be piece-wise smooth, i.e. it may contain discontinuities [Natterer, 1986]. In this case (3.23) becomes an approximation. Furthermore, the inner integral in (3.23) suggests that the projections are filtered with a filter whose Fourier transform is $|\varsigma|$. As we saw in section 3.1.3, the surface of the detector is discretised and the discrete pixels are situated at a certain distance from each other. This limits the spatial resolution to a certain maximum frequency ς_{max} (see next section). For this reason the filter is modified so as to have a frequency response whose maximum frequency equals that of the detector. For this purpose, the filter $|\varsigma|$ is substituted by

$$\hat{g}(\varsigma) = \hat{v}(\frac{\varsigma}{\varsigma_{max}})|\varsigma| \tag{3.24}$$

where $\hat{v}(\varsigma)$ is a weighting function that is zero for $\varsigma > 1$. Substituting this new filter in (3.23) yields the filtered backprojection formula

$$\begin{aligned} \mu^r(\mathbf{x}) &= \frac{1}{2}\int_0^{2\pi}\int_{-\infty}^{+\infty} \hat{v}\left(\frac{\varsigma}{\varsigma_{max}}\right)|\varsigma|\hat{P}_\beta(\varsigma)e^{i2\pi\varsigma u'(\mathbf{x},\beta)}d\varsigma d\beta \\ &= \underbrace{\frac{1}{2}\int_0^{2\pi}\underbrace{\left(P_\beta(\cdot) * g(\cdot)\right)\left(u'(\mathbf{x},\beta)\right)}_{\text{Filtering}}d\beta}_{\text{Backprojection}}, \end{aligned} \tag{3.25}$$

where $\mu^r(\mathbf{x})$ denotes the reconstructed spatial distribution of the attenuation coefficient. The way the algorithm works is better understood if (3.25) is expressed in two steps

$$FP_\beta(u) = \int_{-u_{max}}^{u_{max}} P_\beta(s)g(u-s)ds \tag{3.26}$$

$$\mu^r(\mathbf{x}) = \frac{1}{2}\int_0^{2\pi} FP_\beta(u'(\mathbf{x},\beta))d\beta, \tag{3.27}$$

where $2u_{max}$ is the width of the detector. The reconstruction then works as follows: all projections are filtered with $g(u)$, yielding the filtered projections $FP_\beta(u)$; subsequently, for a given point

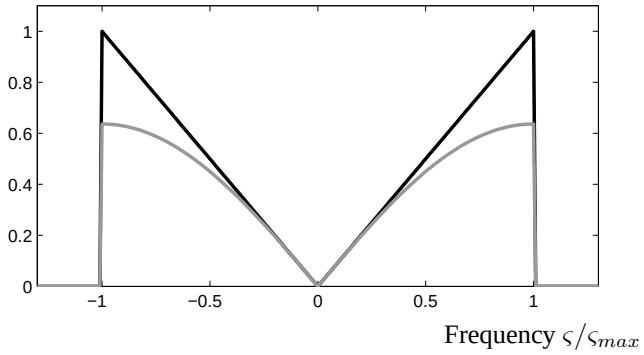

Figure 3.5. Frequency response of the Ram-Lak (black) and the Shepp-Logan (grey) filters.

$\mathbf{x}$, the filtered values of all rays (one for every β) going through $\mathbf{x}$ are averaged, yielding the reconstructed value $\underline{\mu}^r(\mathbf{x})$. This last operation is known as *backprojection*.

The choice of the window $\hat{v}(\varsigma)$ is a trade-off between sharpness and noise. As an example, the Ram-Lak filter with

$$\hat{v}(\varsigma) = \begin{cases} 1 & \text{for} \quad \varsigma \leq 1 \\ 0 & \text{for} \quad \varsigma > 1 \end{cases} \tag{3.28}$$

preserves well the edges but produces more noisy images than the Shepp-Logan filter with

$$\hat{v}(\varsigma) = \begin{cases} \operatorname{sinc}\left(\frac{\varsigma}{2}\right) & \text{for} \quad \varsigma \leq 1 \\ 0 & \text{for} \quad \varsigma > 1 \end{cases} . \tag{3.29}$$

This is due to the fact that the former preserves better the frequencies close to ς_{max} (see figure 3.5). The value of the integral of $\mu(\mathbf{x})$ along a line is independent of the sense of integration. For this reason, the parameters (β, u) describe the same ray as $(\beta + \pi, -u)$ (the same Radon value). These are rays are equivalent . In a full-rotation, the projections in the angular interval $[\pi, 2\pi]$ contain rays that are equivalent to the rays in the projections in the angular interval $[0, \pi]$. Hence, the integral in (3.27) $\int_0^{2\pi}$ can be substituted by $2\int_0^{\pi}$ to obtain the same resulting image with half of the input data. The reconstruction from data in $[0, 2\pi]$ is often referred to as full-scan reconstruction, whereas the reconstruction from data in $[0, \pi]$ is referred to as short-scan reconstruction. In practice, these reconstruction modes are not equivalent since different measurements of the same rays will carry different values of the fluctuation due to the random nature of the quanta detection process. Therefore, averaging over a longer angular interval will reduce noise in the image. Indeed, since two measurements of the same ray are statistically independent, the variance of the noise in the image will be reduced by a factor of 2 (see section 3.2.4.2).

As a marginal note, we remark that in CT literature the term short-scan is usually reserved for the reconstruction in fan-beam geometry (see section 3.2.5). In this thesis, however, we will use it also in parallel-beam geometry to indicate reconstruction from projections in an angular interval of length π.

3.2.4.1. DISCRETISATION OF THE FBP: SAMPLING THE RADON TRANSFORM

As described in section 3.1.3 CT detectors are composed of pixels with a certain area S. We denote by N_u the number of pixels in the detector, and by Δu the distance between pixels. N_u is often referred to as the number of channels of the detector. The object of the scan is situated within a circle of radius $\|\mathbf{x_{max}}\|$. The detector has a width of $2u_{max}$, with $u_{max} \geq \|\mathbf{x_{max}}\|$. Under these conditions, the projections are sampled in u with a sampling interval

$$\Delta u = \frac{2u_{max}}{N_u}. \tag{3.30}$$

In practice, the number of projection angles in a rotation is also finite. We denote the number of projections in the angular interval $[0, 2\pi]$ by N_β. N_β is often referred to in the literature as the number of views. The sampling interval is thus

$$\Delta\beta = \frac{2\pi}{N_\beta}. \tag{3.31}$$

In order to attain a given spatial frequency ς_{max}, the number of channels N_u and the number of projections per rotation N_β have to fulfil [Natterer and Wübbeling, 2001]

$$\begin{aligned} \Delta u &\leq \frac{1}{2\varsigma_{max}} \\ \Delta\beta &\leq \frac{1}{2\varsigma_{max}u_{max}} \end{aligned} \tag{3.32}$$

which leads to

$$\begin{aligned} N_u &\geq 4\varsigma_{max}u_{max} \\ N_\beta &\geq 4\pi\varsigma_{max}u_{max}. \end{aligned} \tag{3.33}$$

3.2.4.2. NOISE IN CT IMAGES

The output signal of every detector pixel is affected by a random error, i.e. noise (see section 3.1.3). In this section, we analyse the effect that the noise in the detector measurements has in the final reconstructed image.

Since the detection of X-ray quanta requires a certain area, the analysis of noise must be performed with the discretised magnitudes. We denote by $q_{\beta_i}(u_j)$, the number of quanta collected by the pixel situated at position u_j in the detector when the detector is situated at the position determined by the projection angle β_i. According to the quantum noise model, the first and second moments of the measurements are

$$E[q_{\beta_i}(u_j)] = \bar{q}_{ij} \tag{3.34}$$

$$\sigma^2_{q_{ij}} = \bar{q}_{ij}, \tag{3.35}$$

where $E[]$ denotes expected value. With this notation we can express the discretised projections as

$$P_{\beta_i}(u_j) = -\ln\left(\frac{q_{\beta_i}(u_j)}{q_0}\right), \tag{3.36}$$

where q_0 is the number of quanta detected without an object between source and detector. In order to characterise the projections statistically, we calculate their first and second moments. As a result, we get [Barret and Swindell, 1981]

$$\begin{aligned} E[P_{\beta_i}(u_j)] &\approx -\ln\left(\frac{\bar{q}_{ij}}{q_0}\right) \\ \sigma^2_{P_{ij}} &\approx \frac{1}{\bar{q}_{ij}}. \end{aligned} \tag{3.37}$$

The propagation of noise through the algorithm is rather complex. It is, however, of practical interest to have an analytical expression for the variance of a pixel value in the image σ_I^2 in order to understand the influence of the different parameters involved in the acquisition-reconstruction process. A way to achieve that, is to consider projections of a geometrically simple object; the most simple case is to choose an object with radial symmetry. We consider therefore the projections of an homogeneous cylinder. In such a case, an approximate expression can be obtained [Dössel, 2000]:

$$\sigma_I^2 = \frac{1}{\bar{q}} \frac{2u_{max}}{N_\beta N_u} f_g, \tag{3.38}$$

where f_g is a constant that depends on the interpolation kernel and $\bar{q}$ is the average number of quanta detected by the central pixel of the detector $\bar{q} = \bar{q}_{i0}$ for all i (due to the radial symmetry).

Since the number of quanta is proportional to the mAs product, we deduce from (3.38) that the noise in the image is inversely proportional to the dose.

3.2.4.3. FBP Reconstruction: a Numerical Example

In order to illustrate the principle of FBP reconstruction, we present in this section a numerical example. The aim is to reconstruct the central slice of the head phantom described in appendix C. The output image should have 256×256 pixels with $\Delta_x = \Delta_y = 1$ mm; the distance between detector pixels is $\Delta_u = \Delta_x$. This choice determines both $\varsigma_{max} = \frac{1}{2\Delta_x} = 0.5$ mm^{-1} and $u_{max} = 128$ mm. With these detector dimensions, a circular region of interest of radius 128 mm is reconstructed. Using (3.33) with these values we get

$$\begin{aligned} N_u &\geq 256 \\ N_\beta &\geq 804.25. \end{aligned} \tag{3.39}$$

Hence, we simulated 800 projections per full rotation with a 256 pixel detector of width 256 mm. The attenuation of the x-ray beam was calculated using the software package *DRASIM (Deterministic Radiological Simulation)* by Karl Stiersdorfer (Siemens AG, Medical Solutions). The simulations were carried out without noise. For the reconstruction the Ram-Lak filter was used. Figure 3.6 shows the reconstruction process. In the initial image matrix all pixels have the value 0. Then, for each angular position β, the value of the filtered projection determined by the detector pixel u is added to all the points along a straight line perpendicular to the detector and intersecting the detector at pixel u. Accumulating the values of projections in the angular interval $[0, \pi]$ produces the reconstructed image.

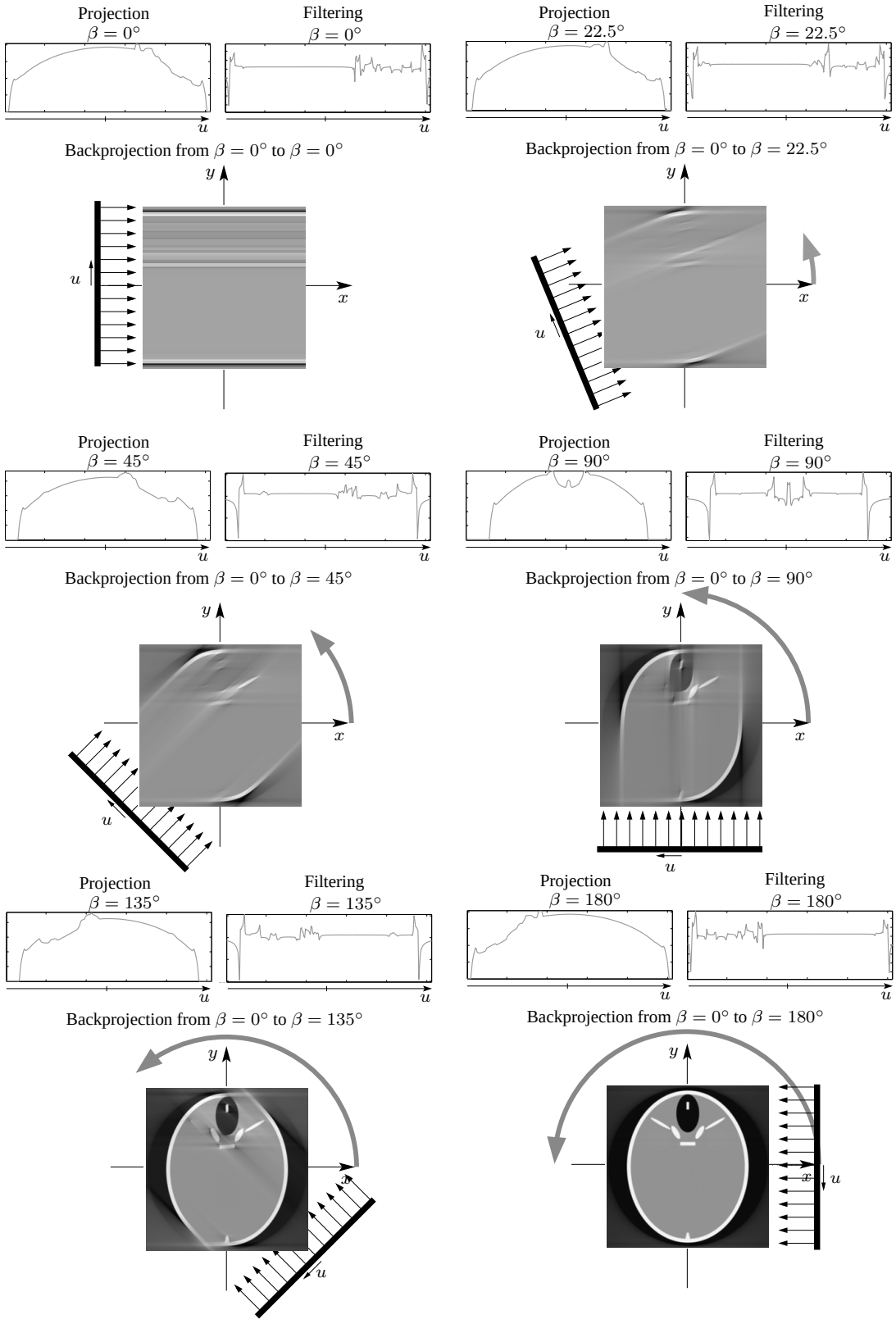

Figure 3.6. Example of FBP reconstruction in parallel-beam geometry.

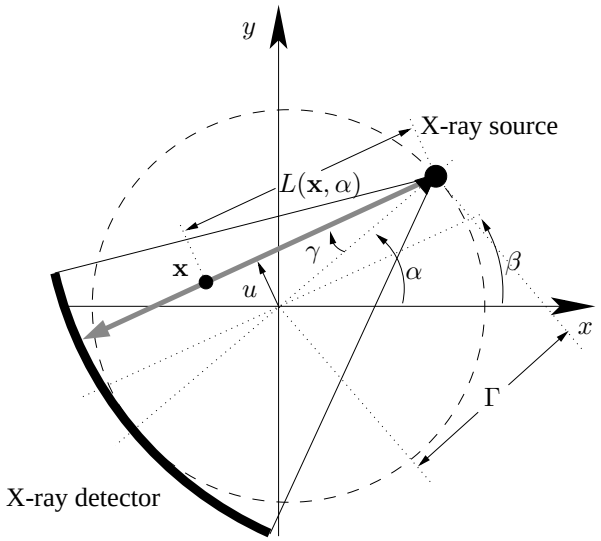

Figure 3.7. Scheme of a CT scanner with fan-beam geometry. The projections are characterised by the angular position of the source α and the fan-angle γ.

3.2.5. Filtered Backprojection in Fan-beam Geometry

The acquisition of projections with a rotation-translation scheme as described in figure 3.3 causes long scan times; indeed, such a scanning geometry was only used in the first generation of CT scanners [Kalender, 2000]. Since the X-ray beam leaving the source is not parallel but divergent, scanning directly in fan-beam geometry spares the translation of the source decreasing thus the acquisition time.

There are two possible ways to use the filtered backprojection algorithm with fan-beam projections. The first consists in reordering the measured data in such a way that they form a parallel beam; the second consists in adapting the algorithm to the geometry. Figure 3.7 shows a scheme of a CT scanner with fan-beam geometry. Fan-beam projections $P_\alpha(\gamma)$ are characterised by the angular position of the source α and the fan-angle γ, whereas parallel-beam projections are characterised by the angle the rays form with the x-axis β and the distance from the ray to the origin, u. The following change of coordinates relates the parallel-beam to the fan-beam parameters

$$\begin{aligned} \beta &= \alpha - \gamma \\ u &= \Gamma \sin(\gamma) \end{aligned} \tag{3.40}$$

where Γ is the distance between the source and its rotation axis. This relationship is illustrated in figure 3.7. The ray (α, γ) (grey) forms an angle $\beta = \alpha - \gamma$ with the x-axis. The distance of the ray to the origin determines the second parameter in parallel-beam coordinates: $u = \Gamma \sin(\gamma)$.

3.2.5.1. Fan-beam Reconstruction by Rebinning

Rebinning can be viewed as adapting not the algorithm but the projections to a new geometry. That is, projections acquired in fan-beam geometry are transformed to parallel-beam geometry

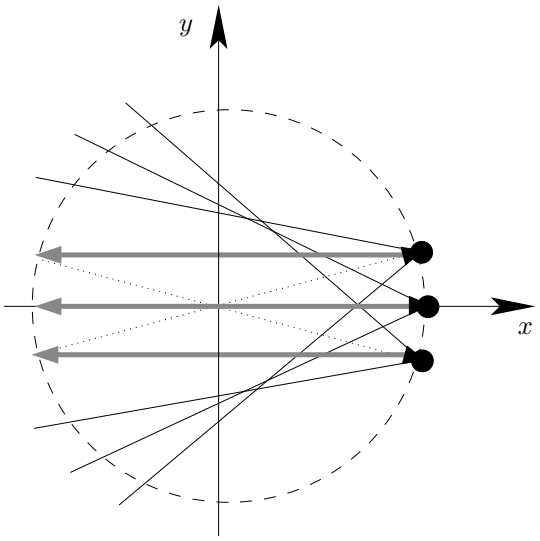

Figure 3.8. Rebinning from a fan-beam to a parallel-beam. The fan-beam rays $\alpha = 15°$, $\gamma = -15°$, $\alpha = 0°$, $\gamma = 0°$and $\alpha = -15°$, $\gamma = 15°$are used to compound the parallel projection $\beta = 0°$.

and then a reconstruction for parallel-beam geometry (see (3.26) and (3.27)) is applied. In order to do this we apply the inverse transform of (3.40) to $P_\alpha(\gamma)$

$$P_\alpha(\gamma) \quad \longrightarrow \quad P_{\alpha(\beta,u)}(\gamma(u)). \tag{3.41}$$

Since in practical scanners only a finite number of rays are measured, rebinning consists in reordering the measurements from a fan-beam projection data set to a parallel-beam projection data set. For each discrete value of the parallel projection angle β the rays of the fan-beam projections whose angle with the x-axis is equal to β are grouped together. These rays are identified by $\beta = \alpha - \gamma$. The principle is illustrated in figure 3.8. Since α and γ are discrete too, there might be no ray whose angle with the x-axis is exactly β, so that the value must be interpolated from the values of the closest rays.

3.2.5.2. Fan-beam Reconstruction by Adapting the FBP

In order to adapt the FBP algorithm to fan-beam geometry, we introduce the transformation described by (3.40) in (3.26) and (3.27). It yields [Kak and Slaney, 1988]

$$FP_\alpha(\gamma) = \int_{-\gamma_{max}}^{\gamma_{max}} (P_\alpha(\kappa)\Gamma\cos(\kappa))\, h(\gamma-\kappa)d\kappa \tag{3.42}$$

$$\mu^r(\mathbf{x}) = \frac{1}{2}\int_0^{2\pi} \frac{1}{L^2(\mathbf{x},\alpha))} FP_\alpha(\gamma'(\mathbf{x},\alpha))d\alpha. \tag{3.43}$$

Hence, the FBP in fan-beam geometry is also a convolution backprojection algorithm. Projections are weighted with a factor depending on γ and are then filtered with a modified version of the filter

used in parallel geometry g:

$$h(\gamma) = \left(\frac{\gamma}{\sin(\gamma)}\right)^2 g(\gamma). \tag{3.44}$$

Subsequently, for a given point $\mathbf{x}$, the values of all rays (one for every α) going through $\mathbf{x}$ are weighted with a factor $1/L^2(\mathbf{x},\alpha)$ and averaged. The factor L corresponds to the distance between the source and the point $\mathbf{x}$ (see figure 3.7):

$$L(\mathbf{x},\alpha) = \sqrt{(\Gamma\cos(\alpha) - x)^2 + (\Gamma\sin(\alpha) - y)^2}. \tag{3.45}$$

Finally, for a given projection angle α, the ray that passes through the point $\mathbf{x}$ is determined by

$$\gamma'(\mathbf{x},\alpha) = \arctan\left(\frac{-x\sin(\alpha) + y\cos(\alpha)}{\Gamma - x\cos(\alpha) - y\sin(\alpha)}\right). \tag{3.46}$$

3.2.5.3. Reconstruction from Data Acquired in a Short-scan

As in the parallel geometry case, a reconstruction with data from less than a full-rotation is possible. In order to find the minimum angular interval necessary for the reconstruction of an image, we use the relationship between parallel-beam rays and fan-beam rays (3.40). According to this equivalence, the extreme cases are given by

$$\begin{aligned}
&\left\{\begin{array}{lcl}\beta &=& 0\\ u &=& -u_{max}\end{array}\right. \longrightarrow \left\{\begin{array}{lcl}\alpha &=& -\gamma_{max}\\ \gamma &=& -\gamma_{max}\end{array}\right.\\
&\left\{\begin{array}{lcl}\beta &=& \pi\\ u &=& u_{max}\end{array}\right. \longrightarrow \left\{\begin{array}{lcl}\alpha &=& \pi + \gamma_{max}\\ \gamma &=& \gamma_{max}\end{array}\right. .
\end{aligned} \tag{3.47}$$

Hence, a short-scan reconstruction in fan-beam geometry requires projections in an angular interval of length $\pi + 2\gamma_{max}$.

However, contrary to the parallel-geometry case, simply substituting the interval of integration in (3.43) leads to strong artifacts in the reconstruction. The reason for this is explained as follows. In fan-beam geometry, the ray equivalent to (α,γ) is $(\alpha+\pi-2\gamma,-\gamma)$; hence, an angular interval of length $\pi + 2\gamma_{max}$ contains equivalent rays. These rays contribute twice to the reconstruction, which causes an unbalance since most of the rays only contribute once. In order to overcome this, Parker proposed in [Parker, 1982] weighting the projections with a smooth weighting function

$$w_\alpha(\gamma) = \left\{\begin{array}{ll} 2\sin^2\left(\frac{\pi}{4}\frac{\alpha}{\gamma_{max}+\gamma}\right) & 0 \le \alpha < 2\gamma_{max} + 2\gamma\\ 2 & 2\gamma_{max} + 2\gamma \le \alpha \le \pi + 2\gamma\\ 2\sin^2\left(\frac{\pi}{4}\frac{\pi+2\gamma_{max}-\alpha}{\gamma_{max}-\gamma}\right) & \pi + 2\gamma \le \alpha < \pi + 2\gamma_{max}\end{array}\right. . \tag{3.48}$$

This function ensures that two equivalent rays are weighted in such a way that the sum of the weights equals 2. Figure 3.9 shows an example of FBP reconstruction from fan-beam projections with and without Parker weighting.

Note that other weighting functions might be used. Smoothness is, however, a desirable property since using non smooth functions might lead to artifacts due to filtering over a sharp edge [Turbell, 2001].

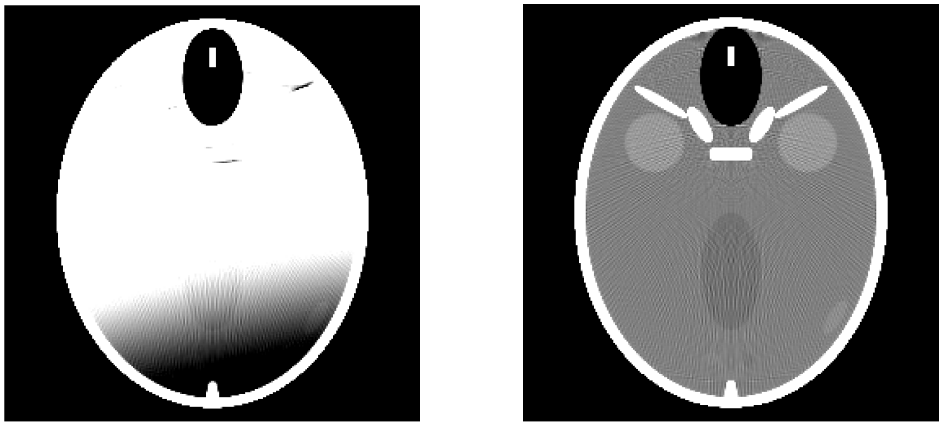

(a) No weighting (b) Parker weighting

Figure 3.9. Example of short-scan reconstruction in fan-beam geometry. Left: without weighting. Right: with Parker weighting. Window: $[0, 100]$ HU.

3.3. 3D Reconstruction for Circular Trajectories

In the previous sections we presented methods to reconstruct 2D images from 1D data. These 2D images represent slices of the object. By shifting the object in z direction a slice at any z position can be reconstructed; thus, if the acquisition reconstruction process is performed for different shift values z, a 3D image is obtained. This is the most straightforward method to obtain 3D images with CT; it often referred to as as sequential CT scanning [Kalender, 2000]. The main drawback of this approach lies in the fact that the acquisition (full or short-scan) is repeated for every slice leading thus to long acquisition times. An improvement was introduced with spiral CT at the end of the 80s. The object is continuously translated in z direction while the source-detector arrangement rotates around it. The translation is performed in such a way that after a half-rotation, it is at most equal to the slice thickness. The value of the projections for the reconstruction of a slice at a given position z are obtained by interpolation of the acquired projections along the z axis. With spiral CT the acquisition time is strongly reduced with respect to sequential CT scanning but still several rotations are necessary to reconstruct a volume. A further improvement was introduced in the middle of the nineties with multi-row detectors. These enable the acquisition of several slices simultaneously. The simultaneous acquisition of M slices allows to increase the speed with which the object is translated, approximately by the same factor, keeping image quality. Hence, the acquisition time for a given volume is reduced. At the time of the writing of this thesis the main manufacturers of CT scanners for medical applications offer models with up to 64 rows.

Future CT scanners will be equipped with large area detectors. These detectors will cover entire organs [Oppelt, 2005] which will make it possible to reconstruct 3D images of organs with data acquired in a single rotation. The corresponding reduction of the acquisition time will enable dynamic volume scanning (4D Computed Tomography). The methods developed during this thesis work under the assumption that we have such a system at our disposal. The 2D detector is assumed to cover the whole region of interest and the source-detector arrangement turns about

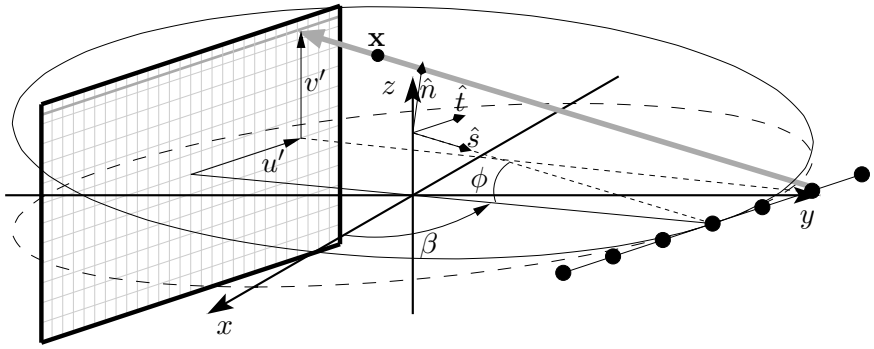

Figure 3.10. CT scan with ideal fan-parallel geometry.

the z axis in a circular trajectory. In this section we discuss 3D reconstruction methods from 2D projections acquired on a circular trajectory.

3.3.1. TUY-SMITH CONDITION

We saw in section 3.2 that for 2D reconstruction all integrals along lines intersecting the object must be known in order to reconstruct an image. The values of these line integrals are often denoted as 2D Radon values. In the 3D case, Radon values are integrals on planes intersecting the object. Again, all Radon values must be known in order to reconstruct a 3D image. However, it is not possible to measure all Radon values with a circular trajectory. In order to acquire all Radon values the source trajectory must intersect all planes intersecting the object. This statement is known as the Tuy-Smith condition [Tuy, 1983]. Even if not all Radon data are acquired, there exist approximate reconstruction methods for circular trajectories. These algorithms are often referred to in the literature as non-exact reconstruction algorithms. The algorithms presented in this chapter are all based on the FDK approach presented by Feldkamp, Davis and Kress in [Feldkamp et al., 1984]. These algorithms can be seen as an extension of the Filtered Backprojection to 2D projection data and are all based on the convolution-backprojection principle.

3.3.2. FDK PRINCIPLE

We present in this section a description of the principle proposed by Feldkamp, Davis and Kress in [Feldkamp et al., 1984] to reconstruct a 3D volume from data acquired on a circular trajectory. The idea we would like to stress is that this principle allows to extend 2D FBP reconstruction to 3D reconstruction from data from a 2D detector acquired on a circular trajectory. For this reason we do not follow the presentation in [Feldkamp et al., 1984] but rather use an idealised acquisition geometry which is the natural extension of a parallel-beam in 2D to 3D acquisition on a circular trajectory. We denote this geometry as ideal fan-parallel beam geometry. A scheme of a CT scanner with this geometry is shown in figure 3.10. An extended source positioned along a straight line parallel to the detector rotates about the z-axis. The plane $z = 0$ that contains the circular trajectory is denoted as the midplane. Each of the source positions emits a fan-beam in the direction orthogonal to the midplane. The fans are parallel to each other. The projections $P_\beta(u, v)$ are characterised by the projection angle β and the Cartesian coordinates of the detector

(u, v). The distance from the central source position to the rotation axis is Γ and to the detector Γ_D. For $v = 0$ we are in the same case as in section 3.2.4; therefore for an $\mathbf{x}$ in the midplane, we can write, from (3.25)

$$\mu^r(\mathbf{x}) = \frac{1}{2} \int_0^{2\pi} \int_{-u_{max}}^{u_{max}} P_\beta(u, 0) g(u'(\mathbf{x}, \beta) - u) du d\beta \tag{3.49}$$

where $u'(\mathbf{x}, \beta) = -x \sin(\beta) + y \cos(\beta)$. The outer integral can be decomposed in differential contributions (DC), corresponding to the contribution to the reconstruction from the projection data for a small increment $d\beta$ of the rotation angle [Feldkamp et al., 1984]. These contributions can be expressed as

$$DC(\mathbf{x}, \beta) = \frac{1}{2} \int_{-u_{max}}^{u_{max}} P_\beta(u, 0) g(u'(\mathbf{x}, \beta) - u) du d\beta. \tag{3.50}$$

For each value β of the projection angle, each row of the detector determines a tilted plane that intersects the detector along a straight line at $z = v$ and the midplane at the extended source. Let $\hat{n}$ denote the normal of this tilted plane, $\hat{s}$ a unit vector on the tilted plane along the central ray from the axis to the source and $\hat{t}$ a unit vector along the detector. The three vectors form a right-handed orthonormal set. The tilted plane can be treated as if it were the midplane of another, tilted 1D source-detector arrangement. Hence, for an $\mathbf{x}$ situated on the tilted plane, we can write the differential contribution as

$$DC(\mathbf{x}, \beta_t) = \frac{1}{2} \int_{-u_{max}}^{u_{max}} P_\beta(u, v'(\mathbf{x}, \beta_t)) g(u'(\mathbf{x}, \beta_t) - u) du d\beta_t \tag{3.51}$$

where β_t is the angle between projection of the x-axis on the tilted plane, and the line from the z-axis to the central source position on the tilted plane. The idea of the FDK approach is to choose $d\beta_t$ such that a differential rotation of $d\beta$ about the z-axis is equivalent to a differential rotation $d\beta_t$ about the normal of the tilted plane $\hat{n}$. The rotation of $\hat{s}$ about $\hat{z}$ can be written as

$$\hat{s}' \approx \hat{s} + d\beta \hat{z} \times \hat{s} = \hat{s} + d\beta \cos(\phi) \hat{t}, \tag{3.52}$$

where $\times$ indicates a vector product. The rotation of $\hat{s}$ about $\hat{n}$ is

$$\hat{s}' \approx \hat{s} + d\beta_t \hat{n} \times \hat{s} = \hat{s} + d\beta_t \hat{t}; \tag{3.53}$$

therefore, we choose

$$d\beta_t = d\beta \cos(\phi). \tag{3.54}$$

If we substitute (3.54) in (3.51), we obtain the expression of the differential contribution for the points $\mathbf{x}$ on the tilted plane that intersects the detector at $z = v$ as a function of the projection angle of the circular trajectory

$$DC(\mathbf{x}, \beta) = \frac{1}{2} \int_{-u_{max}}^{u_{max}} P_\beta(u, v) g(u'(\mathbf{x}, \beta) - u) \cos(\phi) du d\beta. \tag{3.55}$$

Using $\cos(\phi) = \frac{\Gamma_D}{\sqrt{\Gamma_D^2+v^2}}$, the FDK reconstruction algorithm for any $\mathbf{x}$ is obtained by integrating over $[0, 2\pi]$:

$$FP_\beta(u,v) = \int_{-u_{max}}^{u_{max}} \left(P_\beta(s,v) \frac{\Gamma_D}{\sqrt{\Gamma_D^2+v^2}} \right) g(u-s)ds \tag{3.56}$$

$$\mu^r(\mathbf{x}) = \frac{1}{2} \int_0^{2\pi} FP_\beta(u'(\mathbf{x},\beta), v'(\mathbf{x},\beta))d\beta \tag{3.57}$$

The values u' and v' determine for each projection angle β the ray that passes through $\mathbf{x}$, and can be calculated as

$$u'(\mathbf{x},\beta) = -x\sin(\beta) + y\cos(\beta) \tag{3.58}$$

$$v'(\mathbf{x},\beta) = \frac{\Gamma_D z}{\Gamma - x\cos(\beta) - y\sin(\beta)}. \tag{3.59}$$

If we compare (3.56) to (3.26), we observe that FDK simply adds a weighting factor to the projections before filtering. This weighting factor is equal to one for the midplane, so that FDK and FBP are equivalent for $z = 0$. For points outside this plane the algorithm is an approximation and results become worse with increasing distance to the midplane. Expression (3.54) represents the essence of the FDK approach. The same principle can be applied to extend the FBP algorithm in other 2D geometries to 3D reconstruction from data acquired on a circular trajectory. Special attention, however, has to be paid to the filtering step. As we have seen, the FDK approach is based on the fact that on every tilted plane we find again the same 2D geometry as in the midplane. In the artificial setting used in this section, the tilted plane intersects the detector along a straight line (grey line in figure 3.10) that coincides with the direction of the rows in the detector. Since the geometry of the intersection is equal to the geometry in the equivalent 2D setting the filtering operation must not be modified. As we will see in the next sections this is not the case when the detectors are curved.

This approach leads to a whole family of 3D reconstruction algorithms from data acquired in a circular trajectory which are based on convolution and backprojection. Throughout this thesis we denote 3D reconstruction algorithms based on this principle as FDK-like reconstruction algorithms.

3.3.3. Cone-beam FDK-like Reconstruction with Cylindrical Detectors

The geometry used to illustrate the FDK principle is an idealised one. As in the 2D case, it is much more efficient to exploit the divergent nature of X-ray radiation. For this reason, commercial scanners use an X-ray beam that is divergent in 3D, i.e. a cone-beam. Figure 3.11 shows a scheme of a CT scanner with cone-beam geometry. Cone-beam projections acquired with a cylindrical detector $P_\alpha(\gamma,\phi)$ are characterised by the projection angle α, the fan-angle γ and the cone-angle φ. Every row of the detector is determined by a value of the cone-angle φ. Again, the radius of the circular trajectory is Γ. The radius of the cylindrical detector is Γ_D; the centre of the cylinder is situated on the source. We present here two approaches to apply the FDK principle to such

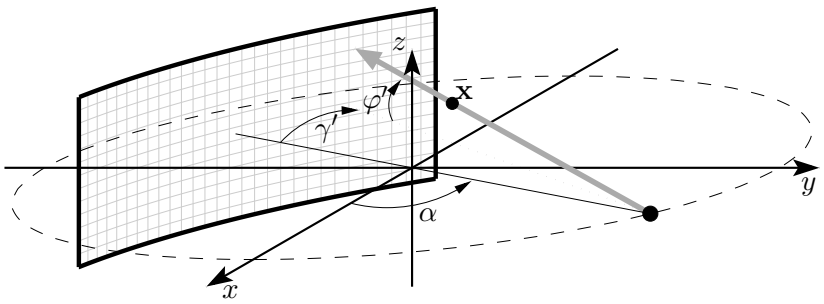

Figure 3.11. Scheme of a CT scanner in cone-beam geometry with a cylindrical detector.

a geometry that lead to two different reconstruction algorithms. In a similar way as in section 3.2.5, the first one is based on rebinning, whereas the second one uses directly the cone-beam projections.

3.3.3.1. FDK Reconstruction by Rebinning: the T-FDK Algorithm

In this section we present the T-FDK algorithm as described in [Grass et al., 2000]. The algorithm consists of two parts: rebinning of the measured projections, and FDK-like reconstruction from the rebinned data.

Since we have a two dimensional detector, so that rebinning is performed in two dimensions. First, rebinning is performed along the horizontal component of the projections γ. We denote this step as row-wise rebinning; it is identical to the rebinning from a fan-beam to a parallel-beam in 2D reconstruction as described in section 3.2.5.1 except that it is performed for every value of the cone-angle φ

$$P_\alpha(\gamma, \varphi) \rightarrow P^b_\beta(u, \varphi). \tag{3.60}$$

In the 2D case, we interpret the reordered rays as data from a straight line detector. Since projections have now two dimensions, we interpret them as data from a planar detector situated at a distance Γ_D from the central source position. We denote this detector as virtual detector. Figures 3.12 a) and b) show the 2D dimensional detector before and after rebinning. The curved form of the rebinned detector illustrates that, for a given value of the cone-angle φ, the distance from the source to the detector (the "length of the ray") is the same for all values of u. The distance from the rebinned detector to the virtual detector plane depends on u. Hence, the rays with a cone-angle φ (i.e. the rays corresponding to a row in the rebinned detector) will intersect the virtual detector at different heights depending on u. As a consequence of this, the rows of the rebinned detector are not parallel to $z = 0$ but go along slightly bent lines, with the exception of the rays with $\varphi = 0$. This is shown in figure 3.12 c). The dashed line follows the direction of the rows of the rebinned detector, whereas the solid line is parallel to the $z = 0$ plane. The second rebinning step consists, precisely, in calculating the value of the projections along lines parallel to the $z = 0$ plane. This can be expressed as

$$P^b_\beta(u, \varphi) \rightarrow P^b_\beta(u, v). \tag{3.61}$$

These values are calculated by interpolation from the values of the φ rows. The maximum height is determined by the minimum height of the virtual detector, which corresponds to the extreme

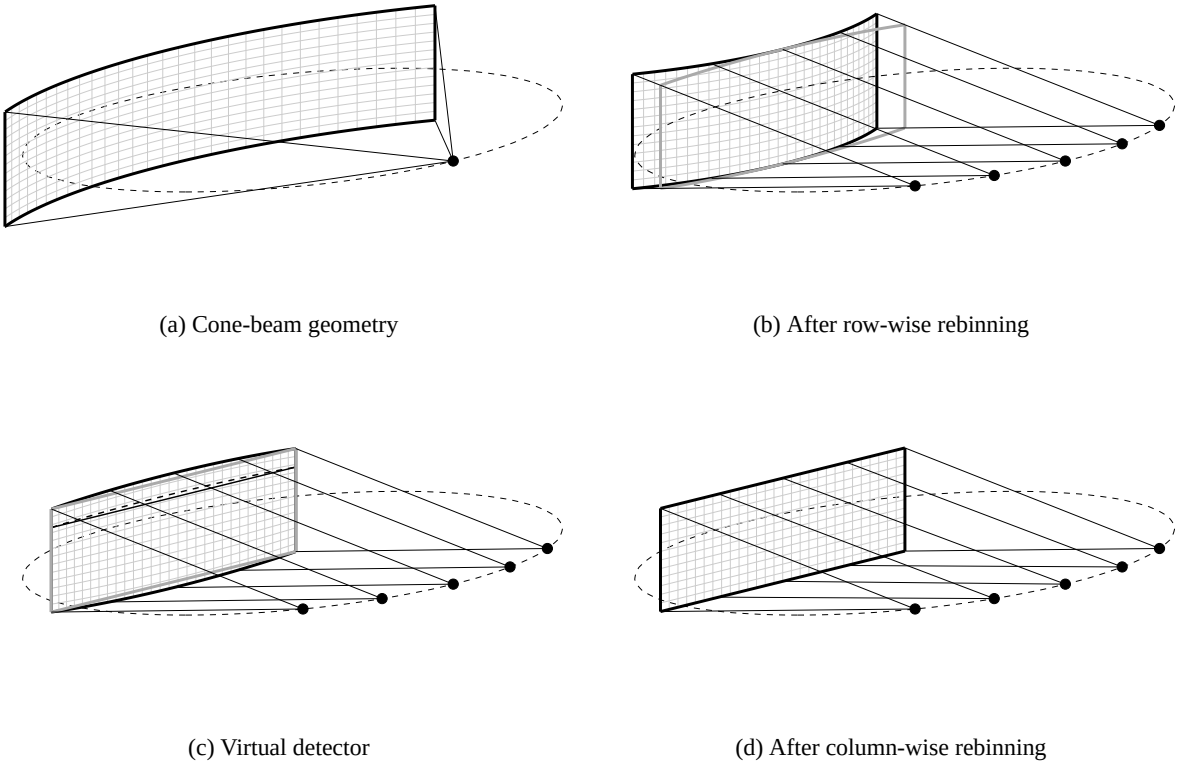

(a) Cone-beam geometry

(b) After row-wise rebinning

(c) Virtual detector

(d) After column-wise rebinning

Figure 3.12. Steps of the 2D rebinning from cone-beam projections to fan-parallel beam projections

positions $\pm u_{max}$; it can be calculated as

$$v_{max} = \Gamma_D \tan(\varphi_{max}) \cos(\gamma_{max}). \tag{3.62}$$

The rays above this value are not used which leads to a rectangular detector which is slightly smaller than the rebinned detector (see figure 3.12 c)). These rays can be easily suppressed in the original cone-beam in order to avoid unnecessary X-ray exposure.

The final rebinned geometry, shown in figure 3.13, is very similar to the geometry described in the previous section. In order to distinguish them, we denote it as fan-parallel beam geometry. As in the ideal fan-parallel beam geometry, the projections $P^b_\beta(u, v)$ are determined by the projection angle β and the Cartesian coordinates of the detector, but now the extended source is not situated along a straight line but on the circular trajectory. We can now formulate the FDK reconstruction algorithm for the rebinned projections; the starting point is the FBP in parallel geometry. The geometry of the detector is the same as in the previous section, i.e. the tilted plane intersects the detector along straight lines which are parallel to the detector rows. Hence, no modification of the filtering step is required. Note that this is the reason for the second rebinning step. As stated previously, after row-wise rebinning, the rows of the virtual detector go along slightly bent curves. A filtering in this geometry would require change of coordinates in the convolution integral; with the column-wise rebinning this is eluded in an elegant way. The difference with respect to the previous section is on the backprojection step. Since the extended source is situated on the circular

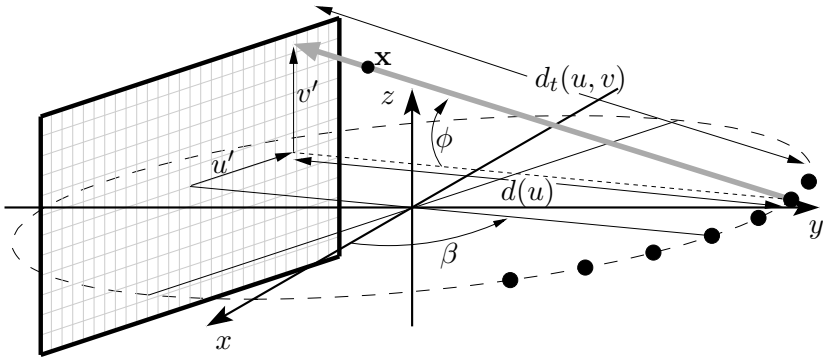

Figure 3.13. Scheme of a CT scanner in fan-parallel beam geometry.

trajectory, the distance from each of the source positions to the detector depends on u. Therefore, every ray in a given row v is on a different tilted plane. The angle of the tilted plane on which the ray u is included is given by

$$\cos(\phi) = w(u,v) = \frac{d(u)}{d_t(u,v)} = \frac{\sqrt{\Gamma^2 - u^2} + \Gamma_D - \Gamma}{\sqrt{\left(\sqrt{\Gamma^2 - u^2} + \Gamma_D - \Gamma\right)^2 + v^2}}. \tag{3.63}$$

where $d(u)$ is the distance from the source position determined by u to the detector on the midplane and $d_t(u,v)$ is the distance from the source position determined by u to the detector on the tilted plane (see figure 3.13). Using this result in (3.54) and following the same approach as in the previous section, we obtain the FDK reconstruction algorithm for fan-parallel geometry

$$FP_\beta(u,v) = \int_{-u_{max}}^{u_{max}} \left(P_\beta^b(s,v)w(u,v)\right) g(u-s)ds \tag{3.64}$$

$$\mu^r(\mathbf{x}) = \frac{1}{2}\int_0^{2\pi} FP_\beta(u'(\mathbf{x},\beta), v'(\mathbf{x},\beta))d\beta. \tag{3.65}$$

The values u' and v' determine for each projection angle β the ray that passes through $\mathbf{x}$, and can be calculated as

$$u'(\mathbf{x},\beta) = -x\sin(\beta) + y\cos(\beta) \tag{3.66}$$

$$v'(\mathbf{x},\beta) = \frac{z\left(\sqrt{\Gamma^2 - u^2} + \Gamma_D - \Gamma\right)}{\sqrt{\Gamma^2 - u^2} - x\cos(\beta) - y\sin(\beta)}. \tag{3.67}$$

3.3.3.2. The C-FDK Algorithm for Cylindrical Detectors

The derivation of an FDK algorithm for projections acquired with a cylindrical detector is somewhat more complicated. Figure 3.14 shows that the tilted plane forming an angle of ϕ with the midplane intersects the cylindrical detector along curves (solid line) which are not parallel to the

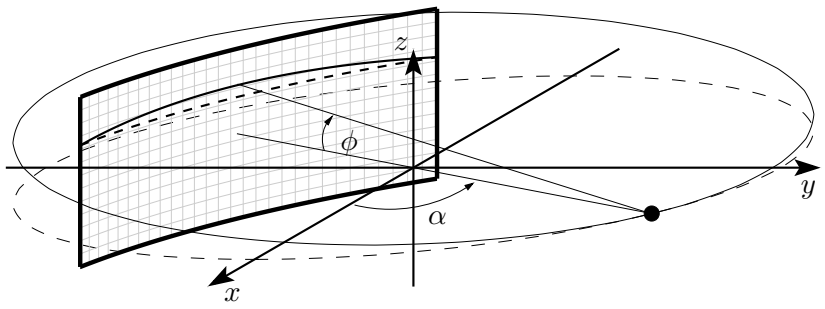

Figure 3.14. Scheme of a CT scanner in cone-beam geometry with a cylindrical detector. The solid line shows the intersection of the tilted plane forming an angle of ϕ with the midplane with the detector. The dashed line follows the direction of the detector rows.

rows of the detector (dashed). A precise formulation of the algorithm is given by Schaller in his thesis [Schaller, 1998]. The author proposes a simplification of the algorithm by simply ignoring the intersection of the tilted plane and filtering along the rows of the detector. This leads to an FDK-like algorithm which can be interpreted as an extension of the FBP for fan-beam geometry to cylindrical detectors. We adopt the nomenclature proposed by Turbell in [Turbell, 2001] and denote the algorithm as C-FDK algorithm. Its expression is

$$FP_\alpha(\gamma,\varphi) = \int_{-\gamma_{max}}^{\gamma_{max}} \left(P_\alpha(\kappa,\varphi)\Gamma\cos(\varphi)\cos(\gamma)\right) h(\gamma-\kappa)d\kappa \tag{3.68}$$

$$\mu^r(\mathbf{x}) = \frac{1}{2}\int_0^{2\pi} \frac{1}{L^2(\mathbf{x},\alpha)} FP_\alpha(\gamma'(\mathbf{x},\alpha),\varphi'(\mathbf{x},\alpha))d\alpha, \tag{3.69}$$

where $\gamma'(\mathbf{x},\alpha)$, $L(\mathbf{x},\alpha)$ and $h(\gamma)$ are the same as in section 3.2.5.2 and $\varphi'(\mathbf{x},\alpha)$ determines the cone-angle for the ray that passes through $\mathbf{x}$ (see figure 3.11)

$$\varphi'(\mathbf{x},\alpha) = \arctan\left(\frac{z}{L(\mathbf{x},\alpha)}\right). \tag{3.70}$$

3.3.3.3. FDK Reconstruction: A Numerical Example

As an example, we reconstruct in this section a 3D image of the head phantom in appendix C. We wish to obtain an image with isotropic resolution, i.e. with the same spatial resolution in all directions. For this purpose we first concentrate on the midplane; here, we have a fan-beam geometry as described in section 3.2.5. The radius of the circular trajectory is $\Gamma = 570$ mm and the radius of the detector $\Gamma_D = 1040$ mm. Since the object is situated within a circle of radius u_{max}, we can use (3.40) to compute the maximum fan-angle of the detector

$$\gamma_{max} = \arcsin\left(\frac{u_{max}}{\Gamma}\right) = 0.2265 \text{ rd}, \tag{3.71}$$

where we have used that $u_{max} = 128$ mm as in section 3.2.4.3. For the number of pixels of the detector and the number of angular positions of the source, we use the same values as in the parallel geometry case:

$$\begin{aligned} N_\gamma &= 256 \\ N_\alpha &= 800. \end{aligned} \tag{3.72}$$

Using the sampling conditions for parallel-beam geometry for a scanner with fan-beam geometry is a rather heuristic approach. A detailed analysis of the sampling of the Radon transform in fan-beam geometry is given in [Natterer and Wübbeling, 2001]. The distance between rows is equal to the height of the detector pixels. Hence, using the sampling condition (see appendix B)

$$\Delta z \leq \frac{1}{2\varsigma_{max}} = 1 \text{ mm}, \tag{3.73}$$

where ς_{max} is the maximum spatial frequency (see section 3.2.4). Note that this height corresponds to the pixel height for a detector situated at the origin. Since our detector is situated at a distance of the source of Γ_D, and the beam is divergent in axial direction as well, we have to apply a magnification factor of Γ_D/Γ. The detector pixels have then a height of 1.825 mm. For the simulation we used a scanner with 128 rows an have reconstructed a volume of $256 \times 256 \times 127$ voxels. The odd number of slices ensures that the central one corresponds to the midplane. In order to illustrate the effect of the FDK approximation, we show in figure 3.15 the yz plane of the phantom and of the reconstructions with T-FDK and C-FDK. The price for reconstructing from an incomplete set of Radon values can be clearly observed; the images exhibit strong artifacts that do not appear in an 2D FBP reconstruction on the trajectory plane. The internal structures of the phantom can be nevertheless well identified. Even elements with low contrast as the ventricle insert (number 12 in the description in Appendix C) are well outlined. The image quality in the T-FDK reconstruction and the C-FDK reconstruction is very similar. T-FDK attains a slightly better quality which can be observed by comparing the artifacts around the sinus insert (7 in figure C.2). This can be explained by the approximation done in the filtering step in C-FDK. However, the main source of error is the incomplete sampling of the 3D Radon space.

3.3.3.4. Reconstruction from Data Acquired in a Short-scan

The cone-beam geometry reduces to fan-beam geometry in the midplane. Likewise, reduce the T-FDK and C-FDK algorithms to rebinning and parallel-beam FBP and fan-beam FBP respectively. As in the 2D case, a short-scan reconstruction can be performed. The principle is the same as in the corresponding 2D cases. For T-FDK it suffices to substitute the backprojection integral by $2\int_0^\pi$. For C-FDK, projections are weighted with the same weighting function as in the 2D case, and then the outer integral is substituted by $\int_0^{\pi+2\gamma_{max}}$. Performing short-scan reconstruction with an FDK-like reconstruction algorithm entails, however, two additional approximations to the FDK principle itself. The first concerns the sampling of the 3D Radon space. In parallel-beam geometry, we saw in section 3.2.4 that the rays (β, γ) and $(\beta+\pi, -\gamma)$ are equivalent. In fan-beam geometry the pairs of equivalent rays are given by $(\alpha, \gamma, \varphi)$ and $(\alpha+\pi-2\gamma, -\gamma, \varphi)$. These pairs of equivalent rays represent the same 2D Radon value so that in a full-scan all Radon values are measured twice. For cone-beam projections, this only holds for the midplane. As an example consider projections in cone-beam geometry $P_\alpha(\gamma, \varphi)$. The rays $(\alpha, \gamma, \varphi)$ and $(\alpha+\pi-2\gamma, -\gamma, \varphi)$

are only equivalent if $\varphi = 0$. Hence, if we only perform a short-scan we are measuring less 3D Radon values than in a full-scan since the projections left out are not equivalent to the measured ones. The second assumption concerns the weighting of projections in cone-beam geometry. In section 3.2.5.3, we introduced the principle of weighting for short-scan reconstruction from fan-beam projections. In a short-scan some line integrals are measured twice, the idea of weighting is to average the rays measured twice in order to compensate their double contribution to the reconstruction of the image. In cone-beam though these rays are only equivalent on the midplane so that rays are averaged which do not really correspond to the same line integral. As a consequence of these two assumptions short-scan FDK-like reconstructions exhibit much stronger artifacts out of the midplane than full-scan FDK-like reconstruction. This is illustrated in figure 3.16. The error for the planes $z \neq 0$ is higher than in the corresponding full-scan reconstruction. This can be clearly observed at the upper and lower end of the frontal sinus insert (number 7 in the description in Appendix C).

Finally, we introduce the concepts of quasi-equivalent rays and of quasi-equivalent rays approximation which will be used throughout the thesis. For a given value of the cone-angle φ_0, the rays $(\alpha_1, \gamma_1, \varphi_0)$ and $(\alpha_2, \gamma_2, \varphi_0)$ are quasi-equivalent if the rays $(\alpha_1, \gamma_1, 0)$ and $(\alpha_2, \gamma_2, 0)$ are equivalent. For small cone-angles, it may be assumed that these rays represent the same line integral; we denote this approximation as quasi-equivalent rays approximation. The two assumptions discussed previously in this section imply this approximation.

3.4. Discussion. Image Quality

In this chapter we provided a short introduction to CT imaging from the physical principles to 3D reconstruction. All along the chapter we described several factors that influence image quality. These are mainly due to approximations of physical or mathematical nature in the reconstruction process or to noise. We did, however, provide any quantitative estimation for the quality of the produced images. The reason for this is that the assessment of the quality of CT images depends strongly on the application. As an example consider the examples of short-scan reconstruction with the T-FDK and C-FDK algorithms shown in figure 3.16. The images exhibit strong artifacts which might lead to the conclusion that they have a very low quality. Before coming to this conclusion, we should take into account that the window used for the visualisation is very narrow. In some applications, i.e. for the visualisation of bone, windows of a width over 1000 HU are used so that these artifacts become negligible.

Throughout the next chapters, we will try to keep the results as general as possible. In some cases, however, for the assessment of error measurements or to adjust the values of reconstruction parameters of the algorithms, we will use as a reference application perfusion CT.

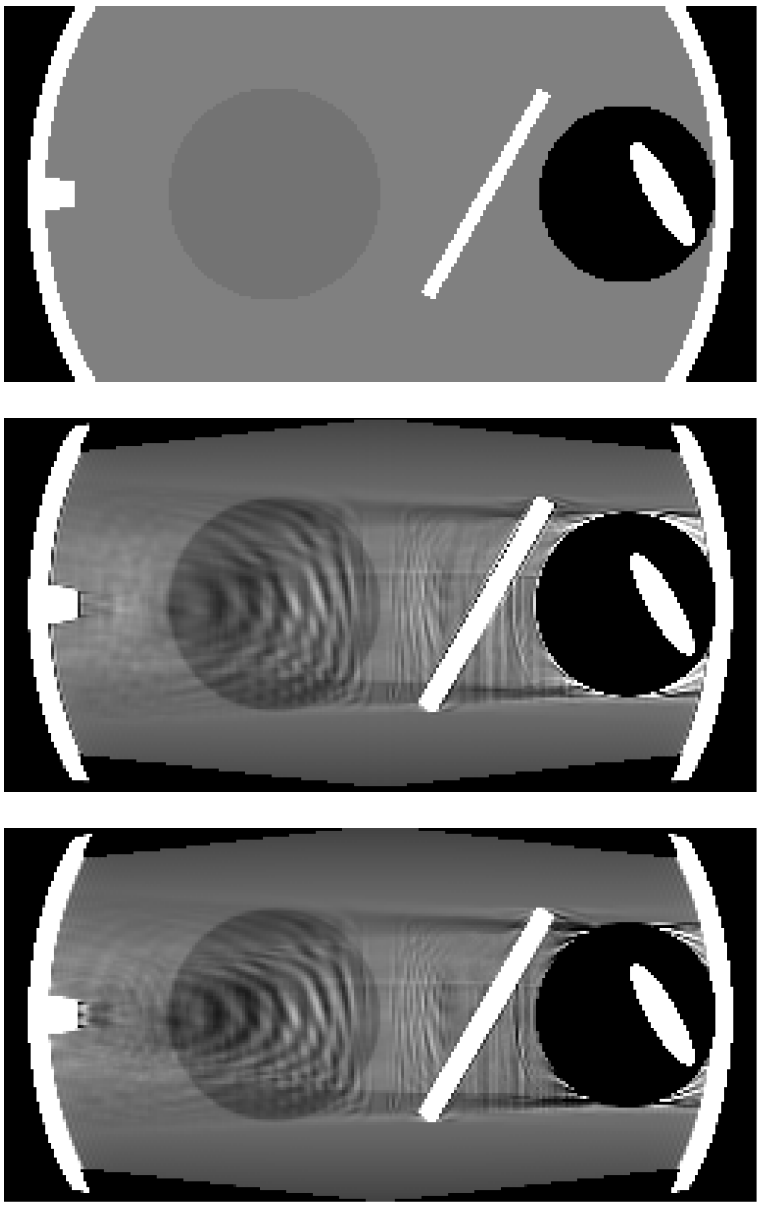

Figure 3.15. Examples of reconstructions with FDK-like algorithms. The images show the yz plane of the head phantom. Top: phantom, middle: T-FDK and bottom: C-FDK. Window $[0, 100]$ HU.

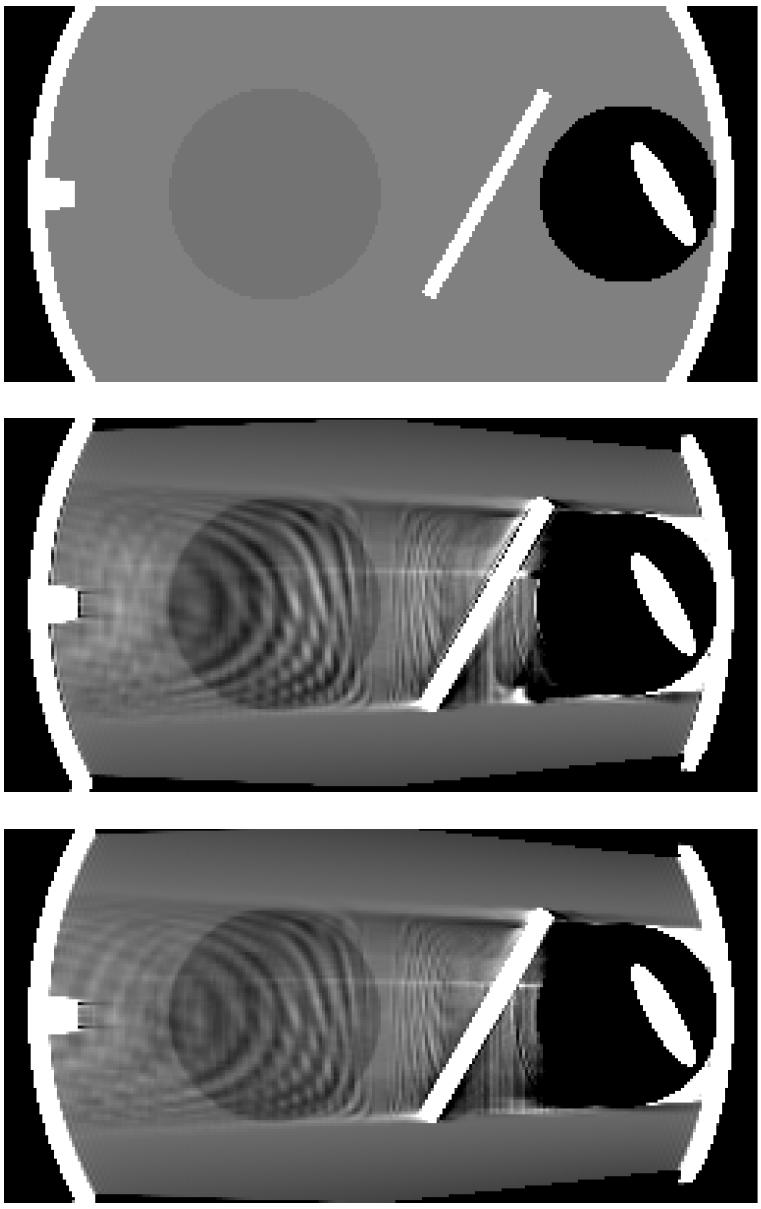

Figure 3.16. Examples of short-scan reconstructions with FDK-like algorithms. The images show the yz plane of the head phantom. Top: phantom, middle: T-FDK and bottom: C-FDK with Parker weighting. Window $[0, 100]$ HU.

CHAPTER 4.

DYNAMIC RECONSTRUCTION FOR OBJECTS WITH TIME DEPENDENT ATTENUATION

We start here the presentation of the original work carried out during this thesis. The chapter is devoted to the problem of reconstructing a sequence of images of an object whose attenuation changes during acquisition time. It addresses two of the main limitations of perfusion CT: the time dependence of the attenuation coefficent and the fast reconstruction from the input data. We first formulate the problem and discuss the state-of-the-art algorithms for dynamic reconstruction. All these approaches have in common that they ignore the time dependence of the attenuation coefficient during certain periods of time. For this reason, we present in the next section an analysis of dynamic acquisition and static reconstruction with projections of an object with time dependent attenuation coefficient. The results of this analysis are the starting point for the derivation of two dynamic reconstruction algorithms based on partial block backprojection with the T-FDK and the C-FDK algorithms respectively, and time interpolation with polynomial splines. These reconstruction algorithms can be adapted according to the maximum frequency of the dynamic process, optimising thus the amount of data acquired. For slow processes, fewer data are acquired reducing dose and computational cost. For fast processes, the algorithms reach a high temporal resolution. In the last section, we present numerical simulations both to verify the theoretical analysis provided and to assess the performance of the algorithms.

4.1. INTRODUCTION. DYNAMIC CT

The reconstruction methods presented in chapter 3 make implicitly the assumption that the object does not change while the projections in a full-scan (or a short-scan) are acquired. For most clinical applications of Computed Tomography, this is a reasonable assumption. However, this assumption is eventually violated if the patient moves during acquisition time. In dynamic CT, the objective is to reconstruct a time sequence of two or three-dimensional CT images which contains the changes in a region of interest over a period of time. Hence, the assumption that the object is static during acquisition time does not hold anymore.

During acquisition time, two kinds of dynamic changes might take place: changes due to motion or deformation and changes due to temporal evolution. If we consider an infinitesimal volume in the object, motion or deformation imply its change of position whereas temporal evolution entails the change of its composition. Dynamic changes due to motion or deformation include among other cases the movement of an extern object as a needle or a catheter in the region of interest, breathing in lung imaging or muscle contraction in cardiac imaging. Several approaches have been proposed to overcome the problem of motion or deformation during acquisition time. Algorithmic approaches try to estimate motion or deformation in order to compensate it in the

reconstruction [Li et al., 2006, Grangeat et al., 2002]. Other approaches include the fixation of the patient to avoid motion during scan time. This procedure is followed in some applications in neuroradiology where the position of the patient must be determined with high accuracy because the acquired images will be used for a guiding system during an intervention. For this purpose, the patient is fixed with a stereotactic frame and cannot move.

Temporal evolution is typically due to the flow of contrast agent; this causes no structural change in the region of interest but a change of the attenuation value. In section 2.3.2 we described a typical perfusion CT protocol. After injection of a contrast agent, projections are acquired over a period of time comprising several full-rotations. During acquisition time, contrast agent flows in and out of the region of interest so that the attenuation value in blood vessels depends on time.

In this thesis we concentrate on dynamic changes due to temporal evolution and assume that neither motion nor deformation occur. The methods developed might be combined with a motion/deformation compensation algorithm if necessary for a particular application.

As discussed in section 3.3, the trend in Computed Tomography is the development of large area detectors that cover the whole region of interest. Under these conditions, it is possible to reconstruct the volume of interest from data acquired in a single rotation or less. In a typical perfusion CT protocol 40 full-scans are performed during 40 s. As an example, consider a state-of-the-art scanner which typically delivers pro rotation 1800 projections with 1400 channels (pixels per row) each. Each pixel in the detector codes the detected intensity with 20bits. The total amount of acquired data in 40 full-scans is $\approx$ 240MB. The same acquisition protocol with a scanner with 256 rows would yield ≈ 60GB. This huge amount of data is the input for the dynamic reconstruction algorithm. In medical applications, the reconstruction takes place in the CT scanner or in an accompanying standard PC and the reconstruction time is a crucial issue. This claims for reconstruction algorithms which are efficient in terms of computational cost. For this reason we concentrate on dynamic reconstruction based on analytical methods (see discussion in section 3.2.1).

4.1.1. Problem Setting

The dynamic reconstruction problem for objects with time dependent attenuation can be formulated as follows. A source-detector arrangement with a cylindrical detector as described in figure 3.11 rotates with a constant angular speed ω on a circular trajectory. The plane containing the source trajectory is denoted as xy plane. We assume that the source is situated at $\alpha = 0$ at $t = 0$; hence, the projection $P_\alpha(\gamma, \varphi, t_\alpha)$ is acquired at $t_\alpha = \alpha/\omega$. The object is represented by a time dependent distribution of an attenuation coefficient $\mu(\mathbf{x}, t)$ where $\mathbf{x} \in \mathbb{R}^3$ denotes the spatial coordinate and t denotes time. The object is located within a cylinder of radius $\|\mathbf{x_{max}}\|$, i.e.

$$\mu(\mathbf{x}, t) \approx 0 \quad \text{for} \quad \|\mathbf{x}\| \geq \|\mathbf{x_{max}}\|. \tag{4.1}$$

The goal of dynamic CT is the estimation of $\mu(\mathbf{x}, t)$ in time intervals of T_{fr} during a total time of T_{tot}. For this purpose, the source rotates continuously on the same plane during a period of time of T_{tot}. During this continuous rotation the source may be switched off during regular periods of time.

In some of the approaches presented in this thesis acquisition parameters as the number of scans performed during T_{tot} or the rotation time $T_{2\pi}$ are part of the algorithm. These methods should be therefore denoted as dynamic acquisition and reconstruction algorithms. In order not

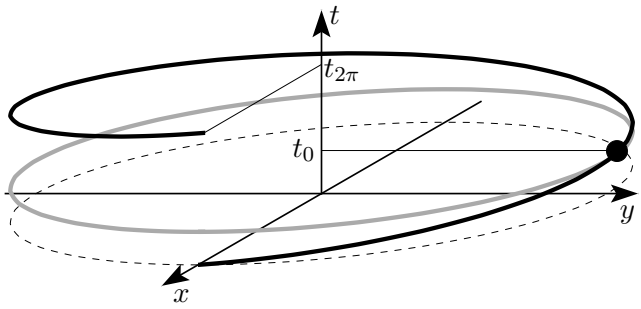

Figure 4.1. Circular trajectory in dynamic CT.

to complicate the terminology unnecessarily we use the term *dynamic reconstruction algorithm* to denote the computation of a sequence from projections of a time dependent object, even if acquisition parameters are involved in the algorithm.

4.1.2. Inconsistent Projection Datasets

The main limitations of dynamic CT comes from the simultaneous time dependence of the scanned object and the position of the source-detector arrangement. For every value of t, $\mu(\mathbf{x}, t)$ describes a different spatial distribution of the attenuation coefficient; hence, from the CT point of view, a different object. This is illustrated in figure 4.1. The trajectory of the source depends on time. If we include the temporal dimension in the description of the source trajectory, the circular trajectory becomes a spiral with a step equal to the rotation time of the scanner $T_{2\pi}$. In the static case discussed in the previous chapter, the spiral reduces to a circle because the density of the object does not depend on time. In order to perform a full-scan reconstruction of the object at a given time t_0 we need projections from all angular positions at this time. This projection dataset is represented by the grey curve in figure 4.1. However, at time t_0, only one projection is acquired, namely $\alpha_0 = \omega t_0$. The spiral trajectory represents the acquired projection dataset, whereas the grey trajectory represents the necessary projection dataset for the reconstruction at t_0; they intersect only at α_0. A dataset containing projections acquired at different times is said to be inconsistent because the projections it contains do not correspond to the same object or at least do not correspond to the object in the same state. Static reconstruction algorithms require consistent projection datasets. Using static reconstruction with inconsistent projection datasets yields two kinds of errors. First, the value of the reconstruction at a given position deviates from the real value of the attenuation at this position at the desired reconstruction time. Second, the time dependence at a given position cause an error in form of artifacts in the area around this position. Figure 4.2 shows an example of such artifacts; it shows a reconstruction of phantom A (described in appendix C). The reconstruction was performed by rebinning a parallel-beam from the acquired fan-beam projections and then using short-scan FBP as described in section 3.2.5.1.

The basic principle of dynamic reconstruction is to remove or at least reduce the inconsistencies in the data in order to use results from static reconstruction [Bonnet et al., 2003b]. Note that the degree of inconsistency depends on the rotational speed of the source. Indeed, in the idealised case of a source with infinite rotational speed, all projections would be acquired at the same time and inconsistency would disappear; in figure 4.1 the step would be equal to 0 and the trajectory

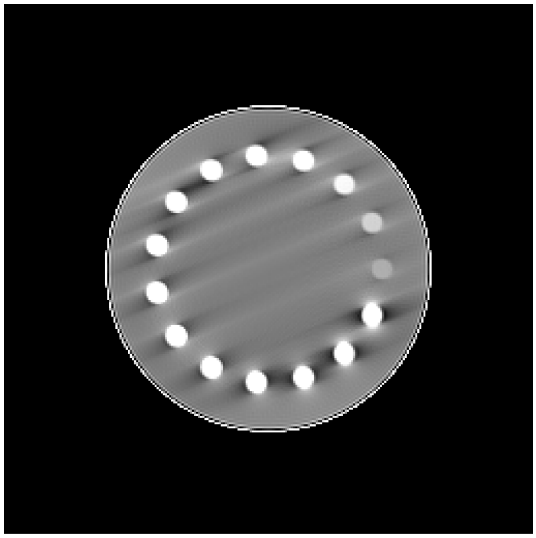

Figure 4.2. Example of artifacts due to data inconsistencies. Short-scan FBP reconstruction from rebinned projections of phantom A (see appendix C). Window $[30, 70]$ HU.

would reduce to a circle. On the other hand, the frequency of the dynamic changes plays also a crucial role. Very slow changes will cause almost no inconsistency and therefore almost negligible artifacts, whereas fast changes cannot be ignored. Of course, the meaning of ”slow” has to be interpreted relative to the rotation time.

4.2. State-of-the-art Dynamic Reconstruction Algorithms

As stated at the beginning of the chapter, the aim of dynamic reconstruction is to compute a sequence of CT images (frames) from projection data acquired over a period of time comprising several full-rotations. Since each projection is acquired at a different time, any projection dataset containing more than one projection is inconsistent. Several methods have been proposed in the literature to tackle the reconstruction problem. We provide in this section a brief survey in order to motivate the work presented in this chapter. The methods described are all based on FDK-like reconstruction (see section 3.3.3).

Standard Reconstruction The most straightforward approach for dynamic reconstruction consists in ignoring data inconsistencies and use a static reconstruction algorithm for every frame. In order to reconstruct a frame at a given time t_0, projections in an angular interval of length 2π around $\alpha_0 = \omega t_0$ are used. As a result, the images exhibit a bias in the time dependent values and artifacts around them. However, these errors are negligible if the rate of change of the attenuation values is low compared to the rotation time of the scanner. This is the method used in perfusion CT.

Generalised Parker Weighting Taguchi observed in [Taguchi, 2003] that including redundant data in an appropriate way, the artifacts due to data inconsistencies can be reduced. He proposes to reconstruct a sequence frame by frame using static reconstruction by weighting

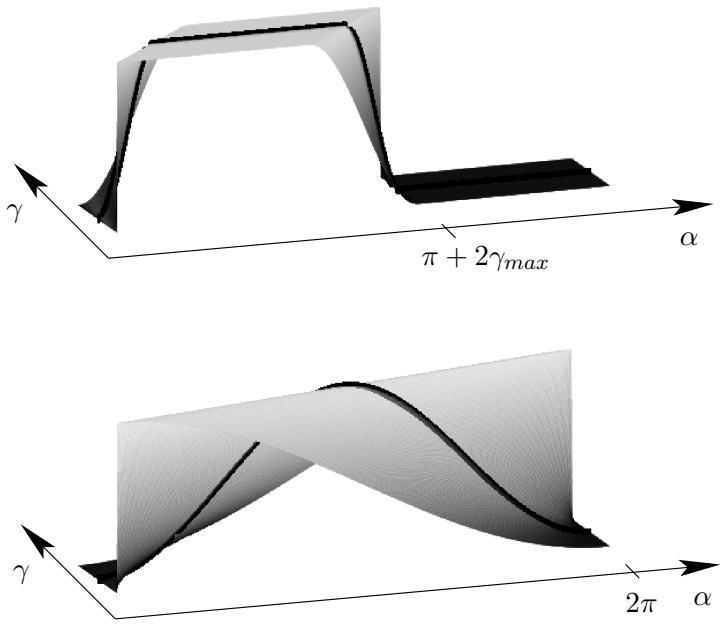

Figure 4.3. Generalised Parker weighting functions. Top: angular interval $[0, \pi + 2\gamma_{max}]$ (short-scan), bottom: angular interval $[0, 2\pi]$ (full-scan). The black curves represent the weights for the central ray $\gamma = 0$.

the projections. Taguchi, compares several weighting schemes for dynamic reconstruction purposes. They are all based in the weighting principle presented in sections 3.2.5.3 and 3.3.3.4, i.e. projections are weighted with a weighting function $w_\alpha(\gamma)$ before the filtering step. Among the proposed weighting schemes, the best results are obtained by using the generalised Parker weighting scheme proposed in [Silver, 2000]. This weighting scheme allows to include projections from an angular interval of flexible length; it is a generalisation of the Parker weighting used for short-scan reconstruction. For the case of an angular interval of length $\pi + 2\gamma_{max}$ (short-scan), it reduces to Parker weighting; using Taguchi's naming convention we denote this algorithm as HS-FDK. The other interesting case is given for an interval of length 2π (full-scan). The resulting dynamic reconstruction algorithm is denoted as NHS-FDK. Taguchi observed that the reconstructions from projections in a full-scan (NHS-FDK) presented a stronger reduction of the artifacts than the short-scan reconstruction (HS-FDK). The reason for this can be better understood if we take into account the form of the weighting functions for both cases; these are shown in figure 4.3. Since the sum of the weights of quasi equivalent rays (see section 3.3.3.4) is constant, the weighting can be interpreted as the averaging of rays. Rays that are weighted with the maximum value 2 are not averaged. It can be observed that much more rays are averaged in the full-scan reconstruction than in the short-scan reconstruction and so, artifacts are stronger reduced. However, there are other factors which play an important role in the quality of the reconstructed frames. As we discussed in section 3.3.3.4, the short-scan reconstruction from cone-beam projections uses less Radon data and this leads to stronger artifacts than in full-scan reconstruction for the planes $z \neq 0$. On the other hand, the weighting function

for full-scan reconstruction extends over a longer angular interval and the projection dataset used is therefore less localised in time. This results in a worse temporal resolution than in the short-scan case.

$k\pi$-mode Linear Regression Grangeat and co-workers presented in [Grangeat et al., 2002] a more sophisticated approach for dynamic reconstruction. The dynamic reconstruction algorithm is based on short-scan reconstruction with the T-FDK algorithm presented in section 3.3.3.1. First, cone-beam projections are rebinned to fan-parallel beam projections. In a second step, projections are filtered as described by (3.64). The backprojection integral is divided in 3 angular intervals of length $\pi/3$. These incomplete backprojections are denoted as partial block backprojections (PBBs). The PBB corresponding to the angular interval $[j\frac{\pi}{3}, (j+1)\frac{\pi}{3}]$ is associated to the time at which the central projection $(2j+1)\frac{\pi}{6}$ is acquired $t_{(2j+1)\frac{\pi}{6}}$. Thus, the expression of the jth PBB is

$$PBB_j(\mathbf{x}, t_{(2j+1)\frac{\pi}{6}}) = \frac{1}{2} \int_{j\frac{\pi}{3}}^{(j+1)\frac{\pi}{3}} FP_\beta(u'(\mathbf{x},\beta), v'(\mathbf{x},\beta), t_\beta) d\beta \quad \text{for} \quad j = 0, 1, 2. \tag{4.2}$$

As a consequence of the dynamic acquisition scheme, the values of each PBB are known every half-rotation. Hence, for every voxel in the PBB, we have a time series of values observed every T_π. In order to reconstruct a frame at a given time t_0, we must know the values of the three PBBs at this time. The estimated values of the jth PBB at t_0 $\underline{PBB}_j(\mathbf{x}, t_0)$ are calculated for every voxel by performing linear regression on the closest k values of the time series. A frame at time t_0 is then computed as

$$\underline{\mu}^r(\mathbf{x}, t_0) = 2 \sum_{j=0}^{2} \underline{PBB}_j(\mathbf{x}, t_0). \tag{4.3}$$

This approach introduces two new aspects: the concept of partial block backprojection and the temporal estimation of the value at the frame time from the values of a time series. The partial block backprojection approach reduces the data inconsistency in the projection dataset. Even if the projections in a block are acquired at different times, the effect is less critical since the angular intervals are shorter than in short-scan reconstruction. The estimation by linear regression compensates for the temporal evolution.

4.2.1. Discussion and Motivation

All these approaches for dynamic reconstruction have in common that they are strongly based on FDK-like static reconstruction. Indeed, the first two of them consist in applying a static reconstruction algorithm frame by frame. Let us consider for a moment the input cone-beam projections $P_\alpha(\gamma, \varphi, t_\alpha)$; if we use them with the C-FDK algorithm what we notice first is that the filtering step is not affected by the time dependence of the projections. The data inconsistency problem is only patent at the backprojection step, since the acquisition time of each projection depends on the projection angle. In order to illustrate this aspect, we reproduce here the backprojection step

of the C-FDK algorithm for full-scan reconstruction:

$$\mu^r(\mathbf{x}) = \frac{1}{2}\int_0^{2\pi} \frac{1}{L^2(\mathbf{x},\alpha)} FP_\alpha(\gamma'(\mathbf{x},\alpha),\varphi'(\mathbf{x},\alpha),t_\alpha)d\alpha. \tag{4.4}$$

In both the standard reconstruction and the generalised Parker weighting approach the reconstructed frame is associated to the time at which the projection in the middle of the interval has been acquired, i.e. t_π. By doing this, we are implicitly assuming that

$$FP_\alpha(\gamma'(\mathbf{x},\alpha),\varphi'(\mathbf{x},\alpha),t_\alpha) \approx FP_\alpha(\gamma'(\mathbf{x},\alpha),\varphi'(\mathbf{x},\alpha),t_\pi) \quad \text{for} \quad 0<\alpha<2\pi. \tag{4.5}$$

This approximation is present in some way or another in all the approaches presented in the previous section. In short-scan reconstruction, the assumption is restricted to a time interval of length $T_{\pi+2\gamma_{max}}$, whereas in the $k\pi$-mode linear regression approach it is restricted to time intervals of length $T_{\frac{\pi}{3}}$. We denote this approximation as *dynamic backprojection approximation*.

This is, however, not the only situation where the acquisition times of the projections are ignored. The first step of the $k\pi$-mode linear regression approach is to rebin a fan-parallel beam from the acquired cone-beam projections. As we saw in section 3.2.5.1, in order to compound the projection $P^b_\beta(u,v,t_\beta)$, we use cone-beam projections in the angular interval $[\beta-\gamma_{max},\beta+\gamma_{max}]$. Hence, we have a similar situation as in (4.5) since, for a given β, we implicitly assume that

$$P_\alpha(\gamma,\varphi,t_\alpha) \approx P_\alpha(\gamma,\varphi,t_\beta) \quad \text{for} \quad \beta-\gamma_{max}<\alpha<\beta+\gamma_{max}. \tag{4.6}$$

We denote this approximation as *dynamic rebinning approximation*.

While these both approximations are surely reasonable under certain conditions, there might be situations where they lead to non-negligible errors. Intuitively, this will occur when the dynamic changes are fast compared to the rotational speed of the source. The questions that remain open are: when are these approximations acceptable and which are their effects? Another important issue is to determine which kind of dynamic processes can be reproduced with the proposed reconstruction algorithms and, more general, which kind of dynamic processes can be reproduced from the acquired data. Moreover, the presented approaches have all the common drawback that they cannot be adapted to a dynamic process, even if we had of some prior information about it. In this chapter we address all these aspects of dynamic reconstruction. We first present a theoretical analysis of dynamic acquisition and static reconstruction with projections of a dynamically changing object. Based on these theoretical results, we propose a dynamic reconstruction approach which exploits the acquired data efficiently. Finally, we present numerical simulations both to confirm the theoretical analysis and to assess the performance of our approach.

4.3. Theoretical Analysis of Dynamic Acquisition and Reconstruction

In this section we present a theoretical analysis of dynamic acquisition of projections of an object with time dependent attenuation; and of reconstruction from these projections with an FDK-like algorithm. The goal is to provide a theoretical foundation that serves in the next section to derive an efficient dynamic reconstruction algorithm proposed in the next section. Our analysis of the

problem concentrates on the error caused by the time dependence of the attenuation coefficient, i.e. the errors due to finite spatial resolution of the scanner or to the static reconstruction algorithm are not taken into account. For this purpose, we exploit the fact that both the projection and the reconstruction with FBP are considered as linear operations. In such a case, the acquisition-reconstruction process can be characterised by a point spread function. This point spread function is the output of the system when the input is a density situated at the origin of coordinates, i.e. when the input spatial distribution of the attenuation coefficient is of the form

$$\mu(\mathbf{x}) = \delta(\mathbf{x}), \tag{4.7}$$

where $\delta(\mathbf{x})$ is the three-dimensional Delta function. Ideally, the acquisition-reconstruction system should deliver as output the same input density. This is in practice, however, not possible since we do not have an infinite spatial resolution. For this reason, the reconstruction will be a smooth function with a maximum spatial frequency limited to ς_{max} (see section 3.2.4.1). This function, converges to a Delta function in distribution sense when $\varsigma_{max} \to \infty$ [Ye et al., 2003].

As stated previously in this section, the aim of the analysis is to describe the effects of the time dependence of the attenuation coefficient. In order to evaluate dynamic reconstruction algorithms, we take as a reference the quality obtained with static reconstruction. This can be interpreted equivalently as the reconstruction from projections acquired with a source rotating with infinite angular speed.

4.3.1. Dynamic Acquisition as Temporal Sampling

Projections of a time dependent object depend themselves on time. As we saw in section 4.1.1, the projection characterised by the projection angle α is acquired at $t_\alpha = \alpha/\omega$. After a full rotation of the source, a projection is acquired from the same projection angle but $T_{2\pi}$ later. Hence, what we acquire is, for each angular position α, a discrete sequence in time

$$P_\alpha(\gamma, \varphi, k) = P_\alpha\left(\gamma, \varphi, t_\alpha + kT_{2\pi}\right). \tag{4.8}$$

This dynamic acquisition process can be interpreted as the sampling of a time dependent projection $P_\alpha(\gamma, \varphi, t)$ with a sampling period of $T_s = T_{2\pi}$. This is illustrated in figure 4.4. The black curve represents the trajectory of the source during three full-rotations. For a given projection angle α, the grey arrow represents the values of the projection characterised by this projection angle at any time. This line intersects the source trajectory in a regular pattern every $T_s = T_{2\pi}$. According to the sampling condition (see appendix B), the maximum frequency that can be reproduced from regularly sampled data is equal to the half of the sampling frequency $1/(2T_s)$. Hence, the maximum frequency of $P_\alpha(\gamma, \varphi, t)$ should be lower than $1/(2T_{2\pi})$.

In section 3.3.3.4 we introduced the quasi-equivalent rays approximation. In the context of dynamic acquisition, this assumption yields a reduction of the sampling interval. However, due to the cone-beam scanning geometry, the time interval between samples is different for each ray and the sampling scheme is not regular. According to the correspondence between equivalent rays given in section 3.2.5.3, the resulting sampling scheme can be described by two alternating sampling intervals which can be expressed as

$$\begin{aligned} T_{s_1}(\gamma) &= t_{\alpha+\pi-2\gamma} - t_\alpha \\ T_{s_2}(\gamma) &= t_\alpha + T_{2\pi} - t_{\alpha+\pi-2\gamma}. \end{aligned} \tag{4.9}$$

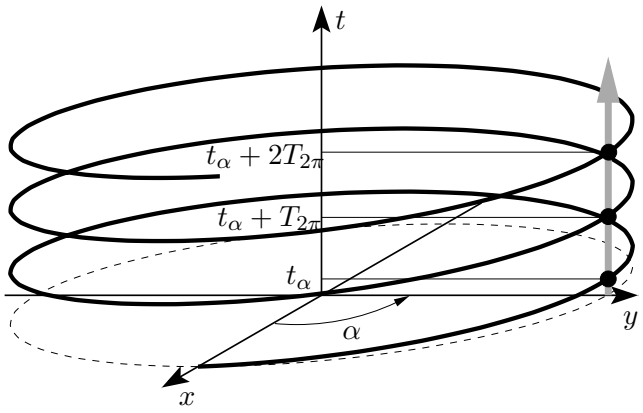

Figure 4.4. Dynamic acquisition as temporal sampling.

Some estimation techniques can be very efficiently implemented in the case where the samples are equidistant. In order to be able to use these approaches we can make use of the dynamic rebinning approximation and rebin the cone-beam projections to a fan-parallel beam as described in section 3.3.3.1. In fan-parallel beam geometry, the sampling becomes regular with a sampling interval equal to a half rotation time $T_s = T_\pi$. With rebinned projections the maximum frequency of $P_\alpha(\gamma, \varphi, t)$ can be increased, but it should be lower than $1/T_{2\pi}$.

Note, however, that we have made two approximations to get to this result. As we saw in section 3.3.3.4, the quasi-equivalent rays approximation reduces the quality of the reconstructed images at planes with increasing distance to the midplane. The effect of the dynamic rebinning approximation is analysed in the next section.

Before continuing with our analysis, let us introduce a simplification on the notation. The cone-beam projection $P_\alpha(\gamma, \varphi)$ is acquired at $t_\alpha = \alpha/\omega$, i.e. the acquisition time depends only on the projection angle α. If we perform rebinning as in section 3.3.3.1, the acquisition time of each ray of the rebinned projection is different. That is, the acquisition time of the rays depends on the transaxial coordinate as well. However, the acquisition time does not depend on the axial coordinate of the detector in any case. For this reason, we skip in the following analysis the axial coordinate without loss of generality. The presented analysis is thus made for fan-beam or parallel-beam projections in the midplane. In the cases where the axial coordinate may have an influence, this will be appropriately indicated.

4.3.2. Model for the Dynamic Process

Before we start with the analysis of the approximations, we make here a short digression to characterise the kind of dynamic processes we are interested in. In section 2.3.1 we saw that the estimation of functional parameters is based on the measurement of the temporal evolution of the concentration of contrast agent at every point of the region of interest. This temporal evolution was denoted as time-attenuation curve (TAC). We also saw that TACs are proportional to the temporal evolution of a pixel value in a sequence of CT images. Hence, the goal of the dynamic reconstruction step in the perfusion CT protocol is to measure the time-attenuation curves in the region of interest as accurately as possible. For this purpose, it is of practical interest to

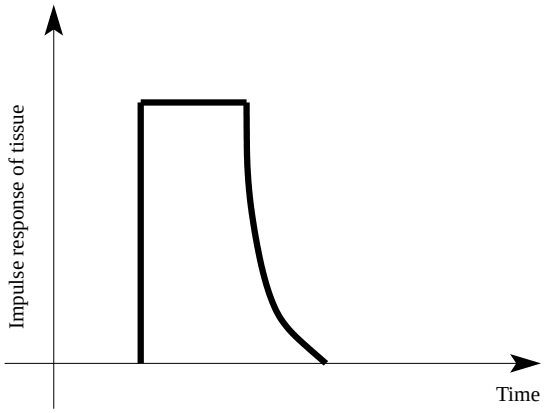

Figure 4.5. Typical impulse response of tissue in the linear systems approach.

characterise these TACs.

We derive here a model for time-attenuation curves based on the linear systems approach for the modelling of tracer kinetics [Miles and Griffiths, 2003]. The idea of this approach is that a tissue can be modelled as a linear time invariant system. Such systems can be characterised by an impulse response which represents the output of the system to an idealised impulse input. The impulse response of a tissue represents the distribution of transit times in the tissue. Figure 4.5 shows a typical impulse response of a tissue. It raises instantaneously to a plateau and then falls smoothly to zero. According to the linear systems approach, the time-attenuation curve of a tissue is obtained by convolution of the time-attenuation curve of the input artery with the impulse response of the tissue.

Contrast agent is normally injected with an automatic injector so that the injection rate can be considered to be constant. The temporal evolution of the concentration of contrast agent at the point of the injection is then a rectangular pulse of a certain duration. If we assume that 50 ml are injected at an injection rate of 20 ml/s then the pulse has a duration of 2.5 s. The flow through the cardiopulmonary system has a low-pass filtering effect, with a response which depends on each individual [Blomley and Dawson, 1997]. This low-pass filtering effect is a consequence of the transport process in blood and the flow through the heart and the lungs. As a consequence, the time-attenuation curve of an input artery has typically a fast raise and a slower decay. This is illustrated in figure 4.6. The time-attenuation curve of an input artery will change from one patient to another but the changes concern mainly the arrival time of the bolus and its width but not the form. As an example, in old patients the TAC of an input artery tends to arrive later and to extend over a longer period of time.

This linear systems approach for the modelling of the propagation of time-attenuation curves through tissues entails less constraining assumptions than the compartment model used to derive the slope method in section 2.3.1 [Zierler, 1965]. As a direct consequence of the linear systems hypothesis, the process of flow through a tissue makes that TACs in and after the tissue are smoother than the TACs of the input artery. Furthermore, since the time-attenuation curves of tissue are the result of successive convolution of an initial curve we can deduce that TACs are smooth curves.

Our previous discussion might give the false impression that the form of time-attenuation curves can be easily modelled by a parametric curve. However, even if we assume that the linear systems

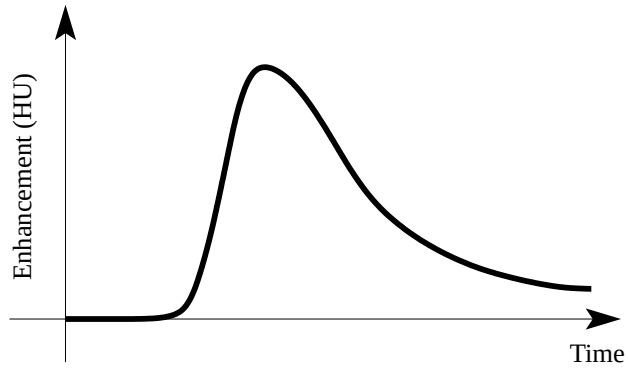

Figure 4.6. Typical time-attenuation curve of an input artery.

approach applies, we do not know the impulse responses of the individual systems between the injection point and the tissue. The general impulse response described in figure 4.5 is only a sketch and even for this sketch the parameters that describe it would be different for every tissue. Furthermore, it only refers to a single tissue so that the effect of transport in blood and flow through the heart are not included. Last but not least, the perfusion CT protocol covers a certain period of time; it may happen that during this time the outflow phase is not reached so that the curve only grows or reaches a plateau and remains constant. This is for example typical in areas where the blood-brain barrier is damaged since the contrast agent diffuses to the interstitium and remains therefore longer in the tissue. Hence, finding a parametric model that describes the form of all possible time-attenuation curves is not a simple task. We can nevertheless exploit the linear systems approach to formulate a simple mathematical model for time-attenuation curves. We denote by $c(t)$ the temporal evolution of the concentration of contrast agent in blood. This TAC might correspond to a tissue or a large vessel (e.g. input artery or output vein) after flow through the cardiopulmonary system. The injection function is a rectangular pulse, i.e. it concentrates its energy in the frequencies around 0 Hz. According to the linear systems approach, the function $c(t)$ is the result of successive convolutions with low-pass filters. Hence, $c(t)$ concentrates its energy in the low frequencies as well. Furthermore, as a consequence of the successive convolutions, $c(t)$ is a smooth function, which is several times differentiable; therefore, its Fourier transform, $\hat{c}(\nu)$ fulfils [Mallat, 1998]

$$\hat{c}(\nu) < C\frac{1}{1+|2\pi\nu|^{\alpha}}, \tag{4.10}$$

where α is the order of differentiability. This indicates that the Fourier transform of $c(t)$ has a fast decay. We can exploit this fact and neglect the values of the Fourier transform over a certain threshold. This leads to the formulation of our model for time-attenuation curves in form of the following hypothesis:

Hypothesis 4.1 *The temporal evolution of the concentration of contrast agent at one point $c(t)$ is a low-pass dynamic process and is essentially band-limited. That is, its energy is concentrated in the low frequencies and the value of its Fourier transform can be neglected over a certain frequency ν_{max}:*

$$\hat{c}(\nu) \approx 0 \quad \textit{for} \quad |\nu| > \nu_{max}. \tag{4.11}$$

The threshold ν_{max} should be defined in an appropriate way for every application.

We now analyse the implications of this hypothesis within the framework of dynamic acquisition. According to the discussion in the previous section the temporal evolution of the projections can be reproduced if they fulfil

$$\hat{P}_\alpha(\gamma, \varphi, \nu) \approx 0 \quad \text{for} \quad \nu \geq \frac{1}{T_{2\pi}}. \tag{4.12}$$

The condition (4.11) applies to every point in the time dependent spatial distribution of the attenuation coefficient. This can be expressed as

$$\hat{\mu}(\mathbf{x}, \nu) \approx 0 \quad \text{for} \quad \nu \geq \nu_{max}. \tag{4.13}$$

If we assume that Beer's law applies (see section 3.1.2), projections are integrals along lines of the spatial distribution of the attenuation coefficient. Hence, their Fourier transform is calculated as

$$\begin{aligned} \hat{P}_\alpha(\gamma, \varphi, \nu) &= \int_{-\infty}^{+\infty} \left(\int_{L(\alpha,\gamma)} \mu(\mathbf{x}, t) dl \right) e^{-i2\pi\nu t} dt \\ &= \int_{L(\alpha,\gamma)} \hat{\mu}(\mathbf{x}, \nu) dl. \end{aligned} \tag{4.14}$$

As a consequence, if $\mu(\mathbf{x}, t)$ fulfils (4.13) then it follows from (4.14) that the projections $P_\alpha(\gamma, \varphi, t)$ fulfil (4.12) as long as $\nu_{max} < 1/T_{2\pi}$. This shows that the essentially band-limited model for the temporal evolution suits well to the dynamic acquisition process and provides an expression for the maximum temporal resolution of any dynamic reconstruction algorithm. This is formulated in the following statement.

Statement 4.1 *The maximum temporal resolution of a dynamic reconstruction algorithm ν_{max}^{id} is defined as the maximum frequency of the dynamic process $\mu(\mathbf{x}, t)$ that it is able to reproduce. For a given scanner, it is limited to*

$$\nu_{max}^{id} < \frac{1}{T_{2\pi}^{min}}, \tag{4.15}$$

where $T_{2\pi}^{min}$ is the minimum rotation time of the scanner.

At this point a remark must be made. In sections 3.2.4 and 3.2.4.1, we saw that due to the discretised acquisition of projections (finite number of detector pixels and finite number of projection angles), the reconstructed spatial distribution of the attenuation coefficient is limited to a certain spatial frequency ς_{max}. For this spatial frequency we used the unit mm^{-1}. In order to characterise the spatio-temporal distribution of the attenuation coefficient $\mu(\mathbf{x}, t)$, we now introduce the temporal frequency ν, with units of s^{-1} =Hz. Thus, according to the spatial and temporal sampling conditions, the spatio-temporal distributions of the attenuation coefficient that can be reproduced are limited by the spatial and temporal frequencies ς_{max} and ν_{max} respectively. Mathematically this can be expressed as

$$\hat{\mu}(\varsigma_x, \varsigma_y, \varsigma_z, \nu) \approx 0 \quad \text{for} \quad \varsigma_x, \varsigma_y, \varsigma_z \geq \varsigma_{max}, \nu \geq \nu_{max}, \tag{4.16}$$

where ς_x, ς_y and ς_z are the spatial frequencies corresponding to the axes x, y and z.

4.3.3. Effect of the Dynamic Rebinning Approximation

Rebinning of fan-beam projections to parallel-beam projections was discussed in section 3.2.5.1 as a method to adapt the projections to the FBP algorithm in parallel-beam geometry. In the light of dynamic acquisition and reconstruction, it offers the additional advantage to increase the sampling rate to $1/T_\pi$ (see section 4.3.1). However, in the rebinned set of projections every ray in a projection is acquired at a different time. In an approximation, this is ignored by associating each rebinned projection to the time at which its central projection is acquired. We present in this section an analysis of the error committed when ignoring the individual time of each ray in the rebinning step. A similar analysis can be found in [Bonnet et al., 2003a].

Let us denote by $P_\alpha(\gamma, t_\alpha)$ the acquired fan-beam projections and with $P^b_\beta(u, t_{\alpha(\beta,u)})$ the rebinned parallel-beam ones. The expression of the fan-beam coordinates as a function of the parallel-beam coordinates can be calculated from (3.40):

$$\begin{aligned} \gamma(u) &\rightarrow \arcsin\left(\frac{u}{\Gamma}\right) \\ \alpha(\beta, u) &\rightarrow \beta + \gamma(u). \end{aligned} \tag{4.17}$$

The correspondence between fan-beam rays and parallel-beam ones is shown in figure 3.7. The maximum extension of the rebinned detector can be obtained from (4.17)

$$u_{max} = \Gamma \sin(\gamma_{max}). \tag{4.18}$$

Since $\mu(\mathbf{x}, t)$ is localised in a circle of radius $\|\mathbf{x_{max}}\|$, $u_{max} \geq \|\mathbf{x_{max}}\|$.

Let us now consider an object consisting of a density point following a temporal law $c(t)$ and situated at a given position $\mathbf{x_0} = (x_0, y_0)$,

$$\mu(\mathbf{x}, t) = c(t)\delta(\mathbf{x} - \mathbf{x_0}). \tag{4.19}$$

Its corresponding fan-beam projections will be

$$P_\alpha(\gamma, t_\alpha) = c(t_\alpha)\frac{\cos(\alpha - \gamma)}{\Gamma\cos(\gamma) - x_0}\delta(\gamma - \gamma_0(\alpha)), \tag{4.20}$$

where $t_\alpha = \alpha/\omega$ is the time at which the projection is acquired and $\gamma_0(\alpha)$ is the fan-angle corresponding to the ray that goes through $\mathbf{x_0}$ for each projection angle α

$$\gamma_0(\alpha) = \alpha - \arctan\left(\frac{\Gamma\sin(\alpha) - y_0}{\Gamma\cos(\alpha) - x_0}\right). \tag{4.21}$$

Applying the transformation defined by (4.17) to (4.20),

$$\begin{aligned} P^b_\beta(u, t_{\alpha(\beta,u)}) &= P_{\alpha(\beta,u)}\left(\gamma(u), t_{\alpha(\beta,u)}\right) \\ &= c\left(\frac{\beta}{\omega} + \frac{1}{\omega}\arcsin\left(\frac{u}{\Gamma}\right)\right)\delta\left(u - u_0(\beta)\right) \end{aligned} \tag{4.22}$$

where $u_0(\beta) = -x_0\sin(\beta) + y_0\cos(\beta)$.

Therefore, if we associate the rebinned projection $P^b_\beta(u)$ with the time $t_\beta = \beta/\omega$, we have an error produced by a time delay $\Delta(u_0(\beta))$ that depends on the position of the density point and the angular position of the source

$$\Delta(u_0(\beta)) = \frac{1}{\omega}\arcsin\left(\frac{u_0(\beta)}{\Gamma}\right). \tag{4.23}$$

Since $|u_0(\beta)| < \Gamma$, the maximum time delay will occur for the maximum value of $u_0(\beta)$. This maximum is attained for $\beta = \arctan(y_0/x_0) \pm \frac{\pi}{2}$ and its value is $|u_0(\beta)|_{max} = \|\mathbf{x_0}\|$. We summarise these results in the following statement:

Statement 4.2 *As a consequence of the dynamic rebinning approximation, each ray in a rebinned projection has a delay with respect to the central ray of the projection. This time delay is different for every point in the plane and for every angular position of the source. The maximum time delay at a given point* $\mathbf{x_0}$ *is given by*

$$\max\{|\Delta(u_0(\beta))|\} = \frac{T_{2\pi}}{2\pi} \arcsin\left(\frac{\|\mathbf{x_0}\|}{\Gamma}\right). \tag{4.24}$$

Hence, the delay is small with

- *a small distance from the point to the origin,* $\|\mathbf{x_0}\| \to 0$,
- *a large source-origin distance,* $\Gamma \to \infty$,
- *a low rotation-time,* $T_{2\pi} \to 0$.

4.3.4. Effect of the Dynamic Backprojection Approximation

In this section we analyse the effect of the dynamic backprojection approximation (see section 4.2.1) in temporal resolution. For the sake of simplicity the analysis is carried out for parallel-beam geometry, but the obtained conclusions can be applied to fan-beam geometry as well.

In section 4.1.2 we saw that the level of inconsistency depends both on the angular speed of the source and on the rate of change of dynamic process. An additional factor that plays a decisive role is the length of the backprojection interval. The use of partial backprojections (PBB) in the $k\pi$-linear regression approach reduces data inconsistency problems by integrating over angular intervals of length $\pi/3$. In order to avoid problems caused by data inconsistencies one might think of increasing the number of intervals in a full-rotation. If we observe the $k\pi$-mode linear regression approach, we easily identify that this should not be done unnecessarily since for every further interval the estimation step must be repeated and, depending on the implementation, the memory requirements might increase. Hence, for the sake of efficiency the number of angular intervals in a full-rotation should be kept as low as possible. For the purpose of the following analysis, we consider partial block backprojections over angular intervals of length $2\pi/N$. Similarly as in section 4.2, these are defined as

$$PBB_j(\mathbf{x}, t_{\frac{\pi}{N}(2j+1)}) = \frac{1}{2} \int_{\frac{2\pi}{N}j}^{\frac{2\pi}{N}(j+1)} FP_\beta(u'(\mathbf{x},\beta), t_\beta) d\beta \quad \text{for} \quad j = 0, 1, \ldots N-1. \tag{4.25}$$

It is clear from (4.25) that for a static object:

$$\mu^r(\mathbf{x}) = \sum_{j=0}^{N-1} PBB_j(\mathbf{x}), \tag{4.26}$$

for a full-scan reconstruction (for a short-scan reconstruction, $2\sum_{j=0}^{N/2-1}$). Note that the jth PBB is associated to the time at which the central projection of the corresponding angular interval

is acquired $t_{\frac{\pi}{N}(2j+1)}$. The inconsistency in the projection dataset corresponding to the angular interval $[\frac{2\pi}{N}j, \frac{2\pi}{N}(j+1)]$ depends on the length of the angular interval $2\pi/N$, on the rotation time of the source $T_{2\pi}$ and on the maximum frequency of the dynamic process ν_{max}. Let us consider again the density point object described by (4.19). Its parallel-beam projections are

$$P_\beta(u) = c\left(\frac{\beta}{\omega}\right)\delta(u - u_0(\beta)) \tag{4.27}$$

with $u_0(\beta) = -x_0\sin(\beta) + y_0\cos(\beta)$. We first develop (4.25) using (3.25)

$$PBB_j(\mathbf{x}, t_{\frac{\pi}{N}(2j+1)}) = \frac{1}{2}\int_{\frac{2\pi}{N}j}^{\frac{2\pi}{N}(j+1)}\int_{-u_{max}}^{+u_{max}} P_\beta(u, t_\beta)g(u'(\mathbf{x},\beta) - u)du d\beta. \tag{4.28}$$

If we evaluate the PBB at the point where the density is situated $\mathbf{x} = \mathbf{x_0}$ (4.28) reduces to

$$PBB_j(\mathbf{x_0}, t_{\frac{\pi}{N}(2j+1)}) = \frac{g(0)}{2}\int_{\frac{2\pi}{N}j}^{\frac{2\pi}{N}(j+1)} c\left(\frac{\beta}{\omega}\right)d\beta. \tag{4.29}$$

Using the transformation rule with $\tau = \beta/\omega$ and $\frac{d\beta}{d\tau} = \omega$ we get

$$PBB_j(\mathbf{x_0}, t_{\frac{\pi}{N}(2j+1)}) = \frac{2\pi}{N}\frac{g(0)}{2}\underbrace{\frac{\omega N}{2\pi}\int_{\frac{2\pi}{\omega N}j}^{\frac{2\pi}{\omega N}(j+1)} c(\tau)d\tau}. \tag{4.30}$$

The under-braced part of (4.30) is a temporal average over the time interval $[t_{\frac{2\pi}{N}j}, t_{\frac{2\pi}{N}(j+1)}]$. We now define the average filter $\xi_T(t)$ as a filter that is constant equal to $1/T$ during a time interval of length T, i.e.

$$\xi_T(t) = \frac{1}{T}\text{rect}\left(\frac{t}{T}\right), \tag{4.31}$$

where rect(t) is the rectangular pulse (see appendix B). According to this definition, (4.30) can be expressed as a low-pass filtering with $\xi_{\frac{T_{2\pi}}{N}}(t)$

$$\begin{aligned} PBB_j(\mathbf{x_0}, t_{\frac{\pi}{N}(2j+1)}) &= \frac{2\pi}{N}\frac{g(0)}{2}\int_{-\infty}^{+\infty} c(t)\xi_{\frac{T_{2\pi}}{N}}(t_{\frac{\pi}{N}(2j+1)} - \tau)d\tau \\ &= \frac{2\pi}{N}\frac{g(0)}{2}c * \xi_{\frac{T_{2\pi}}{N}}(t_{\frac{\pi}{N}(2j+1)}). \end{aligned} \tag{4.32}$$

Thus, the value of the jth PBB at $\mathbf{x} = \mathbf{x_0}$ is, except for a constant, the result of filtering $c(t)$ with a low-pass filter $\xi_{\frac{T_{2\pi}}{N}}(t)$ and sampling at $t_{\frac{\pi}{N}(2j+1)}$. In the ideal case, the filter $\xi_{\frac{T_{2\pi}}{N}}(t)$ should be a delta function. Since this is not the case, it is clear that the samples obtained will contain a certain bias. This bias can be expressed as

$$b(t) = \frac{2\pi}{N}\frac{g(0)}{2}(c(t) - c * \xi_{\frac{T_{2\pi}}{N}}(t)). \tag{4.33}$$

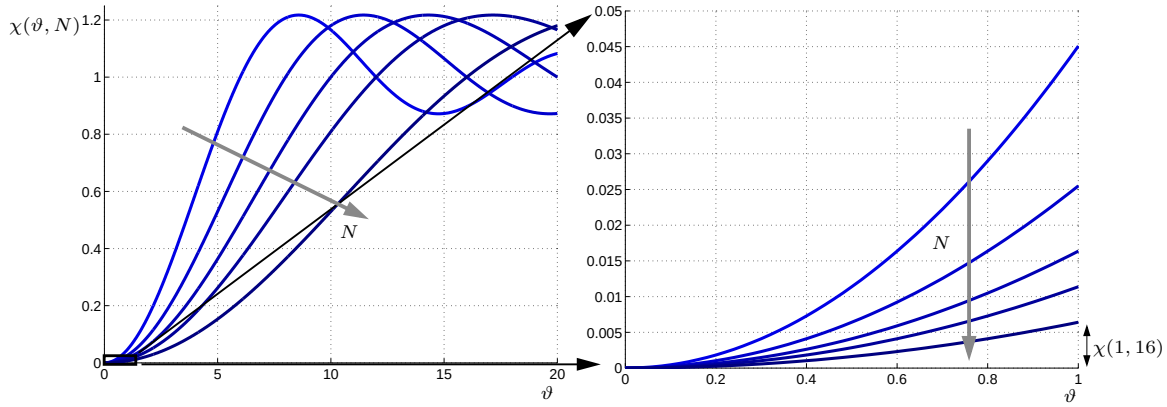

Figure 4.7. Plot of $\chi(\vartheta, N)$ for increasing values of N ($N = 6, 8, 10, 12, 16$, the grey arrow indicates the increasing direction). On the right: detail of the interval $\vartheta \in [0, 1]$.

In frequency domain the bias becomes

$$\hat{b}(\nu) = \frac{2\pi}{N} \frac{g(0)}{2} \hat{c}(\nu) \underbrace{\left(1 - \hat{\xi}_{\frac{T_{2\pi}}{N}}(\nu)\right)}_{\chi(\nu, T_{2\pi}, N)}. \tag{4.34}$$

Hence, the multiplicative factor $\chi(\nu, T_{2\pi}, N)$ is responsible for the bias. We can express this factor analytically as

$$\chi(\nu, T_{2\pi,N}) = 1 - \text{sinc}\left(\frac{T_{2\pi}\nu}{N}\right). \tag{4.35}$$

The first remarkable aspect of (4.35) is that it shows that the term that is responsible for the bias does not depend directly on the frequency ν but on the product $T_{2\pi}\nu$. Hence, if we consider a scanner with a rotation time $T_{2\pi}$ and a dynamic process with maximum frequency ν_{max}, the error due to the backprojection approximation will be the same as if we use a scanner that is K times slower as long as the maximum frequency of the process is also K times lower. In order to simplify notation, we introduce $\vartheta = T_{2\pi}\nu$. The multiplicative factor becomes then

$$\chi(\vartheta, N) = 1 - \text{sinc}\left(\frac{\vartheta}{N}\right). \tag{4.36}$$

We now make use of the model for perfusion signals introduced in section 4.3.2. According to it, $\hat{c}(\nu) \approx 0$ for $|\nu| > \nu_{max}$ and ν_{max} should not exceed $1/T_{2\pi}$ (see section 4.3.1). Hence, it is sufficient to ensure that $\chi(\vartheta, N)$ is small in the interval $[0, 1]$.

Figure 4.7 shows $\chi(\vartheta, N)$ for different values of N. For $\vartheta = 0$, $\chi(0, N) = 0$ and the bias is zero which is not surprising since $\vartheta = 0$ corresponds to a static process. For $\vartheta \neq 0$, $\chi(\vartheta, N)$ increases monotonically in the interval of interest $[0, 1]$. Hence, it reaches its maximum value at $\vartheta = 1$. It is clear that the value of $\chi(1, N)$ decreases for increasing values of N. It can be easily shown that

$$\lim_{N \to \infty} \chi(1, N) = 0 \tag{4.37}$$

since $\xi_{\frac{T_{2\pi}}{N}}(t)$ is a sequence that approximates the Delta function. If $\chi(\vartheta, N) = 0$ then $\hat{b}(\nu) = 0$ and therefore the error due to the dynamic backprojection approximation is zero. Another way to see this is that, for a given value of $\vartheta \in [0, 1]$ and a $\varepsilon > 0$, we can always find a value N_{min} such that if $N > N_{min}$ then $\chi(\vartheta, N) < \varepsilon$. The threshold N_{min} is of the form $N_{min} = C\vartheta$ where $C = \vartheta/\text{sinc}^{-1}(1 - \varepsilon)$.

We summarise the results in the following statement:

Statement 4.3 *The temporal backprojection approximation causes a bias in the reconstruction of a time dependent density value. This bias depends in frequency domain on a multiplicative factor of the form*

$$\chi(\vartheta, N) = 1 - \text{sinc}\left(\frac{\vartheta}{N}\right) \tag{4.38}$$

where $\vartheta = T_{2\pi}\nu$. According to this, we can affirm that

- *the bias goes to 0 when $\vartheta \to 0$,*
- *the bias goes to 0 when $N \to \infty$, and*
- *for any $\varepsilon > 0$ we can find, by appropriate choice of a constant C, an $N_{min} = C\vartheta$ such that*

$$\chi(\vartheta, N) < \varepsilon \quad \textit{for} \quad N \geq N_{min}. \tag{4.39}$$

In our analysis of the effect of the temporal backprojection approximation we only took into account the error at the point where the time dependent density is located. We showed that this error is due to temporal averaging during the duration of each PBB. Therefore, the error at $\mathbf{x_0}$ is a good indicator for temporal resolution. But the time dependent density also causes an error at other points $\mathbf{x} \neq \mathbf{x_0}$. In the following we analyse this error. The value of the PBB in (4.29) is exact when $c(\beta/\omega) = c(t_{\frac{\pi}{N}(2j+1)})$ in the PBB interval. Hence, the error caused by the temporal averaging at $\mathbf{x_0}$ can be expressed as

$$e(\mathbf{x_0}) = \frac{g(0)}{2} \int_{\frac{2\pi}{N}j}^{\frac{2\pi}{N}(j+1)} \left| c(t_{\frac{\pi}{N}(2j+1)}) - c(\beta/\omega) \right| d\beta. \tag{4.40}$$

In a similar way, we can express the error at $\mathbf{x} \neq \mathbf{x_0}$ as

$$e(\mathbf{x}) = \frac{g(0)}{2} \int_{\frac{2\pi}{N}j}^{\frac{2\pi}{N}(j+1)} \left| \Big(c(t_{\frac{\pi}{N}(2j+1)}) - c(\beta/\omega) \Big)\, g(u(\mathbf{x}, \beta) - u_0(\beta)) \right| d\beta, \tag{4.41}$$

where $u(\mathbf{x}, \beta) = -x\sin(\beta) + y\cos(\beta)$ and $u_0(\beta) = -x_0\sin(\beta) + y_0\cos(\beta)$. Using the Hölder inequality

$$\int_\Omega |fg| \leq \left(\int_\Omega |f|^p \right)^{\frac{1}{p}} \left(\int_\Omega |g|^q \right)^{\frac{1}{q}} \tag{4.42}$$

with $p = 1$ and $q = \infty$

$$e(\mathbf{x}) \leq \frac{1}{2} \sup \{g(u(\mathbf{x}, \beta) - u_0(\beta))\} \int_{\frac{2\pi}{N} j}^{\frac{2\pi}{N}(j+1)} \left| c(t_{\frac{\pi}{N}(2j+1)}) - c(\beta/\omega) \right| d\beta. \tag{4.43}$$

$g(u)$ can be computed as the inverse Fourier transform of (3.24) and is therefore continuous and bounded. Additionally, for the usual choices of $\hat{v}(\varsigma)$, $g(u) \leq g(0)$. Hence, we obtain

$$e(\mathbf{x}) \leq \frac{g(0)}{2} \int_{\frac{2\pi}{N} j}^{\frac{2\pi}{N}(j+1)} \left| c(t_{\frac{\pi}{N}(2j+1)}) - c(\beta/\omega) \right| d\beta = e(\mathbf{x_0}). \tag{4.44}$$

Therefore, we can conclude that, since the error at $\mathbf{x} \neq \mathbf{x_0}$ is bounded by the error at $\mathbf{x_0}$, we can concentrate on the error at $\mathbf{x_0}$ for the choice of N.

4.3.5. Effect of Backprojection with Rebinned Projections

In the previous sections we separated the effect in temporal resolution of the dynamic rebinning and backprojection approximations. We now combine them for the case of backprojection with rebinned projections of a time dependent object.

The starting point is the expression of the jth PBB for parallel-beam geometry given in (4.28). We apply it to the rebinned projections of the density point described by (4.22) and evaluate it at $\mathbf{x_0}$

$$PBB_j(\mathbf{x_0}, t_{\frac{\pi}{N}(2j+1)}) = \frac{g(0)}{2} \int_{\frac{2\pi}{N} j}^{\frac{2\pi}{N}(j+1)} c\left(\tau(\beta)\right) d\beta \tag{4.45}$$

with

$$\tau(\beta) = \frac{\beta}{\omega} + \frac{1}{\omega} \arcsin\left(\frac{u_0(\beta)}{\Gamma}\right), \tag{4.46}$$

and $u_0(\beta) = -x_0 \sin(\beta) + y_0 \cos(\beta)$. We apply again the transformation rule

$$PBB_j(\mathbf{x_0}, t_{\frac{\pi}{N}(2j+1)}) = \frac{g(0)}{2} \int_{\tau\left(\frac{2\pi}{N} j\right)}^{\tau\left(\frac{2\pi}{N}(j+1)\right)} c(\tau) \frac{d\beta}{d\tau}(\tau) d\tau. \tag{4.47}$$

Equation (4.46) shows that the dependence of τ on β is non linear. This means that in some intervals there will be a contraction of time whereas in others there will be an expansion. The term $d\beta/d\tau$ acts as a weighting function that compensates for these distortions, it weights more the intervals where the time is contracted and less the ones where it is expanded. This is illustrated in figure 4.8. The distortion effect depends on the ratio $\frac{\|\mathbf{x_0}\|}{\Gamma}$; the smaller this ratio, the less the distortion effect, and the less $d\beta/d\tau$ deviates from a constant value. For $\|\mathbf{x_0}\| = 0$, $d\beta/d\tau = \omega$ as with non-rebinned projections.

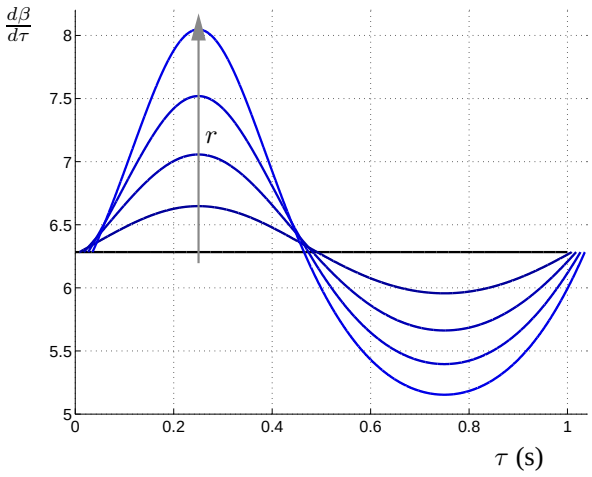

Figure 4.8. $\frac{d\beta}{d\tau}$ for different values of $\frac{\|\mathbf{x_0}\|}{\Gamma}$. The following values were used for the plot: $T_{2\pi} = 1$ s and $\mathbf{x} = (0, r)$ with $\frac{r}{\Gamma} = 0.2265 \times (0, \frac{1}{4}, \frac{1}{2}, \frac{3}{4}, 1)$. The grey arrow indicates the direction of increasing r.

As in the previous section, we would like to express (4.47) as a filtering operation. This can be easily done by interpreting $d\beta/d\tau$ in the jth interval as a low-pass filter. Both the temporal duration of the filter T_j and its central time τ_{c_j} depend on the interval. Their expressions are

$$\begin{aligned} T_j &= \tau\left(\frac{2\pi}{N}(j+1)\right) - \tau\left(\frac{2\pi}{N}j\right) \\ \tau_{c_j} &= \frac{\tau\left(\frac{2\pi}{N}(j+1)\right) + \tau\left(\frac{2\pi}{N}j\right)}{2}. \end{aligned} \tag{4.48}$$

We define now the filters $\lambda_j(\tau)$ as

$$\lambda_j(\tau) = \frac{N}{T_{2\pi}} \frac{d\beta}{d\tau}(-\tau + \tau_{c_j}) \text{rect}\left(\frac{-\tau + \tau_{c_j}}{T_j}\right). \tag{4.49}$$

The factor $\frac{N}{T_{2\pi}}$ ensures that

$$\int_{-\frac{T_j}{2}}^{\frac{T_j}{2}} \lambda_j(\tau) d\tau = 1. \tag{4.50}$$

In order to express (4.47) in terms of these filters, we must take into account that the central times of the intervals τ_j are no longer $t_{\frac{\pi}{N}(2j+1)}$. Each interval is delayed by a quantity

$$\Delta_j = \tau_{c_j} - t_{\frac{\pi}{N}(2j+1)}. \tag{4.51}$$

Using (4.49) and (4.51) we can now rewrite (4.47) as

$$\begin{aligned} PBB_j(\mathbf{x_0}, t_{\frac{\pi}{N}(2j+1)}) &= \frac{2\pi}{N}\frac{g(0)}{2} \int_{-\infty}^{+\infty} c(\tau)\lambda_j(t_{\frac{\pi}{N}(2j+1)} + \Delta_j - \tau) d\tau \\ &= \frac{2\pi}{N}\frac{g(0)}{2} c * \lambda_j(t_{\frac{\pi}{N}(2j+1)} + \Delta_j). \end{aligned} \tag{4.52}$$

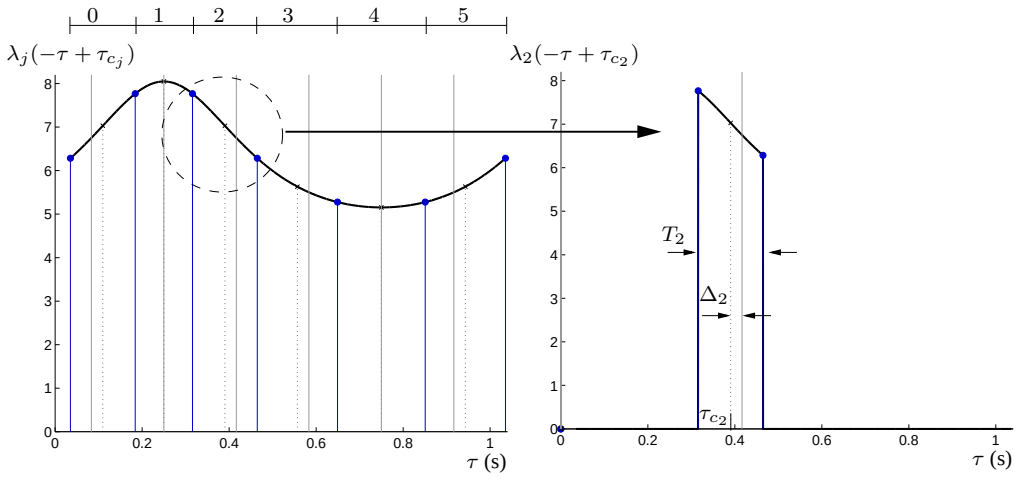

Figure 4.9. Temporal response $\lambda_j(-\tau+\tau_{c_j})$ for every PBB for $N=6$. On the right: $\lambda_2(-\tau+\tau_{c_2})$. The grey lines indicate the times to which the filtered values are associated, the blue lines separate the PBB intervals, the dotted lines indicate the centre of the PBB intervals. The following values were used for the plot: $T_{2\pi}=1$ s and $\mathbf{x}=(0,r)$ with $\frac{r}{\Gamma}=0.2265$.

As an example, figure 4.9 shows the filters λ_j for $N=6$ and a point situated at $\mathbf{x}=(0,r)$ with $\frac{r}{\Gamma}=0.2265$. With respect to the non-rebinning case, we identify several differences:

a) The averaging filters are not constant.

b) Each interval has a different length.

c) Each interval has a different delay.

In order to study the implications of a), we compare the frequency response of the filters $\lambda_j(\tau)$ with the frequency response of $\xi_{T_j}(\tau)$. The last are constant filters as defined in (4.31) with a duration equal to the duration of the jth interval, i.e. T_j. On the left part of figure 4.10, the frequency responses of $\lambda_1(\tau)$ (top) and $\lambda_4(\tau)$ (bottom) are plotted in blue in the Nyquist band ($\nu' \in [0,0.5]$) for $N=6$ and a point situated at $\mathbf{x}=(0,r)$ with $\frac{r}{\Gamma}=0.2265$. As can be seen in figure 4.9, 1 and 4 correspond to the shortest and the longest interval respectively for this parameter choice. The frequency responses of the filters $\xi_{T_1}(\tau)$ and $\xi_{T_4}(\tau)$ are plotted in grey in figure 4.10. Finally, the black curves represent the frequency response of $\xi_{T_{\frac{2\pi}{N}}}(\tau)$. The frequency responses of $\lambda_1(\tau)$ and $\xi_{T_1}(\tau)$ ($\lambda_4(\tau)$ and $\xi_{T_4}(\tau)$) can only be differentiated in the detail of the plots shown on the right. On the other hand, the frequency response for the shortest interval $\lambda_1(\tau)$ lies clearly over the response of $\xi_{T_{\frac{2\pi}{N}}}(\tau)$ whereas the frequency response of the longest interval $\lambda_4(\tau)$ lies clearly under it. Hence, we conclude that the deviation from a constant of the filters $\lambda_j(\tau)$ has no significant effect in the frequency band of interest whereas the difference of duration of the intervals has a strong influence in the frequency response. This can be empirically shown to hold for values of N and ρ in the range of our application, i.e. $N>1\in\mathbb{N}$ and $\rho<0.4\in\mathbb{R}$. For this reason, we can substitute the filters $\lambda_j(\tau)$ by $\xi_{T_j}(\tau)$ for analysis purposes. As a result, we can write the bias as

$$b_j^b(t)=\frac{2\pi}{N}\frac{g(0)}{2}(c(t)-c*\xi_{T_j}(t+\Delta_j)). \tag{4.53}$$

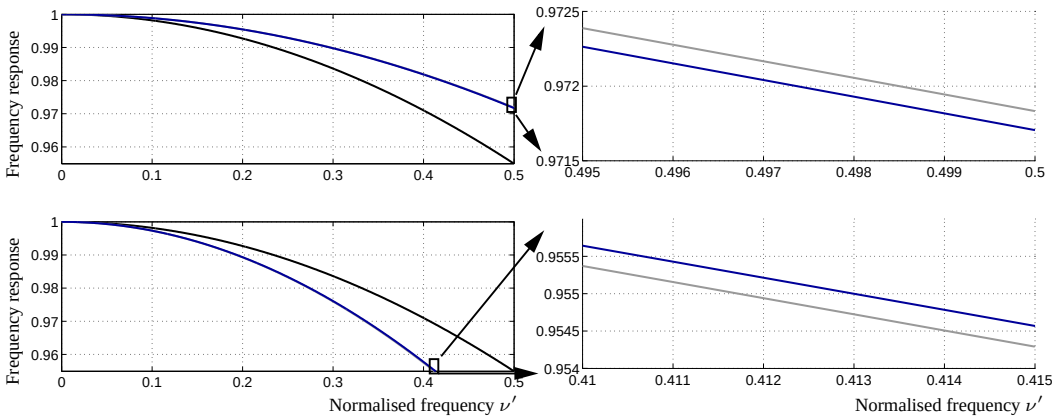

Figure 4.10. Frequency responses of the filters $\lambda_j(\tau)$ corresponding to the shortest (top) and the longest (bottom) PBBs for $N = 6$ and a point situated at $\mathbf{x} = (0, r)$ with $\frac{r}{\Gamma} = 0.2265$ (detail on the right). The blue curves are the frequency responses of the filters $\lambda_j(\tau)$, the grey curves of $\xi_{T_j}(\tau)$ and the black curves of $\xi_{T_{\frac{2\pi}{N}}}(\tau)$.

In frequency domain it becomes

$$\hat{b}_j^b(\nu) = \frac{2\pi}{N}\frac{g(0)}{2}\hat{c}(\nu)\left(1 - \mathrm{sinc}(\nu T_j)e^{i2\pi\nu\Delta_j}\right). \tag{4.54}$$

As in the non-rebinning case discussed in the previous section, a multiplicative factor is responsible for the bias. This factor is now, as the bias itself, different for every interval. It depends on the length of the interval T_j and the delay Δ_j which are a priori not known since they depend on the position of the point $\mathbf{x_0}$. The dependence of T_j and Δ_j on the position of the point $\mathbf{x_0}$ comes from the dependence of τ on $u_0(\beta)$. In section 4.3.3 we saw that the closer the point to the origin, the lower the range of the values of $u_0(\beta)$ and therefore the smaller the delay. In order to determine the value of $u_0(\beta)$ it is not enough to know the distance to the origin but we need to know the exact position of the point. This is illustrated in figure 4.11 with two points located at a distance r from the origin; for the same angular position $\beta = 0$, the values $u(\mathbf{x_0}, 0)$ and $u(\mathbf{x_1}, 0)$ are different. Our goal is to derive an expression for the bias that depends on the distance to the origin. For this purpose, we express the points at a given distance r in polar coordinates (r, θ) and consider the angle θ as a random variable uniformly distributed in $[-\pi, \pi]$. Substituting $(x_0, y_0) = (r\cos(\theta), r\sin(\theta))$ in (4.46) yields

$$\tau(\beta) = \frac{\beta}{\omega} + \frac{1}{\omega}\arcsin\left(\frac{-r\sin(\beta - \theta)}{\Gamma}\right). \tag{4.55}$$

More than the distance to the origin r, the significant quantity is the distance normalised to the source-origin distance r/Γ. Hence, in order to simplify the notation we introduce $\rho = r/\Gamma$. Substituting (4.55) in (4.48) we obtain expressions for T_j

$$T_j = \frac{T_{2\pi}}{N} - \frac{T_{2\pi}}{2\pi}\left(\arcsin\left(\rho\sin\left(\frac{2\pi}{N}(j+1) - \theta\right)\right) - \arcsin\left(\rho\sin\left(\frac{2\pi}{N}j - \theta\right)\right)\right), \tag{4.56}$$

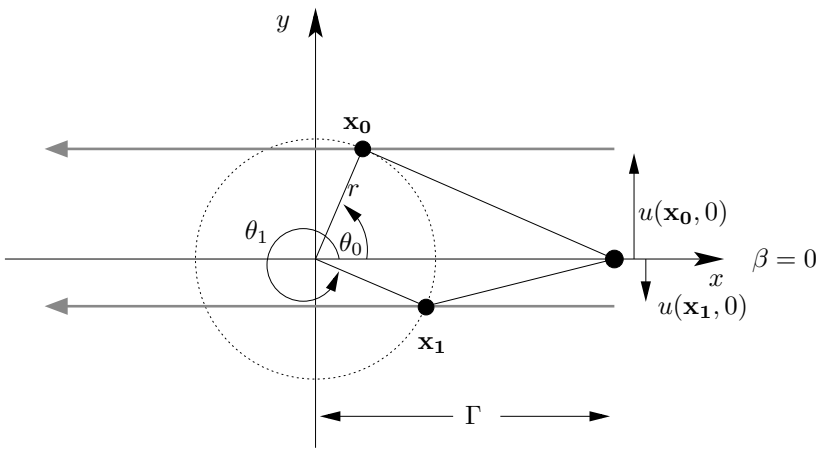

Figure 4.11. Values of $u(\mathbf{x}, \beta)$ for two points situated on the circle $\|\mathbf{x}\| = r$ for $\beta = 0$.

and Δ_j

$$\Delta_j = -\frac{1}{2}\frac{T_{2\pi}}{2\pi}\left(\arcsin\left(\rho\sin\left(\frac{2\pi}{N}(j+1)-\theta\right)\right)+\arcsin\left(\rho\sin\left(\frac{2\pi}{N}j-\theta\right)\right)\right). \quad (4.57)$$

Since T_j and Δ_j depend on the random variable θ, the bias is a random value for every value of N, $T_{2\pi}$ and ν. Hence, we are interested in computing the expected value of the bias

$$E[\hat{b}_j^b(\nu)] = \frac{2\pi}{N}\frac{g(0)}{2}\hat{c}(\nu)\underbrace{\left(1 - E\left[\text{sinc}(\nu T_j)e^{i2\pi\nu\Delta_j}\right]\right)}_{\chi^b(\nu,T_{2\pi},N,\rho)}. \quad (4.58)$$

Note that the multiplicative term depends on νT_j and $\nu\Delta_j$; hence, according to (4.56) and (4.57), it is clear that the term depends on $\vartheta = T_{2\pi}\nu$ as in the non-rebinning case. We use therefore ϑ for the rest of the analysis. As in the previous section, our aim is to explain the behaviour of the error by analysing the multiplicative factor $\chi^b(\vartheta, N, \rho)$ in (4.58). However, the complexity of (4.56) and (4.57) does not allow to give an analytical expression for $\chi^b(\vartheta, N, \rho)$. It is possible though to obtain an approximate expression. For this purpose, we remark that for a point situated at the origin, $\rho = 0$ and therefore (4.56) and (4.57) do no longer depend on θ. Their values are then same as in the non-rebinning case and therefore

$$\chi^b(\vartheta, N, 0) = \chi(\vartheta, N). \quad (4.59)$$

This suggests to expand $\chi^b(\vartheta, N, \rho)$ as a Taylor series around $\chi(\vartheta, N)$. Using (4.59) we can write

$$\chi^b(\vartheta, N, \rho) = \chi(\vartheta, N) + \sum_{m=1}^{M}\frac{\partial^m\chi^b}{\partial\rho^m}(\vartheta, N, 0)\frac{\rho^m}{m!} + R_{M+1}(\rho^{M+1}). \quad (4.60)$$

Since the terms of first and third order vanish, a third order approximation adds only a ρ^2 term to $\chi(\vartheta, N)$. The error term is of fourth order which is a reasonable approximation since the functions

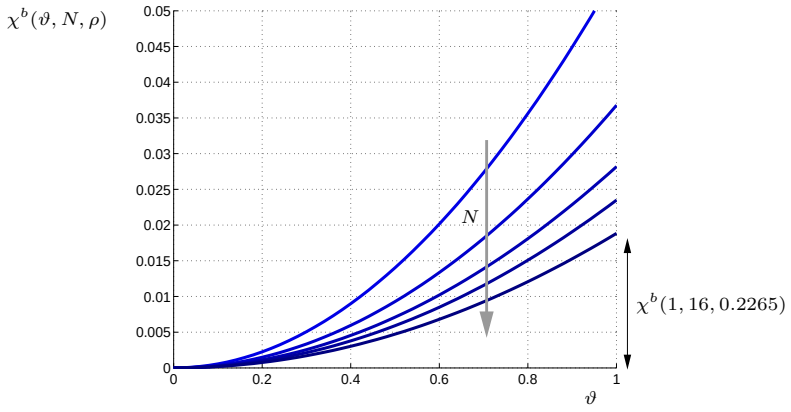

Figure 4.12. Plot of $\chi^b(\vartheta, N, \rho)$ for $\rho = 0.2265$ and increasing values of N ($N = 6, 8, 10, 12, 16$, the grey arrow indicates the increasing direction).

involved in (4.58) are smooth and ρ is small, with typically $\rho < 0.4$. With this approximation we get

$$\begin{aligned}\chi^b(\vartheta, N, \rho) &\approx \chi(\vartheta, N) + \frac{1}{4}\,\mathrm{sinc}\left(\frac{\vartheta}{N}\right)\vartheta^2\rho^2 \\ &+ \left(\frac{N^2}{2\pi^2}\cos\left(\frac{\pi\vartheta}{N}\right) - \frac{N^3}{2\pi^3\vartheta}\sin\left(\frac{\pi\vartheta}{N}\right)\right)\sin^2\left(\frac{\pi}{N}\right)\rho^2. \qquad (4.61)\end{aligned}$$

A plot of $\chi^b(\vartheta, N, \rho)$ as a function of ϑ is shown in figure 4.12 for $\rho = 0.2265$ and different values of N. The curves are similar as in the non-rebinning case with $\chi(\vartheta, N)$, but the bias is now larger (see figure 4.7). The left part of figure 4.13 shows the behaviour of $\chi^b(\vartheta, N, \rho)$ as a function of N for $\vartheta = 1$ and different values of ρ. For low values of N all curves are very close. This indicates that the most restrictive effect is temporal averaging. For higher values of N, all curves fall but they do it at different rates. A fundamental difference with the non-rebinning case is that the curves fall slower and converge to a minimum value which is different from zero. The limit of $\chi^b(\vartheta, N, \rho)$ when $N \to \infty$ can be calculated directly from the original expressions (4.56), (4.57) and (4.58) by exchanging the limit and the expectation integral. It yields

$$\lim_{N\to\infty} \chi^b(\vartheta, N, \rho) = \frac{1}{2\pi}\int_{-\pi}^{\pi}\left(1 - e^{i\vartheta\arcsin(\rho\sin(\theta))}\right)d\theta. \qquad (4.62)$$

Since $\rho < 0.4$, we can approximate $\arcsin(x) \approx x$ to obtain

$$\lim_{N\to\infty} \chi^b(\vartheta, N, \rho) \approx 1 - J_0(\rho\vartheta), \qquad (4.63)$$

where $J_0(x)$ denotes the Bessel function of the first kind of order 0. This is illustrated in the right part of figure 4.13. The blue curve represents $\chi^b(\vartheta, N, \rho)$ for $\vartheta = 1$ and $\rho = 0.2265$, the black curve corresponds to the term $\chi(\vartheta, N)$ and the grey curve to second order term. The approximate limit value is shown as a dashed line.

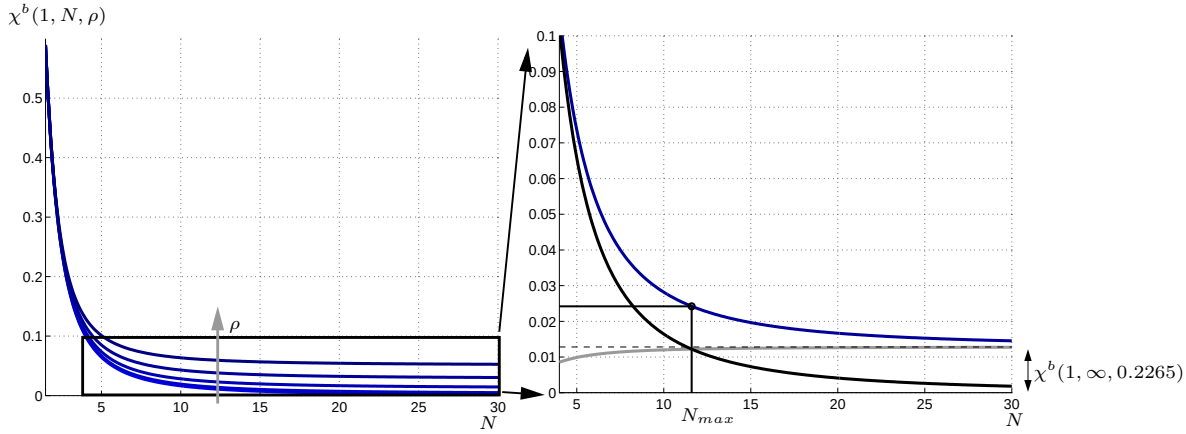

Figure 4.13. Plot of $\chi^b(\vartheta, N, \rho)$ for $\vartheta = 1$ and increasing values of ρ ($\rho = 0.2265 \times 0, 0.5, 1, 1.5, 2$, the grey arrow indicates the increasing direction). On the right: decomposition of $\chi^b(\vartheta, N, \rho)$ in $\chi(\vartheta, N)$ (black) plus the second order term (grey). N_{max} is defined as the intersection point.

In the non-rebinning case, the error can be made arbitrarily small by increasing the number of intervals in a full-rotation N. With rebinned projections, the error due to temporal averaging predominates for low values of N, so that it behaves similarly as in the non-rebinning geometry case. For higher values of N, however, the error due to the time delay becomes more significant and it makes it useless to increase N over a certain threshold N_{max}. This threshold depends, of course, on the value of ρ. We provide a heuristic approach to estimate this threshold. The idea is to exploit the decomposition of the bias shown in figure 4.13 and find the value of N for which the second order term is equal to the bias without rebinning $\chi(\vartheta, N)$

$$\chi(\vartheta, N) = \frac{\partial^2 \chi^b}{\partial \rho^2}(\vartheta, N, 0)\frac{\rho^2}{2}. \tag{4.64}$$

This value is a good compromise since at this point the second order term has almost reached its maximum and the total bias is close to the limit given by (4.63). In the right part of figure 4.13, this is shown as the point where the black and the grey curves meet. Our purpose is to find an analytical expression for N_{max} which serves as a guideline for the choice of the number of angular intervals N. Hence, we do not need an exact solution of (4.64). In order to find an approximate analytical solution of (4.64), we first simplify the second order term. This is fortunately a simple task since the sum of the terms in the second line of (4.61) converge fast to 0 when $N \to \infty$. Indeed, for $N > 5$ the value of the sum can be neglected. After this approximation the equation to solve is

$$1 - \text{sinc}\left(\frac{\vartheta}{N}\right) = \frac{1}{4}\text{sinc}\left(\frac{\vartheta}{N}\right)\vartheta^2\rho^2, \tag{4.65}$$

which leads to

$$\text{sinc}\left(\frac{\vartheta}{N}\right) = \frac{1}{1 + \frac{1}{4}\vartheta^2\rho^2}. \tag{4.66}$$

Substituting the function sinc by its second order Taylor approximation yields

$$1 - \frac{\pi^2\vartheta^2}{6N^2} = \frac{1}{1 + \frac{1}{4}\vartheta^2\rho^2}. \tag{4.67}$$

The solution is then

$$N = \pi\sqrt{\frac{2}{3}\left(\frac{1}{\rho^2} + \frac{\vartheta^2}{4}\right)}. \tag{4.68}$$

Since $1/\rho^2 \gg \vartheta^2/4$, we get a simplified expression for N_{max}

$$N_{max} \approx \sqrt{\frac{2}{3}}\frac{\pi}{\rho}. \tag{4.69}$$

Finally, we summarise the results of the analysis in the following statement:

Statement 4.4 *The combination of the temporal backprojection and the rebinning approximations causes a bias in the reconstruction of a time dependent density value. This bias depends on the distance from the point to the origin relative to the source-origin distance, i.e.* $\rho = r/\Gamma$. *It is caused by a multiplicative factor which can be approximated by*

$$\begin{aligned}
\chi^b(\vartheta, N, \rho) &\approx \chi(\vartheta, N) + \frac{\partial^2 \chi^b}{\partial \rho^2}(\vartheta, N, 0)\frac{\rho^2}{2}, \\
&= \chi(\vartheta, N) + \frac{1}{4}\,\mathrm{sinc}\left(\frac{\vartheta}{N}\right)\vartheta^2\rho^2 \\
&+ \left(\frac{N^2}{2\pi^2}\cos\left(\frac{\pi\vartheta}{N}\right) - \frac{N^3}{2\pi^3\vartheta}\sin\left(\frac{\pi\vartheta}{N}\right)\right)\sin^2\left(\frac{\pi}{N}\right)\rho^2.
\end{aligned} \tag{4.70}$$

where $\vartheta = \nu T_{2\pi}$. *Where* $\chi(\vartheta, N)$ *is the multiplicative factor obtained without rebinning and* $\partial^2_\rho \chi^b \frac{\rho^2}{2}$ *is an additional term that describes the dependence with the position of the point.*

The following results were derived from $\chi^b(\vartheta, N, \rho)$*:*

- *the bias goes to* 0 *when* $\vartheta \to 0$.
- *for* $\rho = 0$, *i.e. for the central ray,* $\chi^b(\vartheta, N, 0) = \chi(\vartheta, N)$, *and the bias behaves as in the parallel-beam geometry case.*
- *the bias cannot be made arbitrarily small by increasing* N, *since*

$$\lim_{N\to\infty} \chi^b(\vartheta, N, \rho) \approx 1 - J_0(\rho\vartheta), \tag{4.71}$$

  where $J_0(x)$ *is the Bessel function of the first kind of order* 0.

- *for high values of* N, *the time delay effect predominates so that increasing* N *does almost not reduce the values of the bias. The threshold over which the time delay effect predominates can be used as an upper bound for* N. *It can be estimated as*

$$N_{max} \approx \sqrt{\frac{2}{3}}\frac{\pi}{\rho}. \tag{4.72}$$

4.3.6. DISCUSSION

We have seen that dynamic acquisition can be seen as a temporal sampling of time dependent projections and that this acquisition scheme limits the temporal resolution to $\nu_{max}^{id} = 1/T_{2\pi}$ (see statement 4.1). This projection sampling can be interpreted as an ideal sampling with a Delta comb (see appendix B). In section 4.3.4, we analysed the partial block backprojection of projections of a density point in parallel-beam geometry. We saw that the value of the reconstruction at the position of the density point $\mathbf{x_0}$ is obtained by filtering the temporal evolution of the attenuation at this point with a constant filter $\xi_{\frac{T_{2\pi}}{N}}(t)$ and then sampling at the central time of the PBB interval. We also showed that, if the error due to the time dependence of the attenuation value can be neglected at $\mathbf{x_0}$, then it can be neglected as well at $\mathbf{x} \neq \mathbf{x_0}$. In general we do not only have a time dependent density value at $\mathbf{x_0}$ but rather a time dependent spatial distribution $\mu(\mathbf{x}, t)$. Since all operations involved in the acquisition and PBB reconstruction are linear, the spatial distribution can be considered as a spatial distribution of density points. The output will be then the accumulation of the contributions of all density points. For a certain point $\mathbf{x_0}$, the value of the PBB reconstruction will consist of its own contribution plus the contribution of the rest of the points. As we have seen, its own contribution corresponds to the temporal average of the attenuation value. According to this, the reconstruction of the jth PBB can be expressed as

$$PBB_j(\mathbf{x_0}, t_{\frac{\pi}{N}(2j+1)}) = \frac{2\pi}{N}\frac{g(0)}{2}\mu(\mathbf{x_0}, \cdot) * \xi_{\frac{T_{2\pi}}{N}}(t_{\frac{\pi}{N}(2j+1)}) + \Phi_j(\mathbf{x_0}, t_{\frac{\pi}{N}(2j+1)}), \tag{4.73}$$

where $\Phi_j(\mathbf{x_0}, t_{\frac{\pi}{N}(2j+1)})$ is the contribution of other points to the value of the PBB at $\mathbf{x_0}$. As we have shown, if the first term in 4.73 is close to $\mu(\mathbf{x_0}, t_{\frac{\pi}{N}(2j+1)})$, then the contribution of other points will be very close to the value that it would have if all projections had been acquired at $t_{\frac{\pi}{N}(2j+1)}$. Since we acquire several rotations, we have a time series of PBBs acquired at different times

$$\begin{aligned} PBB_j(\mathbf{x_0}, t_{\frac{\pi}{N}(2j+1)} + kT_{2\pi}) &= \frac{2\pi}{N}\frac{g(0)}{2}\mu(\mathbf{x_0}, \cdot) * \xi_{\frac{T_{2\pi}}{N}}(t_{\frac{\pi}{N}(2j+1)} + kT_{2\pi}) \\ &+ \Phi_j(\mathbf{x_0}, t_{\frac{\pi}{N}(2j+1)} + kT_{2\pi}). \end{aligned} \tag{4.74}$$

The first term of (4.74) indicates that we are performing a non-ideal sampling of the time dependent attenuation value $\mu(\mathbf{x_0}, t)$ every $T_{2\pi}$ with a filter $\xi_{\frac{T_{2\pi}}{N}}(t)$. Hence, if we can ensure that the effect of filtering with $\xi_{\frac{T_{2\pi}}{N}}$ is negligible, the dynamic reconstruction problem reduces to the problem of reconstructing a continuous signal from its samples. The same argumentation is valid for the case of backprojection with rebinned projections, just that the filters $\xi_{\frac{T_{2\pi}}{N}}(t)$ are substituted by $\xi_{T_j}(t)$ and have an additional delay (see previous section).

4.4. DYNAMIC RECONSTRUCTION ALGORITHMS

We provided in section 4.3 the necessary information to tackle the problem of the design of a dynamic reconstruction algorithm. Our main goal is to develop an algorithm that is able to compute accurately a dynamic sequence with a minimum of input data. For this purpose, we exploit the fact that the dynamic process is essentially band-limited and the temporal sampling nature of the dynamic acquisition process.

4.4.1. Temporal Interpolation of Projections

In section 4.3.1 we saw that the dynamic acquisition process can be interpreted as a temporal sampling of time dependent projections. Based on this interpretation we determined the maximum temporal resolution of a dynamic acquisition-reconstruction process as a function of the full-rotation time of the scanner: $\nu_{max}^{id} = 1/T_{2\pi}$. According to this interpretation the most straightforward approach for dynamic reconstruction is to estimate for every projection a continuous function from the projection samples.

In order to reduce the amount of necessary input data, we can use the maximum frequency of the dynamic process as prior information and adapt accordingly the sampling rate. From the sampling condition, we can calculate the maximum sampling interval in order to be able to recover a signal from its samples as

$$T_s < \frac{1}{2\nu_{max}}. \tag{4.75}$$

The continuous signal is computed by ideal interpolation (see appendix B). In such a case, the sampling interval can be chosen as the maximum value that fulfils (4.75) and the projections can be expressed as

$$P_\alpha(\gamma, \phi, t) \approx \sum_{k\in\mathbb{Z}} P_\alpha(\gamma, \phi, k)\psi\left(\frac{t - t_\alpha - kT_s}{T_s}\right) \tag{4.76}$$

using $\psi(t) = \frac{\sin(\pi t)}{\pi t} = \text{sinc}(t)$, i.e. the ideal interpolator. Hence, we propose to use (4.76) to estimate the value of the projections at any time. With the temporal interpolation of projection data, the data inconsistencies are compensated; therefore, a time series of reconstructed 3D images at any desired time can be obtained with any static reconstruction algorithm for circular trajectories. We denote this general theoretical approach as temporal interpolation approach (TIA).

An additional advantage of the proposed method is that for very fast processes the sampling rate can be increased up to $1/T_\pi$ and therefore the frequency range than can be reconstructed is $[0, 1/T_{2\pi}]$. That is, the maximum frequency that the algorithm can reproduce coincides with the maximum temporal resolution determined by the dynamic acquisition scheme (see section 4.3.1).

The interpolation of projections is useful to illustrate the reason for an efficient estimation scheme. It is not, however, of practical interest. The reason for this is twofold. First, ideal interpolation is very inefficient from the computational point of view; second, due to the high number of acquired views, performing interpolation on the projections is also inefficient. The first aspect can be improved by substituting ideal interpolation by a more efficient interpolation scheme. A reduction of the number of interpolations performed can be achieved if we exploit some of the approximations discussed in section 4.3. We address these aspects in the next sections.

4.4.2. Temporal Interpolation with Polynomial Splines

Let us consider a signal $f(t)$ that is sampled every T_s producing the samples $f(mT_s)$. The sampling rate or sampling frequency is $\nu_s = 1/T_s$. The ideal interpolator is an ideal low-pass filter and calculates an estimate of $f(t)$ as (see appendix B)

$$\underline{f}(t) = \sum_{k\in\mathbb{Z}} f(kT_s)\psi\left(\frac{t - kT_s}{T_s}\right), \tag{4.77}$$

where $\psi(t) = \text{sinc}(t)$. If $f(t)$ is strictly band-limited, i.e. $\hat{f}(\nu) = 0$ for $|\nu| \geq \frac{1}{2T_s}$, then $\underline{f}(t) = f(t)$. The ideal interpolator has an infinite support and decays very slowly ($\propto 1/|t|$) so that samples that lie far from the position of the point to interpolate will still make a significant contribution to its value. This makes it very inefficient for practical purposes. An efficient interpolation scheme should have a frequency response close to the ideal low-pass filter and be nevertheless well localised around the point to interpolate. Polynomial splines have been shown to be a very good compromise [Unser, 2000]. The nth polynomial spline interpolator is a piece-wise polynomial of order n. A polynomial is fitted in every interval between two samples in such a way that the connection with the polynomial in the next interval is smooth. The resulting function is $n-1$ times differentiable at the connecting points. Polynomial spline interpolation can be implemented in a very efficient way in the case where the sampling scheme is regular, i.e. the distance between samples T_s is constant. We follow here the presentation in [Unser et al., 1993a] and [Unser et al., 1993b]. As usual in digital signal processing the distance between samples is normalised to 1 without loss of generality [Oppenheim and Schafer, 1998]. The corresponding normalised time and frequency are $t' = t/T_s$ and $\nu' = \nu T_s$ respectively. Note that, in the general case the functions in each interval between samples do not have to be polynomials [Unser and Blu, 2005a]. In this thesis we refer in most of the cases to polynomial splines. Hence, in order to simplify formulation, the term *splines* will be used for polynomial splines if not otherwise indicated.

According to Schönberg's theorem, any spline function $s^n(t)$ can be represented as linear combination of shifted elementary functions:

$$s^n(t') = \sum_{k\in\mathbb{Z}} c[k]\beta^n(t'-k). \tag{4.78}$$

The elementary functions $\beta^n(t)$ are the so-called B-splines of order n. B-splines are, for a given order n, the splines with smallest support; they are localised in the interval $]-(n+1)/2, (n+1)/2[$. For a given set of samples of a continuous function $f[m] = f(mT_s)$, the spline interpolation problem consists in finding a spline function that takes the values $f(mT_s)$ at the sampling points, i.e. $s^n(m) = f[m]$. Using (4.78), this can be expressed as

$$f[m] = \sum_{k\in\mathbb{Z}} c[k]\beta^n(m-k). \tag{4.79}$$

If we interpret $\beta^n(m)$ as a discrete sequence, $b^n[m] = \beta^n(m)$, (4.79) can be expressed as a discrete convolution

$$f[m] = c * b^n[m]. \tag{4.80}$$

In Fourier domain, (4.80) becomes a product (see appendix B)

$$\hat{F}\left(e^{i2\pi\nu'}\right) = \hat{C}\left(e^{i2\pi\nu'}\right)\hat{B}^n\left(e^{i2\pi\nu'}\right), \tag{4.81}$$

so that the coefficients of the B-spline decomposition can be easily found as

$$\hat{C}\left(e^{i2\pi\nu'}\right) = \frac{\hat{F}\left(e^{i2\pi\nu'}\right)}{\hat{B}^n\left(e^{i2\pi\nu'}\right)}. \tag{4.82}$$

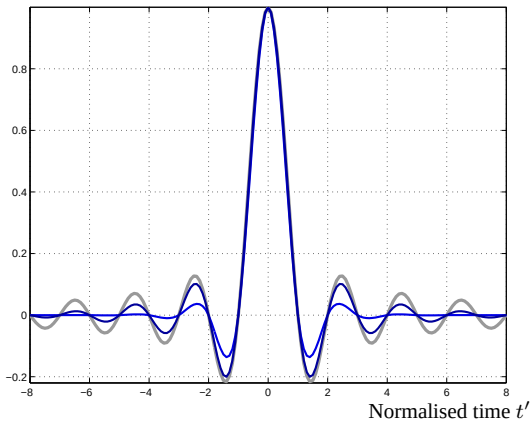

Figure 4.14. Polynomial spline interpolator for $n = 3$ (light blue), $n = 9$ (dark blue) and $n \to \infty$ or ideal interpolator (grey).

Hence, the coefficients $c[m]$ can be calculated by filtering the samples with the filter $1/\hat{B}(e^{i2\pi\nu'})$ or in time domain $(b^n)^{-1}[m]$. The filter $(b^n)^{-1}[m]$ has an infinite support but can be efficiently implemented as a recursive filter (IIR filter, see [Oppenheim and Schafer, 1998]). Since $\hat{B}^n(e^{i2\pi\nu'})$ does not vanish, the problem is well-posed. Knowing the coefficients of the B-spline decomposition, the value of the interpolated spline function at any time can be computed using (4.78). For the case where we want to evaluate the function at a fixed time before or after every sample, the computation can be performed in a more efficient way. Assume that we want to evaluate the interpolated spline at times shifted by δ after every sample. The time can be expressed as $t' = m + \delta$. If we evaluate the B-spline at times shifted by δ from the sampling positions, we obtain again a discrete filter $b^{n,\delta}[m] = \beta^n(m+\delta)$. Since the B-splines have a compact support, the filter $b^{n,\delta}[m]$ has a finite length (FIR filter, see [Oppenheim and Schafer, 1998]). Hence, for the computation of every sample, only few operations are needed. We do not develop the technical details of the implementation (they can be found in [Unser et al., 1993b]). In appendix D we give a description of the computational complexity of the algorithm.

In order to compare spline and ideal interpolation it is interesting to express the estimated spline function $s^n(t')$ as a linear combination where the coefficients are the samples of the continuous function $f[k]$. The simplest way to do this is in Fourier domain. We first calculate the Fourier transform of (4.78)

$$\hat{s}^n(\nu') = \hat{C}\left(e^{i2\pi\nu'}\right)\hat{\beta}^n(\nu'). \tag{4.83}$$

an then substitute (4.82) in (4.83)

$$\begin{aligned}\hat{s}^n(\nu') &= \frac{\hat{F}\left(e^{i2\pi\nu'}\right)}{\hat{B}^n\left(e^{i2\pi\nu'}\right)}\hat{\beta}^n(\nu') \\ &= \hat{F}\left(e^{i2\pi\nu'}\right)\underbrace{\frac{\hat{\beta}^n(\nu')}{\hat{B}^n\left(e^{i2\pi\nu'}\right)}}_{\hat{\eta}^n(\nu')}.\end{aligned} \tag{4.84}$$

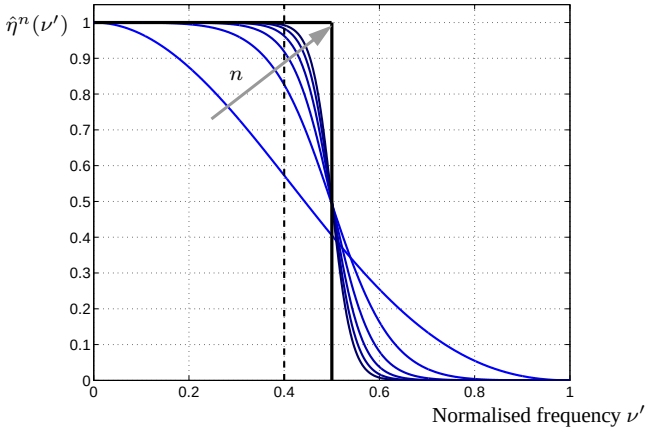

Figure 4.15. Fourier transform of the spline interpolator $\eta^n(t')$ for different orders n ($n = 1, 3, 5, 7, 9, 11$), the grey arrow indicates the direction of increasing n. The dashed line indicates 80% of the Nyquist band.

In time domain this becomes

$$s^n(t') = \sum_{k\in\mathbb{Z}} f[k]\eta^n(t' - k). \tag{4.85}$$

$\eta^n(t')$ is the spline interpolator of order n. It is shown in figure 4.14 for orders $n = 3$ and 9 and compared with the ideal interpolator. Even for $n = 9$, the spline interpolator decays much faster than the ideal interpolator. Nevertheless, as shown in the left side of figure 4.15, the frequency response of the spline interpolator approaches the one of the ideal interpolator as n increases. It has indeed been proven that the spline interpolator converges to the ideal interpolator when $n \to \infty$ [Aldroubi et al., 1992]. The convergence is very fast for the low degrees. Convergence to the ideal interpolator is a very comfortable property for our purposes since we can use n as a parameter that controls how close we are from ideal interpolation.

For practical purposes, we denote hereafter by p the proportion of the Nyquist band that can be reproduced from a given set of samples. This leads to a modified sampling condition

$$\nu_{max} \leq \frac{p}{2T_s}. \tag{4.86}$$

The value of p depends on the order n. For the purpose of this thesis we use as criterion that the frequency response deviates less than 2% from a constant in the frequency band $[0, p/(2T_s)]$. For $n = 9$, $p \approx 0.8$. This corresponds in figure 4.15 to the frequency band until the dashed line. In the following, we propose to substitute the ideal interpolator $\psi(t)$, by an nth order spline interpolator $\eta^n(t)$ in the interpolation step.

4.4.3. TIA-FDK Algorithms

The temporal interpolation of projections proposed above, estimates the value of every projection at every frame time. The estimated values are used to compute every frame with static reconstruction methods. Intuitively, the computational cost of CT reconstruction is much higher than the cost of interpolation. Since all operations involved in FDK-like reconstruction are linear, we could perform the interpolation after backprojection. Furthermore, in section 4.3.6 we saw that

the reconstruction of PBBs over several full-rotations in dynamic CT can be seen as a non-ideal sampling. Hence, the reconstruction can be performed by interpolating in the PBBs and the interpolated values only have to be accumulated. In this section, we use these ideas to derive efficient dynamic reconstruction algorithms.

A remark should be made before we start with the derivation of the algorithms. In section 4.4.1, we assumed that we can adapt the sampling rate with arbitrary precision. In practice, however, there are several possibilities to do this. We consider in the following a continuous and a discontinuous scanning mode. In continuous scanning mode, the rotation time is set to the largest value such that the time between samples fulfils the modified sampling condition (4.86). In discontinuous scanning mode, the rotation time is set to the minimum value $T_{2\pi}^{min}$. The source is then regularly switched off during several full-rotations. In the following sections the algorithms are formulated for continuous scanning mode. The differences to discontinuous scanning mode are commented in section 4.4.3.4 when we discuss the choice of the parameters.

4.4.3.1. TIA-TFDK ALGORITHM

The TIA-TFDK algorithm is a dynamic acquisition-reconstruction algorithm that exploits the dynamic acquisition process in order to use the maximum sampling rate for a given sampling interval $T_s = T_\pi$. It is based on the T-FDK reconstruction algorithm described in section 3.3.3.1. We start thus its derivation with the rebinning of the acquired cone-beam projections $P_\alpha(\gamma, \varphi, t_\alpha)$ to a fan-parallel beam (see section 3.3.3.1). This first step can be expressed as

$$P_\alpha(\gamma, \varphi, t_\alpha) \longrightarrow P_\beta^b(u, v, t_\beta), \tag{4.87}$$

and corresponds to the dynamic rebinning approximation discussed in section 4.3.3. According to the dynamic acquisition scheme, the projections are sampled every $T_{2\pi}$

$$P_\beta^b(u, v, k) = P_\beta^b(u, v, t_\beta + kT_{2\pi}). \tag{4.88}$$

For the estimation of the projection values, we use spline interpolation of order n; the interpolation order is left as an input parameter of the algorithm. Projection β and projection $\beta + \pi$ are quasi-equivalent (see section 3.3.3.4) so that the sampling interval is actually T_π. For this reason, we use for the estimation shifted versions of $\eta^n(t/T_\pi)$. This yields

$$\underline{P}_\beta^b(u, v, t) = \sum_{k \in \mathbb{Z}} P_\beta^b(u, v, t_\beta + kT_{2\pi}) \eta^n \left(\frac{t - t_\beta - kT_{2\pi}}{T_\pi} \right). \tag{4.89}$$

Note that this is not a good estimation of $P^b(u, v, t)$ since the samples are every $T_{2\pi}$ and the interpolating function vanishes every T_π; but this will be compensated later by combining the quasi-equivalent projections. With an estimation of the projection values at any time, we can use (3.64) and (3.65) to compute a frame at any time. In order to simplify notation we introduce

$$w_t(u, v) = \frac{\sqrt{\Gamma^2 - u^2} + \Gamma_D - \Gamma}{\sqrt{\left(\sqrt{\Gamma^2 - u^2} + \Gamma_D - \Gamma \right)^2 + v^2}}, \tag{4.90}$$

and write $u'(\mathbf{x},\beta)$ and $v'(\mathbf{x},\beta)$ simply as u' and v'. The complete expressions are given in section 3.3.3.1. Using (4.89) in (3.64)

$$\begin{aligned}
\underline{FP}_\beta(u,v,t) &= \int_{-u_{max}}^{u_{max}} \left(\underline{P}^r_\beta(s,v,t)w_t(s,v)\right) g(u-s)ds \\
&= \sum_{k\in\mathbb{Z}} \underbrace{\left(\int_{-u_{max}}^{u_{max}} P^b_\beta(s,v,t_\beta+kT_{2\pi})w_t(s,v)g(u-s)ds\right)}_{FP_\beta(u,v,t_\beta+kT_{2\pi})} \eta^n\left(\frac{t-t_\beta-kT_{2\pi}}{T_\pi}\right) \\
&= \sum_{k\in\mathbb{Z}} FP_\beta(u,v,t_\beta+kT_{2\pi})\eta^n\left(\frac{t-t_\beta-kT_{2\pi}}{T_\pi}\right). \qquad (4.91)
\end{aligned}$$

Hence, the estimated value of the filtered projections does not change if the filtering is performed before or after interpolation. The next step is now the backprojection with (3.65)

$$\begin{aligned}
\underline{\mu}^r(\mathbf{x},t) &= \frac{1}{2}\int_0^{2\pi} \underline{FP}_\beta(u',v',t)d\beta \\
&= \frac{1}{2}\int_0^{2\pi} \left(\sum_{k\in\mathbb{Z}} FP_\beta(u',v',t_\beta+kT_{2\pi})\eta^n\left(\frac{t-t_\beta-kT_{2\pi}}{T_\pi}\right)\right) d\beta. \qquad (4.92)
\end{aligned}$$

According to (4.92), every projection is interpolated. Due to the high number views, it would be desirable to reduce the number of interpolations to carry out. For this purpose we make use of the dynamic backprojection approximation discussed in section 4.3.4

$$FP_\beta(u,v,t_\beta) \approx FP_\beta(u,v,t_{\frac{\pi}{N}(2j+1)}) \quad \text{for} \quad \frac{2\pi}{N}j < \beta < \frac{2\pi}{N}(j+1) \qquad (4.93)$$

that is, we assume that the value of the filtered projections is almost constant during a time interval of length $2\pi/N$. We leave the number of PBB intervals in a full rotation N as an input parameter. If we rewrite (4.92) for an angular interval of length $2\pi/N$ we get a partial block backprojection as (see section 4.2)

$$\begin{aligned}
\underline{PBB}_j(\mathbf{x},t) &= \frac{1}{2}\int_{\frac{2\pi}{N}j}^{\frac{2\pi}{N}(j+1)} \left(\sum_{k\in\mathbb{Z}} FP_\beta(u',v',t_\beta+kT_{2\pi})\eta^n\left(\frac{t-t_\beta-kT_{2\pi}}{T_\pi}\right)\right) d\beta \\
&\approx \sum_{k\in\mathbb{Z}} \underbrace{\left(\frac{1}{2}\int_{\frac{2\pi}{N}j}^{\frac{2\pi}{N}(j+1)} FP_\beta(u',v',t_{\frac{\pi}{N}(2j+1)}+kT_{2\pi})d\beta\right)}_{PBB_j(\mathbf{x},t_{\frac{\pi}{N}(2j+1)}+kT_{2\pi})} \eta^n\left(\frac{t-t_{\frac{\pi}{N}(2j+1)}-kT_{2\pi}}{T_\pi}\right) \\
&= \sum_{k\in\mathbb{Z}} PBB_j(\mathbf{x},t_{\frac{\pi}{N}(2j+1)}+kT_{2\pi})\eta^n\left(\frac{t-t_{\frac{\pi}{N}(2j+1)}-kT_{2\pi}}{T_\pi}\right). \qquad (4.94)
\end{aligned}$$

The jth and the $(j + N/2)$th PBB are quasi-equivalent, so that we can write

$$\underline{PBB}_{j+N/2}(\mathbf{x}, t) \approx \sum_{k\in\mathbb{Z}} PBB_j(\mathbf{x}, t_{\frac{\pi}{N}(2j+1)} + T_\pi + kT_{2\pi})\eta^n \left(\frac{t - t_{\frac{\pi}{N}(2j+1)} + T_\pi - kT_{2\pi}}{T_\pi}\right). \tag{4.95}$$

If we combine (4.95) and (4.94), we get

$$\underline{PBB}_j(\mathbf{x}, t) \approx \sum_{k'\in\mathbb{Z}} PBB_j(\mathbf{x}, t_{\frac{\pi}{N}(2j+1)} + k'T_\pi)\eta^n \left(\frac{t - t_{\frac{\pi}{N}(2j+1)} - k'T_\pi}{T_\pi}\right). \tag{4.96}$$

The final reconstruction is obtained by accumulating the values of the PBBs at the desired reconstruction times:

$$\underline{\mu}^r(\mathbf{x}, t) = 2 \sum_{j=0}^{N/2-1} PBB_j(\mathbf{x}, t) \tag{4.97}$$

The dynamic reconstruction algorithm is summarised in the following steps:

Algorithm 4.1 (TIA-TFDK) *Steps for dynamic reconstruction with TIA-TFDK:*

1st *Reconstruction of N PBBs for $T_{tot}/T_{2\pi}$ rotations with T-FDK:*

$$\begin{aligned} FP_\beta(u, v, t_\beta + kT_{2\pi}) &= \int_{-u_{max}}^{u_{max}} P^b_\beta(s, v, t_\beta + kT_{2\pi}) w_t(s, v) g(u - s) ds \\ PBB_j(\mathbf{x}, t_{\frac{\pi}{N}(2j+1)} + kT_{2\pi}) &= \frac{1}{2} \int_{\frac{2\pi}{N}j}^{\frac{2\pi}{N}(j+1)} FP_\beta(u', v', t_\beta + kT_{2\pi}) d\beta \end{aligned} \tag{4.98}$$

2nd *Combination of the samples of the jth and the $(j + N/2)$th PBBs.*

3rd *Interpolation of PBB values:*

$$\underline{PBB}_j(\mathbf{x}, t) = \sum_{k\in\mathbb{Z}} PBB_j(\mathbf{x}, t_{\frac{\pi}{N}(2j+1)} + kT_\pi)\eta^n \left(\frac{t - t_{\frac{\pi}{N}(2j+1)} - kT_\pi}{T_\pi}\right) \tag{4.99}$$

4th *Accumulation:*

$$\underline{\mu}^r(\mathbf{x}, t) = 2 \sum_{j=0}^{N/2-1} PBB_j(\mathbf{x}, t) \tag{4.100}$$

Due to the underlying continuous spline model, the TIA-FDK algorithm returns a continuous function. In practice, however, we are only interested in reconstructing frames every T_{fr} during a certain time T_{tot} (see 4.1.1).

The parameters T_s and n determine the temporal resolution of the algorithm, whereas N controls the level of inconsistency in the PBBs. As we saw in section 4.1.2, these concepts depend on each other. In section 4.4.3.4 we discuss about the choice of the input parameters.

Using a sampling rate of $1/T_\pi$ means that we make the further approximation that quasi equivalent rays represent the same line integral (see section 3.3.3.4). Hence, one should expect that the error increases fast out of the midplane.

4.4.3.2. TIA-CFDK ALGORITHM

For processes that do not require a sampling rate of $1/T_\pi$, the rotation time can be adjusted in such a way that $T_{2\pi} < 1/(2\nu_{max})$ and therefore a sampling rate of $1/T_{2\pi}$ can be used. The advantage of this is twofold. First, there is no need to rebin the cone-beam projection dataset to a fan-parallel beam geometry so that the dynamic rebinning approximation is spared. Second, since the time between samples is equal to the rotation time we do not need the quasi-equivalent rays approximation. The result is a dynamic reconstruction algorithm based on the C-FDK algorithm presented in section 3.3.3.2. In order to simplify notation, we introduce

$$w_c(\gamma, \varphi) = \Gamma \cos(\gamma) \cos(\varphi) \tag{4.101}$$

and write $\gamma'(\mathbf{x}, \alpha)$ and $\varphi'(\mathbf{x}, \alpha)$ simply as γ' and φ'. The complete expressions are given in section 3.3.3.2.

The derivation of the algorithm is very similar to the one in the previous section but simpler since no combination is needed. The resulting algorithm is summarised in the following steps:

Algorithm 4.2 (TIA-CFDK) *Steps for dynamic reconstruction with TIA-CFDK:*

1st *Reconstruction of N PBBs for $T_{tot}/T_{2\pi}$ rotations with C-FDK:*

$$\begin{aligned} FP_\alpha(\gamma, \varphi, t_\alpha + kT_{2\pi}) &= \int_{-\gamma_{max}}^{\gamma_{max}} P_\alpha(\kappa, \varphi, t_\alpha + kT_{2\pi}) w_c(\kappa, \varphi) h(\gamma - \kappa) d\kappa \\ PBB_j(\mathbf{x}, t_{\frac{\pi}{N}(2j+1)} + kT_{2\pi}) &= \frac{1}{2} \int_{\frac{2\pi}{N} j}^{\frac{2\pi}{N}(j+1)} \frac{1}{L^2(\mathbf{x}, \alpha)} FP_\alpha(\gamma', \varphi', t_\alpha + kT_{2\pi}) d\alpha \end{aligned} \tag{4.102}$$

2nd *Interpolation of PBB values:*

$$\underline{PBB}_j(\mathbf{x}, t) = \sum_{k \in \mathbb{Z}} PBB_j(\mathbf{x}, t_{\frac{\pi}{N}(2j+1)} + kT_{2\pi}) \eta^n \left(\frac{t - t_{\frac{\pi}{N}(2j+1)} - kT_{2\pi}}{T_{2\pi}} \right) \tag{4.103}$$

3rd *Accumulation:*

$$\underline{\mu}^r(\mathbf{x}, t) = \sum_{j=0}^{N-1} PBB_j(\mathbf{x}, t) \tag{4.104}$$

The input parameters of the algorithm are given in table 4.2.

4.4.3.3. DISCUSSION

The dynamic reconstruction algorithms presented in the previous sections have in common that they are based on temporal interpolation of partial block backprojections, i.e. that they make use of the temporal backprojection approximation. The main difference between them is that the TIA-TFDK algorithm exploits better the acquisition scheme to use a shorter sampling interval. In order to illustrate the consequence of this, consider a dynamic process with a maximum frequency ν_{max}; if we assume that $n = 9$ the frequency range that can be reproduced from samples taken every T_s is $0.8/(2T_s)$ (see section 4.4.2). Hence, the rotation times for each of the algorithms will be

$$\begin{aligned} \text{TIA-CFDK}: \quad & T_s = T_{2\pi} \quad \Rightarrow \quad T_{2\pi} = \tfrac{0.8}{2\nu_{max}} \\ \text{TIA-TFDK}: \quad & T_s = T_{\pi} \quad \Rightarrow \quad T_{2\pi} = \tfrac{0.8}{\nu_{max}}. \end{aligned} \tag{4.105}$$

A longer rotation time implies that less rotations are performed during the protocol time and therefore less data are acquired, with the corresponding reduction of computational complexity. Another interpretation of the shorter sampling interval is that if we take the minimum rotation time of a scanner $T_{2\pi}^{min}$, the TIA-TFDK algorithm is able to reproduce higher frequencies, that is

$$\begin{aligned} \text{TIA-CFDK}: \quad & T_{2\pi}^{min} \quad \Rightarrow \quad \nu_{max} \leq \tfrac{0.8}{2T_{2\pi}^{min}} \\ \text{TIA-TFDK}: \quad & T_{2\pi}^{min} \quad \Rightarrow \quad \nu_{max} \leq \tfrac{0.8}{T_{2\pi}^{min}}. \end{aligned} \tag{4.106}$$

On the other hand, TIA-TFDK makes use of the dynamic rebinning approximation and of the quasi-equivalent rays approximation which are not necessary for the derivation of the TIA-CFDK algorithm. Hence, while in the TIA-CFDK algorithm the error induced by the temporal backprojection approximation can be reduced arbitrarily by increasing N, in the TIA-TFDK algorithm this error cannot be made smaller than a certain threshold depending on the size of the object (see section 4.3.5). Furthermore, as a consequence of the quasi-equivalent rays approximation the error in the planes $z \neq 0$ will be larger for the TIA-TFDK algorithm.

Table 4.1 summarises the differences between the TIA-TFDK and the TIA-CFDK algorithms.

	TIA-TFDK	TIA-CFDK
Sampling interval	T_{π}	$T_{2\pi}$
Max. temporal resolution	$\frac{p}{T_{2\pi}^{min}}$	$\frac{p}{2T_{2\pi}^{min}}$
Reconstruction mode	short-scan	full-scan
Approximations	dyn. backpr. appr. dyn. rebinning appr. quasi-eq. rays	dyn. backpr. appr.

Table 4.1. Summary of the differences between the TIA-TFDK and TIA-CFDK algorithms (continuous scanning mode).

4.4.3.4. CHOICE OF THE PARAMETERS

In this section we provide a short guide for the choice of the parameters for dynamic acquisition-reconstruction with the TIA-TFDK and TIA-CFDK algorithms. The input parameters for the

Parameter	Meaning
ν_{max}	maximum frequency
$T_{2\pi}^{min}$	minimum rotation time
T_{tot}	total acquisition time
T_{fr}	time between reconstructed frames
$T_{2\pi}$	rotation time
n	order of the spline interpolation
N	number of PBB intervals in a full-rotation

Table 4.2. Input parameters for the TIA-FDK algorithms. The last three are computed from the first four.

TIA-FDK algorithms are listed in table 4.2. Hence, we assume that the we have at our disposal an estimation of the maximum frequency of the dynamic process ν_{max} and that we know the minimum rotation time of the scanner $T_{2\pi}^{min}$, the total protocol time T_{tot} and the time interval between output frames T_{fr}.

The first parameter to adjust is the spline interpolation order n. This determines the frequency band that can be recovered from the samples which is decisive to adjust the rotation time $T_{2\pi}$ and therefore N as well. According to this choice of n we will be able to reconstruct the frequency band $[0, p/(2T_s)]$ (see section 4.4.2).

Before we choose the parameters, we have to choose between both algorithms. The choice of one algorithm or the other depends on the particular application. As a general rule we might formulate the following procedure to choose between both:

- If $\nu_{max} \leq \frac{p}{2T_{2\pi}^{min}}$
  - If the object is large or a very high precision is required $\Rightarrow$ TIA-CFDK.
  - If the amount of input data is constraining $\Rightarrow$ TIA-TFDK.
- If $\frac{p}{2T_{2\pi}^{min}} < \nu_{max} \leq \frac{p}{T_{2\pi}^{min}} \Rightarrow$ TIA-TFDK.

The rotation time is adjusted so that the modified sampling condition (4.86) is fulfilled. This yields, as already shown in the previous section:

$$\begin{aligned} \text{TIA-CFDK}: \quad & T_s = T_{2\pi} \quad \Rightarrow \quad T_{2\pi} = \tfrac{p}{2\nu_{max}} \\ \text{TIA-TFDK}: \quad & T_s = T_{\pi} \quad \Rightarrow \quad T_{2\pi} = \tfrac{p}{\nu_{max}}. \end{aligned} \tag{4.107}$$

Finally, the number of partial block backprojections N has to be adjusted. For this purpose we use the results of sections 4.3.4 and 4.3.5. For the TIA-CFDK algorithm, we only have to consider the temporal backprojection approximation so that we can use the results summarised in statement 4.3. According to these results, we can always find a value N_{min} such that the term responsible for the bias $\chi(T_{2\pi}\nu, N)$ is smaller than a given ε for any value of $T_{2\pi}\nu_{max} \in [0, 1]$; the threshold N_{min} is of the form

$$N_{min} = CT_{2\pi}\nu_{max}. \tag{4.108}$$

The analysis given in section 4.3.4 is not of quantitative nature, so that we cannot derive from it a particular value of the constant C. Nevertheless, it is possible to derive a value of C using

an heuristic argument based on efficiency considerations. For this purpose, we consider the worst case where $T_{2\pi}\nu_{max} = 1$. Figure 4.16 shows that $\chi(1, N)$ decreases non-linearly. It falls fast to values around 0.01, after that, large increases of N produce only small reductions of $\chi(1, N)$. We take therefore as a reference $\varepsilon = 0.01$. In order to illustrate the implications of this choice, let us consider a temporal evolution $c(t)$ which is essentially band-limited with maximum frequency ν_{max}. Among all signals of this kind, the worst case concerning temporal resolution corresponds to a signal that concentrates all its frequency components in $|\nu_{max}|$, e.g. $c(t) = \sin(2\pi\nu_{max}t)$. According to (4.34), for such a signal the bias would be

$$\hat{b}(\nu) = \frac{2\pi}{N}\frac{g(0)}{2}\hat{c}(\nu)\varepsilon, \tag{4.109}$$

and in time domain

$$b(t) = \frac{2\pi}{N}\frac{g(0)}{2}c(t)\varepsilon. \tag{4.110}$$

Hence, in our example, $\varepsilon = 0.01$ implies a maximum bias of 1%. According to the model

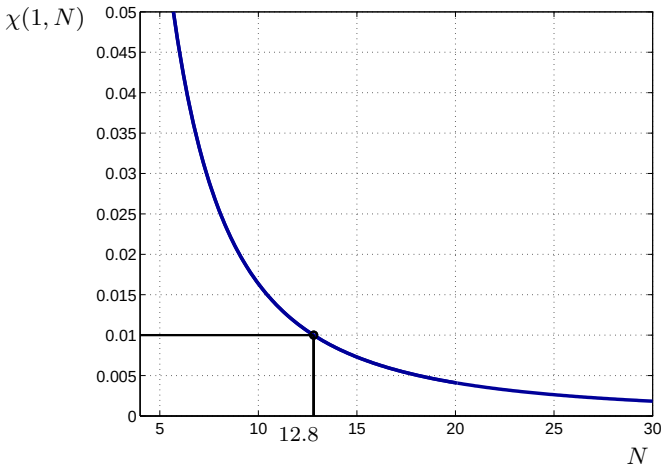

Figure 4.16. Minimum number of angular intervals in a full-rotation N as a function of ε for $\nu_{max} = 1/T_{2\pi}$ in $[0, 1/T_{2\pi}]$.

introduced in hypothesis 4.1, perfusion signals concentrate their energy in the low frequencies so that for our application, $\varepsilon = 0.01$ implies a maximum bias much smaller than 1%. Taking as a reference the value 0.01, we find $\chi(1, N) = 0.01 \Rightarrow N = 12.8$ and

$$12.8 = CT_{2\pi}\nu_{max} = C \Rightarrow C = 12.8. \tag{4.111}$$

In this section we use this value as a reference in order to illustrate the differences between the algorithms concerning the choice of the parameter values. We will revisit the discussion about the choice of N in section 4.5.4.1 in the light of the results of the numerical simulations.

According to (4.107), for TIA-CFDK

$$N_{min} = 12.8 \times 0.4 = 5.12. \tag{4.112}$$

The temporal resolution of the TIA-TFDK algorithm is additionally affected by the effect of the temporal rebinning approximation. In section 4.3.5, we saw that the bias behaves for low values of N as in the previous case but it does not converge to 0 with increasing values of N. We derived a threshold over which the value of N has almost no more influence on the bias. This threshold depends on the size of the object through the normalised distance to the origin ρ. It can be calculated as

$$N_{max} = \sqrt{\frac{2}{3}}\frac{\pi}{\rho_{max}}, \tag{4.113}$$

where ρ_{max} is the normalised radius of a circle enclosing all points with time dependent density. The final choice of N is the smallest value such that

$$N \geq \min\{N_{min}, N_{max}\} \quad \text{with} \quad N \in \mathbb{N} \quad \text{and even.} \tag{4.114}$$

Since for TIA-TFDK the sampling interval is T_π

$$N_{min} = 12.8 \times 0.8 = 10.24. \tag{4.115}$$

In section 4.4.3 we mentioned that an alternative way to adapt the sampling rate is to use the discontinuous scanning mode. In this mode, the source rotates with the minimum rotation time and is regularly switched off during periods of time of several full-rotations. The sampling interval is thus $T_s = mT_{2\pi}^{min}$ for both T-FDK and C-FDK-based approaches. The corresponding formulation for TIA-CFDK is obtained from algorithm 4.2 by substituting $T_{2\pi}$ by T_s. In the case of TIA-TFDK, we exploit the fact that for $m \geq 1$ we can use full-scan reconstruction. We therefore eliminate the 2nd step and perform interpolation on every PBB without combining them. Note that this way we spare the quasi-equivalent rays approximation. The sampling interval is chosen as

$$\text{TIA-FDK} : T_s = \frac{p}{2\nu_{max}} \Rightarrow m = \lfloor \frac{p}{2T_{2\pi}\nu_{max}} \rfloor. \tag{4.116}$$

Since now the minimum rotation time of the scanner is used, the number of angular intervals for TIA-CFDK is calculated as

$$N_{min} = 12.8 T_{2\pi}^{min} \nu_{max}. \tag{4.117}$$

For TIA-TFDK, we use again (4.114) with the new value for N_{min} with the difference that N does not need to be even. This approach has the advantage that it requires less angular intervals. On the other hand, it has the main disadvantage that the sampling interval can only be adapted in steps of $T_{2\pi}$.

We finalise this section with some examples of parameter sets for a scanner with minimum rotation time $T_{2\pi}^{min} = 0.5$ s and a total acquisition time is $T_{tot} = 40$ s. With such a scanner we want to reconstruct a sequence of image frames of a dynamic process with a maximum frequency ν_{max}. We assume for the computation of the parameter values that the object is small enough for N_{max} to be larger than N_{min}, so that $N = N_{min}$ is used for the number of angular intervals. Table 4.3 shows the parameter values for a fast process with $\nu_{max} = 1.6$ Hz while table 4.4 shows the parameters for a slow process with $\nu_{max} = 0.16$ Hz. The parameter values were calculated using $n = 9$ for the spline interpolation. The fast process can only be reproduced using the TIA-TFDK with the minimum sampling interval $T_s = T_{2\pi}^{min}/2$. This can only be achieved in continuous acquisition mode. For the slow process the parameters for TIA-CFDK and TIA-TFDK are slightly different. In continuous scanning mode, we see that less rotations

	Continuous scanning		Discontinuous scanning	
	TIA-CFDK	TIA-TFDK	TIA-CFDK	TIA-TFDK
n	–	9	–	–
$T_{2\pi}$ (s)	–	0.5	–	–
T_s (s)	–	0.25	–	–
N	–	12	–	–
Num. rotations	–	80	–	–

Table 4.3. Example of reconstruction parameters for $\nu_{max} = 1.6$ Hz.

	Continuous scanning		Discontinuous scanning	
	TIA-CFDK	TIA-TFDK	TIA-CFDK	TIA-TFDK
n	–	9	–	9
$T_{2\pi}$ (s)	2.5	5	0.5	0.5
T_s (s)	2.5	2.5	2.5	2.5
N	6	12	1	1
Num. rotations	16	8	16	16

Table 4.4. Example of reconstruction parameters for $\nu_{max} = 0.16$ Hz.

are needed with TIA-TFDK which reduces the computational time. An interesting aspect is also that the rotation time is increased up to 5 seconds which means that using this algorithm the process can be reproduced using a slow rotating system. In discontinuous scanning mode, the parameters are the same for TIA-CFDK and TIA-TFDK. Indeed, as we discussed previously in this section, for $m \geq 1$ TIA-TFDK is used in full-scan mode so that the algorithm becomes very similar to TIA-CFDK except for the use of T-FDK to reconstruct the PBBs. The effect of the dynamic rebinning approximation is only significant when we need large values of N. Since we use the minimum rotation time $T_{2\pi}^{min}$, the values of N are small so that the bound is not reached and therefore the effect of the dynamic rebinning approximation can be neglected. The decision to use TIA-CFDK or TIA-TFDK depends only on the preference for the corresponding static reconstruction algorithms C-FDK or T-FDK. A remarkable aspect is that the number of intervals N is equal to 1. Only one interval means a full-rotation, so that the algorithms reconstruct image frames using static reconstruction with C-FDK or T-FDK and then compute the rest of the output frames by spline interpolation.

In appendix D we show that in order to calculate the computational complexity we can ignore the interpolation step compared to the computational cost of FDK-like reconstruction. In order to compare the computational efficiency we can use the number of acquired rotations and interpret it as "number of equivalent FDK-like reconstructions". Since the number of rotations depends on ν_{max}, the computational complexity depends on ν_{max} as well. Furthermore, since the cost of interpolation can be neglected, the number of output frames can be increased without increasing the computational complexity. In other words, the computational complexity only depends on ν_{max} and is independent of the number of output frames.

4.5. NUMERICAL SIMULATIONS

The aim of this section is to provide numerical simulations both to verify the theoretical results presented and to assess the performance of the TIA-FDK algorithms. All simulations were performed using the software package *DRASIM* (see chapter 6). For the simulations with noise, a random signal was added to the projections according to the Poisson law. All dynamic reconstructions were computed with the C++ library *CT Project* described in chapter 6. The phantoms used for the simulations are described in appendix C.

4.5.1. SIMULATION AND RECONSTRUCTION PARAMETERS

The simulations were performed in cone-beam geometry for a scanner with a cylindrical detector as described in figure 3.11. The dimensions of the scanner are determined by the source-origin distance Γ and the source-detector distance Γ_D. These are

$$\Gamma = 57 \text{ cm} \tag{4.118}$$

$$\Gamma_D = 104 \text{ cm}. \tag{4.119}$$

Γ_D is at the same time the radius of the cylindrical detector. On the midplane, the area reconstructed is situated within a circle of radius $\|\mathbf{x_{max}}\| = 12.8$ cm. The image matrix had 256×256 pixels of 1×1 mm^2. The detector has a height of 23.36 cm. With these dimensions, the scanner has the following maximum fan and cone-beam angles:

$$\begin{array}{rclcl} \gamma_{max} & = & \arcsin\left(\frac{12.8}{57}\right) & = & 0.2265 \text{ rd} \\ \varphi_{max} & = & \arctan\left(\frac{23.36/2}{57}\right) & = & 0.2021 \text{ rd} \end{array} \tag{4.120}$$

If not otherwise indicated the following parameters were used

- Number of views: $N_\alpha = 800$.
- Number of channels of the detector: $N_\gamma = 256$.
- Number of detector rows: $N_{sl} = 128$.

The derivation of these values is given in section 3.3.3.3.

In each case 18 full-rotations were simulated; hence, $T_{tot} = 18T_{2\pi}$. The time interval between frames of the reconstructed sequence is $T_{fr} = T_{2\pi}/4$. The frequency of the signals in the simulations is given relative to the rotation time $T_{2\pi}$. In terms of the discussion in section 4.4.3.4, this is equivalent to adapting the rotation time to the continuous scanning mode.

The input noise levels are given in terms of the standard deviation that they produce in a static short-scan reconstruction.

4.5.2. DYNAMIC RECONSTRUCTION ALGORITHMS

Our aim was to simulate the most constraining case, i.e. when the maximum frequency of the dynamic process is close to $1/T_{2\pi}$. In such a case, the TIA-TFDK algorithm must be used (see section 4.4.3.4). This is, in addition, the most interesting case since in the derivation of the TIA-TFDK algorithm more approximations are used than in the derivation of TIA-CFDK. We

compare the results obtained with the TIA-TFDK algorithm with two other algorithms presented in section 4.2: the generalised Parker weighting for dynamic reconstruction approach by Taguchi and the $k\pi$-mode linear regression approach by Grangeat. If not otherwise indicated, the following parameters are used for the reconstruction algorithms.

TIA-TFDK We choose a high interpolation order for the splines interpolation $n = 9$ in order to achieve a high temporal resolution. In section 4.4.2 we saw that with $n = 9$ we can recover $\approx 0.8/(2T_s)$. Since the frequencies of the phantoms are close to $1/T_{2\pi}$, we choose the parameters of the algorithm for the maximum frequency $0.8/T_{2\pi}$. For the TIA-TFDK in continuous scanning mode, N must be even. In our implementation of the algorithm N_α must be a multiple of N.

Generalised Parker Weighting According to [Taguchi, 2003], a short-scan reconstruction (HS-FDK) provides better temporal resolution whereas a full-scan reconstruction (NHS-FDK) exhibits less noise and stronger artifact reduction. Our aim is to compare it with the TIA-TFDK approach which uses short-scan reconstruction and has a high temporal resolution. For this reason we use HS-FDK.

$k\pi$-mode Linear Regression The first two steps are identical as in the proposed time interpolation approach. Hence, we choose the same values for N as for the reconstruction with TIA-TFDK. The strength of this algorithm lies in its de-noising effect, however, this is with detriment to temporal resolution. The higher k is, the stronger de-noising effect has the linear regression. Note that the TIA-TFDK approach with $n = 1$ is equivalent to the 2π-mode linear regression. In order to have a de-noising effect at least 4π must be chosen. However, choosing a higher mode would limit too much the temporal resolution. Therefore, we choose 4π for our simulations.

4.5.3. Error Measurements

Regions of interest (ROI) were defined within the inserts (4×4 pixels) and around them (a rectangular ring of width 4 pixels), avoiding the discretisation error on the edges due to finite spatial resolution. This way we concentrate on the error due to dynamic reconstruction.

For each reconstructed frame j, mean square error (MSE_j), bias (ϵ_j) and standard deviation σ_j were measured with respect to the phantom within the regions of interest. These errors are related by

$$MSE_j = \epsilon_j^2 + \sigma_j^2. \tag{4.121}$$

ϵ_j indicates how well the mean is estimated and can be interpreted as an indicator for the time resolution of the algorithm. σ_j indicates how large the variations around the mean are and can be interpreted as an indicator for the noise level. Finally the total error $\sqrt{MSE_j}$ takes both effects into account.

In order to present the error measurements in a more compact way these values were averaged over all frames to obtain an average total error ($\sqrt{\overline{MSE}}$), an average of the absolute value of the bias ($\bar{\epsilon}$) and an average standard deviation ($\bar{\sigma}$).

For the simulations without noise, the error is given in terms of the average total error ($\sqrt{\overline{MSE}}$). For the simulations with noise, average absolute value of the bias $\bar{\epsilon}$ and average standard deviation $\bar{\sigma}$ are given separately. All errors are measured in Hounsfield Units (HU).

4.5.4. RESULTS

The first part of the simulations is devoted to verify the theoretical results provided in sections 4.3.4 and 4.3.5. Following, we compare the performance of the TIA-TFDK algorithm with the generalised Parker weighting approach and the $k\pi$-mode linear regression approach. We finalise the section studying the behaviour of the algorithm in the presence of noise.

Before we start with the presentation of the results, we should pay attention to the fact that the errors due to the temporal backprojection and rebinning approximations are not the only possible sources of error in the dynamic reconstruction. The interpolation error should be taken into account as well as the error due to FDK-like reconstruction. Finally, noise is, in practice, a crucial factor but in our simulations it is only relevant for the last section. We summarise the possible sources of error in the following list:

a) Dynamic backprojection approximation.

b) Dynamic rebinning approximation.

c) Spline interpolation.

d) Discretisation of the reconstruction algorithm.

e) Noise.

4.5.4.1. THEORETICAL ASPECTS

In section 4.3.4 we showed that a time dependent density point located at $\mathbf{x_0}$ causes an error in the reconstruction that is maximum at $\mathbf{x} = \mathbf{x_0}$. The error caused by the density point at $\mathbf{x} \neq \mathbf{x_0}$ is a data inconsistencies error in the sense explained in section 4.1.2. In order to study this error we used phantom D. It consists of a single insert with a time dependent attenuation value which follows a sinusoidal law of frequency $0.8/T_{2\pi}$ (see appendix C). This frequency is the maximum frequency that can be reconstructed with the TIA-TFDK algorithm (see section 4.4.3.3) and represents therefore the worst case. Figure 4.17 a) shows the error vs. distance to the origin for a reconstruction with TIA-TFDK. In grey we represent as a reference the discretisation error of a static short-scan reconstruction of the same phantom with the T-FDK algorithm. The black curve is the error of the TIA-TFDK reconstruction measured along rings with increasing radius. It can be clearly seen that the error has its maximum at distance 0, i.e. within the insert itself, and decreases fast outside. This is in accordance with the estimation provided in (4.44) and confirms that if we decide that the error at 0 can be neglected, then it is clear that it can be neglected also elsewhere. Even if this error is small, it is distributed all over the image. This can be observed in figure b), where an image frame of the reconstruction is shown with an extremely narrow window of 2 HU. The darker and brighter areas in the pattern indicate that the error takes both positive and negative values. The star form of the artifact is due to the fact that every PBB is sampled and interpolated independently so that every PBB carries a small but different error than the rest. Since every PBB contributes spatial resolution in a preferential direction, when they are accumulated a star-shaped pattern with as many rays as PBBs are used in the reconstruction appears. Note, however, that the pattern in figure 4.17 b) has been made visible by using a window of 2 HU. In practice, the error is much smaller than the error due to data inconsistencies caused by the other dynamic reconstruction algorithms as will be shown later.

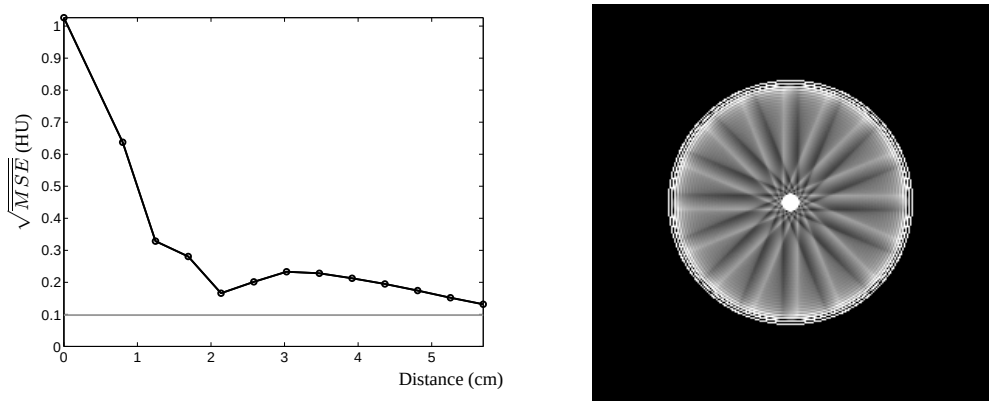

(a) Err. vs distance (phantom D)

(b) Output frame (phantom D)

Figure 4.17. Error due to data inconsistencies in dynamic reconstruction with the TIA-TFDK algorithm with phantom D, the grey line shows the error due to discretisation of the reconstruction algorithm. Right: error vs distance. Left: error artifacts, window $[49, 51]$ HU.

Next we analyse the effect of the dynamic rebinning approximation. For this purpose we use phantom B which consists of a series of inserts with the same frequency, situated at different distances from the origin. In order to better illustrate the effect, the frequency of the inserts is again the highest frequency that can be reproduced by the TIA-TFDK algorithm with $n = 9$, i.e. $\nu = 0.8/T_{2\pi}$. Figure 4.18 shows the error vs. distance to the origin normalised to the source-origin distance Γ. As expected, the error increases with the distance to the origin. The behaviour of this error can be explained using (4.70). According to it, the bias increases approximately with the square of the normalised distance $\rho = \|\mathbf{x}\|/\Gamma$. The blue curve represents a fit of a function of the form $a + b\rho^2$. The fit explains the error quite well, although in order to verify the dependence with ρ^2 more accurately the distance range should be much larger.

Finally, we analyse the dependence of the error with ρ and with N. For this purpose we performed reconstructions of phantom B with the TIA-TFDK algorithm with values of $N = 2, 4, 8, 16$ and 32. The results are shown in figure 4.18 b). Note the similarity of this figure with the left part of figure 4.13. For small values of N, the predominant effect is the temporal averaging due to the dynamic backprojection approximation. For large values of N, the error converges to a certain value which increases with ρ. Note that this value is reached in all cases for values of N between 8 and 16. According to the theoretical analysis of section 4.3.5, the value of N over which the error due to the dynamic backprojection approximation is smaller than the error due to the dynamic rebinning approximation is

$$N_{max} \approx \sqrt{\frac{2}{3}}\frac{\pi}{\rho}. \tag{4.122}$$

For the outer insert of phantom B $\rho = 0.1535$ so that $N_{max} = 16.71$. In figure 4.18 b), however, the error curve for $\rho = 0.1535$ clearly reaches its minimum already for $N = 8$. Moreover, the error curve for $\rho = 0$ does not converge to 0 as expected. The reason for this is that in the analysis of section 4.3.5 we only considered the error due to the dynamic backprojection and rebinning

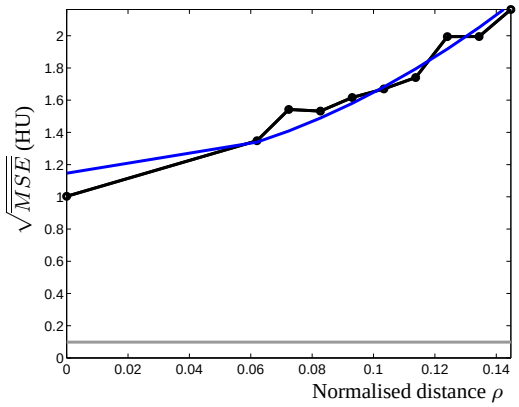

(a) Err. vs normalised distance ρ (phantom B)

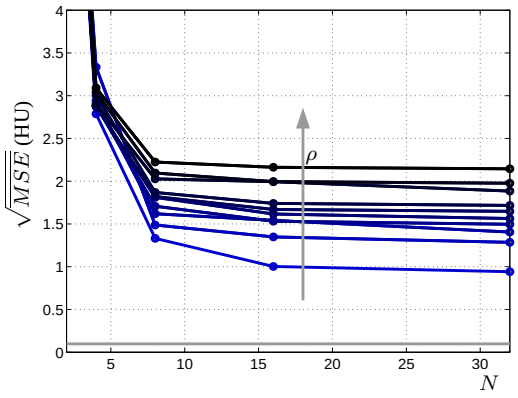

(b) Err. vs N for different values of ρ (phantom B)

Figure 4.18. Error due to the dynamic rebinning and backprojection approximations. Left: error vs normalised distance on phantom B. Right: error vs. N for different values of $\rho \in [0, 0.1535]$ (see appendix C). The grey line shows the error due to discretisation of the reconstruction algorithm.

approximations. As we stated above, there are other possible sources of error which include the spline interpolation and the error due to discretisation of the reconstruction algorithm. These errors are not reduced by increasing N so that they should be taken into account in the derivation of a practical value for the threshold N_{max}. We propose in the following a heuristic approach to modify (4.122) empirically. It consists in considering in (4.64) that there is a background error due to interpolation and discretisation and that it is independent of the errors due to the dynamic backprojection and rebinning approximations. Indeed, as can be observed in figure 4.18 b), the error due to discretisation is very small and in practical applications is even lower since a higher spatial resolution is used. Hence, we can assume that the error is only due to interpolation. This interpolation error is constant for a given frequency $\epsilon(\nu)$. Thus, we can assume that we have a constant error due to interpolation and add a constant $\epsilon(\nu)$ to the right side of (4.64). Solving in a similar way as in section 4.3.5 we get

$$N_{max} \approx \frac{\pi}{\sqrt{6}} \frac{1}{\sqrt{\frac{\epsilon(\nu)}{(\nu_{max} T_{2\pi})^2} + \frac{1}{4}\rho^2}}. \tag{4.123}$$

For $\epsilon(\nu) = 0$, (4.123) becomes (4.122). We now use the curves in figure 4.18 b) to estimate $\epsilon(\nu)$ for spline interpolation with $n = 9$. For $\rho = 0$, N_{max} is close to 10 while for $\rho = 0.1535$, N_{max} is close to 8. Hence, we get $\epsilon(0.8) \approx 0.013$. We can thus provide a guideline to choose N so that the error is the smallest possible given a maximum frequency $\nu_{max} = 0.8/T_{2\pi}$ and a maximum normalised radius ρ

$$N = N_{max} \approx \frac{\pi}{\sqrt{6}} \frac{1}{\sqrt{0.02 + \frac{1}{4}\rho^2}}. \tag{4.124}$$

Note that this expression is valid for TIA-TFDK in continuous scanning mode, since in this case with $n = 9$, the sampling rate is adjusted in such a way that $\nu_{max} T_{2\pi} = 0.8$. For discontinuous mode or TIA-CFDK, the corresponding value of $\epsilon(\nu)$ for the different frequencies is needed. This

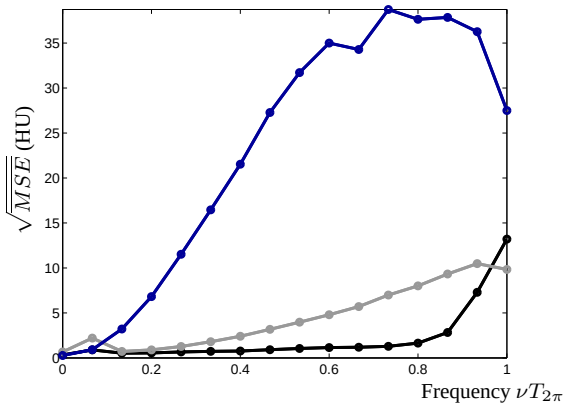

(a) Err. vs norm. freq. within the inserts (phant. A)

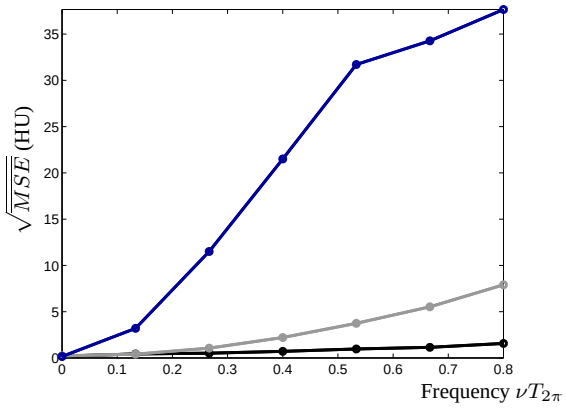

(b) Err. vs norm. freq. within the inserts (phant. C)

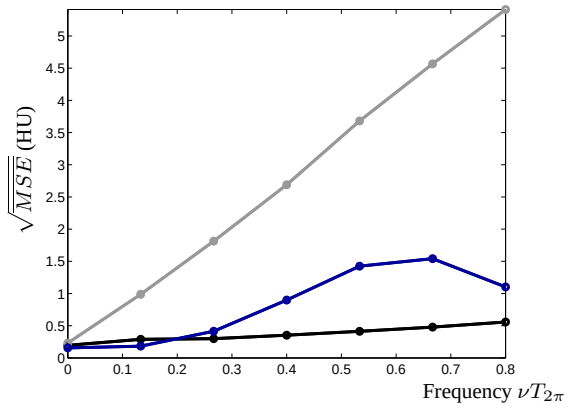

(c) Err. vs norm. freq. around the inserts (phant. C)

Figure 4.19. Error vs frequency with phantoms A and C for the three algorithms: TIA-TFDK (black), 4π-mode linear regression (blue) and HS-FDK (grey).

might be obtained by repeating the same procedure as above for every frequency, i.e. performing simulations with phantom B and finding a value of $\epsilon(\nu)$ that explains the curves. For the rest of the simulations we used phantoms A and C for which $\rho \approx 0.1$. Using (4.124) we get $N = 8.55$, so that we took the next possible value > 8 according to our implementation: $N = 16$.

4.5.4.2. Comparison of Dynamic Reconstruction Algorithms

In order to compare the performance of the three algorithms, we used phantoms A and C. Phantom A is designed on the same principle as phantom C but it contains 16 frequencies in the interval $[0, 1/T_{2\pi}]$. Figure 4.19 a) shows the error vs. frequency within the inserts for the three algorithms for phantom A. Figure 4.20 shows the mean value within two inserts for sequences reconstructed with the three algorithms. The error curve for the TIA-TFDK approach follows qualitatively the frequency response of the polynomial spline interpolation of order $n = 9$ (see figure 4.15); it

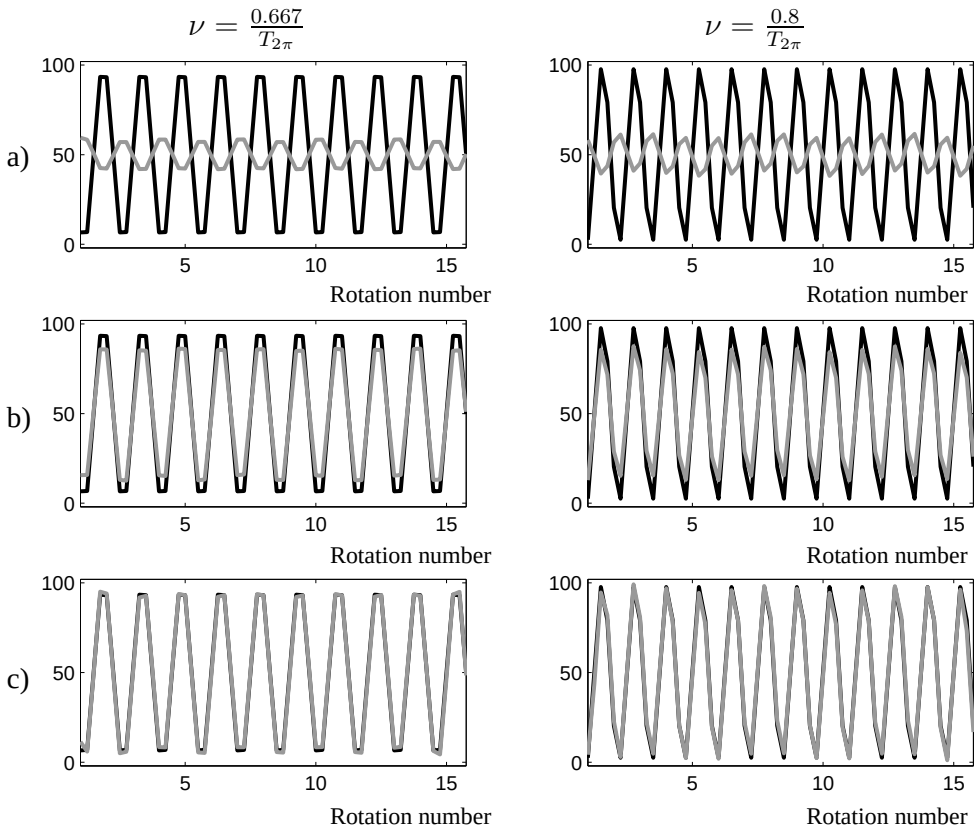

Figure 4.20. Mean value of the reconstruction within two inserts (grey) compared to the phantom (black). a) 4π-mode linear regression, b) HS-FDK and c) TIA-TFDK.

grows slowly until approximately $0.8/T_{2\pi}$, from this point on, the slope of the error curve changes and the error increases much faster.

The error for HS-FDK reconstruction grows faster than for TIA-TFDK but with an almost constant slope. For this reason it is smaller than the error for TIA-TFDK close to the Nyquist frequency. The reconstruction with the 4π-mode linear regression algorithm exhibits a dramatically huge error because within the interval of four half-rotations the exact time curves significantly deviate from the linear assumption. The error increases for the low frequencies and for frequencies above $1/(2T_{2\pi})$ becomes random.

We saw in the previous section that a time dependent density point causes a data inconsistencies error on the whole image. This error is small compared to the error at the position of the density point itself. In phantoms A and C we have several inserts with time dependent density so that it is interesting to study how this error behaves in such a case. For this purpose, the error around the inserts is a good indicator; it is shown in figure 4.19 c). The black curve is almost constant for all frequencies which indicates that the error is the result of the data inconsistencies error caused by all inserts, so that it can be seen as a background error. The reason why the curve is not totally constant is that the closest insert has more influence than the rest. This background error is larger than in the static reconstruction but it is lower than the error within the inserts. This indicates that

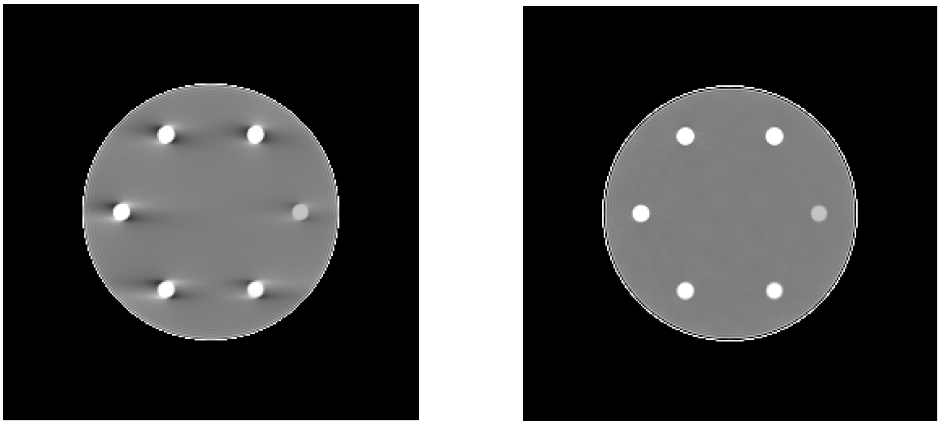

(a) HS-FDK (b) TIA-TFDK

Figure 4.21. Frames of the reconstruction of phantom C with HS-FDK and TIA-TFDK. Window: $[30, 70]$ HU.

the error due to data inconsistencies caused by the different inserts is not accumulative.

For the other two algorithms the error grows with the frequency. The 4π-mode linear regression approach exhibits a much better behaviour around the inserts than within them, causing even less error than the HS-FDK approach. This can be explained by the fact that the value there is constant and the linear regression estimation constrains the variability of the estimated values.

The non-monotone behaviour of the error curves for the lower frequencies in phantom A can be explained by the proximity between the insert with the highest frequency and the insert with the lowest frequency (see figure C.3). The former causes a considerable error since its frequency is out of the frequency range $[0, 0.8/T_{2\pi}]$, the later exhibits a very small error since its frequency is very low. The error induced by the insert with the highest frequency is therefore comparable to the error within the insert with the lowest frequency.

Algorithm	Rec. time
4π-mode LR	420 s
HS-FDK	977 s
TIA-TFDK	466 s

Table 4.5. Reconstruction times for the three algorithms.

We observe that for low frequencies the error for HS-FDK might be considered acceptable so one could argue that there is no need to use TIA-TFDK. There are, however, other significant aspects than the mean square error to take into account. Figure 4.21 shows two frames of the reconstructions with HS-FDK and with TIA-TFDK. The HS-FDK frame exhibits strong artifacts around the time dependent inserts which are due to the use of highly inconsistent datasets in the reconstruction. With the same window value, these artifacts are not visible in the TIA-TFDK frame. Furthermore, for the reconstruction of the output sequence with HS-FDK, 18×4 short-scan reconstructions are performed so that the computational complexity is 36 equivalent FDK-like

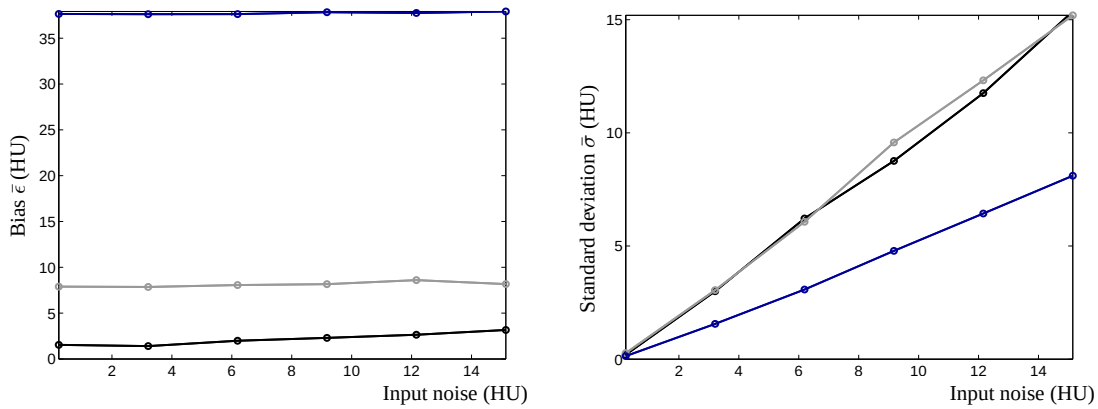

(a) Bias vs. noise level (phantom C)

(b) Standard deviation vs. noise level (phantom C)

Figure 4.22. Bias and standard deviation within insert 5 ($\nu = 0.8/T_{2\pi}$) of phantom C for different noise levels.

reconstructions (see appendix D). For the TIA-TFDK, however, the complexity is 18 equivalent FDK-like reconstructions, i.e. 2 times lower. This is confirmed by the computation times given in table 4.5. The computations were performed in a PC with a Pentium IV processor at 2.8 GHz. Furthermore, for lower values of ν_{max} the rotation time would be correspondingly adapted which would reduce the number necessary rotations for TIA-TFDK. Finally, we saw in section 4.4.3.4 that the computational complexity of TIA-TFDK depends on ν_{max} but not on the number of output frames whereas with HS-FDK every computed frame increases the computational complexity.

4.5.4.3. Behaviour in the Presence of Noise

An aspect of major importance that was ignored throughout this chapter is quantum noise. In order to study its effect in the reconstruction algorithms, we added noise of different levels to the simulated projections of phantom C and measured the error in the reconstructed sequences.

The error was measured within insert 5 ($\nu = 0.8/T_{2\pi}$) and was decomposed into bias and variance. The input noise levels are in the range 0 to ≈ 15 HU. Figures 4.22 a) and b) show the bias and the standard deviation respectively. As can be observed, for the three algorithms the bias is almost not affected by the input noise level. Only the standard deviation increases in the reconstruction. While the reconstructions with the TIA-TFDK and HS-FDK algorithms do not change the noise level, the 4π-mode linear regression approach reduces it by a factor of 2. Indeed, this is where the strength of the linear regression approach lies: it has a strong de-noising effect reducing the standard deviation of the noise by a factor of $k/2$ at the cost of temporal resolution.

4.6. Conclusion

The main difficulty of dynamic reconstruction comes from the fact that every projection is acquired at a different time. This is an inherent problem of the rotational acquisition scheme in Computed Tomography, so that it may be alleviated by increasing the rotational speed of the

source-detector arrangement, but not eliminated. For a given rotation time $T_{2\pi}$, the importance of this effect strongly depends on the rate of change of the dynamic process that takes place in the object. In the first part of this chapter we presented a theoretical analysis of the acquisition and reconstruction for objects with a time dependent density. We saw that the reconstruction of partial block backprojections from projections acquired during several rotations can be interpreted as a temporal sampling. The continuous PBB is sampled with functions with a finite support. The sampling interval corresponds to the rotation time $T_{2\pi}$. In the case of parallel or fan-beam geometry, the support of the filters can be made arbitrarily small by increasing the number of backprojections in a full-rotation N. In the case of rebinned projections an additional error in form of a time delay appears which cannot be reduced by increasing N and predominates when N is increased over a certain threshold.

The second part of the chapter was devoted to the design of an approach for dynamic reconstruction which works with a minimum of input data. Based on the non-ideal sampling interpretation, we proposed two dynamic reconstruction algorithms based on FDK-like reconstruction and spline interpolation. By appropriately choosing N, the bias of the samples is small and then the values of the partial backprojections are estimated at any time with a continuous spline model. Applying this principle to cone-beam projections yields the TIA-CFDK algorithm, which is based on the C-FDK static reconstruction algorithm. If rebinned projections are used, we obtain the TIA-TFDK algorithm, based on the T-FDK static reconstruction algorithm. The later allows to reduce the sampling interval to T_π at the cost of poorer image quality at planes $z \neq 0$. By adapting the rotation time, the acquisition is adapted to the maximum frequency of the object. This allows to minimise the necessary input data for the reconstruction of a given dynamic process. On the other hand, the algorithms are designed to achieve a high temporal resolution for a given rotation time. This opens new possibilities for the use of slow rotating scanners for dynamic imaging purposes.

In the last part of the chapter we provided numerical simulations both to validate the theoretical results presented in the first part and to assess the performance of the proposed algorithms. For this purpose the TIA-TFDK was chosen since it is the most constraining from both. The results with the TIA-TFDK algorithm correspond to what was predicted in the theory except that in the analysis of section 4.3 the error due to interpolation was not considered. Even for high frequencies, the error due to the time delay is not significant. The algorithm can reproduce accurately dynamic processes with $\nu_{max} \leq 0.8/T_{2\pi}$ and was shown to behave well in the presence of noise. This last aspect is decisive to tackle the problem of dynamic reconstruction in the presence of noise in the next chapter.

CHAPTER 5.

DYNAMIC RECONSTRUCTION WITH OPTIMAL SIGNAL TO NOISE RATIO

This chapter deals with dynamic reconstruction in the presence of quantum noise. For this purpose, we first introduce a simple approximative model for the temporal behaviour of noise in dynamic CT. The model is kept as general as possible so that it can be applied to projections, partial block backprojections or images. According to this model, the noise is a stationary random process of zero mean and the values of two samples of this process are uncorrelated. Based on this, we introduce the concept of optimal-SNR estimation as the estimation from noisy samples of a continuous signal with a bandwidth limited to the frequency range of the dynamic process $[-\nu_{max}, \nu_{max}]$. We show that an optimal SNR reconstruction in dynamic CT can performed with any sampling rate, as long the sampling condition is fulfilled, by adapting the dose according to the number of scans performed during the protocol time. We then use these results to extend the TIA-FDK approach presented in the previous chapter to the TSA-FDK approach. The TSA-FDK approach uses spline smoothing instead of interpolation so that the (temporal) frequency band of the output sequence can be adapted to ν_{max} independently of the number of scans performed. We finalise the chapter with a numerical example and an example with clinical data.

5.1. INTRODUCTION. NOISE REDUCTION

In chapter 4 we proposed two dynamic reconstruction schemes that can be adapted to the maximum rate of change of a dynamic process. The algorithms exhibit a high temporal resolution which, in the case of TIA-TFDK, is close to the upper bound given by the dynamic acquisition scheme (see section 4.3.1). This enables the use of slow scanners for dynamic CT imaging. For slow processes the number of scans can be reduced while keeping the necessary temporal resolution, with the corresponding reduction of computational cost. These results, however, were obtained by ignoring the quantum noise in the X-ray detection process. In chapter 3, we saw that the statistical nature of the detection process causes an error in the image in the form of noise. The variance of this noise is inversely proportional to the dose applied. In section 3.1.4 we introduced the mAs product as a measure for dose. According to this measure, the dose is proportional to the exposure time. Hence, the total dose applied during a dynamic acquisition protocol can be calculated as

$$D_{tot} = N_{sc} \times D_{2\pi}, \tag{5.1}$$

where N_{sc} is the number of scans, i.e. the number of full-rotations with the X-ray source switched on, and $D_{2\pi}$ is the dose applied per scan.

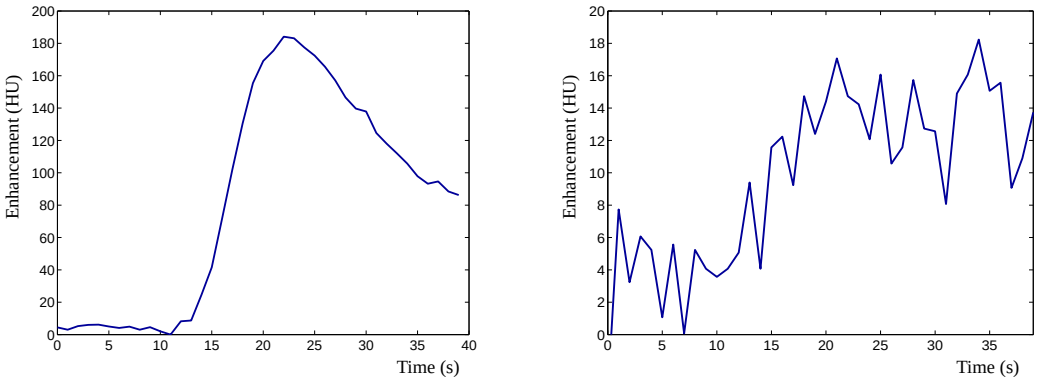

(a) Big vessel (*sinus sagittalis*) (b) Tissue

Figure 5.1. Examples of time-attenuation curves (TACs).

In the standard perfusion CT protocol described in section 2.3.2 the source rotates continuously during 40 seconds with a rotation time $T_{2\pi} = 0.5$ s and it is switched off every second rotation. Therefore, in terms of the mAs product, the total dose is 40 times the dose of a single scan. According to (5.1) there are two possibilities to reduce the total dose. The first is to reduce the number of scans N_{sc} typically by increasing the time between sequence frames. The second, consists in reducing the dose of every scan by turning the tube current down. As stated in section 2.3.2 the aim of dynamic CT is to compute a sequence of images that contains the temporal evolution of the concentration of contrast agent. For this purpose, both reducing the number of scans and reducing the dose have negative effects. Increasing the time between frames entails a reduction of the temporal resolution; this may lead to misestimations of functional parameters [Wintermark et al., 2004]. On the other hand, a reduction of the tube current yields an increase of the noise variance in the image. The increase of the attenuation value due to contrast agent flow in large vessels can reach several hundreds of HU so that compared to it noise is negligible. In small vessels and tissue, however, the enhancement due to contrast agent is very low. As an example, typical enhancement in grey matter is about $10 - 15$ HU and in white matter about $4 - 6$ HU in presence of noise with a standard deviation of $3-4$ HU [Klotz and König, 1999]. Figure 5.1 illustrates this fact; it shows two time-attenuation curves from a perfusion CT dataset acquired with a standard perfusion CT protocol and reconstructed using static reconstruction frame by frame (see section 4.2). The enhancement curve on the left corresponds to the *sinus sagittalis*. This vein collects the contrast after flowing through the brain; hence, the contrast agent concentration is very high and the time-attenuation curve is much higher than noise. The curve on the right corresponds to grey matter, an enhancement level of about 10 HU can be inferred from it. The noise level is about 3.5 HU. The high level of noise makes it difficult to recognise the time-attenuation curve, not to mention to derive any quantitative measurements from it. A further reduction of the tube current would increase the noise level, yielding a degradation in the accuracy of the computed physiological parameters [Murase et al., 2005].

This chapter is devoted to the problem of dynamic reconstruction, with the focus on noise reduction. The goal is to provide a dynamic reconstruction algorithm that takes into account both

the dynamic properties of the object and the random nature of the X-ray detection process.

5.1.1. CHARACTERISATION OF TACS

The computation of physiological parameters from time-attenuation curves is based on compartmental model analysis (see section 2.3.1). In section 4.3.2 we proposed a simple model for time-attenuation curves which adapts well to the assumptions made to derive the compartmental analysis methods. The model is also the natural model which comes out when regarding the dynamic acquisition process as a temporal sampling (see section 4.3.1). The idea is to consider the temporal evolution of the concentration of contrast agent $c(t)$ as an essentially band-limited signal, i.e. a signal whose Fourier transform is negligible for frequencies over a given frequency threshold, ν_{max}. This can be expressed as

$$\hat{c}(\nu) \approx 0 \quad \text{for} \quad |\nu| > \nu_{max}. \tag{5.2}$$

Since the temporal evolution is different for every tissue, ν_{max} is taken to be the maximum among the maximum frequencies of all tissues.

Wintermark et al. found in [Wintermark et al., 2004] that reducing the time between frames in a perfusion CT protocol under 1 second did not contribute to improve the accuracy of the computed physiological parameters. In their study, the curves obtained with $T_s = 0.5$ s did not provide more information than the ones obtained with 1 s. Hence, we can conclude that perfusion signals are fully characterised by samples taken every second and therefore that their maximum frequency lies under $\nu_{max} < 0.5$ Hz.

The practical interest of the proposed model depends strongly on the fact that we have a good estimation of ν_{max}. In order to get an idea of the order of magnitude of ν_{max} we analyse in this section some examples of TACs extracted from clinical data. For this purpose we used 10 cerebral perfusion CT datasets with 40 images acquired a rate of one image per second. The data were obtained by courtesy of Dr. Peter Schramm (Department of Neuroradiology of the University of Heidelberg Medical School). From each dataset a TAC was extracted containing the temporal evolution of the pixel values of a small region of interest within the *arteria cerebri anterior*. This is an input artery which is approximately orthogonal to the slice plane; it is shown in figure 5.2 a) in a frame of one of the datasets. The normalised time-attenuation curves are shown in figure 5.2 b). As stated above, these signals are oversampled; hence, the discrete Fourier transform (DFT) of the sequences can be used to approximate the Fourier transform of the signals in the frequency interval $[-0.5, 0.5]$ Hz [Oppenheim and Schafer, 1998]. We can estimate the energy of a signal $c(t)$ in a given frequency interval $[-\nu_c, \nu_c]$ by accumulating the square of the absolute value of the DFT coefficients corresponding to frequencies in this interval

$$E(\nu_c) = \frac{1}{MT_s} \sum_{j=-J}^{J} |\hat{C}\left(e^{i2\pi\nu_j}\right)|^2 \quad \text{with} \quad \nu_J \leq \nu_c, \tag{5.3}$$

where $\hat{C}\left(e^{i2\pi\nu_j}\right)$ are the coefficients of the DFT, $\nu_j = j/(MT_s)$ and M is the number of points of the DFT. If $\nu_c = 1/(2T_s) = 0.5$ Hz, then we get a good approximation of the total energy of the signal E_T. Figure 5.2 c) shows the DFT of the sequences normalised by their total energy, E_T. For every frequency ν_c, we can calculate the percentage of the total energy of the signal that

(a) Sequence frame

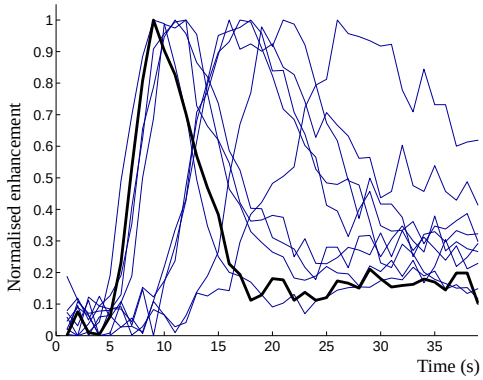

(b) Time attenuation curves

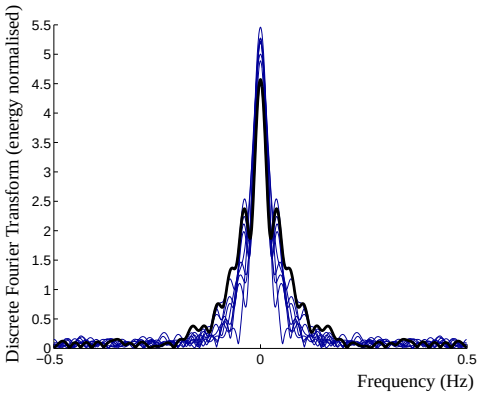

(c) Discrete Fourier transform of the TACs

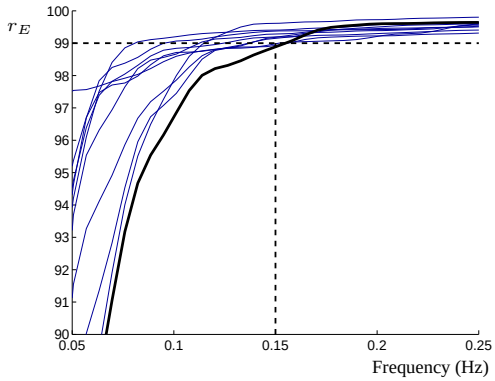

(d) Percentage of the energy in $r_E(\nu_c)$

Figure 5.2. Estimation of ν_{max} from the TAC of the *arteria cerebri anterior* for 10 clinical datasets. The black curve represents the fastest perfusion signal. The red arrow in a) indicates the *arteria cerebri anterior*.

is contained in the frequency interval $[-\nu_c, \nu_c]$ as

$$r_E(\nu_c) = 100\frac{E(\nu_c)}{E_T}. \tag{5.4}$$

Figure 5.2 d) shows $r_E(\nu_c)$ for all curves. As can be observed, 99% of the energy is contained, for all signals, in the frequency range $[-0.15, 0.15]$ Hz. The black curve in figures 5.2 b), c) and d) represents the worst case among the studied TACs and is representative for a very fast perfusion signal. Indeed, in c) can be observed that over ≈ 0.15 Hz, the spectrum reaches a ground level and remains approximately constant. Hence, we can conclude that the rest 1% of the energy is due to noise. We take this worst case as a reference and estimate therefore $\nu_{max} = 0.15$ Hz. We will use this value as a reference throughout this thesis except in the case where a more precise estimation is available. Note, however, that this is a rather conservative value. Indeed, figure 5.2 d) shows that for most of the signals over 99% of the energy is concentrated in $[-0.12, 0.12]$ Hz.

5.2. Noise Reduction Strategies

In the previous section we gave an estimation of the order of magnitude of ν_{max} for perfusion signals. Using this value with the TIA-TFDK algorithm, the rotation time $T_{2\pi}$ could be adjusted as (see section 4.4.3.4)

$$T_{2\pi} = \frac{0.8}{\nu_{max}} \approx 5.33 \text{ s}, \tag{5.5}$$

where we assumed an interpolation order of $n = 9$. With respect to the protocol used for the acquisition of the data in the previous section, this would imply a reduction of the amount of the acquired data by a factor of 5.33. But in the previous section we saw that the limiting factor for the computation of functional parameters is noise. A possible strategy to increase the image quality in the reconstructed sequence would be to use the TIA-TFDK approach and increase the tube current in such a way that the total dose is the same as in the standard protocol. That is, in (5.1), the number of scans is reduced by a factor of 5.33; increasing the tube current by this factor yields a reduction of the variance of the projection noise by the same factor (see section 3.2.4.2). Since the TIA-TFDK uses short-scan reconstruction, the variance of the image noise would be then reduced by a factor 2.66.

If we observe (5.1) we can easily derive a second noise reduction strategy. The total dose is not modified if we increase the number of scans by a certain factor and reduce the tube current by the same factor. The obtained measurements will be very noisy but they will be strongly oversampled as well. By performing a smoothing along the time axis, noise can be reduced.

In this section we try to give an answer to the question of which of these two strategies is more efficient in terms of noise reduction. The analysis is based on a model for the temporal behaviour of noise in dynamic CT which is described in the following section.

5.2.1. Model for the Temporal Behaviour of Noise

We provide in this section a heuristical argumentation based on empirical observations to derive a mathematical model that describes the temporal behaviour of noise in dynamic CT. We formulate the model at the end of the section.

The TIA-FDK algorithms estimate the value of the PBBs at times between samples by using polynomial spline interpolation (see section 4.4.3). In the extreme cases of an infinite number of angular intervals N and $N = 1$, the PBBs correspond to a unique filtered projection and a full-scan reconstruction respectively. Hence, the presented noise model should be as general as possible in order to be used in all these contexts. For this reason we consider an additive noise model where the measured signal $f(t)$ is composed of the searched unknown signal $x(t)$ and an additive noise term $\varepsilon(t)$:

$$f(t) = x(t) + \varepsilon(t). \tag{5.6}$$

The measured signal $f(t)$ corresponds to a pixel (or voxel) value of a filtered projection, a PBB or a reconstructed image. The noise $\varepsilon(t)$ is assumed to be a continuous random process with zero mean and mean square value $\overline{\varepsilon^2}$. Finally, $x(t)$ is the value which would be obtained in the ideal case without noise.

Let us concentrate on the temporal evolution of a single projection value which we denote by

P. In section 3.2.4.2, we saw that P is a random variable characterised by

$$\begin{aligned} \bar{P} &= -\ln\left(\frac{\bar{q}}{q_0}\right) \\ \sigma^2 &= \frac{1}{\bar{q}}, \end{aligned} \tag{5.7}$$

where $\bar{q}$ is the average number of quanta collected by the pixel and q_0 is the average number of quanta detected when there is no object between source and detector. The flow of contrast agent increases the attenuation so that the value of $\bar{q}$ and therefore both the mean and the variance depend on time, i.e. $\bar{P} = \bar{P}(t)$ and $\sigma^2 = \sigma^2(t)$. In terms of the model described by (5.6), the time dependent mean is represented by $x(t) = \bar{P}(t)$ and $\varepsilon(t)$ is the projection noise with zero mean and time dependent variance.

The mean of the projection value can be decomposed into a static value that represents the initial attenuation (without contrast agent) and a time dependent additive term which represents the contribution of contrast agent to the total attenuation. The contribution of contrast agent to the total attenuation is very small compared to the initial attenuation. This is illustrated with an example in figures 5.3 a) and b). Figure a) shows the central part of the first frame of the sequence (left) and of a frame after 20 s with high enhancement due to contrast agent flow (right). A projection in parallel geometry was calculated by accumulating the attenuation values in the direction indicated by the grey arrow. Figure b) shows, as a percentage, the increase of attenuation on the right frame (with contrast agent) with respect to the left frame (without contrast agent). Note that this corresponds (except for noise) to the percentage of attenuation due to contrast agent enhancement. Although this central part of the projection covers the most significant vessels in the scanned region (*sinus sagittalis* and *arteria cerebri anterior* marked in blue and red respectively on the right frame), the attenuation due to contrast agent flow represents in the worst case 1.1% of the total attenuation.

We denote the initial value of the attenuation as $\bar{P}_{ini}$ and the value with enhancement corresponding to the frame shown in figure 5.3 a) as $\bar{P}_{enh}$. In our example, we have

$$\Delta = \bar{P}_{enh} - \bar{P}_{ini} \leq 0.011\bar{P}_{ini}. \tag{5.8}$$

The corresponding values for the average number of detected quanta can be derived using (5.7)

$$\bar{q}(\bar{P}) = q_0 e^{-\bar{P}}. \tag{5.9}$$

This way we can find the values for the corresponding $\bar{q}_{ini}$ and $\bar{q}_{enh}$. For values close to $\bar{P}_{ini}$, (5.9) can be approximated using a first order Taylor series expansion

$$\bar{q}_{enh} = \bar{q}(\bar{P}_{ini} + \Delta) = q_0 e^{-(\bar{P}_{ini}+\Delta)} \approx q_0 e^{-\bar{P}_{ini}} - q_0 e^{-\bar{P}_{ini}}\Delta = \bar{q}_{ini}(1-\Delta). \tag{5.10}$$

We can then use this approximation to calculate the ratio between the variances with and without enhancement

$$\frac{\sigma^2_{enh}}{\sigma^2_{ini}} \approx \frac{1/\bar{q}_{enh}}{1/\bar{q}_{ini}} = \frac{\bar{q}_{ini}}{\bar{q}_{ini}(1-\Delta)} = \frac{1}{(1-\Delta)}. \tag{5.11}$$

From (5.8) we know that $\Delta \leq 0.011\bar{P}_{ini}$. In medical applications the X-ray beam is usually attenuated by a factor in the range 20 to 1000 [Barret and Swindell, 1981] so that $\bar{P} \in [3, 7]$, and

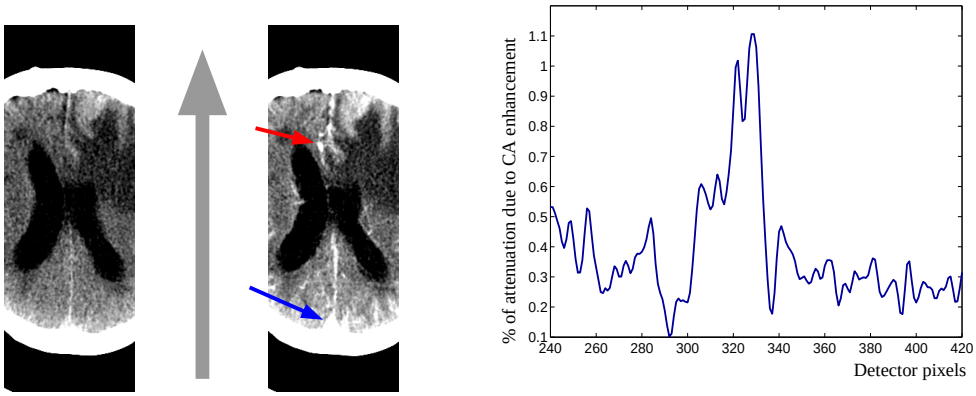

(a) (b)

Figure 5.3. Percentage of the attenuation of the X-ray beam due to contrast agent enhancement.

therefore the product $0.011\bar{P}_{ini}$ is at least one order of magnitude smaller than 1. Using this in (5.11), we conclude that

$$\frac{\sigma^2_{enh}}{\sigma^2_{ini}} \approx 1. \tag{5.12}$$

Hence, it is a reasonable approximation to neglect the time dependence of the variance.

Figure 5.3 refers to only one dataset but it is very representative. We can therefore make the assumption that the flow of contrast agent does not affect the variance of noise in projections, i.e. that the variance of the noise does not depend on time. If both temporal mean and variance are constant, the process $\varepsilon(t)$ is said to be a wide sense stationary process in time [Papoulis, 1965].

An additional important aspect that characterises the measurements of a projection value is that the fluctuations around the mean at two time instants t_1 and t_2 are statistically independent if the system is stable [Barret and Myers, 2004].

At the beginning of the section we stated that the proposed model should be general enough to be applied to filtered projections, PBBs or reconstructed images. If we assume that the variances of the projection values do not depend on time, it is straightforward to conclude that the same holds for the rest. Similarly, the statistical independence of the fluctuations at different times is guaranteed for filtered projections, PBBs and reconstructed images as long as the projection datasets used are disjoint. This leads to the formulation of our model for the temporal behaviour of noise in dynamic CT in form of the following hypothesis.

Hypothesis 5.1 *The temporal evolution of projections, partial block backprojections (PBBs) and images is affected by noise. This noise fulfils:*

- *It is additive.*
- *It is a wide sense stationary random process with zero mean.*
- *Two samples of it at different times are statistically independent random variables.*

For both PBBs and reconstructed images, the last statement is only true if the projection datasets for each PBB (or image) are disjoint.

5.2.2. TEMPORAL SAMPLING OF NOISE

We now analyse the effect of sampling noise with different sampling rates using the model for the temporal behaviour of noise given in the previous section. The presentation is kept general by using the notation introduced in the previous section; the measured signal $f(t)$ may represent a projection, a filtered projection, a PBB value or a reconstructed image value.

We consider a discrete sequence $\varepsilon_1[n]$ of samples of the stationary process $\varepsilon(t)$, described in the previous section, obtained every T_s, i.e. $\varepsilon_1[n] = \varepsilon(nT_s)$. As mentioned above, samples of $\varepsilon(t)$ at different times are statistically independent and therefore uncorrelated random variables. Mathematically, this is expressed by the discrete autocorrelation function R_{ε_1} as

$$R_{\varepsilon_1}[n] = R_\varepsilon(nT_s) = E[\varepsilon_1[k]\varepsilon_1[k+n]] = \overline{\varepsilon^2}\delta[n], \tag{5.13}$$

where $R_\varepsilon(t)$ is the continuous autocorrelation function of $\varepsilon(t)$ and $\delta[n]$ is the Kronecker symbol ($\delta[0] = 1$ and $\delta[n] = 0$ if $n \neq 0$). The discrete power spectral density S'_{ε_1} is defined as [Oppenheim and Schafer, 1998]

$$S'_{\varepsilon_1}\left(e^{i2\pi\nu'}\right) = \sum_{n\in\mathbb{Z}} R_{\varepsilon_1}[n]e^{-i2\pi\nu' n} = \overline{\varepsilon^2}, \tag{5.14}$$

where $\nu' = \nu T_s$ is the normalised frequency with ν as the physical frequency in Hz. $S'_{\varepsilon_1}(e^{i2\pi\nu'})$ owes its name to the fact that integrating it over one period of the normalised frequency $[-1/2, 1/2]$ yields the mean square value or total noise power. Downsampling $\varepsilon_1[n]$ by a factor of K would deliver a sequence with the same discrete autocorrelation as in (5.13) and therefore the same discrete power spectral density as in (5.14).

Definition (5.14), however, does not provide any insight into the physical frequency of the underlying continuous process. For this reason we define the discrete physical power spectral density S_{ε_1} of the samples of a continuous process sampled every T_s as

$$S_{\varepsilon_1}\left(e^{i2\pi\nu T_s}\right) = T_s \sum_{n\in\mathbb{Z}} R_{\varepsilon_1}[n]e^{-i2\pi\nu n T_s} = \overline{\varepsilon^2}T_s. \tag{5.15}$$

Integrating (5.15) over one period we obtain the total power or mean square value of the discrete process

$$\overline{\varepsilon_1^2} = \int_{-\frac{1}{2T_s}}^{\frac{1}{2T_s}} S_{\varepsilon_1}\left(e^{i2\pi\nu T_s}\right) d\nu = \overline{\varepsilon^2}. \tag{5.16}$$

Therefore, $S_{\varepsilon_1}(e^{i2\pi\nu T_s})$ describes the distribution of power density over one period of the *physical* frequency axis. If we now change the sampling rate to $T_s^K = KT_s$, the corresponding discrete physical power spectral density will be increased

$$S_{\varepsilon_K}\left(e^{i2\pi\nu T_s^K}\right) = \overline{\varepsilon^2}T_s^K = K\overline{\varepsilon^2}T_s, \tag{5.17}$$

while the total power remains constant

$$\overline{\varepsilon_K^2} = \int_{-\frac{1}{2KT_s}}^{\frac{1}{2KT_s}} S_{\varepsilon_K}\left(e^{i2\pi\nu T_s}\right) d\nu = \frac{K\overline{\varepsilon^2}T_s}{KT_s} = \overline{\varepsilon^2}. \tag{5.18}$$

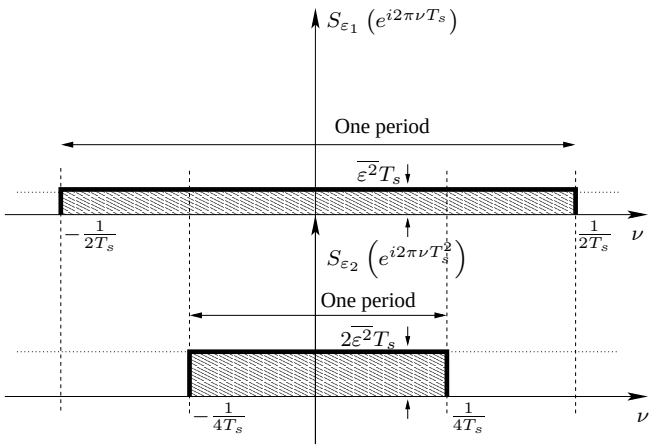

Figure 5.4. Distribution of power density of uncorrelated sequences coming from the sampling of a continuous stationary random process with sampling rates $1/T_s$ (top) and $1/(2T_s)$ (bottom).

From (5.16) and (5.18) we can deduce that when the sampling rate is reduced by a factor of K, the total power remains the same but it is accumulated in a smaller frequency range $]-1/(2KT_s), 1/(2KT_s)[$. This is illustrated in figure 5.4. Note that this result is also valid for $K \in \mathbb{R}$.

5.2.3. Optimal-SNR Estimation

With the models for signal and noise introduced, we can now easily analyse the approaches presented at the beginning of the section. For this purpose, we use the notation introduced in section 5.2.1 and denote by $f[n]$ the temporal samples of the measured signal every T_s. These samples consist of samples $x[n]$ of a deterministic signal $x(t)$ plus samples $\varepsilon_1[n]$ of an additive noise $\varepsilon(t)$. Noise is modelled as a continuous wide sense stationary random process with zero mean. We first concentrate on projection values, so that $f(t)$ denotes the temporal evolution of a projection value. We characterise the acquisition protocol by the total dose applied D_{tot} and its duration T_{tot}. The dose is distributed uniformly among all scans so that the dose per scan can be calculated as $D_{2\pi} = D_{tot}/N_{sc}$ with $N_{sc} = T_{tot}/T_s$. In section 3.2.4.2 we saw that the variance of projection noise is inversely proportional to the dose applied. Hence, the value of $D_{2\pi}$ determines $\overline{\varepsilon^2}$. We assume that $x(t)$ is essentially band-limited and that its maximum rate of change is ν_{max}. Since we only know $x(t)$ during the protocol time, we use as a measure of its power the average power during the protocol duration T_{tot}

$$\overline{x^2} = \frac{1}{T_{tot}} \int_0^{T_{tot}} x^2(t)dt. \tag{5.19}$$

As shown in the previous section, the mean square value of the sampled noise is $\overline{\varepsilon_1^2} = \overline{\varepsilon^2}$. Since $\varepsilon(t)$ is a zero mean process, the mean square value is equal to its variance. Note that this value depends indirectly on T_s, since for a different sampling rate a different dose per scan is applied.

Hence, we can define a reference signal to noise ratio (SNR) for a sampling rate of $1/T_s$ as

$$SNR_{REF} = \frac{\overline{x^2}}{\overline{\varepsilon^2}}. \tag{5.20}$$

We can now exploit the prior knowledge about the dynamic process in terms of ν_{max} to reduce noise. We assumed that the chosen sampling rate $1/T_s$ fulfils the sampling condition so that the signal is oversampled. On the other hand, we know that the power spectral density of noise is constant over all frequencies. The natural conclusion is then that suppressing frequency components over ν_{max}, the signal is preserved and only noise is eliminated, increasing thus the signal to noise ratio. The maximum enhancement of the SNR is obtained when the output signal only contains frequencies in the frequency range of the signal, i.e. $[-\nu_{max}, \nu_{max}]$. Hence, we denote the estimation of a continuous signal adapted to this frequency range as *optimal SNR estimation* and the obtained signals as *optimal SNR signals*. Figure 5.5 illustrates this aspect. As long as $T_s < 1/(2\nu_{max})$, the repetitions of the spectrum do not overlap (see sampling condition in appendix B). In this case, a continuous version of the signal with optimal SNR can be recovered by adapting an ideal low-pass filter to ν_{max} (see appendix B).

The reduction of the variance obtained by optimal-SNR estimation can be easily calculated. As long as we satisfy the sampling condition, we can recover the signal from its samples. Hence, the quantity $\overline{x^2}$ is preserved for different sampling rates. The variance of noise can be obtained by integrating the noise power spectrum in the frequency band $[-\nu_{max}, \nu_{max}]$. Since the power noise spectrum is constant equal to $\overline{\varepsilon^2}T_s$, it yields

$$\sigma^2_{Opt} = 2\nu_{max}\overline{\varepsilon^2}T_s. \tag{5.21}$$

The SNR is then

$$SNR_{Opt} = \frac{\overline{x^2}}{2\nu_{max}\overline{\varepsilon^2}T_s}. \tag{5.22}$$

The ratio between the reference variance and optimal-SNR variance gives the factor by which the variance is reduced

$$r_{\sigma^2} = \frac{1}{2\nu_{max}T_s}. \tag{5.23}$$

We can now analyse what happens if we use a different sampling rate $T_s^K = KT_s$ with the same total dose and protocol time. Again, as long as the sampling condition is fulfilled, the signal $x(t)$ can be recovered from the samples so that we can concentrate on the changes of the variance. As we saw in the previous section, the noise power distributes along the frequency interval $[-1/(2KT_s), 1/(2KT_s)]$ with a constant value. The number of rotations can be calculated as

$$N_{sc}^K = \frac{T_{tot}}{KT_s} = \frac{N_{sc}}{K}. \tag{5.24}$$

Since the dose is distributed uniformly to all rotations,

$$D_{2\pi}^K = K\frac{D_{tot}}{N_{sc}} = KD_{2\pi} \tag{5.25}$$

so that the variance in the projections is reduced by the same factor $\overline{\varepsilon^2}/K$. The value of the noise power spectrum is then $K\overline{\varepsilon^2}/KT_s = \overline{\varepsilon^2}T_s$ and therefore the integral over the frequency interval

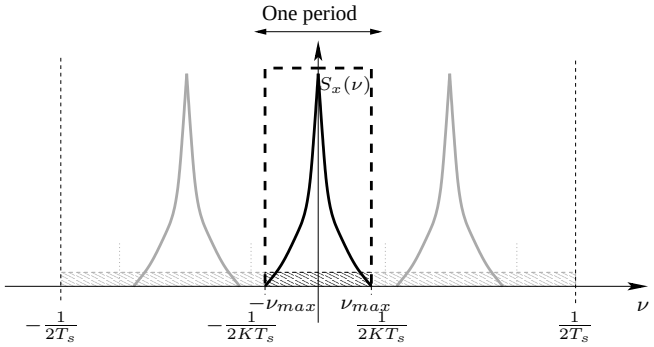

Figure 5.5. Principle of low-pass filtering to obtain an optimal-SNR signal. The ideal low-pass filter adapted to the signal covers the frequency band $[-\nu_{max}, \nu_{max}]$ (black dashed). The shaded area indicates the noise power density. Light shaded indicates masked out noise, whereas dark shaded indicates the noise in the frequency band of the signal.

$[-\nu_{max}, \nu_{max}]$ yields the same variance as in (5.21). Hence, we can conclude that the optimal SNR is independent of the sampling rate as long as the sampling condition is fulfilled.

As we stated in the previous section, the model used for the temporal behaviour of noise can also be applied to noise in partial block backprojections or reconstructed images. The same holds for the frequency characterisation and the dependence of the noise level with the dose (see section 3.2.4.2). Hence, these results can be applied to the dynamic acquisition-reconstruction approaches presented in the previous chapter. We can therefore conclude that

Statement 5.1 *If in a dynamic acquisition process the total dose D_{tot} is uniformly distributed among all scans, the following statements hold for the variance of the optimal-SNR estimation of projection, partial block backprojection or image values:*

- *It depends on the total dose, D_{tot}, and on the maximum frequency of the dynamic process, ν_{max}.*
- *It does not depend on the number of scans performed.*

5.3. Dynamic Reconstruction for Optimal-SNR Perfusion Sequences

In the previous chapter we saw that using an efficient interpolation scheme, dynamic acquisition and reconstruction can be performed either with fewer input data or with higher temporal resolution. We proposed a general approach, the TIA-FDK, which implements this principle using polynomial spline interpolation. We address now the more general problem of dynamic reconstruction in the presence of noise.

In the introduction to the previous section, we provided an example for noise reduction with TIA-TFDK. The idea consists in concentrating the total dose in few scans so that the dose per scan is higher and the projection noise is therefore reduced. In section 5.2, however, we saw that this is just one of the possibilities to attain an optimal SNR in the reconstruction. If the total dose D_{tot} is fixed, the number of scans is not relevant as long as the maximum (temporal) frequency of the output sequence is limited to ν_{max}. If our scanner is fast relative to ν_{max} one

can perform an oversampling and estimate a low-pass continuous signal of bandwidth $2\nu_{max}$ from these samples. But with the algorithms of TIA-FDK approach, we always reconstruct the frequency range $[-1/T_{2\pi}, 1/T_{2\pi}]$ with TIA-TFDK or $[-1/(2T_{2\pi}), 1/(2T_{2\pi})]$ with TIA-CFDK. We therefore propose an extension of the TIA-FDK approaches by substituting the interpolation step by a temporal smoothing.

5.3.1. Optimal-SNR Estimation with Polynomial Splines

Let us consider a signal $f(t)$ as in 5.2.2 which is sampled every T_s, producing the samples $f[k] = f(kT_s)$. This signal consists of a deterministic signal $x(t)$ contaminated with additive noise $\varepsilon(t)$ of zero mean. The process $x(t)$ is assumed to be essentially band-limited with maximum frequency ν_{max}. Our aim is to estimate a continuous function from the noisy samples $f(kT_s)$ which is as close as possible to $x(t)$. The only prior information we have, is its maximum frequency ν_{max}. According to this prior information, the best approximation we can find is obtained by eliminating the frequencies over ν_{max} with an ideal low-pass filter with cut-off frequency ν_{max}. In section 5.2.3 we denoted this procedure as optimal-SNR estimation. As in the case of ideal interpolation, the ideal low-pass filter decays very slowly ($\propto 1/|t|$) which makes it very inefficient for practical purposes. An efficient alternative to ideal low-pass filtering is the smoothing with polynomial splines. The presentation here follows the general lines of [Unser et al., 1993a] and [Unser et al., 1993b]. As in section 4.4.2 we use in this section the time normalised to the sampling interval $t' = t/T_s$.

Smoothing with splines consists in finding a spline function that is smooth and close to the sample values at the sample points. For a given order of the splines, n, the coefficients of the B-spline decomposition (see (4.78)) are found by minimising the functional

$$F\{c, f\} = \sum_{k\in\mathbb{Z}} \left(f[k] - s^n_\lambda[k]\right)^2 + \lambda \left\| D^L s^n_\lambda(t) \right\|^2_{L_2}, \tag{5.26}$$

where $n = 2L-1$, D^L denotes the Lth derivative and $\|\cdot\|_{L_2}$ the L_2 norm. $s^n_\lambda(t)$ denotes the spline function approximating the signal $x(t)$. The first term in (5.26) forces that the estimated function to be close to the samples at the sampling points. The second term is a regularity constraint which favours a smooth estimation of the signal. It is controlled by the smoothing parameter λ. For $\lambda = 0$, $F\{c, f\} = 0$ if $s^n_\lambda[k] = f[k]$, which is the condition for spline interpolation (see section 4.4.2). For large values of the smoothing parameter, the smoothness constraint does not allow the curve to approach the sample values. It can be shown that the coefficients of the nth order polynomial spline that minimise (5.26) can be computed as

$$\hat{C}\left(e^{i2\pi\nu'}\right) = \frac{\hat{F}\left(e^{i2\pi\nu'}\right)}{\hat{B}^n\left(e^{i2\pi\nu'}\right) + \lambda\left(-e^{i2\pi\nu'} + 2 - e^{-i2\pi\nu'}\right)^L}, \tag{5.27}$$

where $\hat{C}(e^{i2\pi\nu'})$, $\hat{F}(e^{i2\pi\nu'})$ and $\hat{B}^n(e^{i2\pi\nu'})$ denote the Fourier transform of the discrete sequences $c[k]$, $f[k]$ and $b^n[k]$ respectively (see section 4.4.2). The Fourier transform of the B-spline repre-

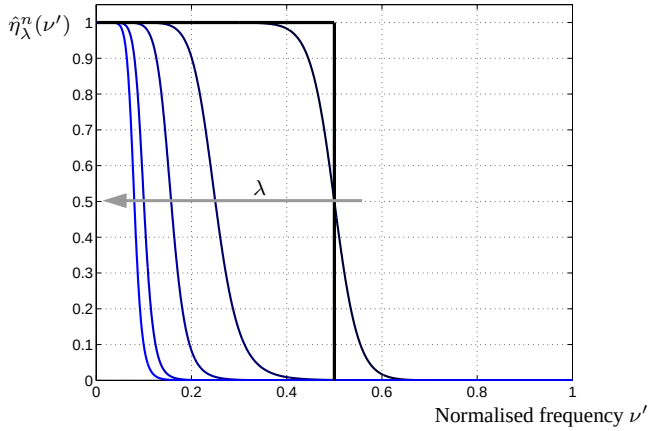

Figure 5.6. Frequency response of the polynomial spline filter $\eta^9_\lambda(t')$ for different values of $\lambda = 0, 0.01, 11.2, 104$ and 971 corresponding to the cut-off frequencies $\nu'_c = 0.5, 0.25, 0.125, 0.1$ and 0.08 respectively. The grey arrow indicates the direction of increasing λ.

sentation is given in (4.83). Substituting the spline coefficients of (5.27) we obtain

$$\begin{aligned} \hat{s}^n_\lambda(\nu') &= \frac{\hat{F}\left(e^{i2\pi\nu'}\right)}{\hat{B}^n\left(e^{i2\pi\nu'}\right) + \lambda\left(-e^{i2\pi\nu'} + 2 - e^{-i2\pi\nu'}\right)^L}\hat{\beta}^n(\nu') \\ &= \hat{F}\left(e^{i2\pi\nu'}\right)\underbrace{\frac{\hat{\beta}^n(\nu')}{\hat{B}^n\left(e^{i2\pi\nu'}\right) + \lambda\left(-e^{i2\pi\nu'} + 2 - e^{-i2\pi\nu'}\right)^L}}_{\hat{\eta}^n_\lambda(\nu')}. \end{aligned} \tag{5.28}$$

This equation is similar to (4.84) and defines the spline low-pass filter $\hat{\eta}^n_\lambda(\nu')$. In the time domain it becomes

$$s^n_\lambda(t') = \sum_{k\in\mathbb{Z}} f[k]\eta^n_\lambda(t'-k). \tag{5.29}$$

Equation (5.29) shows that the smoothing operation can be interpreted as the discrete convolution of the samples of the signal $f[k]$ with a continuous spline low-pass filter $\eta^n_\lambda(t')$. If $\lambda = 0$, $\eta^n_0(t') = \eta^n(t')$ is the spline interpolator of order n described in section 4.4.2. We denote as cut-off frequency the frequency ν'_c at which the frequency response of the filter falls to half of the maximum, i.e. $\hat{\eta}_\lambda(\nu') = 0.5$.

Figure 5.6 shows the frequency responses of spline low-pass filters $\eta^n_\lambda(t')$ for $n = 9$ and different values of λ. By properly choosing these parameters we can obtain good approximations to the ideal low-pass filters used in section 5.2.3. In practice, n is responsible for the sharpness of the edges of the frequency response, i.e. how close the filter is to the ideal low-pass filter (see figure 4.15), and λ for the position of the cut-off frequency (see figure 5.6).

Even if λ is responsible for the position of the cut-off frequency, this dependence is different for different orders n. This is illustrated in figure 5.7. For $\lambda = 0$, $\nu'_c = 0.5$ for all orders. The cut-off frequency decreases slowly for low orders until $\lambda \approx 1$. After this value, the frequency for low orders decreases much faster. For high values of λ the decay is very slow, and therefore large increases in the smoothing parameter provide only a very small reduction of the cut-off frequency.

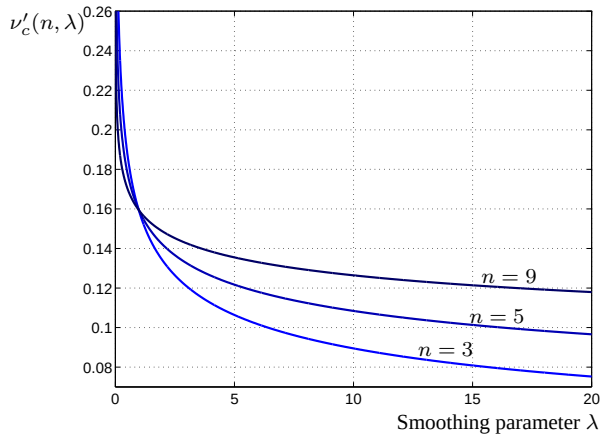

Figure 5.7. Dependence of the cut-off frequency of polynomial spline filters with the smoothing parameter λ for $n = 3, 5$ and 9.

The cut-off frequency as a function of n and λ can be calculated as [Unser and Blu,]

$$\nu_c' = \frac{1}{2\pi}\left(\lambda + \pi^{-n-1}\right)^{\frac{1}{-n-1}}. \tag{5.30}$$

The value of λ can be calculated as

$$\lambda = \left(2\pi\nu_c'\right)^{-n-1} - \pi^{-n-1}. \tag{5.31}$$

For spline interpolation we denoted by p the proportion of the Nyquist band for which the frequency response does not deviate more than 2% from a constant. The value of p depends on the spline order n. Similarly, we denote by q the proportion of the frequency band $[-\nu_c, \nu_c]$ that can be reconstructed with the spline low-pass filter determined by n and λ. In the strict sense, q depends on both n and λ. For practical purposes, however, we may assume that it only depends on n, so that for a given q, the frequency band $[-q\nu_c, q\nu_c]$ can be reproduced. Hence, for a signal with maximum frequency ν_{max}, the cut-off frequency is obtained as

$$\nu_{max} = q\nu_c \quad \Rightarrow \quad \nu_c = \frac{\nu_{max}}{q}, \tag{5.32}$$

where q depends on n. In order to illustrate this, we show in figure 5.8 an example with two perfusion signals from the example in section 5.1.1. The maximum frequency ν_{max} was estimated as the frequency for which 99% of the energy of the perfusion signal is contained in the interval $[-\nu_{max}, \nu_{max}]$. For the filters, we used $n = 9$ and the value of λ was calculated from (5.31) with $q = 0.8$. Note that $\nu_c' = \nu_c$ since $T_s = 1$ s. The estimated signal on the right has still some low frequency oscillations that are apparent after $t = 17$ s. The lower frequency of the signal on the left allows to limit the estimation to a narrower frequency band eliminating more noise.

In section 5.2.3, we provided an estimation of the variance of the filtered sequence. The power spectrum of a filtered stationary process is obtained by integrating the product of the power spectrum of the process with the square of the absolute value of the frequency response of the filter [Barret and Myers, 2004]. Since we used an ideal low-pass filter, the integral from $-\nu_{max}$ to ν_{max}

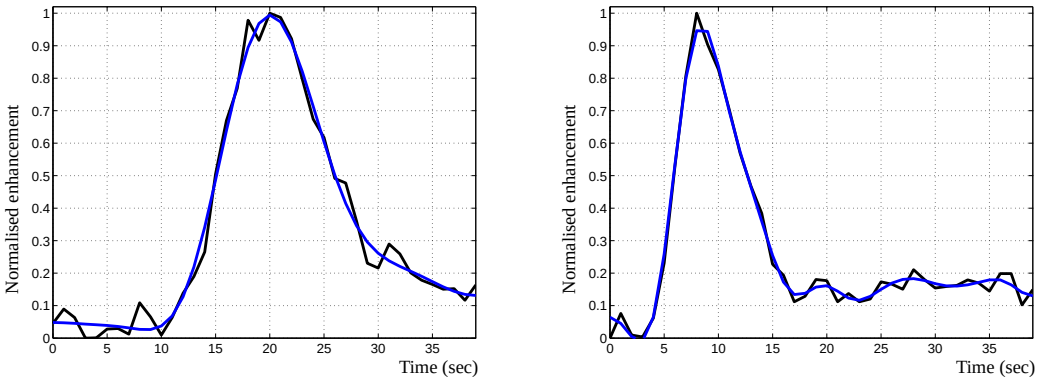

(a) $\nu_{max} = 0.08$ Hz, $n = 9$ and $\lambda = 104$

(b) $\nu_{max} = 0.15$ Hz, $n = 9$ and $\lambda = 0.194$

Figure 5.8. Examples of TACs of the *arteria cerebri anterior* for two data sets (black) and their corresponding optimal-SNR estimated versions (blue). Sampling interval $T_s = 1$ s.

could simply be substituted by $2\nu_{max}$ times the value of the power spectral density. If we use a spline low-pass filter this is no longer true. We now have for (5.21)

$$\sigma^2_{Opt} = \overline{\varepsilon^2} T_s \int_{-\infty}^{+\infty} \left|\hat{\eta}^n_\lambda(\nu')\right|^2 d\nu'. \tag{5.33}$$

The value of the integral depends on n and λ. In figure 5.7, we show the frequency response of $\eta^9_\lambda(t')$ for different values of λ. Qualitatively it is clear that all these filters are very close to an ideal low-pass filter with the corresponding cut-off frequency. Hence, the value of the integral must be close to $2\nu'_c$. In figure 5.9 we show the ratio

$$\frac{\int_{-\infty}^{+\infty} \left|\hat{\eta}^9_\lambda(\nu')\right|^2 d\nu'}{2\nu'_c} \tag{5.34}$$

for values of $\nu'_c \in [0.02, 0.5]$. The values are all between 0.914 and 0.95. We calculate the cut-off frequency as $\nu_c = \nu_{max}/q$ with $q = 0.8$ for $n = 9$. We would like to have a simple rule of thumb to estimate the value of the variance of a sequence filtered with a low-pass spline filter. For this purpose, we propose to use the average value of the curve in figure 5.9, 0.92 as a representative value and then add the factor $0.92/0.8$ to (5.21) as a correction factor for filtering with splines. This yields

$$\sigma^2_{Opt} \approx 2.3\overline{\varepsilon^2} T_s \nu_{max}. \tag{5.35}$$

5.3.2. TSA-FDK Algorithms

We can now formulate the new algorithms as an extension of the TIA-FDK algorithms presented in section 4.4.3. The idea is to substitute the interpolation by a smoothing in the estimation step.

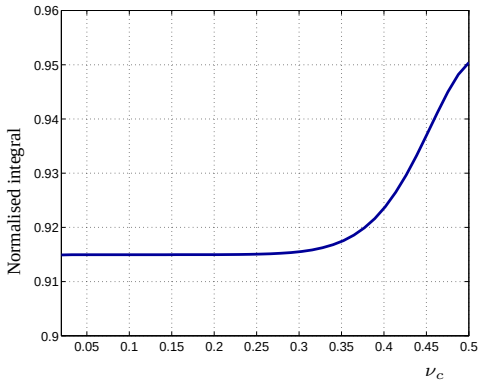

Figure 5.9. Value of $\int |\hat{\eta}^9_\lambda(\nu')|^2 d\nu'$ normalised to $2\nu'_c$.

This way, an optimal-SNR sequence can be obtained independently of the sampling rate used which adds a degree of freedom to the reconstruction algorithm. The algorithms receive therefore the prefix TSA for *temporal smoothing approach*. For the formulation of the algorithms, we assume that the scanning is performed in continuous scanning mode and that the sampling interval is adjusted by adapting the rotation time. As in the TIA-FDK approach, discontinuous scanning with the minimum rotation time is also possible. We discuss this aspect with the choice of the parameters in the next section.

5.3.2.1. TSA-TFDK ALGORITHM

As the TIA-TFDK algorithm, the TSA-TFDK algorithms is based on the T-FDK algorithm presented in section 3.3.3.1. By exploiting the quasi-equivalent rays approximation (see section 3.3.3.4) it reduces the sampling interval to T_π with detriment to image quality for planes $z \neq 0$. The derivation of the algorithm is the same as for TIA-TFDK since the only difference lies in the estimation step. The algorithm is formulated as:

Algorithm 5.1 (TSA-TFDK) *Steps for dynamic reconstruction with TSA-TFDK:*

1st *Reconstruction of N PBBs for $T_{tot}/T_{2\pi}$ rotations with T-FDK:*

$$\begin{aligned} FP_\beta(u,v,t_\beta + kT_{2\pi}) &= \int_{-u_{max}}^{u_{max}} P^b_\beta(s,v,t_\beta + kT_{2\pi}) w_t(s,v) g(u-s) ds \\ PBB_j(\mathbf{x}, t_{\frac{\pi}{N}(2j+1)} + kT_{2\pi}) &= \frac{1}{2} \int_{\frac{2\pi}{N}j}^{\frac{2\pi}{N}(j+1)} FP_\beta(u',v',t_\beta + kT_{2\pi}) d\beta \end{aligned} \tag{5.36}$$

2nd *Combination of the samples of the jth and the $(j+N/2)$th PBBs.*

3rd *Smoothing of PBB values:*

$$\underline{PBB}_j(\mathbf{x},t) = \sum_{k\in\mathbb{Z}} PBB_j(\mathbf{x}, t_{\frac{\pi}{N}(2j+1)} + kT_\pi)\eta_\lambda^n\left(\frac{t - t_{\frac{\pi}{N}(2j+1)} - kT_\pi}{T_\pi}\right) \tag{5.37}$$

4th *Accumulation:*

$$\underline{\mu}^r(\mathbf{x},t) = 2\sum_{j=0}^{N/2-1} PBB_j(\mathbf{x},t) \tag{5.38}$$

The weighting function $w_t(u,v)$ is defined in (4.90) and the expressions for $u' = u'(\mathbf{x},\beta)$ and $v' = v'(\mathbf{x},\beta)$ are given in section 3.3.3.1.

5.3.2.2. TSA-CFDK Algorithm

In a similar way, the TSA-CFDK algorithm is derived from the C-FDK algorithm presented in section 3.3.3.2. The sampling interval is given by the rotation time $T_{2\pi}$. Again, we give here only the algorithm since the derivation is similar as for TIA-TFDK.

Algorithm 5.2 (TSA-CFDK) *Steps for dynamic reconstruction with TSA-CFDK:*

1st *Reconstruction of N PBBs for $T_{tot}/T_{2\pi}$ rotations with C-FDK:*

$$\begin{aligned} FP_\alpha(\gamma,\varphi,t_\alpha + kT_{2\pi}) &= \int_{-\gamma_{max}}^{\gamma_{max}} P_\alpha(\kappa,\varphi,t_\alpha + kT_{2\pi})w_c(\kappa,\varphi)h(\gamma-\kappa)d\kappa \\ PBB_j(\mathbf{x}, t_{\frac{\pi}{N}(2j+1)} + kT_{2\pi}) &= \frac{1}{2}\int_{\frac{2\pi}{N}j}^{\frac{2\pi}{N}(j+1)} \frac{1}{L^2(\mathbf{x},\alpha)} FP_\alpha(\gamma',\varphi',t_\alpha + kT_{2\pi})d\alpha \end{aligned} \tag{5.39}$$

2nd *Smoothing of PBB values:*

$$\underline{PBB}_j(\mathbf{x},t) = \sum_{k\in\mathbb{Z}} PBB_j(\mathbf{x}, t_{\frac{\pi}{N}(2j+1)} + kT_{2\pi})\eta_\lambda^n\left(\frac{t - t_{\frac{\pi}{N}(2j+1)} - kT_{2\pi}}{T_{2\pi}}\right) \tag{5.40}$$

3rd *Accumulation:*

$$\underline{\mu}^r(\mathbf{x},t) = \sum_{j=0}^{N-1} PBB_j(\mathbf{x},t) \tag{5.41}$$

The expression of the weighting function $w_c(\gamma,\varphi)$ is given in (4.101) and the expressions for $\gamma' = \gamma'(\mathbf{x},\alpha)$ and $\varphi' = \varphi'(\mathbf{x},\alpha)$ are given in sections 3.3.3.2 and 3.2.5.2.

5.3.2.3. CHOICE OF THE PARAMETERS

The input parameters for the TSA-FDK algorithms are shown in table 5.1. The last five parameters are computed from the first five. The main difference from table 4.2 is the incorporation of the total dose $D_{2\pi}$ to the input parameters. As parameters to adjust we include now the dose per rotation $D_{2\pi}$ and the smoothing parameter λ.

The choice of the order of the splines n was already discussed in section 5.3.1. According to the value of n, the cut-off frequency of the filter is

$$\nu_c = \frac{\nu_{max}}{q}. \tag{5.42}$$

In order to choose the smoothing parameter λ, we need first to know the sampling rate. If we consider adapting the rotation time of the scanner, we can find a maximum value of the rotation time $T_{2\pi}^{max}$ above which the modified sampling condition (see section 4.4.2) is no longer fulfilled

$$\begin{aligned} &\text{TSA-CFDK}: \quad T_s = T_{2\pi} \quad \Rightarrow \quad T_{2\pi}^{max} = \tfrac{p}{2\nu_{max}} \\ &\text{TSA-TFDK}: \quad T_s = T_{\pi} \quad \Rightarrow \quad T_{2\pi}^{max} = \tfrac{p}{\nu_{max}}. \end{aligned} \tag{5.43}$$

Above this values the For any rotation time $T_{2\pi} \leq T_{2\pi}^{max}$ the sampling condition is fulfilled and we can therefore reconstruct an optimal-SNR sequence. The particular choice depends on the application.

With the computed rotation time, we can now calculate λ using the sampling interval T_s according to the used algorithm. For this purpose, we normalise the cut-off frequency by the sampling frequency $1/T_s$, i.e. $\nu_c' = \nu_c T_s$, and then use

$$\lambda = \left(2\pi\nu_c'\right)^{-n-1} - \pi^{-n-1}. \tag{5.44}$$

The total dose is distributed uniformly among the scans. With a rotation time of $T_{2\pi}$, $N_{sc} = T_{tot}/T_{2\pi}$ rotations will be performed during the protocol time. Hence, the dose per rotation can be calculated as

$$D_{2\pi} = \frac{T_{2\pi}}{T_{tot}} D_{tot}. \tag{5.45}$$

Finally, the number of partial block backprojections in a full-rotation N is calculated as for the TIA-FDK algorithms (see sections 4.4.3.4 and 4.5.4.1).

Note that if $T_{2\pi} = T_{2\pi}^{max}$, then the normalised cut-off frequency is $\nu_c' = 0.5$ and $\lambda = 0$; hence, the TSA-FDK reduces to the TIA-FDK approach. The difference between both approaches is that with TIA-FDK the only possibility of obtaining an optimal-SNR sequence consists in concentrating the dose in few scans, whereas with TSA-FDK an optimal-SNR sequence can be obtained independently of the number of scans as long as the sampling condition is fulfilled.

The noise reduction factor of the algorithms with respect to the standard protocol can be derived from (5.23) by taking into account the correction for spline filtering given in (5.35). As a result we get

$$r_{\sigma^2} = \frac{1}{2.3\nu_{max} T_s^{std}}. \tag{5.46}$$

If we take into account that the sampling interval $T_s^{std} = 1$ (see section 2.3.2), we obtain a simple expression for the reduction of the variance

$$r_{\sigma^2} = \frac{1}{2.3\nu_{max}}. \tag{5.47}$$

Parameter	Meaning
ν_{max}	maximum frequency
D_{tot}	total dose
$T_{2\pi}^{min}$	minimum rotation time
T_{tot}	total acquisition time
T_{fr}	time between reconstructed frames
n	order of the spline interpolation
λ	smoothing parameter
$T_{2\pi}$	rotation time
$D_{2\pi}$	dose per rotation
N	number of PBB intervals in a full-rotation

Table 5.1. Input parameters for the TSA-FDK algorithms. The last five parameters are computed from the first five.

As with the TIA-FDK algorithms, a discontinuous acquisition mode with the minimum rotation time can be used as well (see section 4.4.3.4). In this case, the sampling intervals are $T_s = mT_{2\pi}^{min}/2$ and $T_s = mT_{2\pi}^{min}$ for TSA-TFDK and TSA-CFDK respectively. The sampling rate is adjusted as

$$\begin{aligned} \text{TSA-CFDK}: \quad T_s = \tfrac{q}{2\nu_{max}} \quad &\Rightarrow \quad m = \lfloor \tfrac{q}{2T_{2\pi}^{min}\nu_{max}} \rfloor \\ \text{TSA-TFDK}: \quad T_s = \tfrac{q}{2\nu_{max}} \quad &\Rightarrow \quad m = \lfloor \tfrac{q}{T_{2\pi}^{min}\nu_{max}} \rfloor. \end{aligned} \tag{5.48}$$

The values of λ and $D_{2\pi}$ are calculated as shown above except that the sampling interval is now $T_s = mT_\pi$ or $T_s = mT_{2\pi}$ for TSA-TFDK and TSA-CFDK respectively. Again, the number of intervals N is calculated as in the TIA-FDK algorithms (see section 4.4.3.4).

We finalise this section revisiting the example given in section 4.4.3.4. With a scanner with minimum rotation time $T_{2\pi}^{min} = 0.5$ s we want to reconstruct a sequence of images of a fast process with $\nu_{max} = 1.6$ Hz and a slow process with $\nu_{max} = 0.16$ Hz during $T_{tot} = 40$ s. Using (5.43) for the fast process, we get that the reconstruction is only possible with TSA-TFDK and the rotation time must be set to the minimum value $T_{2\pi} = T_{2\pi}^{max} = T_{2\pi}^{min}$ in continuous mode. In this case, $\lambda = 0$ and therefore TSA-TFDK reduces to TIA-TFDK. Hence, the reconstruction parameters are the same as in table 4.3. For the slow signal, we get a different parameter set for every choice of the sampling rate and of the acquisition mode. In order to illustrate this, we consider the extreme cases of the highest and lowest sampling rates that fulfil the sampling condition, both in continuous and discontinuous acquisition mode. For the lowest sampling rate, we have in continuous scanning mode $T_{2\pi} = T_{2\pi}^{max}$ and in discontinuous scanning mode $T_s = 5T_{2\pi}$. In both cases, $\lambda = 0$ since the signal is not oversampled and therefore the algorithms reduce to the corresponding TIA-FDK approaches. The parameters for this case are given in table 4.4. For the maximum sampling rate the parameters are given in table 5.2. In this case the principle consists in oversampling and smoothing and the highest possible sampling rate in continuous acquisition mode is used, $T_s = T_\pi$ for TSA-TFDK and $T_s = T_{2\pi}$ for TSA-CFDK. The advantage of using the lowest rotation time is that for slow signals the number of partial block backprojections is reduced to 1; hence, the individual frames can be reconstructed using static reconstruction. In such a case, the smoothing reduces to a post-processing. On the other hand, as we have seen, adapting the rotation time reduces the number of scans and consequently

	TSA-CFDK	TSA-TFDK
n	9	9
λ	104	106783
$T_{2\pi}$ (s)	0.5	0.5
T_s (s)	0.5	0.25
N	1	2
Num. rotations	80	80

Table 5.2. Example of reconstruction parameters for $\nu_{max} = 0.16$ Hz with maximum sampling rate.

also the computational cost of the reconstruction.

In this example, we showed the two extreme cases according to the sampling rate. As discussed above, the former is limited by the minimum rotation time of the scanner $T_{2\pi}^{min}$ whereas the later is limited by the maximum frequency of the dynamic process ν_{max}. We also argued that for a given minimum sampling rate, there are several possibilities to adjust the parameters in order to obtain an optimal-SNR sequence. It suffices to choose any sampling rate between the minimum and the maximum and adjust the smoothing parameter correspondingly. The lowest sampling rate has two main advantages. First, fewer data are acquired and thus the computational cost is reduced; second, it allows the use of slow rotating scanners for dynamic CT imaging purposes. On the other hand, for the use of motion correction algorithms it is in general better to have redundancy in the data; hence a higher sampling rate is more appropriate. The final choice depends on the constraints of every particular application.

Finally, an interesting parameter choice for the example above would be to keep the minimum rotation time and adapt the sampling rate by source switching to 1 s. In such case, the TSA-FDK approaches reduce to temporal smoothing of the reconstruction obtained with the standard protocol.

5.3.2.4. DISCUSSION

In this section we discuss some aspects of the dynamic reconstruction algorithms of the TSA-FDK approach. The first one concerns the choice between the algorithms. According to (4.105), the rotation time corresponding to a certain ν_{max} with the T-FDK-based algorithms (meaning both TIA and TSA) is two times longer than for the C-FDK-based algorithms. The amount of rotations acquired during the protocol time $T_{tot}/T_{2\pi}$ will be correspondingly two times lower. An immediate consequence of this would be to think that with the T-FDK-based algorithms two times less dose is applied. This is, however, not true since the T-FDK-based algorithms use short-scan reconstruction whereas the C-FDK-based ones use full-scan. In section 3.2.4 we saw that performing backprojection over a longer angular interval does not contribute new Radon values but averages the existing ones, reducing thus the noise in the reconstruction. The reduction of the variance from short to full-scan reconstruction is estimated in a factor of 2. Acquiring 2 times less rotations would reduce the total dose by a factor of 2 but the variance of the noise would be two times higher since the images are reconstructed in short-scan mode. In section 3.2.4.2 we saw that the variance of the noise is inversely proportional to the dose applied. Hence, in order to compensate the increase of the noise variance we should increase the dose per rotation by the same factor 2, so that at the end no dose reduction would take place. As a conclusion,

the choice of TSA-TFDK has an influence in the computational cost but not on the total dose needed to obtain a certain noise level. Additionally, TSA-TFDK allows for reconstruction for faster dynamic processes or, equivalently, for reconstruction with slower scanners.

Another aspect which requires discussion is the chosen estimation method. In chapter 4 we concluded that the reconstruction of PBBs over several scans can be interpreted as a non-ideal temporal sampling. This interpretation reduces the problem of dynamic reconstruction to the problem of estimating a continuous signal from noisy samples. The algorithms proposed in this chapter are based on the essentially band-limited model for perfusion signals presented in the chapter 4. By limiting the frequency of the estimated continuous signal, the variance of the reconstruction is reduced. This model has several advantages. First, it is very general: it can be applied to the temporal evolution of projections, partial block backprojections or images. Second, it leads to very efficient reconstruction algorithms. As a generalisation of this approach, we tried to substitute the polynomial splines in the estimation by generalised exponential splines. The estimation with generalised exponential splines did not improve the results and was cumbersome to parametrise. A theoretical explanation for can be given for this. Generalised exponential splines are a generalisation of polynomial splines. The functions in the intervals between samples are no longer polynomials but functions in the null-space of a *spline-admissible* operator [Unser and Blu, 2005b]. Smoothing with generalised exponential splines is a quite general method that includes as particular cases Wiener filtering and some types of kriging. From the statistical point of view, these methods are best unbiased linear estimators according to a certain statistical model. The model assumes that the signal is a continuous stationary random process with a known autocorrelation function. Intuitively, this is equivalent to assume that if we took all possible perfusion signals and averaged them we would obtain a constant signal. This is, however, not true since in general the bolus arrives at a certain time during acquisition so that the average signal would have the lowest values at the beginning of the time interval. As a conclusion the underlying model does not apply to perfusion signals. For this reason, we chose polynomial smoothing as the preferred estimation technique.

5.4. Numerical Example

In this section we present an example of optimal-SNR reconstruction with the TSA-TFDK algorithm and compare it to the standard protocol described in section 2.3.2. For the scanner the same parameters as in section 4.5 were used. For the simulations we used phantom E (see appendix C). In this phantom, the inserts follow the temporal law

$$\mu_i(t) = C_i \, (t - p_1)^{p_2} \, e^{-\frac{t-p_1}{p_3}} . \tag{5.49}$$

This curve describes a typical temporal evolution of the concentration of contrast agent as can be found in a large vessel and in some tissues. It is usually denoted in the perfusion CT literature as *gamma variate* and is often fitted to the measured TACs for the computation of physiological parameters [Miles et al., 1997]. The parameters chosen for the curve are given in table C.5. They were chosen so as to obtain a physiologically representative curve. All inserts follow the same law, except for the amplitude. C_i was chosen in such a way that the maximum values of the enhancement are $10, 18, 26, 34, 42$ and 50 HU.

We first simulated acquisition and reconstruction with the standard protocol as described in sections 2.3.2 and 4.2. Hence, $N_{sc} = 40$ scans were simulated with a rotation time of $T_{2\pi} = 0.5$

	Slow scanning	Fast scanning
n	9	9
λ	0	1533
$T_{2\pi}$ (s)	5.33	0.5
T_s (s)	2.66	0.25
N	16	2
Num. rotations	8	80

Table 5.3. Reconstruction parameters for slow and fast scanning reconstruction.

s during 40 s. The source was switched off every second rotation. For the noise parameter, we used a value of 6 which corresponds to a standard deviation in the image of about 6 HU for short-scan reconstruction (see section 4.5.1). In order to set the input parameters for the reconstruction with TSA-TFDK we used for ν_{max} the value estimated in section 5.1.1, i.e. $\nu_{max} \approx 0.15$ Hz. With this value we simulated continuous acquisition and reconstruction with TSA-TFDK with the highest and lowest possible sampling rates. The corresponding parameters are given in table 5.3. The lowest sampling rate implies a slow rotation scanning, in which the signal is not oversampled and therefore $\lambda = 0$. In this case, TSA-TFDK reduced to TIA-TFDK. The highest sampling rate implies a fast rotation scanning such that the signal is strongly oversampled and therefore a high value of λ is needed to adjust the cut-off frequency to ν_{max}. The noise parameter for each simulation was adjusted according to the number of scans in such a way that the total dose is kept constant. We used the principle that increasing the value of the dose per rotation by a factor a decreases the standard deviation by a factor $\sqrt{a}$ (see section 3.2.4.2). With this rule, we obtained the values

$$\begin{aligned} \text{slow scanning:} \quad & 6\sqrt{\tfrac{8}{40}} \approx 2.59 \\ \text{fast scanning:} \quad & 6\sqrt{\tfrac{80}{40}} \approx 8.48. \end{aligned} \tag{5.50}$$

Figures 5.10 a) and b) show a frame of the reconstructed sequence with the standard protocol (left) and with TSA-TFDK with fast scanning (right); the later corresponds to an optimal-SNR sequence. The noise reduction effect can be clearly observed. In figure 5.11, we show the temporal evolution of the mean of the reconstructed attenuation values (ϵ in section 4.5.3) within two inserts: with maximum enhancement 18 HU (top) and 34 HU (bottom) respectively. The black curves represent the phantom value, the grey curves represent the values obtained with the standard protocol and finally the blue curves show the value of the reconstruction with TSA-TFDK fast scanning (left) and slow scanning (right). The curves of the optimal-SNR sequences are clearly smoother than the curves obtained with the standard protocol, but the temporal resolution is preserved. The results with fast and slow scanning are qualitatively similar.

In table 5.4, we show the value of the standard deviation measured within the inserts ($\bar{\sigma}$ in section 4.5.3). As expected, the standard deviation in the TSA-TFDK reconstructions is lower than in the standard protocol sequence. The TSA-TFDK reconstructions exhibit a similar noise level, which is in accordance with statement 5.1. In section 5.3.2.3, we provided an expression to estimate the reduction of the variance by optimal-SNR estimation with respect to the standard protocol. For ν_{max}, the variance is reduced by a factor

$$r_{\sigma^2} \approx \frac{1}{2.3\nu_{max}} = 2.898. \tag{5.51}$$

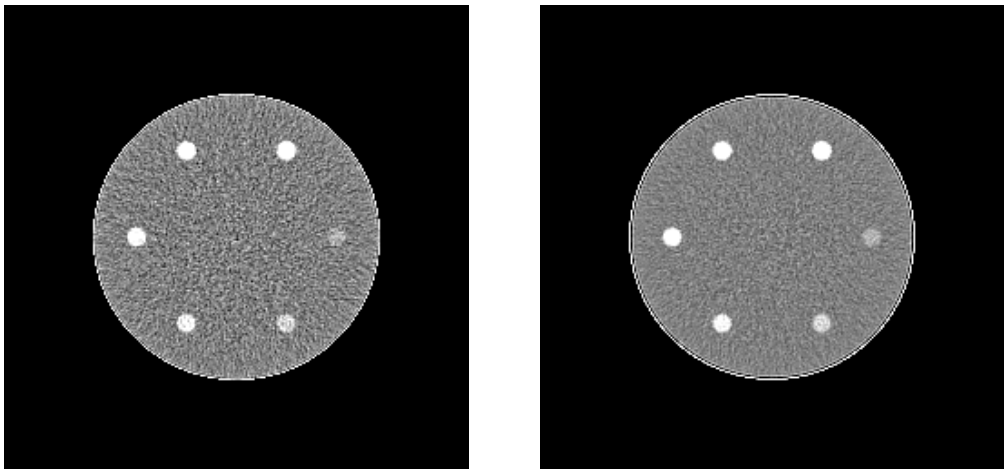

(a) Standard protocol (b) Optimal-SNR

Figure 5.10. Comparison between standard protocol and optimal SNR reconstruction. Left: frame of the sequence reconstructed with the standard protocol. Right: the same frame of the sequence reconstructed with fast scanning with TSA-TFDK. Window $[30, 70]$ HU.

With these values, we can calculate the measured reduction of the variance for, e.g. TIA-CFDK as $4.48/2.62 = 1.71$ and $(1.71)^2 = 2.924$. These results are in accordance with (5.51).

Algorithm	Value
Std. protocol	4.48
TSA-TFDK fast scanning	2.60
TSA-TFDK slow scanning	2.62

Table 5.4. Standard deviation of the values within the inserts for the standard protocol and the TSA approaches.

5.5. Example with Clinical Data

In section 5.3.2.3 we saw that for perfusion signals and fast rotating scanners, the number of partial block backprojections in the dynamic reconstruction with the TSA-FDK approach can be reduced to one without significant loss of accuracy. Hence, the temporal smoothing is performed on reconstructed images becomes a post-processing operation. In this section we show an example of such post-processing with a perfusion CT clinical dataset.

5.5.1. Data and Method

The dataset used consists of a sequence of 40 images obtained with the standard perfusion CT protocol described in section 2.3.2. The protocol parameters are given in table 2.2. The scan was performed with a tube voltage of 120 kVp and at a tube current of 220 mA. Since the rotation

time was $T_{2\pi} = 0.5$ s, the dose per image in mAs was $D_{2\pi} = 110$ mAs. The X-ray beam was collimated to obtain a slice width of 10 mm (see section 3.1.3).

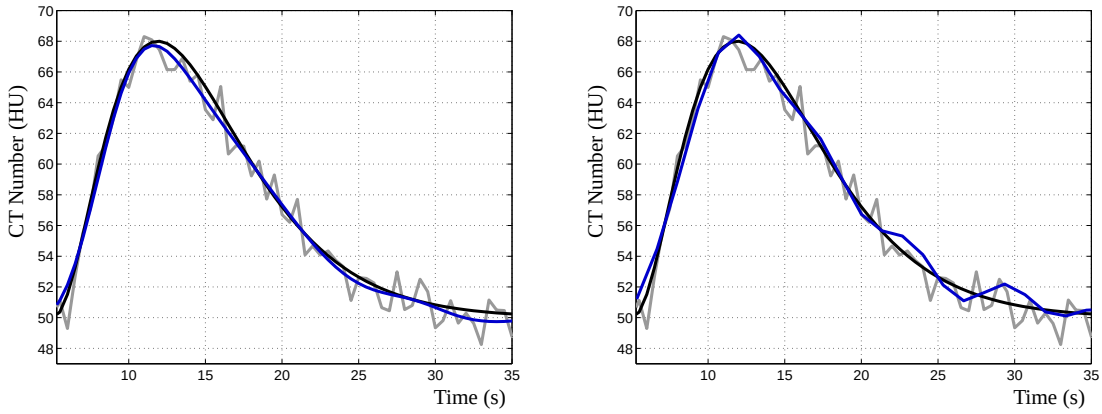

(a) Max. enh.: 18 HU, fast scanning

(b) Max. enh.: 18 HU, slow scanning

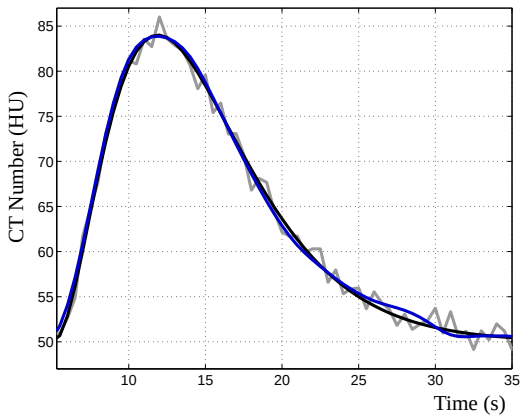

(c) Max. enh.: 34 HU, fast scanning

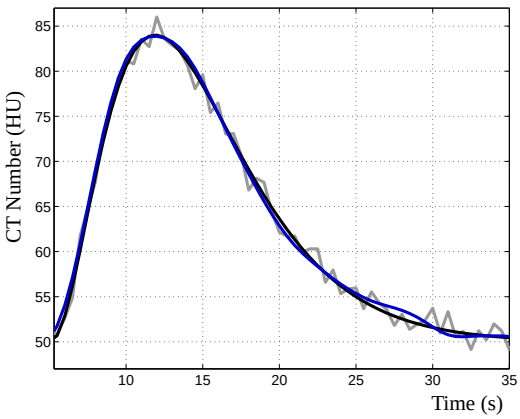

(d) Max. enh.: 34 HU, slow scanning

Figure 5.11. Time-attenuation curves of the inserts with maximum enhancement 18 HU (top) and 34 HU (bottom). Left: fast-scanning, right: slow-scanning.

The advantage of smoothing a reconstructed sequence is that it avoids to use an a priori general estimation of ν_{max} since it can be easily estimated from the sequence itself. As already argued in section 5.1.1, we can use for this purpose an ROI within the *arteria cerebri anterior*. The temporal evolution of the concentration of contrast agent in this arteria can be assumed to be the fastest in the dataset. Additionally, the *arteria cerebri anterior* is approximately orthogonal to the slice plane so that partial volume effects are avoided (see section 3.1.3). With this TAC we estimated ν_{max} as the value for which $[-\nu_{max}, \nu_{max}]$ contains 99% of the energy of the signal. We obtained a value of $\nu_{max} \approx 0.0966$ Hz.

According to the discussion in section 5.3.2.3 one of the possibilities of adjusting the sampling

rate consists in using a discontinuous acquisition mode with the minimum rotation time. In such a case the sampling interval is $T_s = mT_\pi$ for TSA-TFDK and $T_s = mT_{2\pi}$ for TSA-CFDK. The number of angular intervals N is chosen according to (4.117). For our example

$$N \geq 12.8 T_{2\pi}^{min} \nu_{max} = 0.618. \tag{5.52}$$

Therefore, the error due to static full-scan reconstruction of a time dependent object can be neglected. The maximum value of m is calculated according to (5.48):

$$\begin{aligned} &\text{TSA-CFDK}: \quad m = 8 \\ &\text{TSA-TFDK}: \quad m = 16. \end{aligned} \tag{5.53}$$

Hence, we can interpret the clinical dataset as the first step of either the TSA-TFDK or the TSA-CFDK algorithm with $T_s = 2T_{2\pi}$. As we saw earlier in this section, the sampling interval can be increased up to $T_s = 8T_{2\pi}$ while keeping enough temporal resolution for the reconstruction. According to the discussion in section 5.3.2.3, it is possible to reconstruct an optimal-SNR sequence for any choice of $m \leq 8$ if the total dose is kept constant. Since we cannot modify the dose per image, if we downsample the dataset by a factor of K, the total dose applied is reduced by the same factor. Hence, the theoretical estimation for the reduction of the variance given in (5.47) must be divided by the factor K

$$r_{\sigma^2} = \frac{1}{2.3 \nu_{max} K}. \tag{5.54}$$

Sequences of different sampling rates were obtained by removing image frames from the original series. Since $m \leq 8$, we obtained four sequences downsampling by factors $K = 1, 2, 3$ and 4 respectively. For every sequence, a temporal estimation using a spline low-pass filter adapted to ν_{max} was performed. The corresponding parameters for each sequence are given in table 5.5. With the continuous spline low-pass filter, an output sequence with the same number of frames as the original series was calculated. Note that, since no increase of dose was carried out, the only sequence with optimal SNR corresponds to $K = 1$.

5.5.2. Results

In figure 5.12, we show some examples of time-attenuation curves of the original (grey) and the optimal-SNR sequence (blue). The curves show the temporal evolution of the average value of the pixels within a ROI in different tissues. As can be seen, the enhancement curve for the *arteria cerebri anterior* in the optimal-SNR sequence is smooth but can still follow the original curve. The same can be observed for the *sinus sagittalis*. In such large vessels, the enhancement due to contrast agent flow is higher than in tissue or in small vessels, and the SNR is high enough to ignore noise for the purpose of the computation of physiological parameters. In other regions, enhancement is larger than noise but of the same order of magnitude. An example for such regions is shown in curve c) where the TAC of an ROI within a tumour is shown. The TAC of the optimal-SNR estimation clearly eliminates noise and delivers a curve which is physiologically more plausible than the curve obtained with standard reconstruction. Finally, figure d) shows the TAC of a ROI within grey matter. While in the original curve the enhancement cannot really be perceived, the TAC of the optimal-SNR sequence clearly shows an increase in the concentration of contrast agent. On the other hand, the TAC of the optimal-SNR sequence contains low frequency

Sequence	Num. inp. images	$T_s\ (s)$	$\nu_c'\ (Hz)$	n	λ
Seq. 1	40	1	0.121	9	15.82
Seq. 2	20	2	0.241	9	0.0154
Seq. 3	13	3	0.362	9	$2.57e-4$
Seq. 4	10	4	0.483	9	$4.41e-6$

Table 5.5. Input sequence and filter parameters for every sequence.

oscillations which are not of physiological nature. These are due to low-frequency noise in the frequency band $[-\nu_{max}, \nu_{max}]$.

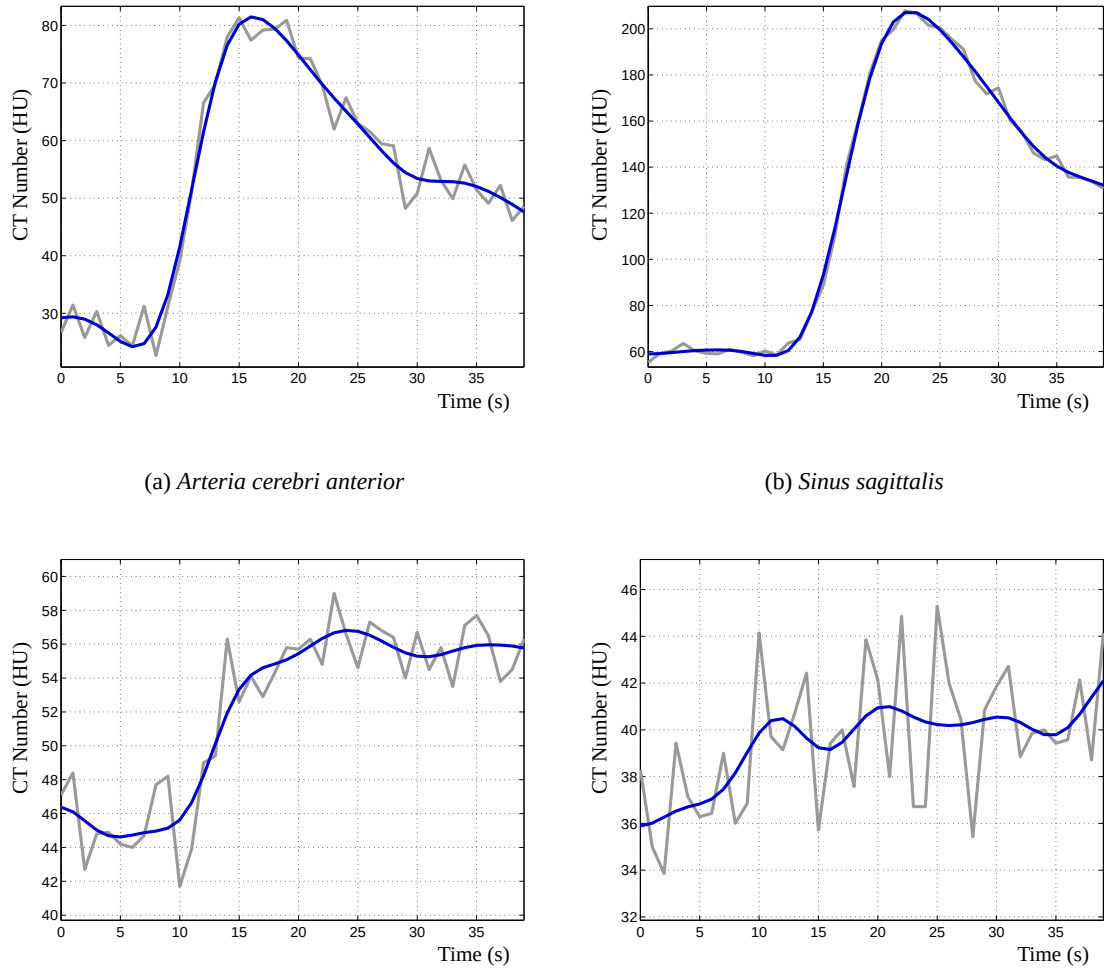

(a) *Arteria cerebri anterior*

(b) *Sinus sagittalis*

(c) Tumour

(d) Grey matter

Figure 5.12. Example of TACs in different tissues. The grey curve corresponds to the original dataset. The blue curve corresponds to the optimal-SNR sequence.

Sequence	Measured	Estimated
1	4.90	4.5
2	2.32	2.25
3	1.54	1.5
4	1.04	1.12

Table 5.6. Sequences and reduction of the variance.

We want now to verify if the reduction of the variance caused by the temporal smoothing is in accordance with the predictions of our model. The variance in a certain region might be due not only to quantum noise but also to pixels in the region of interest that correspond to different tissues and have therefore a different temporal behaviour. Since our model concerns the temporal behaviour of the statistical fluctuations caused by quantum noise, we must segment a region within a tissue where all points have the same temporal behaviour. The easiest way to do this is to choose a region in the image with constant attenuation, i.e. without contrast agent flow. We therefore segmented an ROI within the ventricular system. But not all pixels within the ventricular system are constant over all sequence frames. In some of them, partial volume effects caused by the large slice thickness (see section 3.1.3) induce a temporal dependence. For this reason, we segmented a region within the ventricular system by choosing the pixels with a temporal mean of 6 ± 0.5 HU and a temporal standard deviation < 7 HU. This delivered a set of 2300 pixels with the same temporal behaviour. We used the whole 2300×40 pixels to estimate the variance in each reconstructed sequence. The ratio of the variance of the original sequence to the variance of every one of the post-processed sequences is shown in the first column of table 5.6. The second column shows the values estimated using (5.54). The estimated values match approximately the measured values. According to the proposed model for the temporal behaviour of noise, the reduction of the variance should be inversely proportional to the sampling rate. This is approximatelyin accordance with the values in table 5.6. The effect on image quality is shown in figures 5.13 and 5.14. The frame shown corresponds to $t = 19$ s and lies for sequence 4 between a sample at $t = 16$ s and a sample at $t = 20$ s. The image quality of the frame estimated from the sequence 4 appears to be equivalent to the original frame although four times fewer input data were used for the computation of the sequence. Certainly the noise levels are comparable since the dose per frame was not increased in this experiment. The sequence with strong temporal smoothing presents substantially reduced noise while visually preserving spatial resolution.

The reconstructed sequences were used as input for the Perfusion CT software (Siemens AG, Medical Solutions, Forchheim, Germany) that computes the functional parameter maps. This software first segments vessels and bone, performs a strong spatial smoothing and subsequently computes the functional parameters. The segmented regions are excluded from the functional maps and represented in black. The algorithm returns the lowest value (magenta) if it is not able to compute a functional parameter value. Figure 5.15 shows cerebral blood flow maps computed from the original sequence (a), sequence 4 (b), and sequence 1 (c). Map (a) presents many small isolated segmented regions compared to map (c). These correspond to areas where the noise level led to a wrong classification as vessels. Most of them disappear in map (c). Moreover, the magenta areas are reduced in map (c) compared to map (a) which indicates that the algorithm was able to deliver results on more points. Finally, map (c) is smoother in space which is physiologically

more plausible. The quality of maps (a) and (b) is equivalent although (b) was computed from a sequence reconstructed with four times fewer data (equivalent to four times less dose).

(a) Original (b) Sequence 4 (c) Sequence 1

Figure 5.13. Detail of the left hemisphere in a frame of the perfusion sequence with high contrast enhancement ($t = 19$ s). Left: original sequence. Middle: sequence 4 ($T_s = 4$ s). Right: sequence 1 ($T_s = 1$ s). Window $[16, 56]$ HU.

(a) Original (b) Sequence 4 (c) Sequence 1

Figure 5.14. Detail of the right hemisphere in a frame of the perfusion sequence with high contrast enhancement ($t = 19$ s). Left: original sequence. Middle: sequence 4 ($T_s = 4$ s). Right: sequence 1 ($T_s = 1$ s). Window $[16, 56]$ HU.

5.6. CONCLUSION

Quantum noise is one of the most limiting factors in perfusion CT. The enhancement due to contrast agent flow in tissue is low and often comparable to noise. The reconstruction of a sequence with the standard procedure only allows the reduction of noise by increasing the total dose or concentrating the dose on fewer sequence frames. The former option is not of practical interest since the dose levels applied in perfusion CT are much higher than in normal CT and dose is therefore

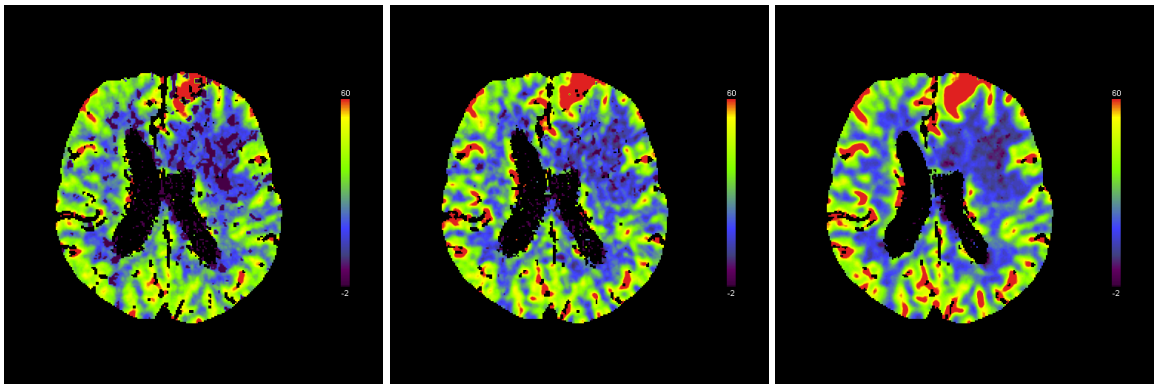

(a) Original (b) Sequence 4 (c) Sequence 1

Figure 5.15. Cerebral blood fbw maps computed from (a) the original sequence, (b) sequence 4 ($T_s = 4$ s) and (c) sequence 1 ($T_s = 1$ s).

a limiting issue. The later option, implies the loss of temporal resolution since the time between frames is increased.

In this chapter, we proposed a new approach for dynamic acquisition and reconstruction which achieves an optimal SNR for a given applied total dose and a maximum frequency of the dynamic process. For this purpose, we introduced a simple model for the temporal behaviour of noise in dynamic CT. According to it, noise can be approximately modelled as a zero mean wide sense stationary random process, and samples of this process at different times are statistically independent. If we have prior information about the dynamic process in form of a maximum frequency ν_{max} we can obtain an optimal SNR continuous estimation from the noisy samples by limiting the frequency range of the estimation to $[-\nu_{max}, \nu_{max}]$. The application of this principle to the estimation of a continuous signal from temporal samples of PBBs leads to the extension of the TIA-FDK approaches based on interpolation to the TSA-FDK approaches based on smoothing. With them it is possible to reconstruct a sequence of image frames with optimal SNR with any sampling rate as long as the sampling condition is fulfilled. The temporal estimation step is performed by smoothing with polynomial splines. As the TIA-FDK approaches, the TSA-FDK approaches are based on the T-FDK and C-FDK static reconstruction algorithms.

With the TSA-TFDK algorithm an optimal-SNR sequence of dynamic process with a maximum frequency of $\nu_{max} = 0.15$ Hz can be reconstructed by scanning with a rotation time of $T_{2\pi} = 5.33$ s. With TSA-CFDK, the maximum rotation time is $T_{2\pi} = 2.66$ s but the algorithm makes less approximations and the reconstruction is more accurate for the planes $z \neq 0$. This opens the possibility of using slow rotating scanners for functional CT imaging purposes. Indeed, as we saw in section 5.1.1, in many cases the maximum frequency ν_{max} is lower than 0.15 Hz and therefore even slower scanners might be used for the reconstruction. The acquisition with a slower rotation produces fewer scans during the protocol time which leads to a reduction of the input data and thus of the computational cost. If the scanner used has a high rotational speed, the reduction of the input data can be achieved by performing the acquisition in discontinuous scanning mode, switching off the source during regular periods of time. On the other hand, for motion correction algorithms, it is better if more data are available. For this reason, with fast scanners often a higher

sampling rate might be preferred as long as computational cost is not a constraining issue.

Finally, for fast scanners we saw that the time dependence of the attenuation coefficient can be neglected and the reconstruction of every frame of the sequence can be performed using static reconstruction methods. In such a case, the sequence can be smoothed a posteriori. The estimation becomes then a post-processing operation. In an example of post-processing with a clinical dataset, we could observe a strong reduction of the noise in the optimal-SNR sequence. The time-attenuation curves obtained were physiologically more plausible than in the original sequence obtained with the standard procedure. However, on tissues where the enhancement due to contrast agent flow is very low and comparable to the noise level, the remaining low-frequency noise was still comparable to the signal itself.

CHAPTER 6.

SOFTWARE TOOLS

This chapter is devoted to the description of the software tools used and developed within the framework of this thesis. We first briefly describe the tools provided by Siemens AG, Medical Solutions for the simulation of X-ray attenuation and noise. Following, we give an overview of the software tools developed and describe the structure of the Matlab code programmed. The kernel of the developed tools is *CT Project*, a C++ library for cone-beam static and dynamic reconstruction. The main focus of the chapter is on the description of this library.

6.1. OVERVIEW

The results presented in this thesis were all obtained by numerical computation. The aim of this chapter is to provide a description of the software tools used for this purpose. The tools used can be coarsely classified in

- X-ray simulation tools.
- Perfusion CT software.
- Reconstruction tools.
- Visualisation and error measurement tools.

The simulation tools and the Perfusion CT software were provided by Siemens AG, Medical Solutions. The rest of the tools was developed during this thesis. The main focus of the chapter is on the description of the *CT Project* C++ library for static and dynamic reconstruction.

The numerical computation of X-ray attenuation maps were performed with the software package *DRASIM (Deterministic Radiological Simulation)* by Karl Stiersdorfer (Siemens AG, Medical Solutions). This software calculates the attenuation of the X-ray beam when passing through an object which is defined in an appropriate scripting language. The computations are performed using X-ray transport equations; neither scattering nor beam-hardening are taken into account (see section 3.2.4). The software computes the logarithm of the normalised attenuation and provides as output projection files in binary format.

The functional maps in chapter 5 were obtained with the Perfusion CT software by Siemens AG, Medical Solutions. This is a commercial software for the computation of functional parameters from perfusion sequences. It implements the slope method described in section 2.3.1.

The simulation of Poisson noise in the computed projections was performed with a software library developed within the framework of the Forbild project [Fuchs, 2006].

The major part of the software tools developed during this thesis are devoted to the implementation of CT reconstruction algorithms from cone-beam projections. These tools were developed in the form of a C++ software library which we called *CT Project*. This library is described in the next section. The C++ code was complemented with a series of Matlab functions with different purposes. These functions can be classified into three groups:

Visualisation and error measurement These tools include a series of Matlab GUIs (Graphical User Interfaces) whose aim is the evaluation of the results obtained with the developed algorithms. They include functions for the visualisation of 2D/3D images, 2D/3D sequences and the quantification of the error by comparing with a reference (if available).

Interface to *CT Project* These functions were designed to convert input data to data formats compatible with the *CT Project* library functions and to convert again the output to the original format. Their aim is to use the *CT Project* library with clinical data in DICOM format [NEMA, 2006].

Splines toolbox This toolbox is a collection of functions for interpolation and smoothing with polynomial, exponential and generalised exponential splines for 1D data on a regular grid [Unser and Blu, 2005b]. The toolbox was developed to test the performance of smoothing with generalised exponential splines to further develop the TSA-FDK approach (see section 5.3.2.4).

Finally, an additional Matlab function performs the rebinning of fan-parallel beam projections from cone-beam projections (see section 3.3.3.1).

6.2. *CT Project* LIBRARY

CT Project is a C++ library for static and dynamic reconstruction from cone-beam projections. It implements all algorithms described in this thesis and is designed to be easily expanded. The library was developed to be fully compatible with the functions of the *Numerical Recipes in C++* library for scientific computing (NR library) [Press et al., 2002]. In this section, we first describe the function modules, with the algorithms and the basic program flow. Subsequently, we describe the class hierarchy of the library and include a short explanation about the aim of each class. As a notational convention we use `CTAsciiInputFile` to denote a class and **`CTAlgInterface`** to denote a module of functions. We use in the description of the library some basic concepts of object oriented programming and particularly of the C++ programming language. We refer to [Eckel, 2000] and [Stroustrup, 1997] for a detailed explanation of these concepts.

6.2.1. FUNCTION MODULES AND PROGRAM FLOW

The functions used for the implementation of reconstruction algorithms or particular tasks within them are distributed in different modules. Each module contains functions with a similar task (different algorithms with the same purpose) or functions that perform a part of an algorithm. The modules are the following:

`CTSplines` This module contains functions for interpolation and smoothing with polynomial splines. It implements the algorithms described in sections 4.4.2 and 5.3.1 and other related tasks.

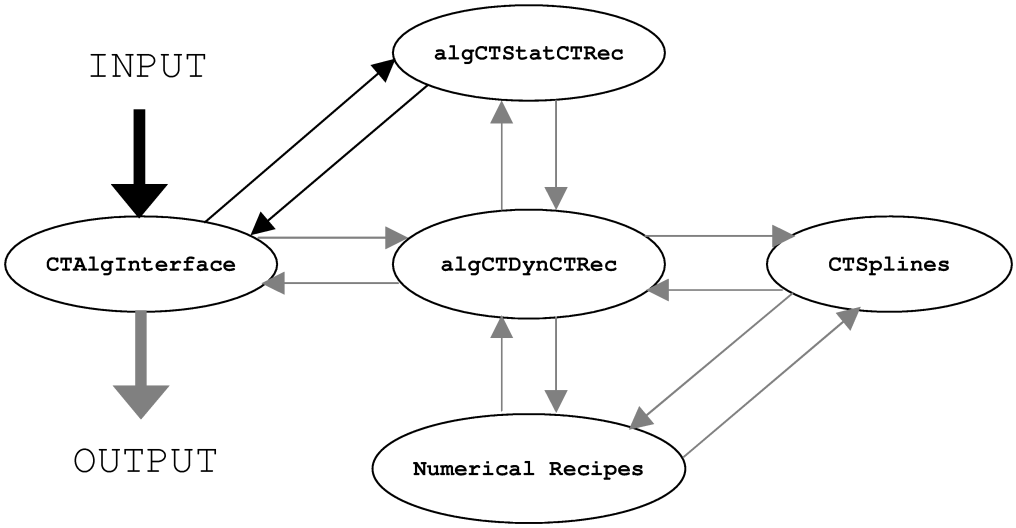

Figure 6.1. Program flows in the *CT Project* library.

`algCTStatCTRec` Contains the implementation of the 3D static reconstruction algorithms for cylindrical detectors, C-FDK and T-FDK, described in section 3.3.3. They can be used as well for PBB reconstruction as needed in some dynamic reconstruction algorithms. The implementation of the algorithms was adapted from the algorithm for planar detectors for C-arm systems proposed in [Wiesent et al., 2000]. It uses projection matrices in homogeneous coordinates in the backprojection step.

`algCTDynCTRec` This module contains dynamic reconstruction algorithms. These include the algorithms developed during this thesis (TIA and TSA-FDK approaches) and the state-of-the-art algorithms described in section 4.2 (standard reconstruction, generalised Parker weighting and $k\pi$-mode linear regression).

`CTAlgInterface` Provides an interface for the functions in the dynamic and static reconstruction modules. The functions that implement the reconstruction algorithms perform the reconstruction and return an object of the class `CTVol` (for static reconstruction) or `CTSeq` (dynamic reconstruction). The interface functions additionally perform the measurement of the computational time and create an output directory where the result and a parameter file are stored.

6.2.1.1. PROGRAM FLOW

In this section we describe the typical program flow of a reconstruction with the *CT Project* library. The program flow is shown in figure 6.1. The reconstruction algorithm is called using an interface function in `CTAlgInterface`. The following input data are needed:

- Dynamic reconstruction parameters (function parameters).

- Static reconstruction parameters (input file).
- Projections (input files).
- Detector-focus tables (input file).

The dynamic reconstruction parameters concern the number of acquired rotations, number of frames per acquired rotation, etc. They are given in the function call. Static reconstruction parameters concern the size of the images, geometry of the detector, etc. They are given in a separated input file. Projections are the result of the simulations of the X-ray attenuation through the object at each projection angle. The projection corresponding to each angular position is stored in a different file in binary format. Finally, the detector-focus table file contains information about the position of the source and the detector for every projection angle. It is generated by the simulation software.

The interface function calls the corresponding static or dynamic reconstruction function. In the case of static reconstruction, a `CTVol` is returned and the interface function writes the result to disk. If the reconstruction is dynamic, the corresponding dynamic reconstruction function calls a static reconstruction function of **`algCTStatCTRec`** for the reconstruction of PBBs or images along several full-rotations. Following, the temporal estimation step is performed. For this purpose, the **`CTSplines`** (for TIA or TSA-FDK approaches) module or the NR library might be required. Some functions of the **`CTSplines`** module need the NR library as well. Finally, the reconstructed sequence is returned to the interface function which writes the result to disk. The possible interactions between the different modules in a static reconstruction are shown with black arrows in figure 6.1. For a dynamic reconstruction they is shown with grey arrows.

6.2.2. Class Hierarchy

Figure 6.2 shows a scheme of the structure of the *CT Project* library. The solid arrows indicate that the classes are related by inheritance. The dashed arrows indicate that they are related by composition, i.e. the class contains member variables which are objects of the upper class. Apart from inheritance and composition, a member function of a class might use objects of another one; this is not indicated in the scheme in figure 6.2 in order not to complicate it unnecessarily. This is for example the case of `CTParamCFDK` and `CTParamTFDK` which are not linked to any other class because they simply use a `CTAsciiInputFile` object in their constructor. In order to make *CT Project* fully compatible with the functions of the *Numerical Recipes in C++* library, its basic classes are derived (inherited) from the basic classes of the NR library. `NRVec`, `NRMat`, `NRMat3d` are container classes for numerical data types, representing 1D vectors, 2D matrices and 3D matrices respectively, with basic operations. The basic classes of the *CT Project* library, `CTVec`, `CTMat` and `CTVol`, are derived from `NRVec`, `NRMat`, `NRMat3d` respectively. Since we only work with real signals, the classes are restricted to double type. The only exception are `CTVecCplx` and `CTSig1DCplx` used for the computation of spline coefficients. With this principle, the derived classes can be directly used with the NR library functions. They preserve the original structure of the original NR classes but are provided with extended capabilites such as I/O interfaces for different binary and ASCII formats, additional operations or print on screen functions. The rest of the classes are either derived from `CTVec`, `CTMat` or `CTVol` or related by composition to them. The only exception to this are `CTAsciiInputFile`, `CTParamCFDK` and `CTParamTFDK` which are used to read parameter files in ASCII format and only contain a

`CTAsciiInputFile` object in their constructor. A description of the class hierarchy is provided in the following.

6.2.2.1. CLASSES

Figure 6.2 shows the class hierarchy of the library. Every class is defined in a separated header file with the prefix ”class” followed by the name of the class itself and with the extension ”.h”. This file contains the declaration and the member functions defined as inline functions. The implementation of the member functions is provided in a separated file named as the header file but with the extension ”.cpp”. In the following, we briefly describe the classes and their tasks.

CLASSES RELATED BY INHERITANCE

`CTVec` A container class for 1D vectors of double type derived from `NRVec` of the NR library. The class contains extended functionalities with respect to `NRVec`. These include: several constructors, extended operators, additional functions for the manipulation of the data and extended I/O capabilities. Vectors are considered as column vectors except when they are multiplied with another vector, where they are automatically treated as row vectors.

`CTMat` A container class for 2D matrices of double type derived from `NRMat` of the NR library and expanded following the same philosophy as with `CTVec`.

`CTVol` A container class for 3D volumes of double type derived from `NRMat3d` of the NR library and expanded following the same philosophy as with `CTVec`.

`CTVecCplx` This class is identical to `CTVec` except for the fact that it contains elements of `complex<double>` type. It is derived directly from `NRVec`.

`CTSig1D` This class is derived from `CTVec` and is used to represent 1D signals of double type. The main differences to `CTVec` is that an object of the class `CTSig1D` has ”signal character”, meaning that operations such as product or division of signals are performed element-wise and that a convolution operation is included. In the `CTVec` class the product is interpreted as a scalar product and division is only possible by a scalar. The product of a signal with a vector is again interpreted as a scalar product.

`CTSig1DCplx` This class is identical to `CTSig1D` except for the fact that it contains elements of `complex<double>` type. It is derived directly from `CTVecCplx`.

`CTSig2D` This class is derived from `CTMat` and is used to represent 2D signals of double type. As in `CTSig1D`, operations as multiplication and division with another signal are defined element-wise and it includes a 2D convolution operation.

`CTProj` This class is designed to be used as projections in FDK-like reconstruction. It is derived from the `CTSig2D` class. Every row of the 2D signal is at the same time a 1D signal, i.e. an object of the class `CTSig1D`. This way, the row-wise convolution in FDK-like reconstruction can be performed by simply calling the corresponding member function of `CTSig1D`. This class is therefore also related by composition to `CTSig1D`.

CLASSES RELATED BY COMPOSITION

`CTDftMat` This class reads the information in the detector-focus table file and stores it in a set of four vectors for each angular position. These vectors describe the position of the source, the position of the centre of the detector and the orientation of the detector coordinate system.

`CTProjMatCFDK` Contains projection matrices in homogeneous coordinates for every angular position. The projection matrices are computed by the constructor of the class from the parameters for static reconstruction stored in a `CTParamCFDK` object and the information about source and detector position stored in a `CTDftMat` object.

`CTProjMatTFDK` Is the same class as `CTProjMatCFDK` but for T-FDK reconstruction parameters. Therefore, it takes the static reconstruction parameters from a `CTParamCFDK` object.

`CTBlocks` This class is used to store the reconstruction of N PBBs over several rotations. Each PBB is a `CTVol` object.

`CTSeq` Represents a sequence of `CTVol`. It is used to store the result of dynamic reconstruction.

OTHERS

`CTParamCFDK` Stores the parameters for static reconstruction with C-FDK. The constructor of the class reads the parameter file and stores the values in member variables.

`CTParamTFDK` The equivalent to `CTParamCFDK` for T-FDK.

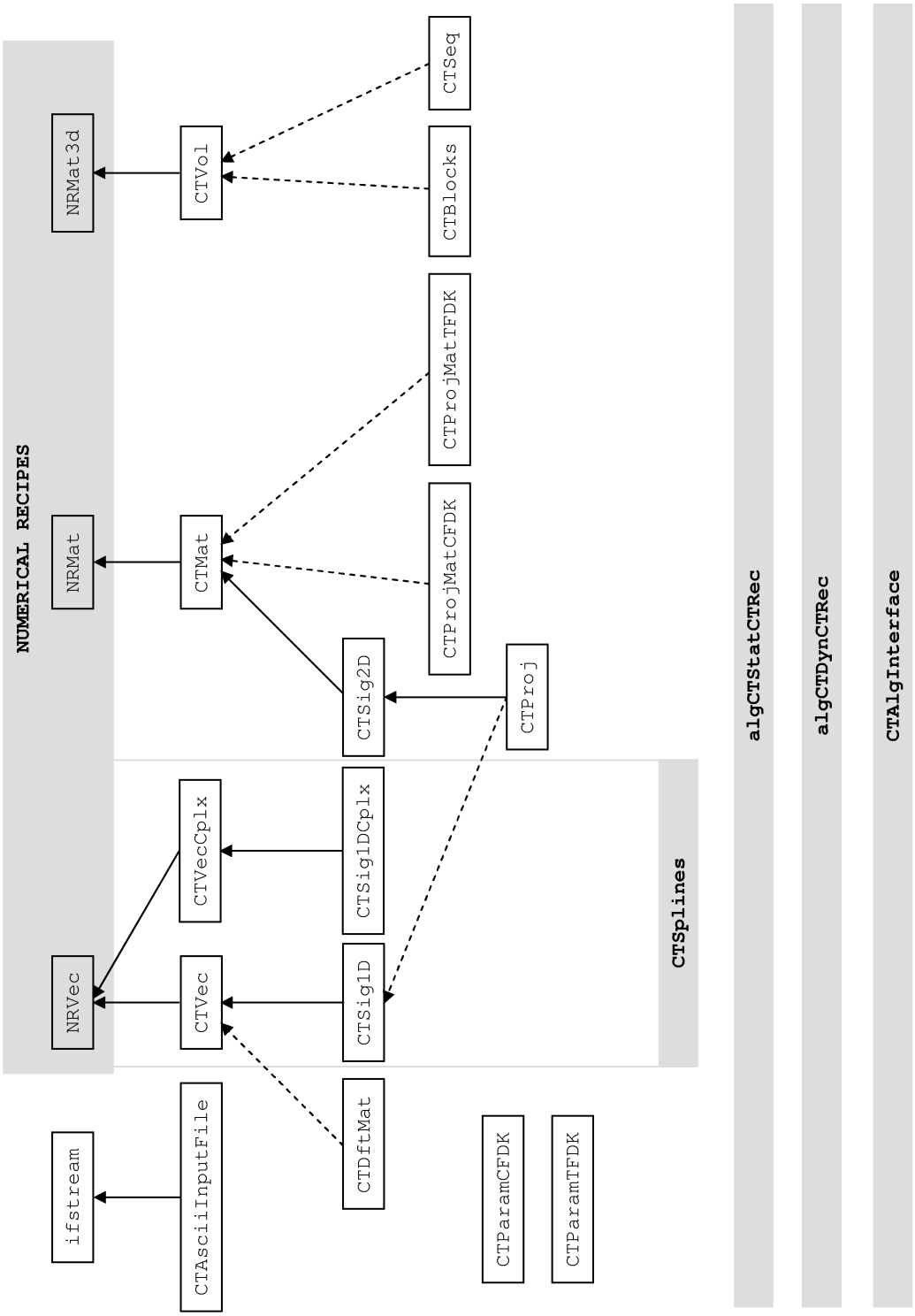

Figure 6.2. Structure of the *CT Project* C++ library.

CHAPTER 7.

CONCLUSION AND OUTLOOK

7.1. CONCLUSION

The introduction of large area detectors in Computed Tomography will enable to perform perfusion studies of a volume of interest. This will on the one hand increase the clinical relevance of perfusion CT but on the other hand it will also increase patient exposure and the requirements for the reconstruction hardware as a consequence of the huge amount of acquired data. Within this context, the aim of this thesis was the development of efficient dynamic reconstruction algorithms for perfusion Computed Tomography.

Under the assumption that no motion or deformation occurs, we showed in a theoretical analysis that the partial reconstruction from projections acquired over several rotations can be interpreted as a non-ideal sampling on a regular grid. The maximum rate of change of the dynamic process ν_{max} that can be reproduced by a dynamic reconstruction algorithm is the Nyquist frequency corresponding to the sampling interval. The dynamic reconstruction can then be performed by estimating a continuous signal from the samples using an efficient interpolation scheme. We proposed a temporal interpolation approach based on polynomial spline interpolation that allows to reproduce 80% of the Nyquist band accurately. This approach increases the temporal resolution for a given sampling rate enabling the use of slow rotating scanners for dynamic imaging purposes. Assuming that we have an estimation of the maximum frequency of the dynamic process, we can adapt the sampling rate according to this frequency in order to acquire only the necessary data to estimate the continuous signal accurately. This leads to a reduction of the acquired data and thus of the computational complexity.

The temporal interpolation approach does not take noise into account. The noise level in the images is inversely proportional to the applied dose. According to our sampling interpretation, we can minimise noise if we limit the maximum frequency of the estimated continuous signal to the frequency range of the fastest perfusion signal in the volume of interest. We denoted this as optimal-SNR estimation. Based on this principle, we substituted interpolation by smoothing with polynomial splines. In the temporal interpolation approach the only way to adapt the temporal frequency range of the reconstruction is by adapting the sampling rate. With the temporal smoothing approach the frequency range of the reconstruction becomes independent of the sampling rate. It includes the temporal interpolation approach as a particular case.

The presented reconstruction algorithms can be adapted to a wide variety of scanners and situations. State-of-the-art CT scanners have high rotational speeds relative to the typical rate of change of perfusion signals. In such a case, either a fine or a coarse sampling can be used. A fine sampling provides an acquired dataset with a lot of redundancy which is appropriate for motion correction algorithms. On the other hand, due to the huge amount of input data it entails a high computational cost. A coarse sampling reduces the input data and the computational cost

but it requires a good estimation of ν_{max} to avoid undersampling. In both cases, an optimal-SNR sequence is obtained. Such a sequence exhibits a reduced variance with respect to a sequence obtained with standard reconstruction. The reduction of the variance with respect to standard reconstruction depends on the maximum frequency of the dynamic process, the reduction factor is in the range 3 to 5.5. This efficient use of the acquired data can be exploited in two ways. If the applied dose is not modified with respect to the standard protocol, the obtained sequences exhibit a lower noise level and therefore the precision in the computation of the functional parameters is increased. If the noise level in the reconstruction is kept as in the standard protocol, less dose needs to be applied.

Additionally to the aspects of reduction of noise and computational complexity, the algorithms proposed in this thesis make it possible to use scanners with rotation times of 5 s or even more for perfusion imaging purposes. This result might find immediate application in prototype scanners with large area detectors. Such detectors generate huge amounts of data which must be transmitted from the detector system to the image reconstruction unit. The high transmission rates force a limitation of the rotation time with the corresponding loss of temporal resolution. An alternative method which has been proposed to increase the volume covered in perfusion CT, consists in shifting a multislice detector on the z-axis between two positions after every rotation. In such a case, the rotation time is fast, but the sampling interval is increased anyway so that standard reconstruction methods are not appropriate. The algorithms presented in this thesis provide solutions for the reconstruction with an optimal noise level in both cases.

7.2. OUTLOOK

As in any research project there is a number of aspects which were not treated and that shall be the object of future research. We discuss here briefly some of them.

On the reconstruction side, one of the aspects concerns the estimation step. We showed in this thesis that the dynamic reconstruction problem can be reduced to static reconstruction plus the estimation of a continuous signal from noisy samples. In this thesis, we proposed to use estimation methods based on the assumption that perfusion signals are essentially band-limited. This has the advantage to be a very general model with high applicability and which leads to computationally efficient algorithms. In a further development, other possible models should be investigated. With an appropriate model it might be possible to further reduce the input data or equivalently to increase the dose efficiency. The second interesting aspect is the further development of the algorithms to use them with C-arm systems. C-arm systems have been successfully used in the last five years for CT imaging purposes. Their mechanical structure allows them a rotation of 220°so that dynamic acquisition is only possible by rotating the C-arm in forward-backward mode. This leads to a non-regular sampling scheme in time. With minimal forward-backward rotation times of about 8 s, the projections are sampled with an average sampling interval of about 4 s. An interesting research topic would be the analysis of the temporal resolution that can be achieved by using a temporal estimation technique for samples on a non-regular grid. Finally, for the sake of completeness the algorithms should be combined with a motion correction algorithm in a unified framework. On the application side, an interesting research topic would be to try to influence the maximum frequency ν_{max} by modifying the injection profile of contrast agent.

APPENDIX A.

ABBREVIATIONS AND NOTATIONAL CONVENTIONS

A.1. ABBREVIATIONS

ART	Algebraic Reconstruction Technique
CBF	Cerebral Blood Flow
CBV	Cerebral Blood Volume
C-FDK	Cylindrical FDK, reconstruction algorithm by Schaller
CT	Computed Tomography
DFT	Discrete Fourier Transform
FBP	Filtered Backprojection
FDK	Static reconstruction algorithm by Feldkamp, Davis and Kress
FIR	Finite Impulse Response
FP	Filtered Projection
HS-FDK	Half-scanning FDK, dynamic reconstruction algorithm by Taguchi
HU	Hounsfield Unit
IIR	Infinite Impulse Response
MRI	Magnetic Resonance Imaging
NHS-FDK	New half-scanning FDK, dynamic reconstruction algorithm by Taguchi
NR	Numerical Recipes
PBB	Partial Block Backprojection
PET	Positron Emission Tomography
ROI	Region Of Interest
SNR	Signal to Noise Ratio
SPECT	Single Photon Emission Computed Tomography
TAC	Time Attenuation Curve
TIA	Temporal Interpolation Approach
TIA-CFDK	Temporal Interpolation Approach for dynamic reconstruction based on C-FDK
TIA-TFDK	Temporal Interpolation Approach for dynamic reconstruction based on T-FDK
T-FDK	Tent FDK, static reconstruction algorithm by Grass, Köhler and Proksa
TSA	Temporal Smoothing Approach
TSA-CFDK	Temporal Smoothing Approach for dynamic reconstruction based on C-FDK
TSA-TFDK	Temporal Smoothing Approach for dynamic reconstruction based on T-FDK

A.2. NOTATIONAL CONVENTIONS

The following notational conventions are used in the text:

- The spatial coordinates are denoted by $\mathbf{x} \in \mathbb{R}^3$ where $\mathbf{x} = (x, y, z)$.
- The temporal variable is denoted by $t \in \mathbb{R}$. A particular time instant is denoted with a subindex, e.g. t_x. If x is an angle, t_x indicates the time at which the X-ray source is at position x, i.e. $t_x = x/\omega$, where ω denotes the rotational speed of the X-ray source.
- The length or duration of a time interval is denoted by $T \in \mathbb{R}$. The duration of a particular time interval is denoted with a subindex, i.e. T_x. If x is an angle, T_x is the time the source takes to run through an angular interval of length x, i.e. $T_x = x/\omega$, where ω denotes the rotational speed of the X-ray source. Here is a list of the most used time interval lengths in the text:

T_s	sampling interval
T_{tot}	total scan time
$T_{2\pi}$	rotation time
$T_{2\pi}^{min}$	minimum rotation time

- The temporal frequency is denoted by $\nu \in \mathbb{R}$ whereas the spatial frequency is denoted by $\varsigma \in \mathbb{R}$.
- Functions are denoted by $f(t)$ meaning $f : t \rightarrow f(t)$. We use indistinctly $f(t)$ to denote a function value or the function itself.
- Continuous signals (meaning non-discrete) in time are represented as $f(t)$.
- For discrete signals (or sequences) we use the square bracket convention from the signal processing literature [Oppenheim and Schafer, 1998], e.g. $f[k]$. Again, $f[k]$ is used to denote a sequence value or the sequence itself.
- Discrete signals are usually the result of sampling a continuous signals with a sampling interval T_s, i.e. $f[k] = f(kT_s)$. For signals which are discrete in only one variable, we use parenthesis. As an example, $f(x, k)$ denotes a sequence of signals continuous in space and discrete in time. This can be again represented as a sampled continuous function, $f(x, k) = f(x, kT_s)$.
- The time normalised by the sampling interval T_s is denoted by $t' = t/T_s$.
- The temporal frequency normalised by the sampling frequency is denoted by $\nu' = \nu/\nu_s = \nu T_s$.
- The Fourier transform of a continuous signal $f(t)$ is denoted as $\hat{f}(\nu)$. The Fourier transform of one variable of a function depending on two or more variables $\mu(\mathbf{x}, t)$ is written as $\hat{\mu}(\mathbf{x}, \nu)$.
- The Fourier transform of a discrete signal $f[k]$ is denoted as $\hat{F}(e^{i2\pi\nu'})$. If the signal comes from the sampling of a continuous signal and the sampling interval is known $f[k] = f(kT_s)$, the Fourier transform might be equivalently written as $\hat{F}(e^{i2\pi\nu T_s})$.

- The average value of a continuous or discrete function f over a period time is denoted as $\bar{f}$.
- The continuous temporal estimation of a signal from a set of samples is indicated by $\underline{f}$.
- The expected value of a random variable x is denoted by $E[x]$.
- The estimation of the spatial distribution of the attenuation coefficient $\mu(\mathbf{x})$ with a CT reconstruction algorithm is denoted by $\mu^r(\mathbf{x})$.
- The estimation of the time dependent spatial distribution of the attenuation coefficient $\mu(\mathbf{x}, t)$ with a dynamic CT reconstruction algorithm is denoted by $\underline{\mu}^r(\mathbf{x}, t)$.

APPENDIX B.

SIGNAL PROCESSING PRINCIPLES

The purpose of this appendix is to provide a short description of some signal processing tools used in the text.

B.1. CONTINUOUS AND DISCRETE SIGNALS

We interpret discrete signals (sequences) as the result of evaluating a continuous function at regularly distributed sampling points. In order to formulate this mathematically we make use of the following property of the Delta function

$$\int f(t)\delta(t)dt = f(0)\int \delta(t)dt. \tag{B.1}$$

In order to simplify notation, we leave the integral and write

$$f(t)\delta(t) = f(0)\delta(t) \tag{B.2}$$

or simply $f(0)$. In order for (B.1) to make sense, we have to impose some constraints on the function $f(t)$. It is sufficient to assume that it is piece-wise continuous and that it has a finite number of bounded discontinuities or jumps. Without loss of generality for our purposes, we assume that at any point t, the function fulfils

$$f(t) = \frac{f(t^+) + f(t^-)}{2}. \tag{B.3}$$

In such a case, (B.2) makes sense even at a point t_0 where $f(t)$ is discontinuous, since

$$f(t)\delta(t-t_0) = \frac{f(t_0^+) + f(t_0^-)}{2}\delta(t-t_0). \tag{B.4}$$

With these conventions, we can now interpret the sequence $f[k]$ as values of $f(t)$ taken every T_s, i.e. $f[k] = f(kT_s)$. The values $f(kT_s)$ are interpreted in the sense of (B.1)

$$f(t)\delta(t-kT_s) = f(kT_s)\delta(t-kT_s). \tag{B.5}$$

We can therefore express the sequence $f[k]$ as

$$f[k] = f(kT_s) = f(t)\sum_{k\in\mathbb{Z}} \delta\left(t-kT_s\right). \tag{B.6}$$

The functional $\sum_{k\in\mathbb{Z}} \delta(t - kT_s)$ is usually denoted in the signal processing literature as Delta comb. Other names as Dirac comb or Shah functional are common as well.

The Fourier transform of a signal $f(t)$ is defined as

$$\hat{f}(\nu) = \int_{-\infty}^{+\infty} f(t)e^{-i2\pi\nu t}dt. \tag{B.7}$$

Its inverse is

$$f(t) = \int_{-\infty}^{+\infty} \hat{f}(\nu)e^{i2\pi\nu t}d\nu. \tag{B.8}$$

In principle, the Fourier transform is defined for absolutely integrable functions. The validity of expressions (B.7) and (B.8), however, can be generalised to expressions of the kind of (B.6) [Mallat, 1998].

In order to define a Fourier transform for discrete signals, we use the following result known as Poisson formula

$$\sum_{k\in\mathbb{Z}} e^{-i2\pi\nu kT_s} = \frac{1}{T_s}\sum_{k\in\mathbb{Z}} \delta\left(\nu - \frac{k}{T_s}\right). \tag{B.9}$$

This equality holds in the sense of distribution equalities [Mallat, 1998]. Based on (B.9) it is easy to derive the following Fourier transform pair

$$\sum_{k\in\mathbb{Z}} \delta\left(t - kT_s\right) \overset{FT}{\longleftrightarrow} \frac{1}{T_s}\sum_{k\in\mathbb{Z}} \delta\left(\nu - \frac{k}{T_s}\right). \tag{B.10}$$

The representation of a discrete signal as the product of a continuous signal with a Delta comb (B.6) is exploited to define the Fourier transform of a sequence. Substituting (B.6) in (B.7) yields

$$\hat{F}\left(e^{i2\pi\nu T_s}\right) = \sum_{k\in\mathbb{Z}} f(kT_s)e^{-i2\pi\nu kT_s}. \tag{B.11}$$

The notation $(e^{i2\pi\nu T_s})$ indicates that it is a periodic function with period $1/T_s$. Since the notation $f[k]$ does not provide any information about the sampling interval T_s, often a normalised frequency is used $\nu' = \nu T_s$. In this case the Fourier transform is

$$\hat{F}\left(e^{i2\pi\nu'}\right) = \sum_{k\in\mathbb{Z}} f[k]e^{-i2\pi\nu' k}. \tag{B.12}$$

The Fourier transform of the convolution of two continuous signals is

$$f * g(t) = \int_{-\infty}^{+\infty} f(\tau)g(t-\tau)d\tau \overset{FT}{\longleftrightarrow} \hat{f}(\nu)\hat{g}(\nu). \tag{B.13}$$

Using (B.12) and (B.6), this result can easily be generalised to the convolution of discrete signals

$$f * g[k] = \sum_{n\in\mathbb{Z}} f[n]g[k-n] \overset{FT}{\longleftrightarrow} \hat{F}\left(e^{i2\pi\nu'}\right)\hat{G}\left(e^{i2\pi\nu'}\right) \tag{B.14}$$

and to the convolution of a discrete signal with a continuous signal

$$f * g(t) = \sum_{k\in\mathbb{Z}} f[k]g(t-k) \overset{FT}{\longleftrightarrow} \hat{F}\left(e^{i2\pi\nu'}\right)\hat{g}(\nu). \tag{B.15}$$

B.2. BASIC FUNCTIONS

Some basic functions which are frequently used in the text:

Rectangular pulse Also known in the literature as indicator function

$$\text{rect}(t) = \begin{cases} 1 & \text{for} \quad -\frac{1}{2} < t < \frac{1}{2} \\ \frac{1}{2} & \text{for} \quad |t| = \frac{1}{2} \\ 0 & \text{otherwise} \end{cases} \tag{B.16}$$

Sinc function We use here the normalised version which is typically used in the signal processing literature [Bracewell, 1978]

$$\text{sinc}(t) = \frac{\sin(\pi t)}{\pi t} \tag{B.17}$$

These two functions form a Fourier transform pair

$$\text{rect}(t) \overset{FT}{\longleftrightarrow} \text{sinc}(\nu). \tag{B.18}$$

B.3. SAMPLING AND INTERPOLATION

With ideal regular sampling we get, given a continuous function $f(t)$, a sequence of values of the function every T_s. T_s denotes the sampling interval. The term ideal means that the values obtained correspond exactly to $f(kT_s)$ while the term regular indicates that the sampling interval is constant. In section B.1, we showed that ideal sampling can be represented by a weighted sum of Delta functions. In this section, we exploit this representation to illustrate the process of recovering the original continuous function from its samples.

For this purpose, we reinterpret the Fourier transform of a sequence using the Fourier transform of a Delta comb. If we consider (B.6) and (B.10), we can express the Fourier transform of a discrete signal as

$$\hat{F}\left(e^{i2\pi\nu T_s}\right) = \frac{1}{T_s}\hat{f} * \sum_{k\in\mathbb{Z}} \delta\left(\nu - \frac{k}{T_s}\right) = \frac{1}{T_s}\sum_{k\in\mathbb{Z}} \hat{f}\left(\nu - \frac{k}{T_s}\right). \tag{B.19}$$

Hence, the Fourier transform of a sampled signal is a periodic signal obtained by summing shifted versions of $\hat{f}(\nu)$ every $1/T_s$. The quantity $1/T_s$ is denoted as sampling frequency or sampling rate. This is illustrated in figure B.1. In order to recover the continuous signal from the samples, we must eliminate the repetitions of the spectrum by filtering. For this purpose the signal and the sampling rate must fulfil two conditions:

- The Fourier transform of the signal has a compact support, i.e. if $\hat{f}(\nu) = 0$ for $|\nu| > \nu_{max}$. The signal is then said to be band-limited with a maximum frequency ν_{max}.
- The sampling rate must be high enough for the spectra not to overlap. From figure B.1 a), we can easily discern that this happens for

  $$\nu_{max} < \frac{1}{2T_s}. \tag{B.20}$$

  This condition is known as the sampling condition or the Nyquist condition. The frequency $1/(2T_s)$ is often referred to as the Nyquist frequency $\nu_{Nyq} = 1/(2T_s)$.

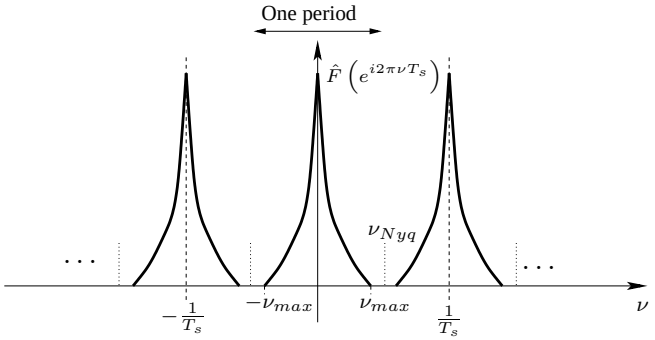

(a) Sampling

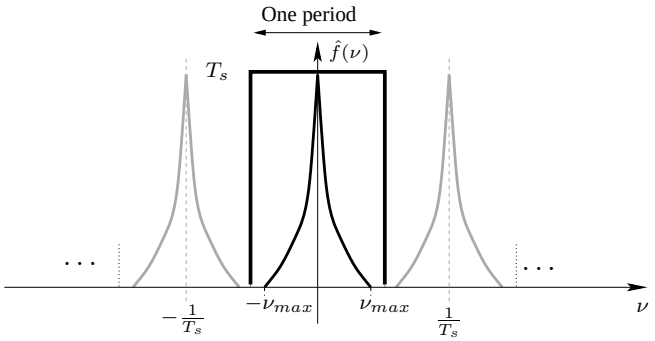

(b) Ideal interpolation

Figure B.1. Sampling and ideal interpolation in Fourier domain.

Figure B.1 b) shows the corresponding filter to recover the original function. Note that the Fourier transform of the filter is not periodic so that the filter is a continuous signal. We denote this filter as $\psi(t)$, its Fourier transform is

$$\hat{\psi}(\nu) = T_s \text{rect}(\nu T_s), \tag{B.21}$$

and in time domain

$$\psi(t) = \text{sinc}\left(\frac{t}{T_s}\right). \tag{B.22}$$

This filter is known as the ideal interpolator. The original signal is then obtained by multiplying $\hat{F}(e^{i2\pi\nu T_s})$ and $\hat{\psi}(\nu)$, or in time domain (using (B.15))

$$f(t) = \sum_{k \in Z} f(kT_s) \text{sinc}\left(\frac{t - kT_s}{T_s}\right). \tag{B.23}$$

If the maximum frequency of the signal ν_{max} is lower than the Nyquist frequency, the signal can be recovered with any filter of the form

$$\hat{\psi}_c(\nu) = T_s \text{rect}\left(\frac{\nu}{2\nu_c}\right) \quad \text{for} \quad \nu_{max} < \nu_c \leq \nu_{Nyq}. \tag{B.24}$$

This is a filter which is constant equal to $1/T_s$ in the frequency band $]-\nu_c, \nu_c[$. We denote such filter as ideal low-pass filter.

B.4. SCHWARTZ SPACE

The Schwartz space $\mathscr{S}(\mathbb{R}^n)$ is the space of smooth and rapidly decreasing functions. It is defined as [Natterer, 1986]

$$\mathscr{S}(\mathbb{R}^n) = \left\{ f \in C^\infty | \sup_{\mathbf{x}\in\mathbb{R}^n} \|f\|_{\alpha,\beta} < \infty \quad \forall \alpha, \beta \right\}, \tag{B.25}$$

where

$$\|f\|_{\alpha,\beta} = \|\mathbf{x}^\alpha D^\beta f\|_\infty \tag{B.26}$$

$\|\cdot\|_\infty$ is the supremum norm and α and β are multi-indices. The functions $f \in \mathscr{S}$ are denoted as Schwartz functions. Other names can be found in the literature such as particularly well-behaved functions [Bracewell, 1978] or good functions [Barret and Myers, 2004].

APPENDIX C.

PHANTOM DEFINITIONS

C.1. HEAD PHANTOM

The head phantom used in the simulations is a simplified version of the head phantom described in [Lauristch and Bruder, 2006]. The phantom imitates a head and consists of an ellipsoid of bone (800 HU) filled with soft tissue (50 HU). Several inserts distributed in the interior of the ellipsoid represent different parts of the anatomy. The external ellipsoid representing the skull has the following dimensions:

- x-axis: 19.2 cm.
- y-axis: 24 cm.
- z-axis: 25 cm.

Figure C.1 shows a 3D visualisation of the phantom obtained by surface rendering with MATLAB. Figure C.2 shows the central slice of the phantom ($z = 0$). The attenuation values of the inserts are given in table C.1.

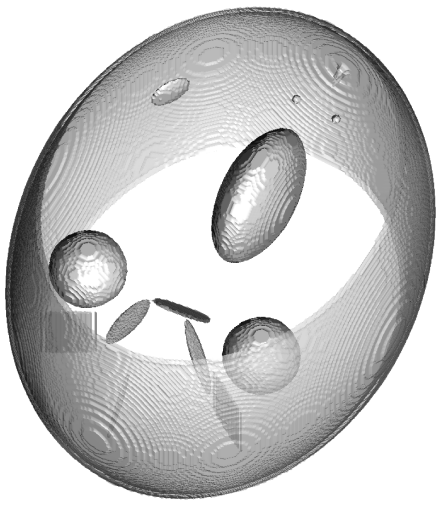

Figure C.1. 3D visualisation of the head phantom.

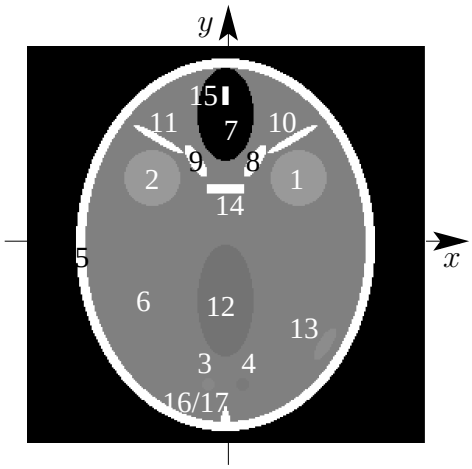

Figure C.2. Central slice ($z = 0$) of the head phantom. Window $[0, 100]$ HU.

Label	Geometry	CT-Number	Anatomical relation
1	sphere	60	eye
2	sphere	60	eye
3	sphere	52.5	
4	sphere	47.5	
5	ellipsoid	800	calotte
6	ellipsoid	50	homogeneous brain matter
7	ellipsoid	-1000	frontal sinus
8	ellipsoid	800	bone surrounding frontal sinus
9	ellipsoid	800	bone surrounding frontal sinus
10	elliptical cylinder	800	bone surrounding frontal sinus
11	elliptical cylinder	800	bone surrounding frontal sinus
12	ellipsoid	45	ventricle
13	ellipsoid	55	subdural hematoma
14	elliptical cylinder	800	bone surrounding frontal sinus
15	elliptical cylinder	800	bone surrounding frontal sinus
16	cone	800	internal occipital protuberance
17	cone	800	internal occipital protuberance

Table C.1. Attenuation values for the inserts in the head phantom. From [Lauristch and Bruder, 2006].

C.2. TIME-DEPENDENT PHANTOMS

In this section we describe a series of dynamic phantoms used for the numerical simulations in chapter 4. They all consist of a cylinder of 50 HU with cylindrical inserts of a much smaller radius. The attenuation value within each insert $\mu_i(t)$ depends on time according to the following sinusoidal law

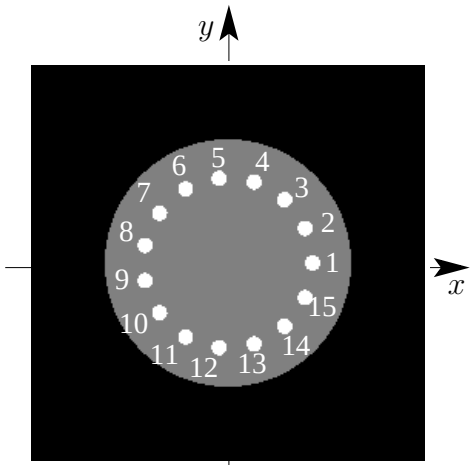

Figure C.3. A slice of phantom A. Window $[0, 100]$ HU.

$$\mu_i(t) = 50(1 + \sin(2\pi\nu_i t)) \text{ HU}. \tag{C.1}$$

The values of the frequencies ν_i are different for each phantom.

C.2.1. PHANTOM A

The purpose of this phantom is to produce a plot of the temporal resolution of a dynamic reconstruction algorithm. The phantom consists of a cylinder of 50 HU with 15 cylindrical inserts situated at the same distance from the origin. It is shown in figure C.3. The cylindrical inserts follow an attenuation law with increasing frequency. The highest frequency corresponds to the upper bound of the temporal resolution limited by the acquisition scheme (see section 4.3.1). The frequencies of the inserts are linearly distributed on the frequency interval $[1, 1/T_{2\pi}]$. The phantom geometry is determined by the phantom radius R_P, the radius of the inserts R_I and the distance from the origin to the centre of the inserts R_C. These are respectively

- $R_P = 8$ cm.
- $R_I = 0.5$ cm.
- $R_C = 5.5$ cm.

The position of the inserts corresponds to points at equiangular intervals on a circle of radius R_C. It is calculated as follows

$$\begin{cases} x_i &= R_C \cos(\theta_i) \\ y_i &= R_C \sin(\theta_i) \end{cases} \quad \text{with} \quad \theta_i = (i-1)\frac{2\pi}{15} \quad \text{for} \quad i = 1 \ldots 15. \tag{C.2}$$

The frequencies of the inserts are given in table C.2.

Label	Frequency (ν_i) $\times \frac{1}{T_\pi}$	Label	Frequency (ν_i) $\times \frac{1}{T_{2\pi}}$
1	0.068	9	0.6
2	0.134	10	0.668
3	0.2	11	0.734
4	0.268	12	0.8
5	0.334	13	0.868
6	0.4	14	0.934
7	0.468	15	1
8	0.534		

Table C.2. Frequencies for the inserts in phantom A.

C.2.2. PHANTOM B

This phantom is used to illustrate the effect of the dynamic rebinning approximation (see section 4.3.3). It consists of a cylinder of 50 HU with 10 cylindrical inserts situated at increasing distances from the origin. It is shown in figure C.4. All inserts follow the sinusoidal law described by (C.1) with the highest frequency that can be reproduced with TIA-TFDK, i.e. $0.8/(2T_\pi)$. The phantom geometry is determined by the phantom radius R_P the radius of the inserts, R_I and the distance from the origin to the centre of the inserts R_C. These are respectively

- $R_P = 10$ cm.
- $R_I = 0.5$ cm.
- R_C: $\|\mathbf{x_i}\|$.

The position of the inserts corresponds to points at equiangular intervals on a spiral. It is calculated as follows

$$\begin{cases} x_i &= \theta_i \frac{4.125}{2\pi} \cos(\theta_i) \\ y_i &= \theta_i \frac{4.125}{2\pi} \sin(\theta_i) \end{cases} \quad \text{with} \quad \theta_i = i\frac{2\pi}{15} \quad \text{for} \quad i = 0 \ldots 15. \tag{C.3}$$

In the phantom, the values $i = 1 \ldots 5$ are skipped. Table C.3 shows the values of the distances for each insert. In section 4.3.3, we saw that the decisive parameter is the distance normalised to the source detector distance Γ. In the second column, we give this normalised distance with the value used in the simulations of chapter 4, i.e. $\Gamma = 57$ cm.

C.2.3. PHANTOM C

Phantom C is a reduced version of phantom A. Its purpose is to provide error measurements for different frequencies without direct influence of the closest inserts. For this reason, the distance between inserts is increased so that error caused by an insert does not directly affect its neighbours. The phantom consists of a cylinder of 50 HU with 6 cylindrical inserts situated at the same distance from the origin. It is shown in figure C.5. The phantom geometry is determined by the phantom radius R_P, the radius of the inserts, R_I and the distance from the origin to the centre of the inserts R_C. These are respectively

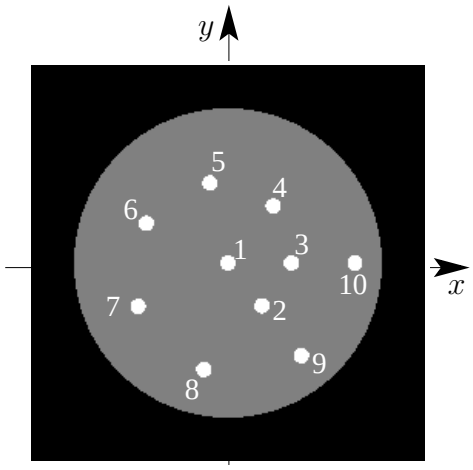

Figure C.4. A slice of phantom B. Window $[0, 100]$ HU.

Label	Distance $\|\mathbf{x_i}\|$ (cm)	Distance $\|\mathbf{x_i}\|/\Gamma$
1	0	0
2	3.536	0.062
3	4.125	0.072
4	4.714	0.083
5	5.304	0.093
6	5.893	0.103
7	6.482	0.114
8	7.071	0.124
9	7.661	0.134
10	8.25	0.145

Table C.3. Distance from each insert to the origin in phantom B.

- $R_P = 8$ cm.
- $R_I = 0.5$ cm.
- $R_C = 5.5$ cm.

The position of the inserts corresponds to points at equiangular intervals on a circle of radius R_C. It is calculated as follows

$$\begin{cases} x_i &= R_C \cos(\theta_i) \\ y_i &= R_C \sin(\theta_i) \end{cases} \quad \text{with} \quad \theta_i = (i-1)\frac{2\pi}{6} \quad \text{for} \quad i = 1 \ldots 6. \tag{C.4}$$

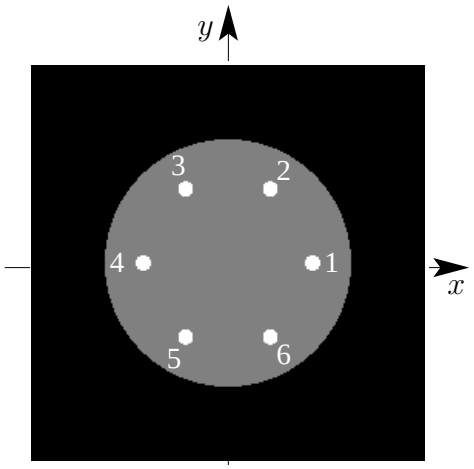

Figure C.5. A slice of phantom C. Window $[0, 100]$ HU.

Label	Frequency (ν_i) $\times \frac{1}{T_{2\pi}}$
1	0.134
2	0.268
3	0.4
4	0.534
5	0.668
6	0.8

Table C.4. Frequencies for the inserts in phantom C.

C.2.4. PHANTOM D

This phantom is used to measure the error due to data inconsistencies. It consists of a cylinder with an attenuation value of 50 HU with a single cylindrical insert situated at the origin. The insert has a time dependent attenuation value following the sinusoidal law (C.1). The frequency of the insert is highest frequency that can be reproduced with the TIA-TFDK algorithm, i.e. $0.8/T_{2\pi}$. The phantom geometry is determined by the phantom radius R_P and the radius of the insert R_I. These are respectively

- $R_P = 8$ cm.
- $R_I = 0.5$ cm.

C.2.5. PHANTOM E

Phantom E has the geometry of phantom C. The difference lies in the attenuation law of the cylindrical inserts which now follows

$$\mu_i(t) = C_i \, (t - p_1)^{p_2} \, e^{-\frac{t-p_1}{p_3}}. \tag{C.5}$$

Parameter	Value
p_1	5
p_2	2.3
p_3	3

Table C.5. Parameters for the gamma variate temporal law.

The values of the parameters $p1, p2$ and $p3$ are chosen so that the curve represents a physiological time attenuation curve. They are given in table C.5.

Each insert has a maximum value of the enhancement which is determined by the parameter C_i. The values of C_i are chosen so that the maximum value of the enhancement is 10, 18, 26, 34, 42 and 50 HU.

APPENDIX D.

COMPUTATIONAL COMPLEXITY ANALYSIS

D.1. INTRODUCTION

In this appendix we provide detailed expression for the computational cost of the temporal interpolation approach presented in section 4.4.3. Our goal is to show that the contribution of the interpolation step to the total computational cost in the TIA-FDK algorithms can be neglected when compared to the cost of FDK-like reconstruction. As a consequence of this, the computational complexity of these algorithms can be expressed in terms of *equivalent FDK reconstructions* as stated in section 4.4.3.4. We derive the result for the TIA-TFDK algorithm. The derivation for TIA-CFDK and the TSA-FDK approaches follows the same general lines.

The computational complexity is expressed in terms of the elementary operations given in table D.1 and of the reconstruction parameters given in table D.2.

Operation	Symbol
Product	P
Addition	S
Division	D

Table D.1. Elementary operations for the computational cost analysis.

Parameter(s)	Symbol(s)
Number of pixels of the detector	$N_u \times N_v$
Number of acquired views	N_β
Size of the reconstructed image	$N_x \times N_y \times N_{sl}$
Number of frames in the output sequence	L_{fr}
Number of performed scans	L_S
Efficiency factor	$\eta = L_{fr}/(2L_S)$
Order of the polynomial splines	n
Number of angular intervals for TIA	N

Table D.2. Reconstruction parameters for the computational cost analysis.

D.2. Computation Cost of PBB Reconstruction and Interpolation

The TIA-TFDK algorithm, described in section 4.4.3.1, is composed of two main steps. The first one consists in the reconstruction of N partial block backprojections using the T-FDK algorithm. Subsequently intermediate values of the PBBs are estimated by interpolating a polynomial spline. In this section we provide expressions for the computational cost of these steps. For the sake of simplicity, the detailed expression of the computational cost is only given for the steps which are relevant for the derivation in the next section.

Cost of T-FDK Reconstruction

The algorithm is described in section 3.3.3.1. Backprojection is performed with projection matrices in homogeneous coordinates as presented in [Wiesent et al., 2000].

We denote by C_{Reb} the cost of rebinning the N_β projections in a full-rotation and by C_F the cost of filtering them. For every voxel and every projection the backprojection step can be decomposed into the following parts:

- Find the filtered value by multiplying the voxel coordinates with a 4×3 projection matrix in homogeneous coordinates:

$$C_B^1 = 12 \times P + 9 \times S. \tag{D.1}$$

- Weighting the obtained value: C_W.
- Bilinear interpolation of 4 projection values:

$$C_B^2 = 4 \times P + 3 \times S + 1 \times D. \tag{D.2}$$

- Accumulation:

$$C_B^3 = 1 \times S. \tag{D.3}$$

The cost of backprojection for $\times N_x \times N_y \times N_{sl}$ voxels and N_β projections is

$$\begin{aligned} C_B &= \left(C_B^1 + 4 \times C_W + C_B^2 + C_B^3\right) \times N_x \times N_y \times N_{sl} \times N_\beta \\ &= (16 \times P + 13 \times S + 1 \times D + 4 \times C_W) \times N_x \times N_y \times N_{sl} \times N_\beta. \end{aligned} \tag{D.4}$$

Finally, the total cost of T-FDK reconstruction for L_S scans is

$$C_{TFDK} = (C_{Reb} + C_F + C_B) \times L_S. \tag{D.5}$$

Cost of Spline Interpolation

The approach for efficient computation of polynomial spline interpolation is described in section 4.4.2. Details on particular parts of the algorithm can be found in [Unser et al., 1993b].

In the TIA-TFDK algorithm, the samples of the jth PBB are combined with the samples of the $(j + N/2)$th PBB. Since L_S scans are performed, the sequence to interpolate has length $2 \times L_S$. The output sequence has length L_{fr}. Therefore, for every scan $\eta = L_{fr}/(2L_S)$ interpolated

values are computed. The spline interpolation algorithm consists in two main steps. First, the spline coefficients are computed by IIR filtering of the input samples with the filter $1/\hat{B}(e^{i2\pi\nu'})$. Second, the interpolated values are computed by FIR filtering. Filtering the obtained coefficients with the FIR filter $\hat{B}^{n,\delta}(e^{i2\pi\nu'})$, a sequence of values of the continuous spline at positions shifted by δ from the last sample is obtained. This operation is repeated η times to obtain the PBB values for all output frames. Finally, the interpolated PBBs are accumulated. This process is repeated for every voxel in every partial block backprojection.

The IIR filtering step consists of the following parts:

- Computation of the zeros of $\hat{B}(e^{i2\pi\nu'})$ for a given n: C_z. This is performed only once in the dynamic reconstruction algorithm.
- For a given interpolation order n, the IIR filter $1/\hat{B}(e^{i2\pi\nu'})$ is decomposed into $\lfloor n/2 \rfloor$ symmetric elements. The computational cost of every symmetric element filtering is
  - for the first term:

$$C_{SE}^1 = (2 \times L_S - 2) \times 2 \times P + (2 \times L_S - 1) \times S + P, \tag{D.6}$$

  - and for the rest of the terms:

$$C_{SE}^2 = 2 \times [(2 \times L_S - 1) \times P + (2 \times L_S - 1) \times S]\,. \tag{D.7}$$

  The total cost of filtering $\lfloor n/2 \rfloor$ with a symmetric element is

$$\begin{aligned} C_{SE} &= (C_{SE}^1 + C_{SE}^2) \times \lfloor \frac{n}{2} \rfloor \\ &= (8 \times L_S \times P - 5 \times P + 6 \times L_S \times S - 3 \times S) \times \lfloor \frac{n}{2} \rfloor. \end{aligned} \tag{D.8}$$

  The obtained coefficients are then multiplied by a constant c_0

$$C_{c_0} = 2 \times L_S \times P. \tag{D.9}$$

  The cost of IIR filtering for $N_x \times N_y \times N_{sl}$ voxels and $N/2$ PBBs is

$$\begin{aligned} C_{IIR} &= (C_{SE} + C_{c_0}) \times N_x \times N_y \times N_{sl} \times \frac{N}{2} + C_z^{Sp} \\ &= [(8 \times L_S \times P - 5 \times P + 6 \times L_S \times S - 3 \times S) \times \lfloor \frac{n}{2} \rfloor \\ &+ 2 \times L_S \times P)] \times N_x \times N_y \times N_{sl} \times \frac{N}{2} + C_z^{Sp}. \end{aligned} \tag{D.10}$$

The FIR filtering step consists of the following parts:

- Computation of the coefficients of the FIR filter $\hat{B}^{n,\delta}(e^{i2\pi\nu'})$ for every interpolated value

$$C_{FIR}^1 = C_\delta \times \eta. \tag{D.11}$$

  This is performed only once for every PBB ($N/2$ times).

- Computation of L_{fr} filtered values

$$C^2_{FIR} = (n \times P + (n-1) \times S) \times L_{fr}. \tag{D.12}$$

The cost of FIR filtering for all voxels and all PBBs is

$$\begin{aligned} C_{FIR} &= C^1_{FIR} \times N + C^2_{FIR} \times N_x \times N_y \times N_{sl} \times N \\ &= C_\delta \times \eta \times N + (n \times P + (n-1) \times S) \times L_{fr} \\ &\times \quad N_x \times N_y \times N_{sl} \times N. \end{aligned} \tag{D.13}$$

The total cost of interpolation is

$$C_{INT} = C_{IIR} + C_{FIR}. \tag{D.14}$$

D.3. Computational Cost of TIA-TFDK

The computational cost of the TIA-TFDK algorithm is the sum of the costs of the PBB reconstruction, interpolation and accumulation steps:

$$C_{TIA-TFDK} = C_{TFDK} + C_{INT} + C_{AC}, \tag{D.15}$$

where

$$C_{AC} = 2 \times S \times L_S \times N_x \times N_y \times N_{sl} \times \frac{N}{2}. \tag{D.16}$$

In order to be able to compare C_{TFDK}, C_{AC} and C_{INT} we need first to simplify C_{INT}. For this purpose, we use the following information

- N_x, N_y and N_β are of the same order of magnitude. Typically > 500.
- n, η and N are of the same order to magnitude. Typically < 16.
- The number of scans is typically $L_S > 8$.

In (D.10), the term C_z is not affected by the factor $N_x \times N_y \times N_{sl}$ and the terms within the parentheses not multiplied by L_S can be neglected. This leads to

$$C_{IIR} \approx \left[(8 \times P + 6 \times S)\lfloor\frac{n}{2}\rfloor + 2 \times P\right] \times L_S \times N_x \times N_y \times N_{sl} \times \frac{N}{2}. \tag{D.17}$$

In a similar way, we can simplify (D.13)

$$C_{FIR} \approx [n \times P + (n-1) \times S] \times 2 \times \eta \times L_S \times N_x \times N_y \times N_{sl} \times \frac{N}{2}. \tag{D.18}$$

With these approximations we get the following expression for the cost of the interpolation step and accumulation

$$\begin{aligned} C_{INT} + C_{AC} &\approx \left[(8 \times \lfloor\frac{n}{2}\rfloor + 2 \times n \times \eta + 2) \times P + (6 \times \lfloor\frac{n}{2}\rfloor + 2 \times (n-1) \times \eta + 2) \times S\right] \\ &\times \quad L_S \times N_x \times N_y \times N_{sl} \times \frac{N}{2}. \end{aligned} \tag{D.19}$$

We rewrite the cost of T-TFDK reconstruction of L_S scans using (D.4) and (D.5)

$$\begin{aligned} C_{TFDK} &= C_{Reb} \times L_S + C_F \times L_S \\ &+ (16 \times P + 13 \times S + 1 \times D + 4 \times C_W) \\ &\times L_S \times N_x \times N_y \times N_{sl} \times N_\beta. \end{aligned} \tag{D.20}$$

If we compare (D.20) and (D.19) we observe that the term in second line of (D.20) and the term in the first line of (D.19) are of the same order of magnitude. These terms, however, are affected by multiplicative factors which only differ in the last term which is N_β for C_{TFDK} and $N/2$ for C_{INT}. Since in general N_β is at least one order of magnitude larger than N, we can conclude that the $C_{INT} + C_{AC}$ is negligible compared to C_{TFDK}. Hence, we can write

$$C_{TIA-TFDK} \approx C_{TFDK} = (C_{Reb} + C_F + C_B) \times L_S. \tag{D.21}$$

Equation (D.21) proves that the computational cost of the TIA-TFDK algorithm can be estimated as the cost of performing L_S full-scan reconstructions with the T-FDK algorithm. Furthermore, the expression obtained does not depend on the number of frames of the output sequence. This results can be easily generalised to TIA-CFDK and the TSA-FDK algorithms. This is summarised in the following statement

Statement D.1 *The computational cost of the TIA-FDK and TSA-FDK approaches*

- *is approximately the cost of the full-scan FDK-like reconstructions of the data acquired, and*
- *it is independent of the number of frames of the output sequence.*

We finalise this appendix with a comparison of the computational cost of reconstruction with the TIA-TFDK algorithm and with standard reconstruction as described in section 4.2. In standard reconstruction each frame is computed independently using static reconstruction techniques. For the purpose of our comparison, we assume that every frame is reconstructed with the T-FDK algorithm from projections in a half-scan. The cost of the reconstruction of L_{fr} is then

$$C_{STD} = (C_{Reb} + C_F + C_B) \times L_{fr}/2, \tag{D.22}$$

where the factor $1/2$ comes from the short-scan reconstruction. If we compute the ratio between (D.22) and (D.21), we get

$$\frac{C_{STD}}{C_{TIA-TFDK}} \approx \frac{L_{fr}}{2L_S} = \eta. \tag{D.23}$$

Hence, the computational cost of the reconstruction with TIA-TFDK is η times lower than with the standard reconstruction algorithm. This justifies the name of efficiency factor for η.

INDEX

BIBLIOGRAPHY

[Aldroubi et al., 1992] Aldroubi, A., Unser, M., and Eden, M. (1992). Cardinal spline filters: stability and convergence to the ideal sinc interpolator. *Signal Processing*, 28:127–138.

[Barret and Myers, 2004] Barret, H. H. and Myers, K. J. (2004). *Foundations of image science*. Wiley.

[Barret and Swindell, 1981] Barret, H. H. and Swindell, W. (1981). *Radiological imaging*, volume I, II. Academic Press.

[Blomley and Dawson, 1997] Blomley, M. J. K. and Dawson, P. (1997). Bolus dynamics: theoretical and experimental aspects. *The British Journal of Radiology*, 70:351–359.

[Bonnet et al., 2003a] Bonnet, S., Koenig, A., Hugonnard, P., and Grangeat, P. (2003a). Time delay analysis in online 4-D CT. In *Fully 3D Image Reconstruction Meeting in Radiology and Nuclear Medicine*, Saint Malo, France.

[Bonnet et al., 2003b] Bonnet, S., Koenig, A., Roux, S., Hugonnard, P., Guillemaud, R., and Grangeat, P. (2003b). Dynamic X-ray computed tomography. *Proceedings of the IEEE*, 91:1574–1587.

[Bracewell, 1978] Bracewell, R. N. (1978). *The Fourier transform and its applications*. McGraw-Hill, 2nd edition.

[Dössel, 2000] Dössel, O. (2000). *Bildgebende Verfahren in der Medizin. Von der Technik zur medizinischen Anwendung*. Springer.

[Eckel, 2000] Eckel, B. (2000). *Thinking in C++*, volume I. Prentice Hall, 2nd edition.

[Edelman et al., 1996] Edelman, R. R., Hesselink, J. R., and Zlatkin, M. B., editors (1996). *Clinical magnetic resonance imaging*, volume 1. Saunders, 2nd edition.

[Farabee, 2006] Farabee, M. (2006). Online biology book: glossary. `http://www.emc.maricopa.edu/faculty/farabee/BIOBK/BioBookglossC.html`. Retrieved June 2006.

[Feldkamp et al., 1984] Feldkamp, L. A., Davis, L. C., and Kress, J. W. (1984). Practical cone-beam algorithm. *Journal of the Optical Society of America*, 1:612–619.

[Fessler, 2000] Fessler, J. A. (2000). *Handbook of medical imaging*, volume II, chapter 8: statistical image reconstruction methods for transmission tomography, pages 1–70. SPIE Bellingham.

[Fuchs, 2006] Fuchs, T. (2006). Noise simulation. `http://www.imp.uni-erlangen.de/forbild/deutsch/results/index.html`. Retrieved June 2006.

[Grangeat et al., 2002] Grangeat, P., Koenig, A., Rodet, T., and Bonnet, S. (2002). Theoretical framework for a dynamic cone-beam reconstruction algorithm based on a dynamic particle model. *Physics in Medicine and Biology*, 47:2611–2625.

[Grass et al., 2000] Grass, M., Köhler, T., and Proksa, R. (2000). 3D cone-beam CT reconstruction for circular trajectories. *Physics in Medicine and Biology*, 45:329–347.

[Guyton and Hall, 1996] Guyton, A. C. and Hall, J. E., editors (1996). *Textbook of medical physiology*. Saunders.

[Hiriyannaiah, 1997] Hiriyannaiah, H. P. (1997). X-ray computed tomography for medical imaging. *IEEE Signal Processing Magazine*, 14:42–59.

[Hounsfield, 1973] Hounsfield, G. N. (1973). Computerized transverse axial scanning (tomography). 1. description of system. *British Journal of Radiology*, 46:1016–1022.

[Kak and Slaney, 1988] Kak, A. C. and Slaney, M. (1988). *Principles of computerized tomographic imaging*. IEEE Press.

[Kalender, 2000] Kalender, W. A. (2000). *Computed Tomography. Fundamentals. System technology. Image quality. Applications*. Publicis MCD Verlag.

[Klotz and König, 1999] Klotz, E. and König, M. (1999). Perfusion measurements of the brain: using dynamic CT for the quantitative assessment of cerebral ischemia in acute stroke. *European Journal of Radiology*, 30:170–184.

[Lauristch and Bruder, 2006] Lauristch, G. and Bruder, H. (2006). Head phantom. `http://www.imp.uni-erlangen.de/forbild/deutsch/results/head/head.html`. Retrieved June 2006.

[Li et al., 2006] Li, T., Schreibmann, E., Yang, Y., and Xing, L. (2006). Motion correction for improved target localization with on-board cone-beam computed tomography. *Physics in Medicine and Biology*, 51:253–267.

[Mallat, 1998] Mallat, S. (1998). *A wavelet tour of signal processing*. Academic Press, 1st edition.

[Miles et al., 1997] Miles, K., Dawson, P., and Blomley, M. (1997). *Functional Computed Tomography*. Isis Medical Media.

[Miles and Griffiths, 2003] Miles, K. A. and Griffiths, M. R. (2003). Perfusion CT: a worthwile enhancement? *The British Journal of Radiology*, 76:220–231.

[Murase et al., 2005] Murase, K., Nanjo, T., Ii, S., Miyazaki, S., Hirata, M., Sugawara, Y., Kudo, M., Sasaki, K., and Mochizuki, T. (2005). Effect of x-ray tube current on the accuracy of cerebral perfusion parameters obtained by CT perfusion studies. *Physics in Medicine and Biology*, 50:5019–5029.

[Natterer, 1986] Natterer, F. (1986). *The mathematics of computerized tomography*. Wiley.

[Natterer and Wübbeling, 2001] Natterer, F. and Wübbeling, F. (2001). *Mathematical methods in image reconstruction*. SIAM.

[NEMA, 2006] NEMA (2006). Digital Imaging and Communications in Medicine. `http://medical.nema.org/`. Retrieved June 2006.

[Oppelt, 2005] Oppelt, A., editor (2005). *Imaging systems for medical diagnostics*. Publicis Verlag, 4th edition.

[Oppenheim and Schafer, 1998] Oppenheim, A. V. and Schafer, R. W. (1998). *Discrete-time signal processing*. Prentice Hall.

[Papoulis, 1965] Papoulis, A. (1965). *Probability, random variables and stochastic processes*. Series In Systems Science. McGraw-Hill.

[Parker, 1982] Parker, D. L. (1982). Optimal short-scan convolution reconstruction for fan-beam CT. *Medical Physics*, 9:254–257.

[Parker, 2006] Parker, K. H. (2006). Notes for cardiovascular fluid mechanics. `http://www.bg.ic.ac.uk/Staff/khparker/`. Retrieved June 2006.

[Press et al., 2002] Press, W. H., Vetterling, W. T., Teukolsky, S. A., and Flannery, B. P. (2002). *Numerical recipes in C++. The art of scientific computing*. Cambridge University Press, 2nd edition.

[Radon, 1917] Radon, J. H. (1917). Über die Bestimmung von Funktionen durch ihre Integralwerte längs gewisser Mannifaltigkeiten. *Berichte Sächsische Akademie der Wissenschaften*, 69:262–277.

[Schaller, 1998] Schaller, S. (1998). *Practical image reconstruction for cone-beam computed tomography*. PhD thesis, Chair of Multimedia Communications and Signal Processing, Friedrich-Alexander-Universität Erlangen-Nürnberg, Germany.

[Schmidt et al., 2000] Schmidt, R. F., Lang, F., and Thews, G., editors (2000). *Physiologie des Menschen*. Springer Verlag.

[Schramm et al., 2004] Schramm, P., Schellinger, P. D., Klotz, E., Kallenberg, K., Fiebach, J. B., Külkens, S., Heiland, S., Knauth, M., and Sartor, K. (2004). Comparison of perfusion Computed Tomography and Computed Tomography Angiography source images with perfusion-weighted imaging and diffusion-weighted imaging in patients with acute stroke of less than 6 hours' duration. *Stroke*, 35:1652–1658.

[Shephard et al., 1983] Shephard, J. T., Abboud, F. M., and Geiger, S. R., editors (1983). *Handbook of physiology*, volume III. Bethesda.

[Silver, 2000] Silver, M. D. (2000). A method for including redundant data in computed tomography. *Medical Physics*, 27:773–774.

[Stroustrup, 1997] Stroustrup, B. (1997). *The C++ programming language*. Addison Wesley, 3rd edition.

[Taguchi, 2003] Taguchi, K. (2003). Temporal resolution and the evaluation of candidate algorithms for four dimensional CT. *Medical Physics*, 30:640–650.

[Teachnet, 2006] Teachnet (2006). The circulatory system. `http://www.teachnet.ie/`. Retrieved June 2006.

[Turbell, 2001] Turbell, H. (2001). *Cone-beam reconstruction using filtered backprojection*. PhD thesis, Department of Electrical Engineering, Linköping Universitet, Sweden.

[Tuy, 1983] Tuy, H. (1983). An inversion formula for cone-beam reconstruction. *SIAM Journal of Applied Mathematics*, 43:546–552.

[Unser, 2000] Unser, M. (2000). Sampling-50 years after shannon. *Proceedings of the IEEE*, 88:569–587.

[Unser et al., 1993a] Unser, M., Aldroubi, A., and Eden, M. (1993a). B-spline signal processing: part I-theory. *IEEE Transactions on Signal Processing*, 41:821–833.

[Unser et al., 1993b] Unser, M., Aldroubi, A., and Eden, M. (1993b). B-spline signal processing: part II-efficient design and applications. *IEEE Transactions on Signal Processing*, 41:834–848.

[Unser and Blu,] Unser, M. and Blu, T. Self-similarity: part I-splines and operators. *Submitted*.

[Unser and Blu, 2005a] Unser, M. and Blu, T. (2005a). Cardinal exponential splines: part I-theory and filtering algorithms. *IEEE Transactions on Signal Processing.*, 53:1425–1438.

[Unser and Blu, 2005b] Unser, M. and Blu, T. (2005b). Generalized smoothing splines and the optimal discretization of the Wiener filter. *IEEE Transactions on Signal Processing.*, 53:2146–2159.

[Wiesent et al., 2000] Wiesent, K., Barth, K., Navab, N., Durlak, P., Brunner, T., Schuetz, O., and Seissler, W. (2000). Enhanced 3D-reconstruction algorithm for C-arm systems suitable for interventional procedures. *IEEE Transactions on Medical Imaging*, 19:391–403.

[Wiesmann et al., 2004] Wiesmann, M., Bohner, G., and Klingebiel, R. (2004). Zerebrale Perfusionsbildgebung mittels Mehrschichtspiral-CT. *Klinische Neuroradiologie*, 13:92–107.

[Wintermark et al., 2002] Wintermark, M., Reichhart, M., Cuisenaire, O., Maeder, P., Thiran, J. P., Schnyder, P., Bogousslavsky, J., and Meuli, R. (2002). Comparison of admission perfusion Computed Tomography and qualitative diffusion- and perfusion-weighted Magnetic Resonance Imaging in acute stroke patients. *Stroke*, 33:2025–2031.

[Wintermark et al., 2004] Wintermark, M., Smith, W. S., Ko, N. U., Quist, M., Schnyder, P., and Dillon, W. P. (2004). Dynamic perfusion CT: optimizing the temporal resolution and contrast volume for calculation of perfusion CT parameters in stroke patients. *American Journal of Neuroradiology*, 25:720–729.

[Ye et al., 2003] Ye, Y., Zhu, J., and Wang, G. (2003). A pointwise limit theorem for filtered backprojection in computed tomography. *Medical Physics*, 30:816–822.

[Zierler, 1965] Zierler, K. L. (1965). Equations for measuring blood flow by external monitoring of radioisotopes. *Circulation Research*, 16:309–321.